University of Nottingham
UK | CHINA | MALAYSIA

School of Veterinary Medicine & Science

Blood-brain barrier "on-a-chip" model to investigate drug permeability into the brain

By Chloe Ann Whitehouse, BSc (Hons)

Thesis submitted to the University of Nottingham
for the degree of Doctor of Philosophy
September 2021

Supervisors:
Dr Stuart Paine, Associate Professor of Veterinary Pharmacology
Dr Bob Robinson, Lecturer in Reproductive Physiology & Pharmacology
Dr Cyril Rauch, Associate Professor of Physical Biology & Biophysics
All Faculty of Medicine & Health Sciences, University of Nottingham, UK.

Table of contents

List of figures

Chapter 4

Chapter 5

List of tables

Abbreviations

× g	Gravity
°	Degree
µg	Microgram
µl	Microlitre
µM	Micromolar
A-B	Apical to basal
ABC	Adenosine triphosphate binding cassette
ACC	Astrocyte co-culture
ACM	Astrocyte conditioned media
AMT	Adsorptive mediated transcytosis
ANOVA	Analysis of variants
AQP4	Aquaporin-4
ATP	Adenosine 5’-triphosphate
B2M	Beta-2-microglobulin
B-A	Basal to apical
BBB	Blood-brain barrier
BBBoaC	Blood-brain barrier on-a-Chip
BCRP	Breast cancer resistance protein
BEC	Brain endothelial cell
BMP	Basement membrane protein
BSA	Bovine serum albumin
C	Celsius
C<*t*>	Average system concentration
cAMP	3’5’-cyclic adenosine monophosphate
C_D	Concentration (donor)
CL	Clearance

cm	Centimetre
CNS	Central nervous system
CO_2	Carbon dioxide
CR	Concentration ratio
C_R	Concentration (receiver)
CSF	Cerebrospinal fluid
C_U	Concentration unbound
CYP	Cytochrome P450
Da	Daltons
DMEM	Dulbecco’s minimum essential medium
DMSO	Dimethyl sulfoxide
DNA	Deoxyribonucleic acid
ECGS	Endothelial cell growth supplement
ECM	Extracellular matrix
EDTA	Potassium ethylenediaminetetraacetic acid
EGM	Endothelial growth media
ER	Efflux ratio
EVOM	Endothelial voltmeter
FBS	Fetal bovine serum
FDA	Food & drug administration agency
FGF	Fibroblast growth factor
FITC	Fluorescein isothiocyanate
F_U	Fraction unbound
g	Gram
GDNF	Glial derived neurotrophic factor
GFAP	Glial fibrillary acidic protein
GGT	γ-glutamyl transpeptidase
HBSS	Hank’s balanced salt solution

HUVECs	Human umbilical vein endothelial cells
Hz	Herts
IgG	Immunoglobulin G
IMS	Industrial methylated spirit
iPSCs	Induced pluripotent stem cells
JAM	Junctional adhesion molecule
Kb	Ratio of $F_{,u,\ brain}$: $F_{,u,\ plasma}$
K_P	Blood to brain concentration ratio
$K_{P,UU}$	Unbound blood to brain concentration ratio
L	Litre
LCMS/MS spectrometry	Liquid chromatography- mass spectrometry/ mass
m	Metres
M	Molar
MC	Monoculture
MDCK	Madin-Darby canine kidney cells
MDR1	Multidrug resistance protein 1 (P-glycoprotein)
MEM	Minimum essential medium
mg	Milligram
min	Minute
ml	Millilitre
mM	Millimolar
MRP1	Multidrug resistance-associated protein 1
MW	Molecular weight
NGS	Normal goat serum
NTC	No template control
NVU	Neurovascular unit
OATPs	Organic anion transporting polypeptides
OATs	Organic anion transporters

OCTs	Organic cation transporters
PAMPA	Parallel artificial membrane permeability assay
P_{app}	Apparent permeability
PBEC	Primary porcine brain endothelial cell
PBS	Phosphate buffered saline
PCR	Polymerase chain reaction
PDMS	Polydimethylsiloxane
PET	Positron emission tomography
P_{exact}	Exact permeability
P-gp	P-glycoprotein (MDR1)
PS	Permeability surface area product
PVDF	Polyvinylidene fluoride
qPCR	Quantitative polymerase chain reaction
RBEC	Primary rat brain endothelial cell
RMT	Receptor mediated transcytosis
RNA	Ribonucleic acid
RO-20-1734	4-(3-Butoxy-4-methoxybenzyl)-2-imidazlidinone
RPM	Revolutions per minute
RT	Room temperature
RT-PCR	Real time polymerase chain reaction
s	Seconds
SD	Standard deviation
SDS-PAGE	Sodium dodecyl sulphate polyacrylamide
SEM	Standard error of means
SEM	Scanning electron microscopy
SLC	Solute carrier
SMA	Smooth muscle actin
SPECT	Single photon emission computerised tomography

t	Time
TAE	Tris acetate EDTA
TEER	Transendothelial electrical resistance
TLCK	Tosyl-lysyl chloromethyl ketone
T_m	Melting temperature
U	Units
UK	United Kingdom
US	United States of America
V	Volume
V_D	Volume in donor
V_R	Volume in receiver
V_U	Volume unbound
ZO	Zona occludens
Ω	Ohms

Abstract

The absence of a gold-standard *in vitro* blood-brain barrier (BBB) model in drug development is a leading cause of high attrition rates of central nervous system drugs through clinical trials. Within the past decade, porcine brain endothelial cells (PBECs) have been established as a leading candidate for BBB modelling. In conjunction, advances in microfluidics have led to a new generation of BBB "on-a-chip" (BBBoaC) models, which allow endothelial cells to be subjected to flow, resulting in the upregulation of genes associated with the BBB phenotype. However, a BBBoaC model has not yet been developed using primary PBECs.

The purpose of this study was to establish a PBEC BBBoaC model for compound permeability screening. Initially, a method was established to isolate PBECs. These cells were characterised to ensure retention of BBB phenotype; this included the implementation of scanning electron microscopy to reveal, for the first time, the detailed surface structure of cell-cell junctions in PBEC cultures, and the novel identification of VE-cadherin expression.

Using Transwell cultures of PBECs, it was shown that the BBB phenotype of PBECs was closer to *in vivo* physiology than an immortalised cell line, HBEC-5i. Furthermore, the PBEC phenotype could be improved through co-culture with immortalised astrocytes. However, drug transport studies undertaken in the PBEC Transwell model may suggest that paracellular movement of compounds is the dominant transport process taking place, which could be indicative of "leaky" cell-cell junctions.

From the static Transwell model, two microfluidic BBBoaC models were developed from PBEC and HBEC-5i cultures. Comparison of the BBBoaC seeding protocols for both cell types showed that PBECs required more adaptations to maintain the cells under flow. However, in spite of more complex technical requirements, PBECs grown in the microfluidic chip showed an increased ability to withstand shear stress by comparison to HBEC-5i cells. Therefore, this project has established a methodology to culture a novel PBEC-BBBoaC model, however, further refinement will be required to establish this model as a candidate for use within drug development.

Covid-19 statement

The work undertaken for the submission of this Thesis commenced on the 2nd of October 2017. The School of Veterinary Medicine & Science at the University of Nottingham closed laboratories as a part of the national Covid-19 lockdown from the 13th of March 2020 until the 2nd of August 2020. Consequently, 20 weeks of laboratory time were lost in total. Furthermore, upon return to research in August, tissue collections from the abattoir were closed until November 2020, creating a bottleneck in the availability of primary porcine brain tissue for cell isolations during this period. Additionally, in order to comply with social distancing laws, laboratory occupancy was extremely limited from August 2020 until July 2021, resulting in a loss of 50% of available research hours to conduct the project. Social distancing laws also prevented the commencement of a laboratory placement at Vertex Pharmaceuticals, Oxford, where the drug transport studies were due to take place.

Multiple mitigations were put in place to compensate for the loss of time and lack of access to necessary laboratory facilities. Firstly, while abattoir access was not possible from August to November 2020, work was replaced with a commercially available human immortalised brain endothelial cell line, which was used as a comparison to the porcine brain endothelial cells. Secondly, the drug transport studies were conducted on a PBEC Transwell blood-brain barrier model instead of the blood-brain barrier on a chip model, in order to allow more time for further development of the latter model. Finally, drug transport study samples had to be shipped to Vertex Pharmaceuticals to be analysed by LC-MS/MS remotely, however, this led to the drug transport studies needing to be repeated in entirety due to transport damage of samples from the initial drug transport studies.

In summary, the work conducted for the submission of this Thesis has been adversely affected by the Covid-19 pandemic in myriad ways, resulting in the presentation of results which have been revised and modified as a consequence of the global unprecedented circumstances.

Acknowledgements

Embarking on a PhD once seemed like an insurmountable mission, and it is one which I would not have been able to complete without the many incredible people who have helped me along this journey.

Firstly, I would like to thank my supervisors at the University of Nottingham, Dr Stuart Paine, Dr Bob Robinson, Dr Cyril Rauch, and my industrial supervisors at Vertex Pharmaceuticals, Dr Peter Eddershaw and Dr Howard Mellor, for their academic expertise and feedback throughout the project. I would also like to acknowledge those whose extra work helped to make this project possible during the pandemic, including Chelsey Cartwright at Vertex, Mel Hagarty for technical assistance with microtome, and Andrew and the team from RB Elliot & Son.

I am so grateful for the friendship which I have experienced during these years, particularly my wonderful B31 friends (Mirelle, Jemma, James, Caleb, Colman, Scott, Kieran, Hayley & Lucy); you were often the reason I showed up on the hardest of days, and you all made me laugh so much that I could never remember to stop my gel from running over in the lab. Also, to my undergraduate friends (Jack, James, Liberty, Asta & Desi), who have been my family in Nottingham for these past 7 years, all of which have been filled with endless happy memories and will forever remain utterly unforgettable.

I would like to thank my partner, Leonard, who has been my biggest fan, my backbone, and my comic relief during these years; you are the best. I would also like to express my love and eternal gratitude to my mom, dad & Becky, who all deserve honorary degrees in biology from listening to me talk incessantly about cells for years on end. I would not be the person I am today without your support and endless encouragement; I can never thank you enough.

Finally, a huge thank you to all of my friends and family who read this thesis in preparation for submission and to my funders BBSRC and Vertex Pharmaceuticals whose financial support made this project possible.

Declaration

I declare that the work presented in this thesis was carried out in accordance with the requirements of The University of Nottingham regulations.

The work is original except as indicated by specific references in the text, and the work has not been submitted for any other academic award at The University of Nottingham or any other institutions.

Name: Chloe Whitehouse

Date: 26/08/2021

Signed: 

Chapter 1

Introduction

1.1 Project background

The lack of effective pharmacological treatments for diseases of the central nervous system (CNS) is a prominent issue within our society. Neurological conditions have a high prevalence, with 1 in 6 people suffering from a form of CNS disease (The Neurological Alliance, 2019). Furthermore, neurological disorders are associated with a 39% increase in deaths in the period of 2001-2014, by comparison with a 6% fall in all-cause deaths (Public Health England, 2018). Thus, the need for effective drugs for common CNS disorders has never been higher.

The bottleneck in production of effective CNS therapeutics can be attributed to designing drugs which are able to overcome three challenges unique to the CNS. Firstly, the incomplete understanding of the multifaceted pathologies underlying most neurological disorders. Secondly, the intrinsic complexity of the brain architecture that prevents compounds reaching targets. Finally, the lack of clinically relevant *in vivo* and *in vitro* pharmacokinetic models. These rate-limiting factors manifest themselves in the high attrition rates of CNS drugs throughout clinical trials; CNS drugs are less than half as successful in FDA approval as non-CNS drugs in the United States (Pardridge, 2012).

The major hurdle to overcome in CNS drug permeability is the restrictive nature of the blood-brain barrier (BBB), which limits the size and structure of compounds that can pass from the blood to the brain compartment (Abbott et al., 2006). The BBB is formed by extremely tight junctions between endothelial cells of the brain microvasculature, eliminating the paracellular diffusion of drug-like molecules and forcing molecules through the transcellular pathway (Liu et al., 2012). High concentrations of metabolic enzymes and non-specific efflux transporters work in addition to the restricted paracellular permeability to limit the entry of 98% of all small molecule drugs, and 100% of all biologics without a transport mechanism, to the CNS (Pardridge, 2005). It is, therefore, imperative to characterise the permeability of the BBB to a novel compound as early as possible in the drug development process.

Many *in vitro* models are currently used within the pharmaceutical industry as affordable and simplified models of the BBB (Wilhelm et al., 2011). However, within recent years the BBB has been shown to have a dynamic and complex structure, which is dependent upon signalling from many external sources (Hayashi et al., 1997; Wang et al., 2020). The majority of widely used *in vitro* BBB models do not allow for a realistic representation of shear-stress, which has been shown to have a significant effect upon the expression and translocation of endothelial cell proteins (Cucullo et al. 2011). It is this limitation, alongside recent developments in microfluidic technologies, which have driven the development of a new generation of dynamic *in vitro* models known as “BBBs- on-a-Chip” (BBBoaC) models (Wilhelm & Krizbai, 2014).

In their simplest form, BBBoaC models consist of “vascular” and “CNS” chambers within a plastic “chip”. The two compartments are separated by a semi-permeable membrane, which allows free movement of molecules between compartments unless diffusion is restricted by the *in vitro* “BBB” (Oddo et al., 2019). BBBoaC models aim to surpass the standards set by current BBB models by maintaining a flow of media through the artificial vasculature, mimicking *in vivo* haemodynamic flow. This project has built upon the foundations presented in published literature in the aim of developing a novel BBBoaC model for use in drug permeability screening in the pharmaceutical industry.

1.2 Evolution and discovery of the BBB

Over the course of evolution, neural tissue has become larger and more centralised, providing the selective advantage of increased control over bodily function and an increased ability of animals to interact with their surroundings. However, a larger and more centralised nervous system requires a more efficient system to deliver nutrients and clear waste, therefore, the CNS evolved in conjunction with a dense vascular system (Mastorakos & McGavern, 2019). Alongside an increase in the surface area for nutrient transport and waste clearance, the modern vertebrate vascular system in the CNS has an increased surface area for the diffusion of potentially harmful xenobiotics. Since the CNS regulates vital for life functions, and neuronal cell division is limited, restricted

transfer of molecules between the blood and brain compartments has a strong selective advantage (Niven & Chittka, 2016).

It has been proposed that when a semblance of the BBB first evolved, the barrier was formed by glial cells (Bundgaard & Abbott, 2008). However, specialisation in the roles of glial cell types within the CNS led to the divergence of pathways, and the evolution of an endothelial BBB with tight junctional adhesion took place; it is suggested that the endothelial BBB evolved separately six times across history, proving its strong selective advantage (Niven & Chittka, 2016).

The first concept of a compartmentalised CNS in scientific research was evident in the work of Paul Ehrlich in 1885 (Ribatti et al., 2006). Ehrlich injected a vital dye into the bloodstream of animals and examined the distribution throughout the organs. As expected, the dye was observed in all parts of the body other than the CNS. Erhlich explained this phenomenon as lack of absorption into the CNS. Edwin Goldman (a student of Erhlich) continued Ehrlich's work in 1909. Goldman demonstrated that the dye could permeate the CNS after injection directly into the cerebrospinal fluid (CSF), whilst the rest of the body remained unstained (Pardridge, 1983). Thereafter, the concept of a barrier between the brain and blood compartments came to be recognised.

1.3 Structure & function of the BBB

As stated, the BBB controls the transport of critical nutrients and waste products in and out of the CNS, maintaining the carefully regulated microenvironment needed for neuronal signalling. The BBB is fundamentally formed by a continuous monolayer of endothelial cells that line the microvessels within the CNS which express tight junctional adhesion proteins, efflux transporters and metabolic enzymes. Supportive cells within the neurovascular unit (NVU), and shear stress, induce and maintain the unique BBB characteristics of the endothelial cells (Cucullo et al., 2011). Figure 1.1 demonstrates the overall structure of the BBB within brain microvessels.

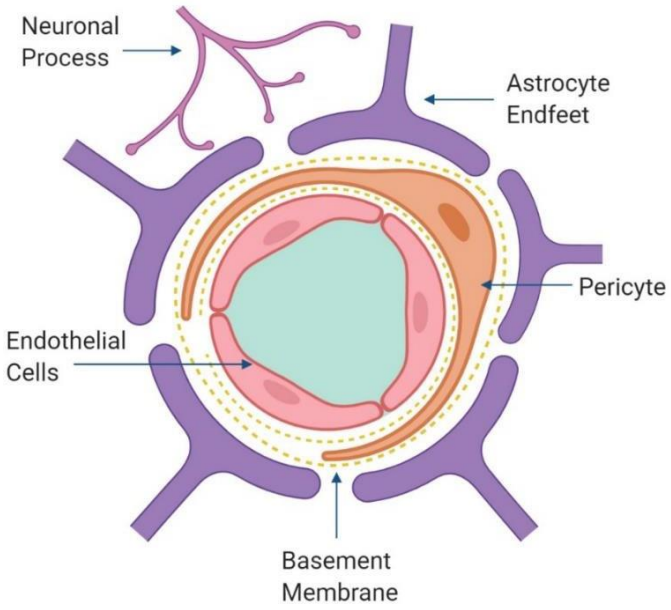

Figure 1.1 - *An overview of BBB structure within a cross section of a brain microvessel. The blood vessel is formed from endothelial cells, and surrounded by pericytes, astrocyte endfeet and being contacted by a neuronal process. Basement membrane is indicated by the yellow dashed line. Adapted from Abbott et al., 2006.*

1.3.1 Junctional adhesion between BECs

The junctional integrity between brain endothelial cells (BECs) forms the physical component of the BBB, restricting the entry of large and polarised molecules into the CNS. The BBB also restricts ion movement across the endothelial membrane, which creates an electrical potential difference between the blood and brain compartments. The potential difference across the membrane is commonly reported in literature as units of resistance per unit of surface area, known as transendothelial electrical resistance (TEER, $\Omega.cm^2$). *In vivo* TEER values have been reported between 1000 and 6000 $\Omega.cm^2$ in rats (Butt et al., 1990).

Two groups of proteins maintain the junctional adhesion between the BECs: tight junctions and adherens junctions. The tight junction group of proteins are claudins, occludin and junctional adhesion molecules (JAMs). Claudins are bound homotopically to other claudins on adjacent cells to form the primary tight junction seal, while occludin forms heteropolymers with claudins and plays a larger role in regulating tight junctions through phosphorylation. Claudins,

occludin and JAMs are all associated with the accessory zona occludens proteins (ZO-1, ZO-2, and ZO-3) which connect these primary membrane proteins to the actin cytoskeleton of the cell (Lochhead et al., 2020; Stamatovic et al., 2016).

The adherens junction group is made up of cadherin-catenin complexes. VE-Cadherin is recognised as a major adherens junction protein, binding to the actin cytoskeleton through alpha and beta catenins (Tietz & Engelhardt, 2015). Figure 1.2 illustrates the organisation of key tight junction and adherens junction proteins and their interactions within BECs.

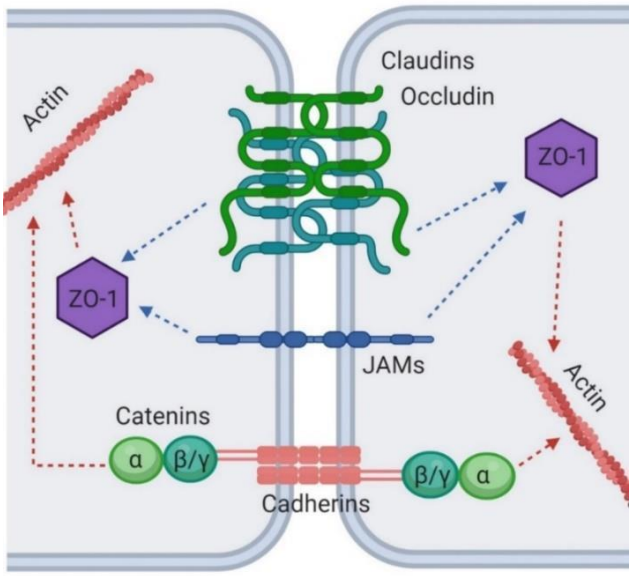

Figure 1.2 – *A simplified schematic of junctional adhesion proteins at endothelial cell junctions in the BBB. Tight junctions (claudins, occludin & JAMs) and adherens junctions (catenins & cadherins) are shown alongside ZO-1 and the actin cytoskeleton. Blue dashed arrows indicate interactions between Junction proteins and ZO-1, and red dashed arrows indicate interactions with the actin cytoskeleton.*

1.3.2 The role of ABC transporters at the BBB

In addition to tight junction proteins, BECs express high levels of adenosine 5'-triphosphate-binding cassette (ABC) transporters compared with other endothelial cell types. ABC transporters are a superfamily of multi-domain membrane proteins, which are classified into seven subfamilies (ABCA-ABCG) (Mahringer & Fricker, 2016). ABC transporters act as an additional line of defence; they are responsible for the efflux of a heterogeneous range of

substrates, from ions to large molecules, and the mechanism underlying this function is not well-defined within published literature (Zhang, 2010). ABC transporters can be responsible for the efflux of lipophilic drug-like compounds, limiting the efficacy of novel CNS drugs designed to enter the brain via transcellular transport. Therefore, awareness and analysis of ABC transporters is critical in any BBB model, as a change in expression levels may result in discrepancies in drug penetration data. The major ABC transporters that have been identified as an obstacle to CNS drug penetration are P-glycoprotein/MDR1 (P-gp) (ABCB1), BCRP (ABCG2), and MRP1 (ABCC1) (Morris et al., 2017).

P-gp (MDR1) was the first ABC transporter to be identified in BECs (Miller, 2010). P-gp is highly conserved in the BECs of many mammalian species and serves as a critical defence mechanism in the mammalian CNS (Borst & Schinkel, 2013). For example, the accumulation of toxic compounds in the CNS increases 10-100-fold in rodent models which have P-gp knocked out (Löscher & Potschka, 2005). The ability to efflux an unlimited number of substrates is an intrinsic property of P-gp, as P-gp can bind with a broad range of compounds with seemingly no structural similarities (Gomez-Zepeda et al., 2020). In 2011, Rauch proposed an “oscillating transporter” hypothesis, where the transporter fluctuates between an open and closed state to stochastically catch drugs and expel them, whilst not relying upon structural binding sites (Rauch, 2011). Another hypothesis, supported by data from Esser et al., 2017, proposes that the structure within the P-gp substrate binding pocket is continuously changing, allowing the substrate to create its own binding site within the pocket (Esser et al., 2017). The effect of P-gp upon the permeability of CNS drugs is demonstrated by the pharmacokinetic profile of Loperamide. Loperamide is an opioid derivative used to reduce gut motility without unwanted CNS side effects (Baker, 2007). However, PET studies have demonstrated that CNS permeability of ^{11}C-N-*desmethyl*-Loperamide is significantly increased when administered alongside the P-gp inhibitor, Tariquidar. Furthermore, oral administration of supratherapeutic doses of Loperamide saturates P-gp efflux transporters to cause activation of μ-opioid receptors in the CNS; this scenario is common in

patients suffering with opioid addiction (Kreisl et al., 2010). Thus, P-gp is of utmost importance when studying BBB pharmacokinetics and therefore will be considered the main ABC transporter of interest during this study.

Breast cancer-resistance protein (BCRP) was identified as a drug efflux transporter in a breast cancer cell line, but has since been identified in intestine, liver, kidney, testis, placenta, and BBB (Miller, 2010). The overlapping tissue distribution of BCRP with P-gp suggests the role of this protein in the efflux of xenobiotics. Although the role of BCRP in drug efflux at the BBB is not as defined as that of P-gp, multiple studies have demonstrated that BCRP influences the permeability of many chemotherapeutic agents into the CNS using rodent knockout models (Morris et al., 2017). Furthermore, BCRP has been implicated in both multidrug resistant cancers, epilepsy, and neurodegenerative diseases (Iorio et al., 2016). BCRP can therefore be considered a major contributor to multidrug resistance at the BBB and should, therefore, be considered when creating representative *in vitro* models.

The expression of a number of organic anion transporters from the multidrug resistance protein family (MRPs) has been quantified at the BBB, with varying levels of MRP1-MRP6 being expressed in mammalian brain capillaries from different species (Löscher & Potschka, 2005). Although there is uncertainty regarding the expression of MRP subtypes in different brain locations, and across species, there is no doubt that the ABC-C family are implicated in the efflux of a broad range of substrates from chemotherapeutics to anticonvulsants (Gomez-Zepeda et al., 2020). As BCRP and MRPs have overlapping tissue distributions and substrates with P-gp and with each other, ABC transporters at the BBB are thought to work in concert with each other to efflux a wide range of drugs with great efficacy.

1.3.3 Solute carrier transporters at the BBB

The solute carrier (SLC) transporter family is the largest family of transporters involved in the exchange of molecules across membranes in the human body (Morris et al., 2017). The SLC superfamily is classified into 65 families with 439 members, many of which are expressed at the BBB (Morris et al., 2017). SLC

transporters are typically involved in the uptake of molecules, whereas ABC transporters are mainly responsible for efflux; however, it has been reported that some SLC transporters can function in efflux or bidirectional transport (Hu et al., 2020). Thus, SLC transporters are relevant to pharmacokinetics in the context of carrier-mediated uptake of drugs, and the efflux of lipophilic compounds.

SLC families considered to be of relevance at the BBB include L-alpha amino acid transporters and monocarboxylate transporters that transport neurotransmitter precursor compounds, and the SLCO family, which consists of organic anion transporters (OATs), organic anion transporting polypeptides (OATPs), and organic cation transporters. OATs and OATPs are bidirectional transporters and are involved in the efflux of CNS drugs, such as bumetanide, across the BBB (Römermann et al., 2017). Figure 1.3 illustrates the location of critical BBB transporters on BECs.

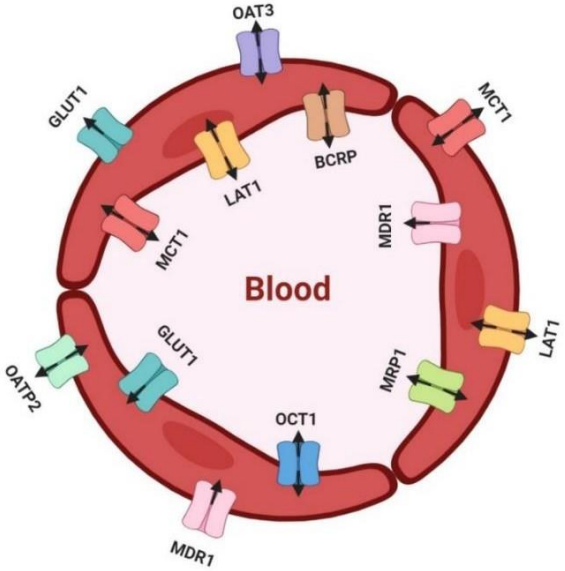

Figure 1.3 - *A schematic showing key ABC and SLC transporters expressed by BECs, using localisation data from Morris et al., 2017. Key: OCT1 – organic cation transporter 1 (SLC22A1), OAT3 – organic anion transporter 3 (SLC22A8), OATP2 – Organic anion transporter protein 2 (SLCO1B1), MCT1 – monocarboxylate transporter 1 (SLC16A1), LAT1 – L-alpha amino acid transporter 1 (SLC7A5), MDR1 – multidrug resistance transporter 1 (P-glycoprotein, ABCB1), BCRP – breast cancer resistance protein (ABCG2), MRP1 – multidrug resistance protein 1 (ABCC1).*

1.3.4 Metabolic enzymes at the BBB

Tight junctions and efflux systems work in conjunction with metabolic enzymes to prevent entry of xenobiotics to the CNS (Decleves et al., 2011). Cytochrome P450 (CYP) enzymes belong to a superfamily of enzymes responsible for the

metabolism of xenobiotics and endogenous compounds. CYP enzymes have been widely studied with regard to drug metabolism in the liver; however, CYP enzymes are also present in extra-hepatic tissues. Multiple studies have identified the presence of CYP enzymes in the brain microvasculature with the CYP1B1 and CYP2U1 isoforms being the most abundant in humans (Ghosh et al., 2011). Alongside the presence of CYP enzymes at the BBB, γ-glutamyl transferase and alkaline phosphatase have been identified, which act to dephosphorylate or transfer functional groups, respectively, from drug-like molecules. Thus, metabolism of centrally acting drugs by enzymes present at the BBB often results in polarised molecules which cannot diffuse across the transcellular pathway and may no longer bind to the sight of action (Ghosh et al. 2010). Thus, in order to be functional and physiologically representative, it is critical that any BBB model expresses high levels of functioning efflux transporters and metabolic enzymes, to provide the appropriate values of drug permeability.

1.4 The neurovascular unit

In 1981, a cornerstone study by Stewart & Wiley investigated the induction of BBB properties in microvessels by expatriating neural tissue into the gut of chick embryos. The study determined that when the tissue was vascularised by gut endothelial cells, the microvessels exhibited restricted permeability. However, when the inverse experiment took place, where gut tissue was transplanted into the brain, the resulting vascularisation was permeable, strongly indicating that the BBB phenotype was not an inherent quality of BECs, but rather a result of signalling in the surrounding tissue. At the time, it was not known which cell types were responsible for the phenotypic change (Stewart & Wiley, 1981).

It is now known that the development, maintenance, and dynamic regulation of the BBB is governed by multiple cellular and protein elements, which act to induce the BBB phenotype in BECs. These individual supportive components are grouped together, alongside the BECs themselves, to create the neurovascular unit (NVU). Astrocytes, pericytes and the basement membrane proteins (BMPs) are widely considered the main supportive components of the

neurovascular unit (NVU); however, neurons, microglia and other immune cells can also contribute to changes within the BBB (Berezowski et al., 2004) (Dohgu et al., 2005). Figure 1.1 shows a schematic of the main NVU components relative to BECs within the microvessel.

1.4.1 The NVU: pericytes

Pericytes are a widely heterogeneous cell type, taking on a range of morphologies and roles within different tissues. All microvessels within the brain are ensheathed by pericytes; the brain has the highest percentage coverage of microvessels by pericytes than any other tissue in the human body, reinforcing their critical role within the CNS (Armulik et al., 2010). Pericytes can signal directly to BECs, as both cell types express transforming growth factor-β (TGF-β) and its receptor TGFβ-R2, activation of which induces increased expression of tight junction proteins (Dohgu et al., 2005).

1.4.2 The NVU: astrocytes

Astrocytes are the most abundant cell type within the CNS; long thought to be simple cells with basic processes that support neuronal function, it is now recognised that astrocytes are a complex and dynamic signalling network (Zonta et al., 2003). Astrocytes extend long processes that contact neurons and cover the outermost layer of microvessels within the CNS, known as astrocytic perivascular endfeet. Ionic and molecular changes, primarily due to neuronal signalling, in the microenvironment surrounding an astrocyte result in the propagation of calcium waves throughout the astrocytic network (). Downstream signalling at perivascular endfeet in response to the calcium wave can result in the release of myriad signalling molecules. These signalling molecules include TGF-β, glial derived neurotrophic factor (GDNF) and basic fibroblast growth factor (bFGF) which act to increase and decrease vascular permeability through the regulation of the expression of tight junction proteins (Cheslow & Alvarez, 2016). However, it should be noted that changes in barrier tightness do not always depend on transcriptional changes, as cAMP and phosphodiesterase inhibitors cause fast and temporary increases in junctional adhesion between BECs (Ishizaki et al., 2003). As gap junctions connect BECs

within a microvessel, it is likely that permeability signals can propagate down the vascular network (Blomstrand et al., 1999). Furthermore, signalling between astrocytes and endothelial cells is reciprocal; with one study demonstrating that the addition of medium conditioned by BECs to a monoculture of astrocytes induces cellular polarisation through expression of aquaporin-4 (AQP4) (Mader& Brimberg, 2019).

The majority of research surrounding astrocyte and endothelial interactions has taken place in *in vitro* models, where the addition of astrocytes in co-culture with BECs has been shown to cause expression changes in metabolic enzymes, tight junction proteins, and transporters including GLUT1 and P-gp (Gaillard et al., 2000). As soluble signalling molecules mediate the majority of astrocyte-endothelial interactions, some of the benefits of astrocyte co-culture can be mimicked by the addition of astrocyte-conditioned medium (ACM) to cell types, which has been shown to decrease BBB permeability in *in vitro* studies (Nielsen et al., 2017). Therefore, it is evident that astrocytes and BECs within the NVU are a carefully orchestrated network, working in synchrony to produce varied and dynamic modulation of BEC phenotype and BBB permeability.

1.4.3 Basement membrane proteins

Basement membrane proteins (BMPs), alongside the interstitial matrix, form the extracellular matrix (ECM) around blood vessels in the CNS (Abbott et al. 2006). BECs, pericytes and astrocytes all contribute to the formation of the ECM, which primarily consists of structural proteins including collagen type IV, laminin, and fibronectin (Zobel et al., 2016). The ECM both connects, and functionally separates, endothelial cells from the surrounding pericytes and astrocytes (as shown in Figure 1.1), acting as an interface for the accumulation of NVU signalling molecules. However, the BMPs also directly interact with cell surface receptors to regulate gene transcription (Abbott et al., 2010). Therefore, the presence of the ECM is essential in maintaining and inducing BBB properties; for example, the addition of BMPs *in vitro* culture increases junctional adhesion between BECs and increase expression of metabolic enzymes (Zobel et al., 2016). Additionally, the presence of an ECM has also been shown to polarise

astrocytes through AQP4 expression in *in vitro* culture (Mader & Brimberg, 2019). As the aim of any BBB model is to create a physiologically representation of *the vivo* system, it is therefore imperative that BMPs are considered as an active component in the BEC culture system.

1.4.4 Shear stress and BEC phenotype

Shear stress is defined as a force that causes deformation of a material by slippage along a plane that is parallel to the imposed stress. BECs that line microvessels within the CNS are constantly exposed to shear stress due to haemodynamic flow, with flow rates within human brain capillaries ranging between 0.5 and 2.3 Pa (Wang et al., 2020). Within recent years, the importance of mechanical stress in maintaining the BBB phenotype of BECs has become widely recognised. Many studies have demonstrated that the force of shear stress upon BECs upregulates the expression of tight junction proteins, multidrug efflux transporters, CYP enzymes and regulates carrier-mediated transport and immune cell invasion across the membrane (Cucullo et al., 2011; Partyka et al., 2017; Rochfort & Cummins, 2019; Santaguida et al., 2006).

The effect of haemodynamic flow upon BBB phenotype is exerted upon BECs through many signalling pathways. Firstly, haemodynamic flow activates mechanoreceptors upon the luminal membrane of BECs. This includes the NOTCH1 receptor, which in turn affects NOTCH inducible ligands, increasing transcription factors and inducing a cell-signalling pathway that results in the activation of the shear stress response element (Jahnsen et al., 2015). Furthermore, the adherens junction protein, VE-cadherin, has been confirmed as a mechanosensory adaptor protein that is capable of transducing mechanical signals through interactions with the tight junction protein occludin, promoting junctional adhesion through tight junction modification (Wang et al., 2020). Figure 1.4 shows an overview of NVU and shear stress signalling across the BBB.

Thus, haemodynamic flow is directly responsible for limiting the paracellular transport of large and hydrophilic molecules, reducing the diffusion of small and lipophilic molecules, increasing metabolism of xenobiotics, and regulating the

disruptive barrier effects of inflammatory mediators. It is therefore evident that shear stress upon BECs will affect drug transport across the BBB into the CNS within the *in vivo* system and will be a critical component of a representative *in vitro* BBBoaC model.

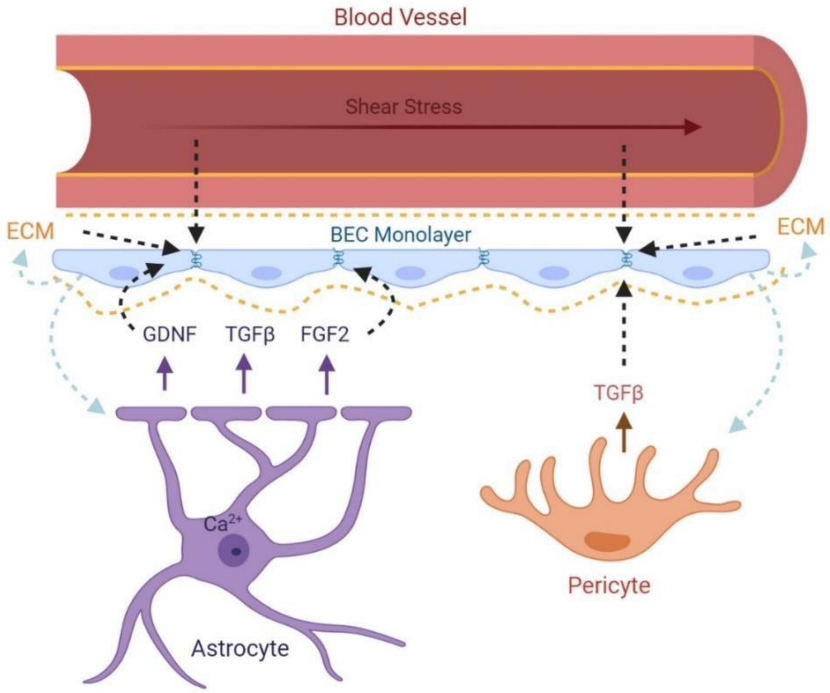

Figure 1.4 - *An illustrative overview of neurovascular unit (NVU) components: astrocytes, pericytes, extracellular matrix (ECM, indicated by yellow dashed line) and shear stress caused by haemodynamic flow in the vessel. Black dashed arrows represent signalling pathways within the NVU that directly modulate barrier integrity, and blue dashed arrows represent reciprocal signalling pathways from endothelial cells.*

1.5 Drug transport across the BBB

The molecular characteristics of the BBB, as described in the previous sections, create the perfect obstacle, one which will always need to be surpassed in the development of novel neurotherapeutics. Consequently, recent advances in the understanding of molecular neuroscience have not led to significant advancements in drug treatments of CNS diseases. As previously stated, drug compounds can pass into most peripheral tissues through the paracellular and transcellular pathways. However, tight junctional adhesion and high expression of multidrug efflux transporters between BECs at the BBB reduces paracellular entry of compounds to a negligible level. Transendothelial transport of

molecules across the BBB are split into three main routes: passive diffusion, transcytosis, and carrier mediated transport (Pardridge, 2005).

1.5.1 Drug transport: passive diffusion

Drug molecules that cross the BBB via passive diffusion have two main features: firstly, the molecular weight must be less than 500 Da, and secondly, the compound must be lipid soluble and form less than 8-10 hydrogen bonds with water (Pardridge, 2012). Thus, drugs that can cross the BBB are often altered by medicinal chemistry so as to make them more lipid soluble. A compound with increased lipid solubility will become more permeable across the BBB; however, it will also become more permeable across all biological membranes in the system, consequently increasing drug clearance. Therefore, increased lipophilicity of the drug can also minimise brain uptake as increased clearance offsets the increase caused by lipidisation (Pardridge, 2005). Furthermore, many molecules that enter via passive diffusion over the transendothelial pathway are also subject to efflux by broad-spectrum multidrug efflux transporters such as P-gp, BCRP and MRPs. One possible solution to this issue could be the administration of a co-drug, which could act as an inhibitor of the multidrug efflux transporter, to allow passive diffusion of the lipophilic small molecule drug without efflux (Löscher & Potschka, 2005).

1.5.2 Drug transport: transcytosis

Transcytosis across the transendothelial pathway is the main route of CNS entry for large molecules. Large molecules are taken into the membrane and an intracellular vesicle is formed, which will travel through the endothelial cytoplasm to fuse with the opposite membrane to release its contents. Transcytosis can take place when proteins bind to specific receptors on the cell membrane (receptor mediated transcytosis; RMT) or when positively charged molecules bind to negatively charged glycolyx in the membrane, inducing internalisation (adsorptive mediated transcytosis; AMT) (Pulgar, 2019). Since large molecule products including antibodies, recombinant proteins and gene therapies cannot enter the CNS via the paracellular pathway, delivery of large molecule drugs could be possible via molecular Trojan horses. These

therapeutic compounds could be re-engineered as a fusion protein with the molecular Trojan horse that would gain access to the CNS via RMT (Pardridge, 2007).

1.5.3 Drug transport: carrier mediated transport

Carrier mediated transport (CMT) of molecules into the CNS is dependent upon SLC transporters as discussed in Section 1.3.3. SLC transporters are responsible for the influx of essential molecules required by the CNS, however, they can also be utilised to aid drug access into the CNS by taking on the structure of a pseudo-nutrient (Morris et al., 2017). Many CNS drugs already utilise these transporters, for example, the pro-drug L-dopa and gabapentin cross the BBB using LAT transporters, and lidocaine, imipramine and propranolol all cross the BBB using OCT transporters (Tsuji, 2005). The main drug entry pathways are illustrated in Figure 1.5.

In summary, although paracellular diffusion of drug compounds is restricted at the BBB, transendothelial transport mechanisms such as RMT and CMT offer exciting potential methods for overcoming the challenge of BBB permeability. This further fortifies the need for a more reliable BBB model; one which is not only capable of measuring drug entry via passive diffusion but can also account for ABC transporter mediated efflux and also represent the advanced transport systems (RMT and CMT) which will be needed for a new generation of biotech generated biologic drugs.

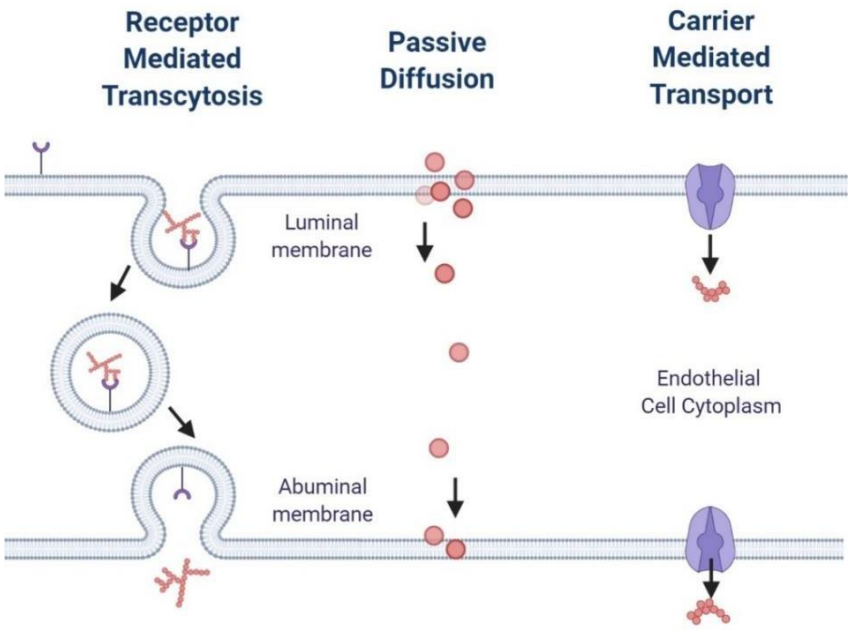

Figure 1.5 - *A schematic showing three types of drug transport across the BBB: receptor mediated transcytosis (large polar molecules), passive diffusion (small lipophilic molecules), and carrier mediated transport (small to mid-sized molecules). The diagram indicates the luminal and abluminal membranes of the BEC.*

1.6 Quantification of drug permeability at the BBB

Quantification of drug permeability across the BBB is necessary to assess the extent to which a novel drug can reach a target within the CNS and be freely available to bind. The most commonly used permeability values to describe drug penetration into the CNS include the blood-to-brain concentration ratio (K_p), unbound blood to unbound brain concentration ratio ($K_{p,uu}$), and apparent and exact permeability values (P_{app} and P_{exact}) (Di et al., 2008; Loryan et al., 2013; Weidman et al., 2016).

1.6.1 Blood-to-brain concentration ratio

The blood-to-brain concentration ratio (K_p) of a drug represents the fraction of total drug between the two compartments. The K_p value of a drug can be calculated experimentally by either 1) administering the drug into the plasma compartment and taking samples at set time points from both the plasma and the brain compartments and comparing the area under the curves of the brain and plasma total concentrations versus time graphs or 2) infusing the drug to

steady-state and comparing the blood-to-brain total concentrations (Fridén et al., 2009). However, the use of K_p as a measure of brain penetration is falling out of favour, as this value includes bound drug in calculations which would not be free to bind at the target site (Loryan et al., 2013).

1.6.2 Unbound blood to unbound brain concentration ratio

Unbound blood to unbound brain concentration ratio ($K_{p,\,uu}$) is often seen as a more useful value than K_p as this is the ratio of concentration of free drug in the brain interstitial fluid to free drug in plasma. Drug-protein binding is the reversible interaction of the drug with a protein, and according to the free drug hypothesis, only unbound drug is available to act pharmacologically at the target site.

Equation 1.1

$$Free\ drug + Free\ protein \leftrightarrow Drug\ Protein\ Complex$$

Therefore, the free (unbound) drug will represent only the drug available in the plasma compartment to cross the BBB, and the drug available within the brain compartment to bind with the target site. When the $K_{p,uu}$ value (the fraction of unbound drug in both compartments) is close to 1, this indicates that the compound that is able to freely diffuse across the barrier and is not a substrate for a multidrug efflux transporter. When $K_{p,uu}$ is greater than 1, this indicates that a drug that is a substrate for uptake transporters and is being transported into the brain through RMT or CMT. Finally, if $K_{p,\,uu}$ is less than 1, this indicates that the drug is not freely permeable across the barrier and the drug could be a substrate for a multidrug efflux transporter (Loryan et al., 2013). $K_{p,\,uu}$ can be calculated experimentally using microdialysis, however, pre-clinical *in vivo* microdialysis studies are low throughput and time consuming. $K_{p,uu}$ values can be calculated using the equation below, where the K_p value generated is multiplied by the fraction unbound in the brain ($F_{u,\,brain}$) over the fraction unbound in the blood ($F_{u,\,blood}$), calculated by equilibrium dialysis (Fridén et al., 2009).

Equation 1.2

$$Kp, uu = Kp, brain \frac{Fu, brain}{Fu, blood}$$

1.6.3 Apparent and exact permeability calculations

Apparent permeability (P_{app}) (Equation 1.3) describes the rate of transport of a compound across the BBB, and thus, can be indicative of uptake or efflux via transporter mechanisms. However, Equation 1.3 is only accurate when drug transport is linear, when there is less than 10% of the drug transported across the monolayer, and there is negligible backflow and a favourable mass balance (Palumbo et al., 2008). More recently, an alternative measure of the rate of drug transport, known as P_{exact} (Equation 1.4, 1.5), has been derived and provides a mathematical solution for the whole transport curve (Tran et al., 2004). Furthermore, P_{exact} remains accurate when there are mass balance issues (Zhang et al., 2016).

Equation 1.3

$$P_{app}\ (cm.s^{-1}) = \left(\frac{\Delta c}{\Delta t}\right).\left(\frac{V}{AC_0}\right)$$

$\Delta c/\Delta t$ = Change in receiver compartment concentration over time (mol. l^{-1}. s^{-1})

V = Volume in receiver compartment (cm^3)

A = Surface area of Transwell insert (cm^2)

C_0 = Initial concentration of compound in donor compartment (mol. l^{-1})

Equation 1.4

$$P_{exact} = -\left(\frac{V_R V_D}{(V_R + V_D)At}\right) \ln \left\{1 - \frac{\langle C_{R(t)} \rangle}{\langle C(t) \rangle}\right\}$$

V_D = Donor compartment volume (cm^3)

V_R = Receiver chamber volume (cm^3)

A = Surface area of the permeability barrier (cm^2)

t = Time of measurement (s)

$C_{R(t)}$ = Drug concentration in the receiver compartment (mol. l^{-1}) at time t

C(t)= Average system concentration of drug defined by Equation 1.5

Equation 1.5

$$\langle C(t) \rangle = \frac{V_D C_D(t) + V_R C_R(t)}{V_D + V_R}$$

C_D = Drug concentration in the donor compartment (mol. L^{-1}) at time t

1.7 Current BBB models

BBB permeability testing within the pharmaceutical industry depends upon high throughput *in vitro* testing during drug discovery and low throughput whole system *in vivo* assays during drug development. However, it is recognised that high throughput *in vitro* assays are low-cost, convenient, and quick while lacking accuracy, and whole system *in vivo* assays reveal detailed analysis of pharmacodynamic and pharmacokinetic properties of the drug, while being high-cost and requiring high levels of technical expertise. This section will examine the *in vivo* and *in vitro* assays currently most widely used within the drug discovery and development processes.

1.7.1 *In vivo* drug transport studies

The use of *in vivo* assays to examine BBB permeability of novel compounds is commonplace within the pharmaceutical industry (Pardridge, 2005). These *in vivo* experiments include: microdialysis, *in situ* perfusion, and equilibrium dialysis, all of which are invasive and usually carried out in rodents to calculate BBB permeability values such as K_p and $K_{p,uu}$ (Deguchi, 2002) (Di & Chang, 2015). There are also non-invasive techniques including single photon computed tomography (SPECT) and positron emission tomography (PET) where radiolabelled compounds are administered, and BBB permeability is examined through dynamic scanning procedures (Bickel, 2005). *In vivo* techniques are considered the most accurate form of BBB permeability assay as they use physiological tissue and, consequently, are considered the gold standard for evaluating drugs that depend upon transport mechanisms such as CMT or RMT (Bickel, 2005). However, *in vivo* experiments also have numerous disadvantages: non-invasive techniques do not allow for analysis of metabolites

present the brain tissue, while invasive techniques require the sacrifice of the animals used in the experiments, and all permeability data are subject to species differences in drug transport and metabolism (Heymans et al., 2018). In broader terms, *in vivo* assays are low throughput, costly and require specialist equipment and training, in exchange for more physiologically results than most *in vitro* techniques.

1.7.2 *In vitro* drug transport studies

No single *in vitro* model has been adopted as a standard across the pharmaceutical industry despite a huge increase in the availability and complexity of *in vitro* BBB models in recent years (Wilhelm & Krizbai, 2014). In fact, the search for an *in vitro* BBB model that offers the representative accuracy of an *in vivo* model has become a holy grail for many researchers. It is widely recognised that current BBB models used within the pharmaceutical industry leave a lot to be desired, as no widely used assay is able to mimic passive permeability, transport, and metabolic functions of the BBB (Bicker et al., 2014).

1.7.2.1 Non-cellular based *in vitro* models

Non-cellular based *in vitro* models of the BBB are high throughput and low-cost indicators of BBB permeability. The most widely used non-cellular based model for BBB permeability testing is the parallel artificial membrane permeability assay (PAMPA). The PAMPA assay was first developed to measure gut absorption of orally administered drugs but has since been optimised for BBB permeability testing with the development of the PAMPA-BBB assay (Di et al., 2009). However, it is evident that PAMPA assay is only capable of determining permeability through passive diffusion across the BEC monolayer, and as previously discussed, this is only accurate for assessing the movement of readily permeable lipophilic small molecule drugs that are not multidrug efflux transporter substrates (Section 1.5). Furthermore, the PAMPA-BBB assay does not allow for analysis of drugs that could be absorbed by CMT or RMT mechanisms.

Another widely used non-cellular method of predicting BBB permeability is through *in silico* modelling (Zhang et al., 2016). Computer models can build

structure-activity relationships through analysis of commonalities in permeable compound structures, predicting permeability depending upon molecular weight, lipophilicity, and hydrogen bond forming ability (Wang et al., 2018). Computational models are typically used during the very early phase of drug discovery and can identify molecules that are most likely to cross the barrier via passive diffusion. However, as previously discussed in Section 1.2.3, the structure-binding relationship of many multidrug efflux transporters at the BBB is poorly defined. Therefore, no current *in silico* model can accurately predict whether a compound would be subject to efflux or uptake at the BBB.

The models described offer high throughput and low-cost benefits that cannot be rivalled by any cell-based model due to the technical cell culture expertise required. However, these models could never be used in isolation, without supportive data from cellular-based systems due to the inability of these methods to account for the complex uptake and efflux mechanisms present at the BBB.

1.7.2.2 The Transwell BBB model

One of the most widely used cell-based *in vitro* models used for BBB research and during drug development is the Transwell BBB model (Bicker et al., 2014). In this model, cells are suspended upon a semi-permeable membrane insert in a cell culture well, creating apical and basal chambers that are separated by a cell monolayer. Drug permeability can be quantified in the Transwell model by administering a compound to the donor compartment and measuring the compound that has passed into the receiver compartment, across the “BBB” formed by BECs on the semi-permeable insert (Oddo et al., 2019). The Transwell system is a versatile model as different cell types can be cultured in the apical and basal compartments, as shown in Figure 1.6.

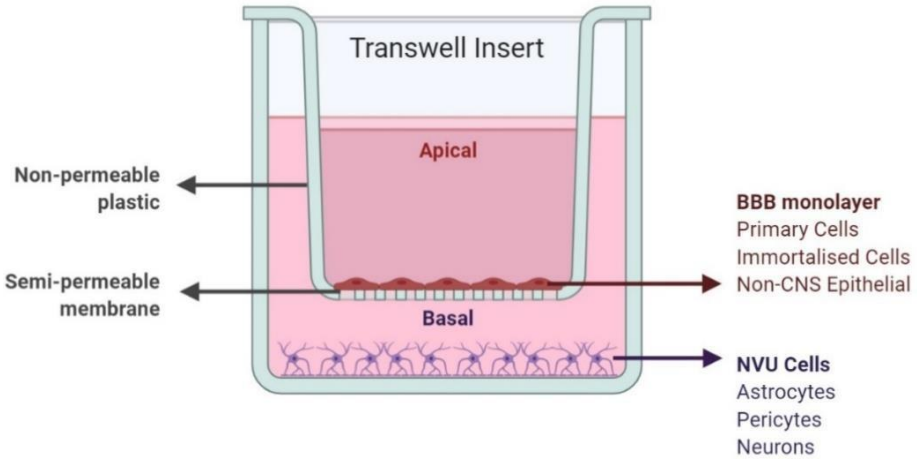

Figure 1.6 - *A diagram of a Transwell model of the BBB: the Transwell insert is placed inside a multi-well culture plate and the BBB monolayer formed is from primary BECs, immortalised BECs, or non-CNS epithelial cells upon the semi-permeable apical insert. Co-cultured NVU cells such as astrocyte, pericytes and neurons can be grown on the bottom culture well. During drug transport studies, compounds are administered to the apical compartment and permeability into the basal compartment is measured.*

There are three widely used cell types in Transwell BBB monolayers for drug permeability testing: isolated primary BECs, immortalised BECs, and immortalised non-CNS epithelial cells (Abbott, 2004). Using primary or immortalised BECs is inarguably more accurate and physiologically representative than non-endothelial alternatives. Primary BECs have been reported high TEER values in Transwell culture, and immortalised cells, although demonstrating reduced junctional adhesion, retain expression of many key BBB uptake and efflux transporters (Neilsen et al., 2017). However, these models are not well standardised for industrial use, and it is for this reason that many Transwell BBB models used within the pharmaceutical industry use immortalised non-CNS epithelial cells, which have been created for *in vitro* gut permeability testing (Hellinger et al., 2012). Human colon adenocarcinoma (Caco-2) and Madin-Darby canine kidney (MDCK) cell lines were originally developed for gut permeability screening assays but are now widely used for CNS permeability screening (Lundquist & Renftel, 2002). Variations of the cell lines have been developed to account for high expression levels of transporters, including VB-Caco-2, a high P-gp expressing vinblastine treated caco-2 cell line, and MDR1-MDCKII, which has increased P-gp expression (Hellinger et al. 2012). Previous studies have shown that these cell lines have a reasonable

correlation with BBB permeability; however, there are some discrepancies, which could be due to differences in efflux transporter expression and passive permeability (Di et al., 2009). Furthermore, another major limitation of Transwell BBB models using non-CNS epithelial cells is that these models could never be considered representative of metabolic or uptake functions of the BBB (Abbott, 2004).

Transwell culture systems allow for monoculture of the endothelial and epithelial cells on the insert, and ease of measurement of drug transport from the apical to the basal compartment. However, another benefit is the ability to co-culture the endothelial/epithelial cells with NVU cells (Bicker et al., 2014). As previously discussed, (Section 1.4.2), astrocytes induce BBB properties through the release of soluble signalling molecules. In line with these studies, including immortalised or primary astrocytes in non-contact co-culture with the above cell types (primary, immortalised, and non-CNS) increases tight junctions and expression of efflux transporters, allowing for a more representative model (Nielsen et al., 2017). However, a major limitation of the Transwell model is that the system does not allow for haemodynamic flow, and thus inductive mechanical signalling pathways from shear stress are not activated, which may result in a loss of the true BBB phenotype of the cells (Cucullo et al., 2011).

Therefore, it is evident that with both *in vitro* and *in vivo* BBB permeability assays there is a balance between convenience and accuracy of the model. It is, therefore, evident that the drug development process remains dependent upon both the costly and technical *in vivo,* and convenient high throughput *in vitro,* assays to deduce BBB drug permeability. However, a second generation of *in vitro* models which more accurately represent NVU signalling, while remaining relatively inexpensive and convenient may offer a solution to this issue.

1.8 BBB on-a-chip models

Recent advances in microfluidic technology and nanofabrication, and a new understanding of the complexities of shear stress upon cellular function, have laid the foundation for the new generation of *in vitro* simulations: “Organ on-a-Chip” models. This new and advanced group of models have been engineered

to represent microphysiological systems within the body, capable of mimicking entire organ function in just centimetres of plastic (Jiang et al., 2019). The complex issues surrounding BBB modelling in the pharmaceutical industry make the BBB an ideal candidate for “on-a-Chip” technology (Yu et al., 2020). Within the past decade, a multitude of “BBB on-a-Chip” (BBBoaC) models have been published with huge variation in methodology (van der Helm et al., 2016). In the simplest form, BBBoaC models consist of “vascular” microfluidic channels alongside “CNS” chamber, which contain endothelial and supportive NVU cells, respectively. A continuous monolayer of endothelial cells lines the vascular microfluidic channel, which are subjected to constant flow, in order to induce shear stress upon the cells and mimic the biophysical properties of the *in vivo* tissue (Oddo et al., 2019). This section will review the key features of BBBoaC models: evaluating design, cell culture, and quantification, and finally evaluating their practicality in drug metabolism and pharmacokinetic studies.

1.8.1 BBBoaC model design

An archetypal BBBoaC model would mimic the key properties of the physiological BBB: a 3D vessel-like structure, NVU cell-cell interactions, flow induced shear stress, and a permeable ECM (Oddo et al. 2019). However, BBBoaC models have a broad range of designs, which represent the above criteria to differing extents. One of the first layouts for a BBBoaC model was the “sandwich” design, which can be considered a natural evolution from the Transwell system. Much like the Transwell system, the “sandwich” design has an upper and lower PDMS chamber separated by a polycarbonate semi-permeable membrane, where the upper compartment contains BECs and lower compartment contains NVU cells (Jiang et al., 2019). However, unlike the Transwell system, this layout is formed from elongated channels where the cells are subjected to flow. This design could be considered flawed; the vertically stacked channels provide poor visibility for continuous monitoring of cell growth and the polycarbonate membrane separating the cell types increases the distance beyond that measured physiologically (Oddo et al., 2019).

The more recent “parallel” BBBoaC design overcomes both limitations. This design also consists of a PDMS-formed BEC vessel and NVU compartment; however, these two sections lie laterally to each other and are separated by PDMS micropillars (Jiang et al. 2019). This results in increased cell-cell contact, particularly with growth of astrocyte endfeet between the micropillars, and allows improved imaging as there is no viewing obstruction (Prabhakarpandian et al., 2013). One mutual limitation with both “sandwich” and “parallel” designs is that most channels are rectangular in cross section, which is not representative of microvessel physiology, and results in issues with shear stress due to a non-uniform flow (van der Helm et al., 2016).

Some of the most recent BBBoaC designs overcome this issue by growing BECs in 3D-microtubules in a collagen-based hydrogel, with NVU cells hosted in the gel matrix, or allowing BECs to construct their own vascular networks, which are then subject to flow (vasculogenesis) (Campisi et al., 2018; Yu et al., 2020). Although these models are undoubtedly more physiologically accurate, microtubules and vascular networks would be unsuitable for drug transport studies, due to the lack of a drug collection chamber where compounds that permeate across the BBBoaC can be quantified (Jiang et al., 2019). Examples of all the above BBBoaC designs are shown in Figure 1.7.

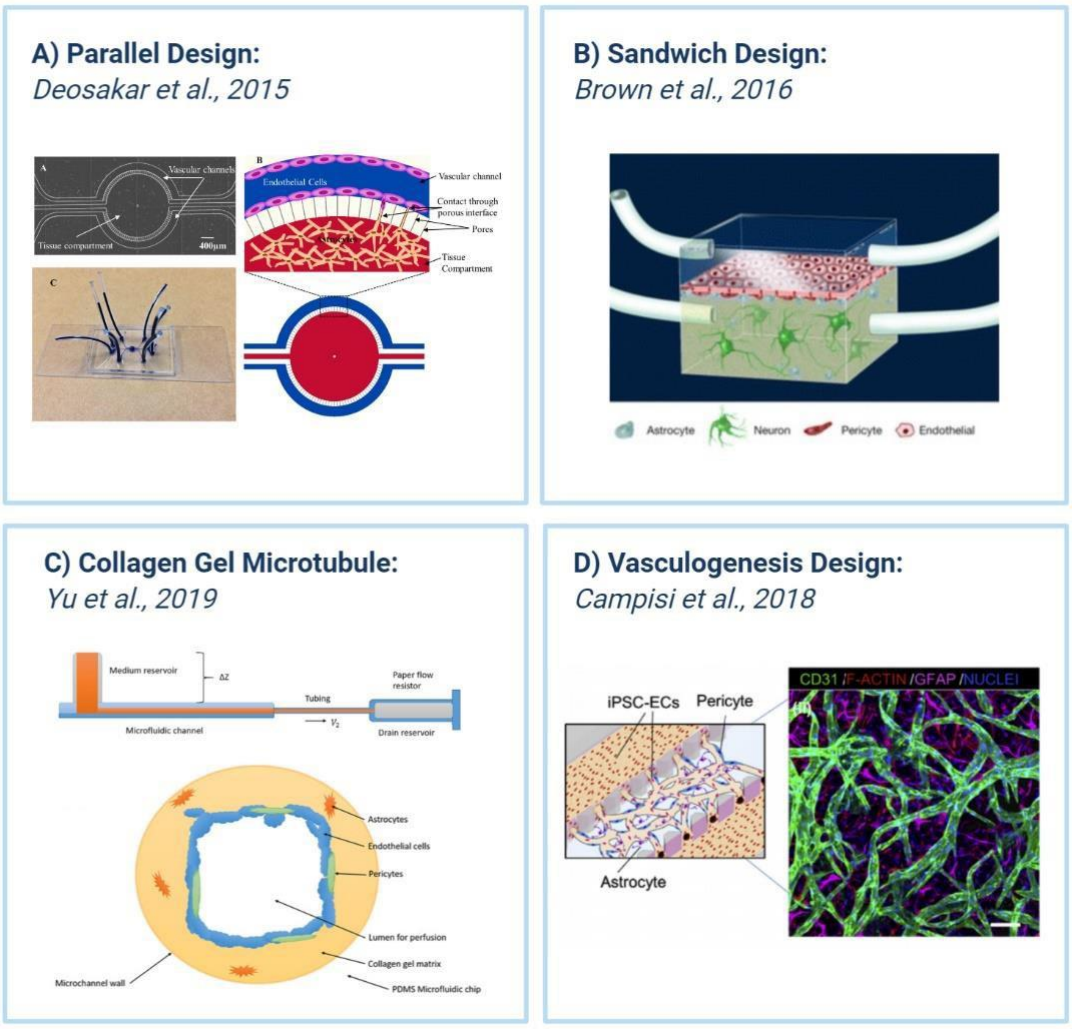

Figure 1.7 - *Illustrations from four key publications of BBB on-a-Chip models representing the main design categories: parallel from Deosarkar et al., 2015, sandwich from Brown et al., 2016, collagen hydrogel from Yu et al., 2019, and vasculogenesis from Campisi et al., 2018. All illustrations were used from original publications.*

1.8.2 Sources of endothelial cells in BBBoaC models

Many different classes of BECs are available for use in BBBoaC models and each have different benefits (Oddo et al. 2019). Primary BECs isolated from mammalian CNS tissue remain the gold standard for cell culture modelling, as these cells maintain several features of the *in vivo* phenotype (Abbott, 2004). BECs isolated from many different species have been used to create BBBoaC models, including rodent, bovine, porcine and human (Oddo et al., 2019). Rodent brains are easy to obtain, but low yield of capillary fragments from the small brains can increase the technical difficulty of the isolation process, whereas porcine and bovine sources circumvent the issue of low capillary yield

and studies have also show increased homology with humans in critical ABC multidrug efflux transporters expressed by BECs (Lundquist & Renftel, 2002; Warren et al., 2009). Primary human BECs would be an ideal model, eliminating any discrepancies in transporter expression between species; however, ethical concerns and availability clearly limit the use of primary human tissue (van der Helm et al., 2016).

Recent studies have used human induced pluripotent stem cells (iPSCs) to derive human BECs that show clear BBB characteristics (Linville et al., 2019). Human derived iPSC-ECs offer nearly unlimited renewal and have high expression levels of tight junction proteins and drug efflux transporters (Workman & Svendsen, 2020). However, despite the fact that derivation of BECs from human iPSCs offer an ethically viable and readily obtainable way to model the human BBB, increased complexity, technical requirements, and cost could outweigh their benefit over primary cells (Jiang et al., 2019).

Immortalised BECs offer some of the benefits of primary BECs without the limitation of complex isolation methodologies and low passage numbers (Oddo et al., 2019). Alongside offering purity and robustness, immortalised cell lines also circumvent issues with species differences, as many immortalised human BEC cell lines are now available (Jiang et al., 2019). However, the immortalisation process often causes a relative loss of phenotype (Lundquist & Renftel, 2002). Immortalised BECs, including the hCMEC/D3 human cell line, both show reduced expression of junctional adhesion molecules, leading to leaky cell-cell junctions, and therefore reducing their benefit in drug transport studies (He et al., 2014; Urich et al., 2012). The endothelial cell types used in different BBBoaC models are described in Table 1.1.

1.8.3 Quantification and evaluation of BBBoaC models

When implementing a new class of model, evaluation through quantification parameters is paramount; this allows direct comparison between BBBoaC models to determine the most accurate system. Most publications of BBBoaC models use a combination of TEER and permeability coefficients of large tracer

compounds to evaluate the BBB phenotype of the BBBoaC model (Oddo et al., 2019).

As previously described in Section 1.3.1, BECs are tightly adhered together to restrict paracellular entry of xenobiotics, and charged ions, into the CNS. The restriction of movement of ions across the barrier sets up a potential difference, and consequently, the membrane has a measurable resistance known as TEER (Srinivasan et al., 2015). To measure TEER experimentally, an electrode must be placed in the “blood” and in the “brain” compartments. TEER measurements can be taken easily in both “sandwich” and “parallel” BBBoaC configurations and many BBBoaC models allow for real-time measurements of TEER without any barrier disruption (Oddo et al., 2019). TEER values can reach up to 6000 $\Omega.cm^2$ *in vivo*, and values of up to 5000 $\Omega.cm^2$ have been reported from BBBoaC models (Brown et al., 2016; Butt et al., 1990). As shown in Table 1.1, primary cell-based models have a TEER of up to 2210 $\Omega.cm^2$, while immortalised cell lines have a TEER up to 280 $\Omega.cm^2$ (Booth & Kim, 2012; Brown et al., 2016). However, models using human iPSCs, where the maximum range of 400-5000 $\Omega.cm^2$ has been reported, supersede both classes (Wang et al., 2017).

An alternative measurement to TEER values is the quantification of the permeability of marker compounds across the barrier (Oddo et al., 2019). Commonly used probes include FITC-dextran, sodium fluorescein, and sucrose (Jiang et al., 2019). The addition of marker compounds to the “blood” chamber and measuring concentration in the “brain” chamber allows the calculation of permeability co-efficients. However, due to variation in the size and structure of marker compounds used, the comparison of permeability co-efficients between models becomes difficult. Therefore, there is need for increased standardisation between BBBoaC testing protocols (Oddo et al., 2019).

Table 1.1: BBBoaC models

Reference	Design	Endothelial Cell Type	Supporting Cells	Shear Stress mPa	TEER value $\Omega.cm^2$
Phan et al., 2017	Vasculogenesis Design	Human colony forming BECs	Human stromal pericytes, human neural stem cell derived astrocytes	Not Stated	Not Stated
Campisi et al., 2018	Vasculogenesis Design	Human iPSC derived BECs	Human pericytes and astrocytes	Not Stated	Not Stated
Yu et al., 2020	Collagen-gel microchannel	Primary rat BECs	Primary rat astrocytes and pericytes	Not Stated	200 – 400
Wang et al., 2017	Sandwich Design	Human iPSC derived BECs	Primary rat astrocytes	2-3	2000 – 4000
Brown et al., 2016	Sandwich Design	Primary human brain derived BECs	Primary human pericytes & astrocytes, hiPSC-derived neurons	2	1950 -2210
Booth & Kim, 2014	Sandwich Design	bEnd.3 immortalised mouse BEC cell line	C6 Astrocytes	1500	223 – 280
Griep et al., 2013	Sandwich Design	hCMEC/D3 immortalised human BEC cell line	N/A	600	37-120

Table 1.1 *- A summary of some of the published BBB-on-a-Chip models, listing different design styles, endothelial cell types, supportove cells, shear stress and corresponding TEER values. If TEER or shear stress values were not presented in the publication these were omitted.*

1.8.4 BBBoaC models for drug transport studies

BBBoaC models have been developed for a wide range of uses, from research to personalised medicine. However, certain aspects of some BBBoaC model designs and qualities would make them able to fulfil the unmet need for a standardised, universal BBB model for drug transport studies. This model would have to allow for real-time TEER measurement, have compound donor and receiver chambers, and must lend itself to medium throughput testing. Some publications to date have tested the permeability of current drugs within BBBoaC models.

In 2014, Booth & Kim tested the permeability of seven neuroactive compounds in their BBBoaC model, which was formed from BEnd.3 immortalised mouse BECs in a sandwich model design. The permeability of drugs from the "vascular" to the "CNS" compartment of the chip was measured by LC-MS, and a highly linear correlation between *in vivo* and *in vitro* permeability was determined (R^2 > 0.85). Furthermore, the correlation between permeability values was determined to be more accurate in the BBBoaC model than in the equivalent Transwell system (Booth & Kim, 2014).

Wang et al., 2017 tested three compounds in their BBBoaC models formed from human iPSCs in a sandwich model design; caffeine is a small lipophilic molecule that readily diffuses across the BBB, cimetidine has moderate BBB permeability through CMT, and doxorubicin has low permeability *in vivo* due to efflux by multidrug efflux transporters such as P-gp. Testing the permeability of these compounds in the BBBoaC model resulted in high permeability of caffeine, moderate permeability of cimetidine, and low permeability of doxorubicin, in line with *in vivo* studies. Furthermore, the ability to measure real-time TEER values within the BBBoaC showed that administration of doxorubicin reduced TEER values by 1500 $\Omega.cm^2$, although this reportedly did not have effect on drug efflux by P-gp (Wang et al., 2017).

Additionally, a publication by Wevers et al. in 2018 demonstrated that BBBoaC models could be used for the high throughput testing of large biologic drugs. Addition of two antibodies to the BBBoaC model, a human transferrin receptor

antibody subject to RMT and a control, resulted in higher uptake of the receptor-targeted antibody through RMT (Wevers et al., 2018). Therefore, it is evident that BBBoaC models have untapped potential for use within the drug discovery process to predict CNS permeability of new compounds.

1.9 The SynVivo idealised microfluidic chip

An analysis of the numerous BBBoaC models published within the past decade demonstrates the wide range of designs, cell types, and quantification parameters. However, if a BBBoaC model were to be successful as a drug quantification assay, this model must be standardised. The ideal BBBoaC model for examining compound permeability across the BBB must be representative of true CNS microvessel diameter, allow induction of shear stress, require a reasonably small amount of compound to achieve results, allow for real-time optical monitoring of cell growth, facilitate real-time measurement of TEER values as a representation of barrier tightness, contain separate vessel and CNS chambers to allow drug permeation across compartments, allow for co-culture of supportive NVU cells at physiological distances, have individual inlet and outlet ports to allow compound collection from each chamber separately, and finally must allow for multiple chips to be run at one time in a medium throughput assay system

A model that is inclusive of all of these properties is the SynVivo idealised BBB model, which has been used in multiple publications over the past decade. This BBBoaC model has a parallel design (Figure 1.7, Deosarkar et al., 2015) consisting of two lateral outer vessel chambers, separated from one inner circular CNS chamber by 3 µm spaced micropillars. This model is made from oxygen-permeable and optically clear PDMS and has built-in electrodes for real-time monitoring of TEER with no risk to cell viability in either chamber. The PDMS chip is connected to a multi-syringe pump via the tubing and has individual inlet and outlet ports for sample collection. One multi-syringe pump is capable of hosting 5-10 microfluidic BBBoaC models in unison (Deosarkar et al., 2015; Prabhakarpandian et al., 2013).

Prabhakarpandian et al., first presented this model in 2013 as the “SyM-BBB” microfluidic system (Prabhakarpandian et al., 2013). In this publication, RBE4 immortalised rat BECs were cultured in the outer chambers, and astrocyte conditioned medium (ACM) was used as the supportive NVU component. Results demonstrated that culturing RBE4 cells in the SynVivo model increases the expression of tight junction protein ZO-1 and multidrug efflux transporter P-gp, and decreases the permeability of FITC-dextran, relative to results from the Transwell model (Prabhakarpandian et al., 2013). A further publication by Deosarkar et al., in 2015, used the SynVivo model to culture neonatal primary rat BECs with neonatal primary rat astrocytes in a model of the neonatal BBB; TEER values were reported in this publication as 171 $\Omega.cm^2$ in Transwell, increasing to 252 $\Omega.cm^2$ in the SynVivo microfluidic chip. Within this publication, immunofluorescence studies show that astrocyte endfeet cross from the CNS chamber through the micropillars to contact the endothelial barrier, giving a physiological organisation to the *in vitro* NVU (Deosarkar et al., 2015). The SynVivo model has also been adapted to model the blood-tumour barrier (BTB), in this study human umbilical vein endothelial cells (HUVECs) were cultured with immortalised rat astrocytes (CTX-TNA2 cell line) and murine metastatic breast cancer cells to model the increased permeability of the BTB by comparison to the BBB (Terrell-Hall et al., 2017). This demonstrated increased permeability of three tracers in the BTB compared to the BBB, with real-time imaging of the permeability of the fluorescent tracer compounds being captured by microscopy techniques. Furthermore, Brown et al., 2019, developed the SynVivo microfluidic chip to model the human BBB using hCMEC/D3 immortalised human BECs which were cultured with primary human astrocytes (Brown et al., 2019).

Thus, the SynVivo microfluidic BBB model has been used with a wide range of cells to model various BBB set-ups, and although few of these publications report TEER values explicitly, one commonality is that the SynVivo model consistently reduces tracer compound permeability and increases tight junction proteins (Brown et al., 2019; Deosarkar et al., 2015; Prabhakarpandian et al., 2013; Terrell-Hall et al., 2017). In the first publication of this model, the primary

aim of this microfluidic model was “to allow predictive screening, evaluation, and optimisation of the ability of a drug candidate to permeate the BBB” (Prabhakarpandian et al., 2013). However, to date, none of the SynVivo BBBoaC publications report having tested common drug compounds within the model and comparing these values to *in vivo* data.

In conclusion, there is a distinct area of unmet need within the field of BBB modelling. It is evident that the restricted entry of xenobiotics across the BBB is critical in protecting the CNS, but consequently creates an insurmountable issue within the drug discovery process. However, the complex molecular biology and biophysics underlying the structure of the BBB has resulted in significant difficulty generating accurate BBB models for the prediction of novel drug permeability into the CNS. Thus, the current drug discovery process depends upon a mix of costly *in vivo* studies with high technical requirements, alongside high throughput yet inaccurate non-CNS cell line or non-biological *in vitro* models. Consequently, the aim of this project was to investigate the use of freshly isolated primary BECs in creating a BBBoaC for use in drug discovery. BECs from porcine brain were isolated, characterised and used to generate a static co-culture model of the BBB, and a more complex primary BBBoaC model using the SynVivo microfluidic system, in a push towards generating a gold-standard BBB model for use in CNS drug discovery.

Chapter 2

Materials and methods

2.0 Materials

The sources for frequently used reagents and equipment are listed in Table 2.1.

Table 2.1: Frequently used reagents & equipment

Reagent	**Source**
Ham's F-10 Media	Lonza, CH
DMEM: F-12 1:1 Media	Lonza, CH
Normal Goat Serum (NGS)	Abcam, UK
Bovine Serum Albumin (BSA)	Thermofisher, UK
Equipment	**Source**
Conical Tube 50 ml	Corning, US
GentleMACS Disassociator, GentleMACS C-Tubes & M-Tubes	Milteny Biotech, US
Culture Flask, Filtered (T-75cm^2, T-25cm^2)	Thermofisher
Microscope	Leica, DE
Digital Camera	Leica, DE
TEER Meter EVOM2 & 6 mm Voltage Cup ENDHOM-6G	World Precision Instruments, UK
Transwell Inserts & Plate (6 mm insert, 24-well plate, 4 µm pore size)	Corning, US

Table 2.1 - *Details of frequently used reagents and equipment throughout methodology with sources.*

PBS was used at a 1 × concentration unless otherwise stated. All other reagents were sourced from Sigma, UK unless otherwise indicated.

2.1 Isolation of primary BECs

Methodologies from Abbott et al., 1992, Rosas-Hernandez et al., 2018, and Nielsen et al., 2017, were used to determine the most effective approach to isolate brain endothelial cells (BECs) across the study. Initial primary BEC isolation methods used rat tissue; however, porcine tissue was pursued in subsequent isolations. The species used for each isolation is indicated in the appropriate methods section.

2.1.1 Isolation method derived from Abbott et al. 1992

The first protocol used to isolate BECs in the study was developed from Abbott et al. 1992, which detailed the isolation of BECs from rats. This methodology was used for male Sprague-Dawley rats. Between one and three brains were taken from rats sacrificed by cervical dislocation for each isolation. The brains were removed by dissecting a triangular flap in the skull with surgical scissors, and a spatula was used to excavate the cerebrum from inside the skull and meninges, discarding the cerebellum and brain stem. The cerebral hemispheres were transferred on ice in Ham's F-10 media to a Class II hood within 15 minutes of dissection. From thereafter, all procedures were conducted in an aseptic manner. Grey matter was extracted by placing each brain in a 15 cm Petri dish containing 10 ml of ice-cold Ham's F10 media and slicing the cerebral hemispheres in a sagittal section using a scalpel blade and cutting as much visible white matter as possible without damaging the outer hemisphere. The remaining hemisphere tissue was rolled on damp laboratory tissue paper to remove meninges and outer vessels. After dissection, each brain was chopped into approximate 1 mm sections and suspended in PBS in a 50 ml conical tube. If multiple brains were used the suspensions were pooled together, before being centrifuged at 600 ×g at 4°C for 5 minutes. After centrifugation, the supernatant was poured off and the brain tissue was resuspended in 7.5 ml of 'Enzyme Mix' per brain used. The 'Enzyme Mix' contained 13 µg/ml collagenase/dispase, 20 U/ml DNase I, and 147 µg/ml TLCK in HBSS without calcium, magnesium, or phenol red (Gibco, UK), with 1× antibiotic-antimycotic. The brain and enzyme suspension mix were digested for 1 hour at 37°C in a

culture incubator at 5% CO_2, with gentle agitation every 10 minutes. After the enzyme digest, the cells were centrifuged at 600 ×g at 4°C for 5 minutes. The pellet of brain tissue was resuspended in 10 ml of ice-cold Ham's F-10 media and added to a GentleMACS C-tube. The C-tubes were placed into a GentleMACS disassociator and homogenised on the pre-programmed "Neural Tissue" setting. After disassociation, the tissue suspension was centrifuged again at 600 ×g at 4°C for 5 minutes. The supernatant was removed, and the brain suspension was added to 50 ml of 25% BSA in PBS. The BSA-cell suspension was centrifuged for 15 minutes at 4°C at 1000 ×g to create a density dependent gradient that will separate buoyant myelin from the blood vessels. The white myelin band was poured from the top of the gradient, and the remaining brain tissue pellet was resuspended in the BSA solution by vigorous shaking. The centrifugation step was repeated to extract more myelin from the vessel fragments. After the second centrifugation, the upper myelin band was again disposed of, along with the BSA supernatant, to leave a red pellet of purified vessels from the brain tissue. This vessel pellet was resuspended in 2.5 ml of 'Enzyme Mix' (as described above) per brain and incubated for 3 hours at 37°C with occasional agitation. During this time, a T-25 cm^2 culture flask was coated with 3 ml of 100 µg/ml fibronectin and incubated for 4 hours at 37°C and then removed. Also, during this incubation period, a Percoll solution was created by adding 15 ml of Percoll (GE Healthcare, UK) to 15 ml of PBS. Then, a Percoll gradient was prepared by centrifuging a 30 ml of this Percoll solution at 20000 ×g at 4°C for 1 hour in an Oak Ridge centrifuge tube (Thermofisher, UK). After the enzyme digest was complete, the suspension was centrifuged at 600 ×g at 4°C for 5 minutes and the supernatant was discarded. The pellet was suspended in 10 ml of PBS and gently pipetted onto the top of the Percoll gradient as to not disturb the density distribution. The Percoll cell suspension was centrifuged at 1000 ×g at 4°C for 10 minutes to create a visible band of vessels and cells 4/5ths of the way down the centrifuge tube. The band was extracted from the Percoll gradient using a Pasteur pipette and was suspended in 40 ml of PBS in a falcon tube. The vessels were centrifuged at 700 ×g at 4°C for 5 minutes, the supernatant was discarded, the pellet was resuspended in 1:1 PBS to culture medium and the suspension was centrifuged again as previously.

The final pellet was resuspended in 10 ml of cell media (Ham's F10 media supplemented with 10% FBS, 2 mM L-Glutamine, 1× antibiotic-antimycotic, 75 µg/ml ECGS), and plated onto the previously coated T-25cm^2 culture flask. Cells were incubated at 37°C in 5% CO_2 overnight, before changing the media to remove debris. The viability of the culture was assessed first at 24 hours and then at 72 hours post-plating.

2.1.2 Isolation methodology developed from Rosas-Hernandez et al., 2018.

This isolation methodology was used for both murine and porcine brains, with adjustments to the amount of enzyme used, respectively. Porcine brains were obtained from a local abattoir (R.B. Elliot & Son Ltd. Chesterfield, UK) and male Sprague-Dawley rats were sacrificed by cervical dislocation for respective isolations. Brains were transported into the laboratory on ice within 1 hour of death. The methodology for dissection and homogenisation of the brains was conducted as Section 2.1.1. At this point, the homogenised brains were added to a dispase solution of 10 mg dispase II per gram of brain tissue, suspended in 5 ml of MEM, for 30 minutes at 37°C with occasional agitation. After 30 minutes, the digest was removed from the incubator and MEM pH 9-10 was added in a 1:1 ratio to the weight of the brain tissue. The solution was then returned to the incubator and left to digest for a further 1 hour at 37°C with occasional agitation. After the digestion with dispase was complete, the suspension was transferred to a 50 ml conical tube and centrifuged at 1500 ×g for 10 minutes at 4°C. After centrifugation, the supernatant was discarded, and the pellet of digested brain tissue was retained in the conical tube. On the day of dissection, 85 ml of dextran solution (65 g of dextran powder (VWR International, US) to 422 ml of distilled water) was added to 10 ml of 10 × MEM (Thermofisher, UK) and 5 ml of 1 M HEPES. The brain tissue pellet was resuspended in 13% dextran solution, and centrifuged at 9170 ×g for 10 minutes at 4°C. After centrifugation, the top semi-solid and liquid layers of myelin were discarded, and the vessel pellet was retained. A collagenase/dispase solution, consisting of 0.55 mg collagenase/dispase (Roche, CH) per gram of brain tissue in 4.5 ml of MEM,

was added to the pellet. The volume in the falcon tube was increased to 20 ml with MEM and the pellet was resuspended in the enzyme mix by aspiration. The tissue/enzyme suspension was incubated in a shaking incubator (37°C, 100 rpm) for 1 hour and 5 minutes. During this time, a T-25cm^2 culture plate was coated with 3 ml of 100 µg/ml fibronectin and incubated for 4 hours at 37°C. The tissue suspension was removed from the incubator and centrifuged at 650 ×g for 10 minutes at 4°C After centrifugation, the supernatant was discarded, and the pellet was resuspended in 4 ml of MEM. The resuspended pellet was added to a Percoll gradient (20 ml of Percoll to 4 ml of 10× MEM, 2 ml of 1M HEPES, and 4.4 ml of 1× antibiotic-antimycotic and centrifuged at 39,700 ×g for 1 hour at 4°C), and the suspension was centrifuged again at 1986 ×g for 10 minutes at 4°C. After centrifugation, a red band of vasculature was observed approximately one inch from the top of the tube. These cells were extracted from the gradient using a 3 ml syringe (BD Medical, UK) with an 18-gauge needle (SGE Analytical, UK). The cells were washed by suspending in 50 ml of MEM and centrifugation at 650 ×g for 10 minutes at 4°C. The pellet was retained and resuspended in 10 ml of complete culture medium (as detailed in Section 2.2). The cell suspension was filtered through a 70 µm cell strainer (Corning, US) into a new falcon tube to remove large pieces of debris. The cell suspension was then plated onto the fibronectin-coated T-25cm^2 culture flask. Cells were incubated at 37°C in 5% CO_2 overnight, before changing the media to remove further debris. The viability of the culture was assessed first at 24 hours and then at 72 hours post-plating.

2.1.3 Isolation methodology developed from Nielsen et al., 2017

The methodology developed by Nielsen et al. 2017 was used exclusively for porcine tissue. Between one and eight pig brains were collected from a local abattoir (R.B. Elliot & Son, Chesterfield, UK) within an hour of slaughter, and transported to the laboratory on ice. Brains were thoroughly washed in ice-cold PBS containing 1× antibiotic-antimycotic. Brains were placed in a Class II hood for dissection. Each brain was dissected in a 20 cm Petri dish that contained 20 ml of DMEM/F12 medium. Firstly, the cerebellum, brainstem and meninges

were removed from all brains using fine point forceps and discarded. All brains were then cut in sagittal section. The grey matter from each half brain was dissected by scraping the surface of the cerebrum with a scalpel in a horizontal motion. The grey matter from each whole brain was placed into 20 ml of DMEM/F12 in a new Petri dish. The tissue suspension was first homogenised by aspirating ten times through a 50 ml syringe (BD Medical, UK), until no large sections of tissue remained. The homogenate was combined and transferred to a sterile 500 ml glass bottle, where the total liquid was brought to a total of 50 ml per brain with DMEM/F12. Next, 100 ml of homogenate was transferred to a 100 ml Dounce tissue homogeniser and homogenised with the small and large clearance pestles with eight up and down strokes. This was repeated until all brain matter had been homogenised. The homogenate was filtered through 150 µm Nylon filter meshes, followed by 60 µm Nylon filter meshes (Plastok Associates Ltd., UK) using a 50 ml syringe and a 47 mm filter holder (Cole-Parmer, UK). A maximum of 50 ml of homogenate per mesh (both sizes) was used. The meshes were retained, and the remaining homogenate was discarded, as all large capillary fragments were adhered to the filter meshes at this point. The filter meshes of both sizes were added to an enzyme mix containing 2000 IU/ml collagenase type 2 (Worthington Biochemical, US), 3400 IU/ml of DNase I, and 2.5% Trypsin EDTA in DMEM/F12 containing 1× antibiotic-antimycotic (20 ml of enzyme mix per 3 meshes). Meshes were incubated at 37°C in the enzyme mix for one hour, with gentle agitation every 10 minutes. After the incubation, any remaining capillary fragments were removed from the meshes by gently scraping with a cell scraper (Greiner Bio-one, UK). The capillary/enzyme suspension was aspirated and added to one 50 ml falcon tube and the final volume brought up to 50 ml with DMEM/F12. The capillary suspension was centrifuged at 250 ×g for 5 minutes at 4˚C. The capillary pellet was resuspended in fresh DMEM/F12 and centrifuged again. This centrifugation step was repeated three times to wash the cell pellet, adding fresh DMEM/F12 each time. After washing, the capillary pellets were aspirated and combined in a 50 ml falcon tube. The capillary pellets were suspended in 1 ml per brain of FBS with 10% dimethyl sulfoxide. The capillary pellet/FBS mixture was evenly added to cryovials, with 1 cryovial per brain used. The

cryovials containing the cell suspension were placed in a freezing container (Nalgene, US) and left at -80°C overnight. After 12 hours, they were transferred to liquid nitrogen storage and were stored for a maximum of 3 months until use.

2.2 Cell culture

2.2.1 Coating flasks for PBECs

PBECs were seeded on a fibronectin-coated T-75cm^2 culture flasks. For fibronectin-coating, 10 ml of 100 mg/ml fibronectin solution was added to the flask and incubated for a minimum 4 hours at 37˚C. After incubation, the fibronectin solution was aspirated and replaced with sterile PBS, at which point the flasks were incubated at 37˚C, 5% CO_2 for up to 24 hours prior to seeding.

2.2.2 Thawing and culturing isolated PBECs

For PBEC culture, one cryovial of capillaries (stored in liquid nitrogen; Section 2.1.3) was raised to 37˚C in a water bath, and three drops of pre-warmed growth media (Table 2.2) was added to the vial. This suspension was added to 10 ml of pre-warmed growth media and centrifuged at 250 ×g for 7 minutes. The supernatant was discarded, and the pellet of capillary fragments was suspended in 10 ml of complete growth media. The suspension was added to the fibronectin-coated T-75cm^2 flask. Cells were left to seed on the fibronectin for 24 hours before the spent media was removed, non-adherent cells were washed off with pre-warmed sterile PBS, and 20 ml of complete media was replaced. Cells were left to grow to confluence (around 72 hours). Puromycin (4 µg/ml) was added to the media for this period to aid with culture purification, and if the cells had not reached confluence after 72 hours, the media was replaced with media without puromycin.

Table 2.2: Endothelial growth media

Growth Media Constituents	Concentration
DMEM/F12	N/A
Antibiotic-Antimycotic	1×
Puromycin (for first 3 days)	4 µg/ml
Endothelial cell growth supplement (ECGS)	2 µg/ml
Heparin	15 U/ml
Fetal bovine serum (FBS)	10%

Table 2.2 – *Endothelial growth media (EGM) constituents for culturing primary pig BECs.*

2.2.3 Passaging PBECs

Spent media was removed from the T-75cm^2 culture flask and the cells were rinsed with sterile pre-warmed PBS. The pre-warmed TrypLE (10 ml) was added to the T-75cm^2 and incubated for 10 minutes at 37˚C 5% CO_2. After 10 minutes, the cells were observed under an inverted microscope to ensure that >80% of the cells were detached. The TrypLE cell suspension was then aspirated and centrifuged for 7 minutes at 250 ×g at 4˚C. The supernatant was discarded, and the pellet was resuspended in 1 ml of endothelial growth media (EGM) without puromycin (Table 2.2). A trypan blue assay was used to elucidate the number of viable cells during passages. A 20 µl volume of cell suspension and 20 µl of 0.4 % (w/v) trypan blue were mixed in an Eppendorf. 20 µl of the trypan blue-cell suspension was placed in a haemocytometer and the number of viable cells (not stained blue) were counted. The estimated number of viable cells per ml was calculated as the average cell count of unstained cells per grid square multiplied by the haemocytometer correction factor of 10,000 and further multiplied by the dilution factor of 2. The viable cell concentration was used to dilute cells in EGM (without puromycin) to a final concentration of 2.2 × 10^5 cells per ml beforebeing plated.

2.2.4 Culture of immortalised HBEC-5i cell line

Immortalised HBEC-5i cells were obtained from American Type Culture

Collections (ATCC, US) at Passage 8. All culture protocols were followed as detailed for PBECs, other than the following exceptions: HBEC-5i cells were seeded upon T-75cm^2 culture flasks coated with 0.1% Gelatine in dH_2O (VWR, UK), where flasks had been incubated at 37˚C, 5% CO_2 for 1 hour, and then dried in a Class II cabinet for 1 hour, before seeding. HBEC-5i cells did not require the addition of puromycin to EGM (Table 2.2) during the first 3 days of culture post-thawing as the cultures were already purified. HBEC-5i cells were

seeded at a concentration of 1×10^4 cells/cm^2, and were passaged at 70-80% confluence, unless being used for Transwell or Chip studies (see section 2.5). HBEC-5i cells were not used past passage 30, as recommended by ATCC.

2.3 Microscopy

2.3.1 Preparation of brain tissue samples

A one-inch section of pig cerebrum was collected from the brain during dissection and washed in PBS in preparation for immunohistochemistry. The cerebral tissue was incubated in 4% paraformaldehyde (VWR International, US) for 48 hours, with the solution being changed after 24 hours. Once removed from the paraformaldehyde, the cerebral tissue was transferred to PBS with 30% sucrose solution for 3 days. The sample was then cut down into 2 cm × 1.5 cm × 0.5 cm blocks and loaded into sample holders and placed in a tissue processor for 26 hours (Leica, DE). The sample progressed through stages of 10% neutral buffered formalin (1 hour), through increasing concentrations of IMS from 80% to 100% (6 hours), xylene and Histoclear (SLS, UK) (4.5 hours), followed by 100% molten paraffin wax (4.5 hours). After processing, the embedded tissue was sliced on a manual rotatory microtome (Leica, DE) in 4 µm sections which were immediately submerged in a 45˚C water bath and placed on adhesive microscope slides. Slides were left to dry for one hour before gentle heating on a hot plate to 60˚C. Sections were dewaxed in xylene twice for 2 minutes each before staining.

2.3.2 H&E staining of brain tissue samples

Haematoxylin and Eosin (H&E) staining was performed on brain tissue sections to identify key structures. Sections were treated with Harris's haematoxylin for 20 minutes and washed in tap water until sections were visibly blued. Sections were then submerged in 70% ethanol with 1% hydrochloric acid for 5 seconds to remove excess dye and rewashed in tap water. Sections were subsequently treated in an Eosin solution for 10 minutes and washed in tap water for 5 minutes. H&E-stained sections were dehydrated by submerging in Histoclear (SLS, UK), and then treated with xylene twice for 2 minutes. Following

dehydration, slides were left to dry overnight in a fume hood and then mounted using Histomount (SLS, UK).

2.3.3 Immunohistochemistry

Embedded brain sections were incubated with 33% acetic acid and 67% ethanol for 10 minutes at -20˚C for fixation. Samples were incubated with 5% hydrogen peroxide (VWR International, US) in methanol for 10 minutes to block endogenous peroxidase activity. Slides were washed twice with PBS for 5 minutes on a shaking plate, and 20% NGS in PBS was added and incubated at room temperature (RT) for 30 minutes. Primary antibodies were diluted in PBS with 2% NGS and 1% Triton X-100 (Table 2.3). Samples were incubated with the primary antibody overnight at 4˚C in a humidified chamber. The primary antibody was removed by washing with PBS twice for 5 minutes on a shaking plate. Biotinylated secondary antibodies (Table 2.3) were diluted in PBS with 2% NGS and incubated at RT for 60 minutes The avidin and biotin (AB) (Vector Labs, UK) were combined and incubated at RT for 30 minutes prior to incubation. The secondary antibody was removed by rinsing in PBS twice for 5 minutes. The AB complex was added to the slides and left to incubate at RT for 30 minutes. The AB complex was removed by washing twice in PBS for 5 minutes on a shaking plate. The DAB solution (Vector Labs, UK) was added and left to develop for up to 5 minutes before rinsing in RO water for 10 minutes. Haematoxylin was added for 20 seconds to counterstain nuclei. Samples were dehydrated by incubating with 100% ethanol for 2 minutes, followed by xylene for 20 seconds, at RT. Staining was viewed using an upright microscope, images were captured using the attached digital camera and processed using Leica Image software.

2.3.4 Immunofluorescence

PBECs were grown on fibronectin-coated glass coverslips (19mm) in a 12-well plate until 80% confluence was reached. Spent media was removed and cells were incubated in a 1:1 solution of acetone: methanol at 4°C for 10 minutes for fixation. Samples were incubated with 5% hydrogen peroxide in methanol for 10 minutes to block endogenous peroxidase activity. Cells were washed twice with

PBS for 5 minutes on a shaking plate, and 20% NGS in PBS was added at RT and left for 30 minutes. After blocking, primary antibodies were diluted in PBS with 2% NGS (Table 2.3). Cells were incubated with the primary antibodies for 2 hours at RT. After incubation, the cells were rinsed by washing with PBS twice for 5 minutes on a shaking plate. Secondary antibodies (Table 2.3) were diluted in PBS with 2% NGS and incubated in the dark at RT for 1 hour. Coverslips were removed from each well using forceps and mounted upon slides using Vectashield mounting medium with DAPI counterstain (Vector Labs, UK). Samples were viewed using an upright microscope, images were captured using the attached digital camera and processed using ImageJ software.

Table 2.3: Antibodies for immunostaining

Primary Antibody	Source	Secondary Antibody	Source
Rabbit anti-ZO1 Polyclonal (1:100) [IHC]	Thermofisher [#40-2200]	Goat anti-Rabbit IgG Peroxidase Antibody (1:5000)	Sigma [A9169]
Rabbit anti-ZO1 (1:100) [IF]	Abcam [ab221547]	Goat anti-Rabbit IgG conjugated to Alexa Fluor 488 (1:800)	Abcam [ab150077]
Rabbit anti-SMA (1:100) [IF]	Abcam [ab5694]	Goat anti-Rabbit IgG conjugated to Alexa Fluor 488 (1:800)	Abcam [ab150077]

Table 2.3 - *Primary and Secondary antibodies used in immunohistochemistry and immunofluorescence*

2.3.5 Scanning electron microscopy of confluent PBEC monolayers

Scanning electron microscopy (SEM) was used to assess the formation of tight junctions between PBECs in a confluent monolayer. Cells were grown to confluence on fibronectin-coated glass inserts in a 12-well cell culture plate. When cells had reached confluence, the medium was aspirated, and cell monolayers were rinsed twice with PBS. The cells were fixed in sodium cacodylate buffer containing 0.1 M glutaraldehyde for 1 hour. The cells were then washed twice with sodium cacodylate buffer and dehydrated in an

increasing concentration of ethanolic solutions (70%, 90%, & 100% ethanol for 30 minutes each). SEM studies were carried out by Nicola Weston at the University of Nottingham, Nanoscale, and Microscale Research Centre. In brief, the scanning electron microscope used was an FEI Quanta 650 ESEM fitted with Peltier cooling stage. The sample was coated in platinum for 90 seconds at a 15-mA current and the dehydrated sample was imaged in high vacuum mode.

2.4 Western blotting

2.4.1 Preparation of cell and tissue samples

Brain tissue samples used in Western blot analysis were collected during dissection and within 2 hours of slaughter. The samples (200 mg) were suspended in 1 ml of ice-cold RIPA lysis buffer with 10 µl of 100× commercial protein inhibitor (both Thermofisher, UK). Samples were homogenised using gentleMACS M-tubes in a gentleMACS Disassociator and centrifuged at 2000 ×g for 15 minutes.

Samples of porcine brain capillaries were collected from the capillary suspension during the isolation procedure, immediately before cryopreservation. Samples of cultured cells were taken after culture for 72 hours, or once the PBECs had reached confluence. Cells or capillary fragments were centrifuged and resuspended in ice-cold RIPA Lysis Buffer with protein inhibitor. The cell and capillary suspensions were incubated on ice for 30 minutes with occasional vortexing. Samples were centrifuged at 13,000 ×g for 10 minutes, and lysates in the supernatant were collected, aliquoted and stored at -80°C. Protein concentration was determined using the Bradford assay (section 2.4.2).

2.4.2 Protein concentration determination using the Bradford assay

Protein concentration of tissue, capillary or cell samples was determined using the Bradford assay against a serial dilution of BSA standards. A stock concentration of BSA in PBS at 2000 µg/ml was doubled diluted 8 times in PBS to a final concentration of 7.8 µg/ml. BSA standards and a PBS blank were

added to a 96-well plate in duplicate. Previously prepared samples were diluted (1:4-10 [cells/capillaries] and 1:10-40 [tissue]) in PBS and added to the 96-well plate in duplicate. Bradford solution (200 µl) was added to each standard and sample well. The wells were gently mixed and left to develop for 30 minutes at RT. Absorbance was measured at 595 nm, using a photometer (FLUOstar optima, BMG lab tech). The protein content of the samples was determined from the linear part of the BSA standard curve using GraphPad Prism.

2.4.3 Sodium dodecyl sulphate polyacrylamide gel electrophoresis

Protein separation by gel electrophoresis was performed using NuPAGE SDS-PAGE pre-cast 12% Bis-Tris protein gels (Thermofisher, UK) in the SureLock Xcell II electrophoresis chamber. The gels were allowed to equilibrate to RT, the comb and protective tape were removed, and the chamber was assembled. 200 ml of MOPS SDS running buffer (Thermofisher, UK) was added to the central chamber to the top of the gel. Samples were vortexed and the required volume for 20 µg of protein was aliquotted. The appropriate volume of SDS-lysis buffer (25 µl β-mercaptoethanol + 475 µl Laemmli buffer (Bio-Rad, UK)) and distilled water were added to each sample according to the protein concentration determined such that the final volume was 20 µl. Samples were heated at 100˚C for 10 minutes. Samples used in P-gp detection were not boiled, as per manufacturers guidelines for the antibody (ab170904) (Abcam, 2021). Samples were loaded into the wells at the top of the gel and the gel was run at 200 Volts for 60 minutes at RT.

2.4.4 Semi-dry protein transfer

PVDF membranes were prepared by soaking in methanol for 10 minutes to activate the membrane. The PVDF membrane was soaked in NuPAGE transfer buffer (Thermofisher, UK) for a minimum of 20 minutes. The Bio-Rad Trans-Blot Turbo Transfer System (Bio-Rad, UK) was used for Transfer. The PVDF membrane and NuPAGE Gel used for electrophoresis were sandwiched between 5 pieces of Whatman paper (soaked in Transfer buffer as above) on

either side and placed in the transfer drawer. The Trans-Blot Transfer System was run for 30 minutes at 25 Volts.

2.4.5 Immunoblotting

The membrane was incubated in blocking solution, 5% milk in PBS-Tween (PBS-T) for one hour on a shaking plate at 40 rpm. After blocking, the membrane was submerged in blocking solution containing the appropriate dilution of primary antibody (Table 2.4) and incubated at 4˚C overnight. Then the membrane was washed five times in PBS-T for 10 minutes on a shaking plate at 40 rpm. Secondary antibodies were diluted in blocking solution (Table 2.4) and the membrane was incubated in the solution for 1 hour at RT with gentle agitation. The membrane was washed five times in PBS-T for 10 minutes on a shaking plate, and then rinsed twice in cold distilled water. The membrane was covered with ECL Prime (GE Healthcare, UK) for 5 minutes at RT. The membrane was drained of detection solution, wrapped in cling film, and imaged in ChemiDoc MP imaging system (Bio-Rad, UK).

Table 2.4: Antibodies for immunoblotting

Primary Antibody	**Source**	**Secondary Antibody**	**Source**
Rabbit Anti-VE-Cadherin Monoclonal (1:1000)	Cell Signalling [D87F2]	Goat anti-Rabbit IgG Peroxidase Antibody (1:50000)	Sigma [A9169]
Rabbit Anti-P-glycoprotein (1:1000)	Abcam [ab170904]	Goat anti-Rabbit IgG Peroxidase Antibody (1:50000)	Sigma [A9169]
Rabbit Anti-aSMA (1:1000)	Abcam [ab5694]	Goat anti-Rabbit IgG Peroxidase Antibody (1:50000)	Sigma [A9169]

Table 2.4 - *Primary and Secondary antibodies used in immunoblotting.*

2.5 PCR

2.5.1 Sample preparation

Samples of porcine brain were collected during dissection within 2 hours of slaughter. Tissue (30 mg) was taken from the cerebrum and homogenised in PBS using gentleMACS M-tubes in a gentleMACS Disassociator and centrifuged at 2000 ×g for 15 minutes. Samples of PBEC cells were collected once the cells had reached confluence. Spent media was removed and replaced with ice-cold PBS; cells were removed from the bottom of the well by scraping. The cell suspension was aspirated from the wells and transferred into a 1.5 ml Eppendorf tube for RNA isolation.

2.5.2 Isolation of RNA

RNA was isolated using the NucleoSpin RNA kit (Machery-Nagel, DE). In brief, cells were suspended in 1:10 β-mercaptoethanol: lysis buffer, and further homogenised using an Eppendorf micropestle. The lysate was filtered through a NucleoSpin filter tube by centrifugation at 11,000 ×g for 1 minute. Following filtration, 350 µl of 70% ethanol was added and the sample was centrifuged at 11,000 ×g for 30 seconds. The silica membrane was desalted through the addition of 350 µl of membrane desalting buffer, and the samples were centrifuged at 11,000 ×g for 1 minute. DNA was digested through addition of 95 µl of DNase reaction mix, which was incubated at RT for 15 minutes. The silica membrane was washed three times: firstly using 200 µl of RAW2 and centrifuged at 11,000 ×g for 30 seconds, followed by a wash with 600 µl of RA3 and centrifugation in the same conditions, and finally using 250 µl of RA3 and centrifugation at 11,000 ×g for 2 minutes. The purified RNA was extracted by suspension in 30 µl of RNase-free water and centrifugation at 11,000 ×g for 1 minute.

2.5.3 cDNA synthesis

The RNA concentration and the A260:A280 ratio of the samples were quantified using a Nanodrop (Thermofisher NanoDrop 8000). Samples were used for amplification if the A260:A280 ratio exceeded 1.8. Once quantified, 1 µg of RNA

was added to a PCR tube with 1 µl of Oligo (DT) $_{12\text{-}18}$ primer (Thermofisher, UK) and 1 µl of deoxynucelotide mix (New England Biolabs, UK). The volume for each sample was made up to 13 µl with RNase-free water. The samples were heated in the thermocycler (Life Touch, BioER) at 65˚C for 5 minutes and incubated on ice for 1 minute. Samples were centrifuged briefly, and 4 µl of 5× first strand buffer, 1 µl of 0.1M Dithiothreitol, 1 µl of RNaseOUT Recombinant Ribonuclease Inhibitor and 1 µl of SuperScript III Reverse Transcriptase were added (all reagents from Thermofisher, UK). Samples were mixed thoroughly, incubated at 50˚C for 60 minutes and inactivated by heating to 70˚C for 15 minutes in the thermocycler.

2.5.4 Amplification

Amplification involved adding approximately 10 ng of cDNA (calculated relative to the RNA concentration) to a PCR tube with 9.5 µl of REDTaq ReadyMix PCR Reaction Mix, 1 µl of both forward and reverse primers (Table 2.5), and 7.5 µl of RNase-free water. No template control samples were made up by replacing the sample with 1 µl of RNase-free water. Samples were vortexed and amplified in the Thermocycler for 3 minutes at 95˚C, followed by 35 cycles of 95˚C for 30 seconds, T_m˚C for 30 seconds (Table 2.5), and 72˚C for 45 seconds. Finally, samples were heated to 72˚C for 10 minutes.

2.5.5 Gel electrophoresis

To make the gel, 3 g of Agarose was mixed with 100 ml of Tris Acetate-EDTA (TAE) buffer and heated until the agarose was fully dissolved. When slightly cooled, 3 µl of ethidium bromide (Thermofisher, UK) was added. The 3% agarose gel was placed in a gel electrophoresis tank filled with TAE buffer. The gel combs were removed and 5 µl of low molecular weight DNA ladder (New England Biolabs, UK) was loaded into the first well, followed by 8 µl of each PCR sample and negative control into subsequent wells. The gel was run at 120 Volts for 30 minutes. Chemiluminescence was measured using the Bio-Rad ChemiDoc MP.

Table 2.5: PCR primers

Gene (protein)	Forward Primer	Reverse Primer	Product Size (bp)	Tm °c	Source
GAPDH (G3P)	CCTGGCCAAGGTCATCCA	CGGCCATCACGCCACAG	123	64	Designed
CDH5 (VE-Cadherin)	TCATCTCGGACAACGGGAGG	GGAGATCACTGCGATGGTGAGG	179	64	Designed
OCLN (Occludin)	GAGGAAGACTGGATCAGGGAATATC	GGCCACTGTCAAAATTTCTCTTG	81	60	Srinivasan et al., 2015
ABCB1 (P-glycoprotein)	CCAAAGTCACAGATCCTGAAACC	GAACCAGCTCACGTCCTGTC	194	64	Designed
ABCC1 (MRP1)	GCCATGCCGTAGAAGAGACC	CAGTTCCATGACTGCACCG	152	60	Designed
ABCG2 (BCRP)	GGACAAAACTTCTGCCCGGGACTCAA	TCAGGTAGGCGATCGTCAGGAAAATG	178	68	Designed
SLC2A1 (GLUT1)	CCCGTCCCTCCCTGCTCAAACACTCT	CCGTCTATACACACAGCAGGGCAGGA	211	68	Designed
GFAP (GFAP)	ACATCGAGATCGCCACCTAC	ACATCACATCCTTGTGCTCC	219	60	Czupalla et al., 2014 Wang et al., 2017
ACTA2 (aSMA)	CCATGAAGATCAAGATCATTGCC	GTGTGCTAGAGACAGACAGC	194	60	Designed
B2M (B2M)	CAAGATAGTTAAGTGGGATCGAGAC	TGGTAACATCAATACGATTTCTGA	161	60	Patabendige et al., 2013

Table 2.5 - *Primer sequences, expected product sizes and T_m values for each gene.*

2.5.6 TaqMan real time RT-PCR

Real time RT-PCR was performed using TaqMan Gene Expression Assays (Applied Biosystems, UK). Sample preparation, RNA isolation and cDNA synthesis was undertaken as described in Section 2.5.1 - Section 2.5.3. TaqMan Gene Expression Assays were used for P-gp (ABCB1) (Ss03373435_m1, Thermofisher), MRP1 (ABCC1) (Ss03376986_u1, Thermofisher) and BCRP

(ABCG2) (Ss03393456_u1, Thermofisher), alongside GAPDH (Ss03374854_g1, Thermofisher) as the endogenous control assay. The TaqMan gene expression assays were thawed and resuspended by vortexing. For accuracy, 4 replicates of each cDNA sample were used per gene expression assay and a no template control was used for each gene. Each PCR reaction mix was prepared to 20 µl total volume in an RNase-free PCR tube using 1 µl TaqMan Gene Expression Assay (20X), 10 µl TaqMan gene expression assay master mix (4369016, Thermofisher), 10 ng cDNA from samples, and 5 µl of RNase-free water. Each reaction was vortexed and centrifuged briefly before samples were transferred to a 96-well real time PCR plate (Bio-Rad, UK). The PCR plate was centrifuged briefly before being loaded into the real time PCR machine (CFX Connect Real Time PCR System, Bio-Rad). The thermal cycling conditions were as follows: hold at 50°C for 2 minutes, hold at 95°C for 10 minutes, before 40 subsequent cycles of 95°C for 15 seconds and 60°C degrees for 1 minute. Real time PCR data was analysed using Bio-Rad CFX Maestro software.

2.6 Assessment of γ-glutamyl transferase activity

Assay adapted from Bentham, 2010. PBECs were grown to confluence on a fibronectin-coated 96-well plate using 45 µl of 100mg/ml fibronectin per well (Section 2.2.1 & 2.2.2). When cells had reached confluence, cell medium was removed, and monolayers were washed twice in pre-warmed PBS. Following the washes, 275 µl of 0.1 M Tris-HCL buffer containing 20 mM glycylglycine and 1 mM L-γ-glutamyl-p-nitroanilide was added to each well. The plate was incubated at 37°^{c} at 5% CO_2 for 40 minutes. The reaction was stopped with the addition of 55 µl of 1 N NaOH per well. The amount of p-nitroanilide product formed was measured spectrophotometrically using a plate reader (FLUOstar Omega, BMG Labtech) at 410 nm. Calibrated using a standard curve of known p-nitroanilide concentrations. Enzyme activity was calculated using Equation 2.1, where *B* is the amount of p-nitroanilide generated between $T_{initial}$ (0 minutes) and T_{final} (40 minutes), *T* is the total reaction time, and *V* is the sample volume of the well.

Equation 2.1

$$\gamma - glutamyl\ transferase\ activity = \frac{B \times [dilution\ factor]}{T \times V}$$

The value for enzyme activity was normalised to the value for total cell protein, which was calculated using a Bradford assay, as described in Section 2.4.2.

2.7 Modelling the BBB

2.7.1 Transwell Monoculture of PBECs and HBEC-5i line

BECs were cultured until 80-90% confluent so the maximum number of cells could be used without contact inhibition being a detrimental factor in future growth. Transwell inserts (24-well plate, 6 mm diameter) were coated with fibronectin (100 µg/ml; 100 µl per insert) and collagen IV (500 µg/ml; 100 µl per insert) in PBS. Cells were passaged according to methodology detailed in Section 2.2.3. The coating solution was removed from the Transwell inserts and 250 µl of cell suspension was added to each insert such that there were 0.5×10^5 cells per insert. Once all inserts were plated, 750 µl of EGM without puromycin was added to the bottom compartment of the Transwell. Cell media was replaced with fresh growth media after 24 hours.

After 48 hours, at which point cells were confluent, cell medium was changed in both compartments to transport medium (Table 2.6). The media within the Transwell insert was refreshed every 48 hours subsequently, or 3 hours before every TEER measurement. Timeline of seeding is shown in Figure 2.1.

Table 2.6: Transport media

Transport Media Constituents	Concentration
DMEM/F12	N/A
Antibiotic-Antimycotic	1×
cAMP	250 µM
Hydrocortisone	550 nM
RO 20-1724	17.5 µM
FBS	10%
Heparin	15 U/ml

Table 2.6 - *Transport Media Constituents for Transwell Insert Culture of BECs.*

2.7.2 PBEC and HBEC-5i line co-culture with astrocytes on Transwell inserts

The immortalised rat astrocyte cell line, CTX-TNA2, was purchased from the European Collection of Authenticated Cell Cultures (ECACC, UK). The ECACC guidelines were followed for the culture of astrocytes, with cells cultured on fibronectin (5 µg/cm^2) coated cell culture flasks. Media was DMEM with L-glutamine and sodium pyruvate (Lonza, CH), supplemented with 10% FBS. Cells were at passage number 6 upon receipt from ECACC and were subsequently passaged when cells reached 70-80% confluence and were used until passage number 30.

Astrocytes were passaged onto the bottom of the Transwell plates 24 hours prior to the end point assay or start of TEER measurements, as indicated in Figure 2.1. Astrocytes were passaged according to the methodology for BECs (Section 2.2.3), and 0.5 × 10^4 cells/cm^2 were plated in each well of the 24-well Transwell plate. During non-contact co-culture, the spent astrocyte media was also changed every 48 hours.

2.7.3 PBEC and HBEC-5i line co-culture with astrocyte conditioned media on Transwell inserts

As per Section 2.2.5, medium removed from CTX-TNA2 astrocyte culture, which had been in contact with cells for more than 48 hours, was aspirated and stored as astrocyte conditioned medium at -20°c for a maximum of 1 month before use. During Transwell culture of HBEC-5i cells or PBECs which were subjected to ACM treatment, ACM was thawed, and cAMP, hydrocortisone, and RO 20-1724 were added in the same concentrations as transport media (Table 2.6). For ACM treatment Transwells, the transport media in the top half of the Transwell was replaced with ACM 48 hours after passage (as shown in Figure 2.1).

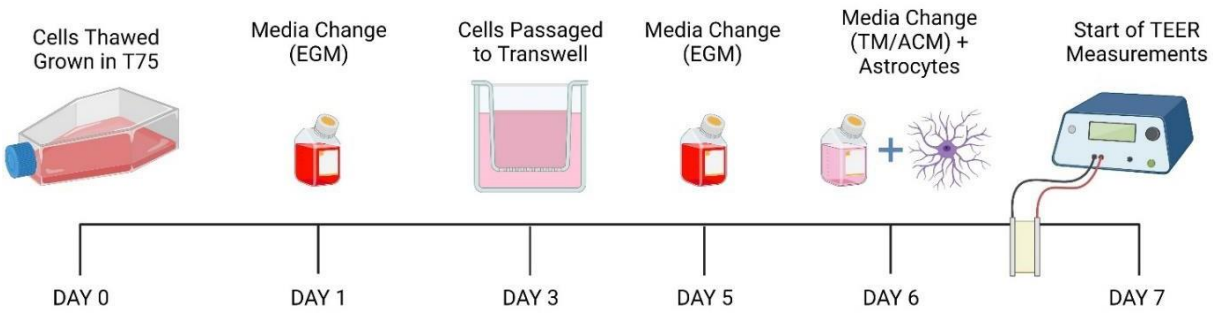

Figure 2.1 - *Schematic of timeline for seeding of BECs in Transwell inserts. EGM represents endothelial cell growth media as described in Table 2.2, and TM represents transport media as described in Table 2.6. ACM (astrocyte conditioned medium) was added to replace the transport medium in the upper insert of Transwells in the corresponding treatment groups.*

2.7.4 Seeding of HBEC-5i line in SynVivo microfluidic chip

HBEC-5i cells were cultured until 80-90% confluent so the maximum number of cells could be used without contact inhibition; 2× T-75cm^2 flasks of cells were used per microfluidic chip. A SynVivo Idealised Microvascular Network Biochip (200 µm outer chamber width, 50 µm slit spacing, 3 µm wide slit, 50 µm travel, 100 µm depth with impedance capacity) (All SynVivo items were purchased through Stratech, UK) was removed from packaging and allowed to reach room temperature. A small section of sterile tubing (0.2” ID × 0.6” OD) was inserted into each inlet and outlet port of the chip using sterile forceps. In order to coat the chip, a solution of 100 µg/ml fibronectin and 500 µg/ml collagen IV in dH_2O

was prepared and loaded into a 1 ml syringe. The 1 ml syringe was loaded into a Harvard Syringe Pump (MA1 70-3, Harvard PHD ULTRA) and the coating solution was infused at a set flow rate of 5 µl/ml. The coating solution was injected into all channels of the chip using the same process. All bar one of the tubing inlets and outlets of all channels on the chip were sealed using SynVivo clamps, and the coating solution was infused again at 5 µl/ml into the closed chip to force remaining air bubbles out from the PDMS. After a 3-minute infusion, the chip was placed in the cell culture incubator at 37˚C, 5% CO_2 for 1 hour. After the incubation, the chip was removed from the incubator, the clamp from one inlet port was removed and the tubing was connected to the SynVivo Pneumatic Primer. The aim of pneumatic priming was to force any remaining air bubbles within the PDMS out of the device. Without removal of the coating solution or the other clamps, nitrogen gas was injected through the pneumatic priming device and into the chip at 7.5 psi for 20 minutes. The pneumatic priming device was then removed, and the clamp was replaced on the tubing. This process was repeated for all three channels. At this point, the chip was incubated at 37˚C, 5% CO_2 for a further 1 hour. 2× T-75cm^2 flasks of HBEC-5i cells were passaged according to Section 2.3. Once the cells had been centrifuged, the cell pellet was resuspended in 100 µl of EGM (Table 2.2). Cells were counted and adjusted to a final concentration of 2 × 10^7 cells/ml. The cell suspension was loaded into a 1 ml syringe connected to the tubing and loaded into the syringe pump. The tubing connected to the channels was swapped using the water bridge technique, where the syringe pump flow was set to 10 µl/min and the cell suspension flowed through the tubing until a meniscus formed at the end of the tubing attached to the syringe, at which point the flow was paused. At this point, a drop of media was placed at the inlet to the chip, and the current inlet tubing was removed without air flowing into the channel. The clamp at the outlet was removed, and the tubing containing the cell suspension was carefully placed into the inlet with forceps, allowing the meniscus to contact the media drop to form a water seal. The flow of the cell suspension was restarted on the syringe pump at 10 µl/ml to allow the chip to fill slowly. Flow from the syringe pump was stopped after the meniscus forming at the outlet tubing was cloudy with cells. Both the outlet and inlet channels were

clamped and cut, and this process was repeated for the other outer channel. The chip was incubated at 37˚C, 5% CO_2 overnight. After 24 hours had passed, EGM media was loaded into 2× 1 ml syringes connected to tubing and loaded into the syringe pump. Once again, media flowed through until a meniscus had formed at the end of the tubing from both syringes, and then were connected to the inlets of the chip. The clamps were removed from the outlets, and the chip was placed in an incubator at 37˚C, 5% CO_2 while connected to the syringe pump. The syringe pump was set to perform a ramp profile for 12 hours, in which flow would increase from 10 nl/min to 1 µl/min. At this point, flow continued at 1 µl/min for 48 hours.

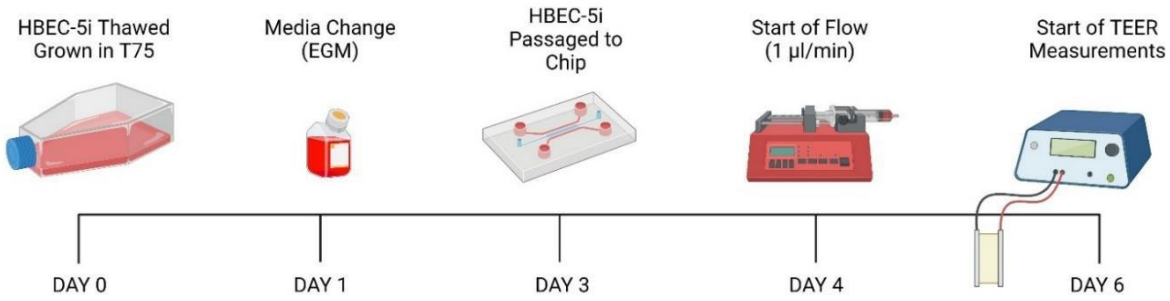

Figure 2.2 - *Schematic of timeline for seeding of HBEC-5i cells into the SynVivo microfluidic chip. EGM represents endothelial cell growth media as detailed in Table 2.2.*

2.7.5 Seeding of PBECs in SynVivo microfluidic chip

The seeding protocol for PBECs within the SynVivo microfluidic chip was identical to the seeding protocol for HBEC-5i (Section 2.2.5) other than the following changes. In order to coat the chip, a solution of 1 mg/ml fibronectin and 1 mg/ml collagen IV in dH_2O was prepared and loaded into a 1 ml syringe. As with the HBEC-5i cells, 2× T-75cm^2 flasks of PBECs were passaged according to Section 2.3 and the cell pellet was resuspended in 100 µl of EGM (Table 2.2). However, for PBECs, cells were counted and adjusted to a final concentration of 4 × 10^7 cells/ml. When infusing the cells into the syringe pump, flow was only set to 3 µl/min. The chip was incubated at 37˚C, 5% CO_2 overnight. After 24 hours, the passage and infusion processes were repeated with a further 2× T-75cm^2 flasks of PBECs as previously but in an inverted position, to allow cells to seed on the upper channel area. After 24 hours, EGM media was loaded

into 2× 1 ml syringes connected to the tubing and loaded into the syringe pump and fresh media was infused into the channel at 1 µl/min for 3 minutes until a meniscus formed, after this process the channels were re-clamped and the chip was placed back into the incubator at 37˚C, 5% CO_2. This media change process was repeated until the cells appeared confluent (up to a maximum of 96 hours post second seeding). Whereupon, induction of shear stress began as with HBEC-5i cells, however, the syringe pump was set to perform a ramp profile for 12 hours, in which flow increased from 30 nl/min to 3 µl/min. At this point, flow continued at 3 µl/min for 48 hours.

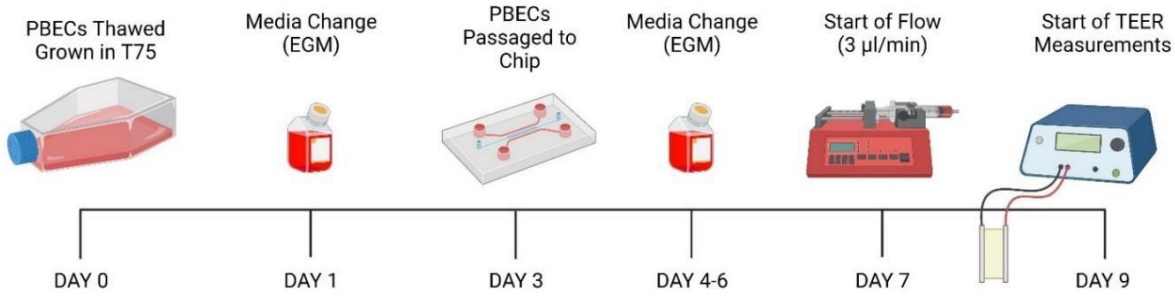

Figure 2.3 - *Schematic of timeline for seeding of PBECs into the SynVivo microfluidic chip. EGM represents endothelial cell growth media as detailed in Table 2.2.*

2.7.6 TEER measurements in Transwell culture

BECs were cultured and passaged onto Transwell inserts as described in Section 2.2.5. Prior to TEER measurements were taken the media in the Transwell inserts was changed and replaced with fresh transport media (Table 2.6). Cells were re-incubated for 3 hours to recover from the media change. TEER was measured using a 6mm Cell Culture Cup Chamber and EVOM2 Epithelial Volt/Ohm Meter. The cup electrode was sterilised using 70% ethanol and equilibrated for 30 minutes in 4 ml of pre-warmed DMEM/F12 before use. TEER values were measured by placing each insert into the electrode cup (containing 3 ml of fresh pre-warmed DMEM/F12) and measuring resistance in triplicate. The resistance of a no-cell control was also taken in triplicate to obtain a value for the resistance of the Transwell insert.

An average of 3 values were used to calculate resistance values, after subtracting the baseline resistance values from the inserts. TEER was

calculated by multiplying the resistance of the monolayer by the surface area of the membrane (0.33 cm^2).

2.7.7 FITC-Dextran permeability measurements in Transwell culture

BECs were cultured and passaged onto Transwell inserts as described in Sections 2.2.5. On the day that permeability measurements were taken the media in the Transwell inserts was changed and replaced with fresh transport media (Table 2.6), cells were then left for a minimum of 3 hours in the cell culture incubator to recover from the media change. FITC-Dextran (average molecular weight 4 kDa) was dissolved in Hank's Balanced Salt Solution (HBSS) without calcium, magnesium, or phenol red (Thermofisher, UK) to a final concentration of 0.5 mg/ml. Prior to the permeability assay, the cells were rinsed with pre-warmed HBSS twice. The FITC-dextran solution was added to the apical insert (100 µl) and pre-warmed HBSS was added to the basolateral plate (600 µl) compartment. No-cell controls were prepared in the same manner. Once prepared the Transwell plate was agitated at 100 rpm at 37^{o}C for 3 hours. After which, a 100 µl sample was taken from each well from the apical and basal compartments. Sample fluorescence was analysed with excitation filter 485 nm and emission filter 535 nm (FLUOstar Omega, BMG Labtech). Amount of FITC-dextran present in each sample was determined using a standard curve of known concentrations. Percentage permeability was calculated as shown in Equation 2.2.

Equation 2.2

$$Percentage\ Permeability = \frac{(Basolateral\ Sample - HBSS\ Blank)}{(FITC{:}\ HBSS\ equilibrated\ mix - HBSS\ Blank)}\ x\ 100$$

2.7.8 FITC-Dextran permeability of PBEC cultures in SynVivo microfluidic chip

PBECs were cultured in the SynVivo microfluidic chip as described in Sections 2.2.5 & 2.2.6. After the PBECs were exposed to 3 µl/min flow of medium for 48 hours to induce shear stress conditions, the syringe pump was stopped. A 1 ml syringe containing HBSS (no calcium, no magnesium, no phenol red) was loaded into the pump. The tubing connected to a channel inlet was removed using the water bridge technique as described in Section 2.2.5. Flow of HBSS into the chip was started at 1 µl/min to rinse away cell growth medium. When the outflow from the channel was visibly clear, indicating that HBSS had flushed out any medium containing phenol red from the chip, the flow of HBSS was stopped. FITC-Dextran (average molecular weight 4 kDa) was dissolved in HBSS to a final concentration of 0.5 mg/ml. FITC-dextran solution was taken up into a 1 ml syringe and loaded into the syringe pump. The HBSS syringe was changed for the FITC-dextran syringe using the water bridge technique, and the chip was placed under a microscope lens (Leica upright microscope DM5000). The flow of FITC-dextran into the channel was started at 1 µl/min. Images of FITC-dextran flow were captured at 480 nm at 0-, 15-, and 30-minutes after the FITC-dextran had filled the channel. This process was repeated for an identical set up which contained no cells act as a control.

2.7.9 Impedance measurements of PBECs in SynVivo microfluidic chip culture & Transwell culture

After the SynVivo microfluidic chip had been coated and primed, but prior to PBEC seeding (Section 2.2.5), blank impedance measurements were taken. The chip was equilibrated to room temperature for 10 minutes and the clamps were removed from the tubing connected to two right hand electrode ports lateral to the right-hand cell channel. Using forceps, the wire connected to the SynVivo impedance electrode was threaded into the tubing of each of the electrode ports on the chip until the wire touched the glass slide underneath the PDMS. The micro grabbers of the impedance analyser were attached to the wires which have been threaded into the electrode ports, and impedance

readings were taken. This process was repeated for the left outer channel using the left-hand electrode ports. The highest frequency on the analyser (10 kHz) was selected for all impedance measurements, as higher frequencies will cause the least electrical response from cell cultures which can adversely impact impedance readings. The ohmic readings from the impedance analyser for the right-hand channel were recorded. After the blank impedance measurements were complete, the chip was returned to the incubator at 37°C in 5% CO_2 for a minimum of 1 hour to reach 37°C before cell seeding. PBECs were then cultured in the SynVivo microfluidic chip as described in Section 2.2.6. After 3 µl/min flow of medium on the PBECs for 48 hours to induce shear stress conditions, the syringe pump was stopped, and the impedance measurements were taken in both channels at 10 kHz using the methodology described above and were recorded.

For impedance measurements of Transwell cultures, PBECs were cultured in Transwell inserts according to methodology described in Section 2.2.5. On the day that TEER measurements were taken the media in the Transwell inserts was changed and replaced with fresh transport media (Table 2.6). Cells were then left to recover in the incubator from the media change for 3 hours. When cells were ready for measurements to be taken, the micro grabbers of the impedance analyser were attached to two wires to create two electrode probes. The first electrode probe was placed in the bottom chamber of the Transwell insert being measured, and the second electrode probe was placed in the upper compartment of the Transwell insert without direct contact with the cell monolayer. The readings were taken at 10kHz. This process was repeated across 3 Transwell inserts so as to provide an average. Impedance readings were also taken of Transwell inserts which had been coated and contained pre-warmed media, but contained no PBECs, for a no cell control.

2.8 Analysis of drug transport in Transwell

2.8.1 Development of drug database

In order to determine the most appropriate drugs to use in the transport studies, a literature search was performed to collate data on permeability parameters

from previous BBB drug transport studies. Data from published sources was used to assemble a database for fraction unbound in brain ($F_{u, brain}$), fraction unbound in plasma ($F_{u, plasma}$), volume unbound in brain ($V_{u, brain}$), blood-to-brain concentration ratio (K_p), unbound blood-to-brain concentration ratio ($K_{p, uu}$), and unbound blood to unbound cerebrospinal fluid concentration ratio ($K_{p, uu, CSF}$). *In vivo* data values across species from rat, mouse, human, pig, and primate were included. Similarly other drug permeability parameters including logP, molecular weight, and known efflux transporter interactions were obtained from publications and existing referenced online databases, such as Drug Bank and PubChem, and included in the database.

2.8.2 Selection of test drugs

From the database described in Section 2.8.1, 10 drugs were selected to be tested in Transwell drug permeability trials. Test drugs are listed in Table 2.7. Criteria for selection were a molecular weight of less than 500 Da and availability *in vivo* data available in either pig or human for evaluation of the Transwell model. Drugs were selected across a range of values for lipophilicity (-1.8 to 5) which had known uptake/efflux transporter interactions and contained both CNS and non-CNS targets.

Table 2.7 – Selected test drugs

Drug	Molecular Weight (Da)	LogP
Loperamide HCl	513.5	4.7
Carbamazepine	236.7	2.5
Levodopa	197.2	-2.7
Amprenavir	505.6	2.9
Chlorpromazine HCl	355.3	5.4
Donepezil HCl	416.0	4.2
Haloperidol	375.9	3.2
Topiramate	339.4	-0.8
Primidone	218.3	0.9
Thiopental	242.3	2.9

Table 2.7 *– A list of test drugs selected for drug permeability studies from the database created, including molecular weight and LogP data which was relevant for selection.*

2.8.3 Test drug preparation

A stock solution (10 mM) of each drug was made in DMSO and stored at -20°C. Immediately prior to experimentation, a working solution (3 µM) of the drug was freshly prepared by dilution of the of the 10 mM stock in HBSS (no magnesium, no calcium, no phenol red). The final solvent concentrations in all test drug concentrations did not exceed 1% (v/v).

2.8.4 Measuring permeability of drugs in porcine Transwell model

Transport assays were conducted using the PBEC Transwell BBB models described in section 2.2.5 with the addition of ACM as detailed in Section 2.2.6. The permeability of the test drugs was assessed bi-directionally by measuring A-B and B-A transport. To assess cell monolayer integrity, TEER measurements were performed as per Section 2.2.5. All test drugs were assayed in triplicate across three independent experiments to accommodate variability in the PBEC monolayers. On the day of study, PBEC monolayers were left to equilibrate for at least 1 hour post TEER analysis. After this period, PBEC monolayers were carefully washed with HBSS twice and equilibrated in HBSS for 30 minutes at 37°C, after which, cells were incubated with 3 µM of test drug in HBSS in the donor compartment (100 µl in apical or 600 µl in basal compartments). The Transwell plates were incubated at 37°C at 100 rpm. Samples were taken at 30-, 60- and 120-minute time points. Samples of 100 µl were taken from the apical and basal compartments. A separate transwell insert was used for each time point replicate. Samples were analysed using liquid chromatography mass spectroscopy (LC-MS/MS) as described in section 2.8.5.

2.8.5 Analysis of test drugs samples using liquid chromatography-mass spectroscopy

Sample analysis was undertaken at Vertex Pharmaceuticals, Oxford. Calibration lines were produced on the day of study using a Hamilton robot linked to Venus software (Hamilton, UK). Serial dilutions of each drug from a 10 mM stock were performed using 1:1 acetonitrile :DMSO to make the following

concentrations: 1, 2.5, 10, 100, 500, 1000, 2500, 5000 nM. Where a higher concentration calibration line was required, the following concentrations were used: 10, 50, 150, 250, 500, 750, 1000, 2500, 5000, 7500, 10000 nM.

Sample extraction was performed using a Hamilton robot. Samples were transferred to a 96-well 800 µl round well block (Waters, US) containing acetonitrile and internal standard (Tolbutamide-D9, Insight Biotech, UK). 25 µl of each study sample or calibration solution was added to 300 µl of acetonitrile with internal standard. The plates were mixed on a plate agitator for 10 minutes before being centrifuged at 4000 rpm for 10 minutes at 4°c to remove debris. Resulting solutions were placed back into the Hamilton robot for supernatant transfer. 100 µl of each study sample and calibration solution was added to 100 µl of water.

Samples, 2 µl, were injected into a Waters BEH C8 column (1.7 µm 30 x 2.1 mm) column operated at 70°C, which was split by an accurate splitter to deliver an initial flow rate of 1 ml/min to the mass spectrometer. Gradient elution of each analyte was achieved over a 0.9-minute runtime. LC gradient conditions are summarised in Table 2.8, where solvent A was water with 0.1% formic acid, and solvent B is acetonitrile with 0.1% formic acid. Samples were analysed by LC-MS/MS on Waters Xevo TQS mass spectrometer (Waters, US) linked to Mass Lynx v4.2 software for processing. All compounds were analysed using ESI ran in positive ion mode with a cone voltage of 40 volts.

Table 2.8 – Liquid chromatography gradient conditions

Time (mins)	Flow (ml/min)	Solvent A (%)	Solvent B (%)	Curve
0.00	1.0	99	1	-
0.15	1.0	99	1	6
0.60	1.5	5	95	6
0.75	1.5	5	95	6
0.80	1.5	99	1	6
0.81	1.0	99	1	6

Table 2.8 *– Conditions for liquid chromatography gradient as conducted on Waters BEH C8 column at Vertex Pharmaceuticals, Oxford.*

Table 2.9 – Mass transitions

Drug	Mass Transition
Loperamide HCl	477.228 > 266.250
Carbamazepine	237.103 > 194.075
Levodopa	198.100 > 107.100
Amprenavir	507.638 > 419.193
Chlorpromazine HCl	319.104 > 85.766
Donepezil HCl	380.223 > 90.700
Haloperidol	376.158 > 122.999
Topiramate	338.000 > 78.000
Primidone	219.200 > 162.200
Thiopental	243.348 > 173.087

Table 2.9 – *Mass transitions of all compounds used for drug transport studies analysed by LC-MS at Vertex Pharmaceuticals, Oxford.*

2.8.6 Equilibrium dialysis measurement of nonspecific drug binding

Fraction unbound drug in plasma and brain for each drug was determined using rapid equilibrium dialysis (ThermoScientific Single use RED Plate, Thermofisher, UK). Brains were weighed, added to PBS (brain: PBS 1:2 (w/v)) and homogenised for 8 up and down strokes in a 100 ml dounce homogeniser using pestle B (Dounce Homogeniser, Jencons, UK). Plasma was diluted (1:1 (v/v)) with PBS. Both brain and plasma samples were vortexed before use. Diluted plasma and brain homogenate samples were spiked with each of the test drugs to give a final concentration of 3 µM. Dialysis buffer was made up of 1x PBS with 100 mM sodium phosphate and 150 mM sodium chloride added. 350 µl of dialysis buffer was added to each corresponding buffer chamber. 100 µl of diluted plasma/brain samples with drug were added to the corresponding wells. All drugs were tested in duplicate across plasma and brain. The plate was covered with a sealing tape and was placed in an orbital shaker at 37°C for 4 hours at 250 rpm. After 4 hours, 50 µl samples were taken from each compartment and pipetted into microfuge tubes. 50 µl of dialysis buffer was added to tissue samples, and 50 µl of corresponding tissue was added to each buffer sample so that all samples were of equal volume and composition. Samples were analysed using LC-MS as detailed in section 2.8.5.

After sample concentration was determined by LC-MS/MS analysis, the apparent fraction unbound ($F_{u,apparent}$) was determined as the ratio of buffer concentration to tissue concentration. The $F_{u,apparent}$ value was used to calculate F_u by correcting for the dilution factor used, as detailed in Equation 2.3.

Equation 2.3

$$Fu = \frac{(1/D)}{(1/Fu, apparent - 1) + (1/D)}$$

D = the dilution factor in diluted plasma and brain homogenate

$F_{u,apparent}$ = Measured ratio of unbound of drug in diluted plasma and brain homogenate

2.8.7 Calculation of drug permeability parameters

The drug peak area to internal standard ratio was used to calculate drug concentrations according to calculated standard curves. Calculations of P_{app} (Equation 1.3) and P_{exact} (Equation 1.4 and 1.5) in both directions and test drug recoveries (Equation 2.4) were performed as detailed below.

Equation 2.4

$$\langle C(t) \rangle = \frac{V_D C_D(t) + V_R C_R(t)}{V_D + V_R}$$

C_D = Drug concentration in the donor compartment (mol. l^{-1}) at time t

Equation 2.5

$$100 \times \frac{(V_R \times C_R final) + (V_D \times C_D final)}{V_D \times C_0}$$

V_R = Volume in the receiver compartment (cm^3)

V_D = Volume in the donor compartment in (cm^3)

C_0 = Concentration of dosing solution (µM)

final C_R = Cumulative receiver concentration at the end of the incubation period (µM)

final C_D = Concentration in the donor compartment at end of the incubation period (µM)

The efflux ratio for P_{app} and P_{exact} values was calculated using equation 2.6

Equation 2.6

$$\text{Efflux Ratio} = \frac{Papp\ B-A}{Papp\ A-B}$$

In vitro unbound blood-to-brain concentration ratio ($K_{p,\ uu}$) was predicted from permeability coefficient (P_{app} or P_{exact}) data. As $K_{p,uu}$ is defined as the relationship between unbound drug concentration in brain and plasma at steady state, allowing for passive diffusion and/or efflux/influx, $K_{p,uu}$ is therefore determined by the relationship between influx and efflux clearances ($CL_{,in}$ and $CL_{,out}$, respectively) (Tran et al., 2004).

Equation 2.7

$$Kp,uu = \frac{CL_{in}}{CL_{out}}$$

Considering the definition of clearance as:

Equation 2.8

$$CL = P_{app}S$$

The *in vitro* $K_{p,uu}$ may be defined as the ratio between apical-to-basal (A-B) and basal-to-apical (B-A) apparent or exact permeabilities obtained *in vitro*, as per Equation 2.9.

Equation 2.9

$$Kp,uu = \frac{P_{app\ A-B}}{P_{app\ B-A}}$$

K_p data was calculated from $K_{p,uu,}$ using fraction unbound data from Section 2.8.6, using the Equation 2.10 to account for plasma and brain binding of drug.

Equation 2.10

$$Kp = Kp,uu \times \frac{Fu,plasma}{Fu,brain}$$

2.9 Statistical Analysis & Ethics Statement

Statistical analyses were performed using GraphPad Prism 7, data were checked for normality and homogeneity of variance and treatment groups were compared by one-way ANOVA or two-way ANOVA as stated. Post-hoc tests were used for multiple comparisons; Tukey's multiple comparisons test was used for one-way ANOVA and Sidak's multiple comparisons test was used for two-way ANOVA. Values presented on figures are mean ± SEM unless otherwise indicated. All experiments using animals were conducted according to ethics approval by the University of Nottingham Biosafety Unit.

Chapter 3

Isolation and characterisation of primary porcine brain endothelial cells

3.1 Background

Brain endothelial cells (BECs), as the major constituent of the blood-brain barrier (BBB), have many morphological and functional differences in drug transport to peripheral endothelial cells. Peripheral endothelial cells are separated by a 6-7 nm intracellular space, allowing the extravasation of circulating xenobiotics from the bloodstream into the peripheral tissue (Gomes et al., 2016). BECs have a greater expression of tight junction proteins, resulting in tighter cell-cell adhesion and reduced paracellular permeability of circulating xenobiotics (Sharif et al., 2018). Restricted paracellular permeability is aided by an increased expression of multidrug efflux transporters and drug-metabolising enzymes in BECs, which restrict the transcellular transport of small lipophilic compounds into the central nervous system (CNS) (Morris et al., 2017). The unique characteristics of BECs can be considered fundamental criteria in creating an accurate and representative model of the BBB.

Many cell types have been used to create *in vitro* models of the BBB, as the cell type selected is one of the most critical determinants of the cost, throughput, practicality, and translational relevance of the model created (Sivandzade & Cucullo, 2018). As previously discussed in section 1.8.2, primary BECs remain the gold standard for BBB modelling, as they retain the tight junctional adherence and multidrug efflux transporter expression that is critical to BBB function in *ex-vivo* culture (Patabendige et al., 2013). Whereas immortalised cell lines consistently show leaky junctions and fluctuating levels of transporter expression (Oddo et al., 2019) (Rahman et al., 2016). The biggest challenges faced in creating a model with primary cells are variability between cultures, specific technical skill required, low cell yield, and culture purity after isolation.

Considering the high level of variability associated with primary cell cultures when compared to immortalised cell lines, it is important to thoroughly assess the phenotype of the isolated cultures to establish the BBB characteristics (Nielsen et al., 2017). Therefore, in this chapter, the development of adapted protocols for the isolation and characterisation of primary porcine brain endothelial cells (PBECs) (Nielsen et al., 2017) will be described. In addition,

the BBB phenotype of the isolated PBECs will be further characterised by establishing 1) the purity of the isolated cell cultures, 2) the presence of tight junctions and 3) the expression and function of multidrug efflux transporters and enzymes, using PCR, Western blotting, immunofluorescence, TEER measurements and fluorescence permeability assays. In summary, this section will present a robust cellular model of the BBB.

3.2 Results

3.2.1 Identification of BBB in porcine brain *ex vivo*

In order to identify the presence of BBB within the microvessels in the brain, immunohistochemistry for ZO-1 was performed on pig cerebrum (Fig 3.1). ZO-1 was used as a BEC marker, as ZO-1 is a critical tight junction protein present at greater levels in BBB cells than any other cell type in the brain (Howarth et al., 1992).

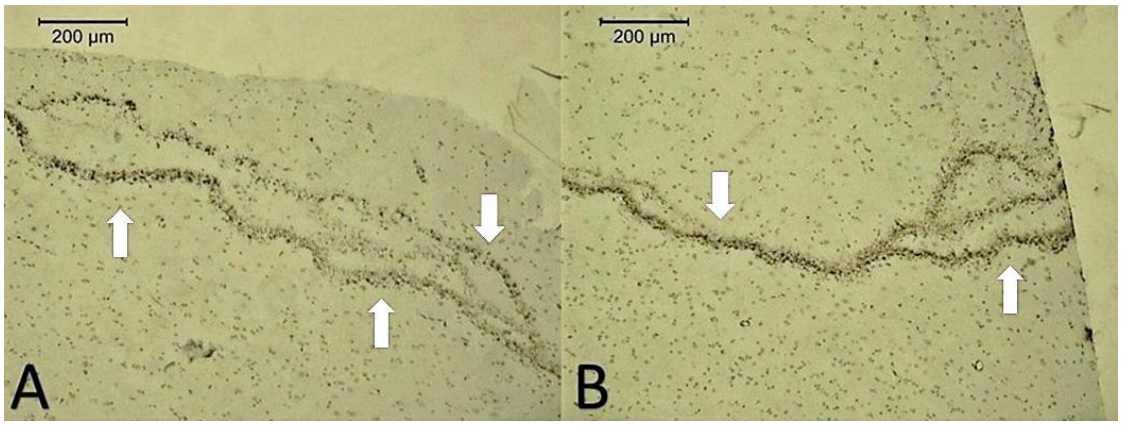

Figure 3.1 - *Immunohistochemical staining of ZO-1 in porcine cerebrum. Positive staining of the brain endothelial cells of blood-brain barrier is indicated with white arrows. ZO-1 was immunostained using primary antibody (#40,2200 Thermofisher, 1:100), and secondary (#A9169 Sigma, 1:5000). Images were captured using Leica microscope DM5000 at 10X magnification. Counterstained with haematoxylin to show nuclei (blue) and scale bar represents 200 µm. The control immunohistochemistry was blank.*

ZO-1 staining (brown) was evident throughout the cerebral tissue, highlighting elongated branched areas which represent brain microvessels (all cell nuclei are shown in blue) (Fig. 3.1). The microvessels within the porcine brain therefore express BBB-associated tight junction proteins.

3.2.2 Isolation of primary porcine cerebral microvessels

3.2.2.1 Progression of developments to isolation protocols

Initially, different methods and species were used to isolate primary BECs for the model in order to find a method which reliably produced robust BEC cultures. Both murine and porcine models were to be created due to the advantages of each species. Firstly, murine species have the benefit of substantial *in vivo* pharmacokinetic data in published literature (Beconi et al., 2012; Gustafsson et al., 2019; Lucchetti et al., 2019). Published *in vivo* pharmacokinetic data in porcine species is less abundant, however, this disadvantage is counterbalanced by a closer genetic homology with humans (Warren et al., 2009). The methods and developmental processes used to isolate BECs from these species are described in Table 3.1.

Table 3.1: Isolation methodology

Culture no#:	Species:	Changes to Methods:	Results:
1	Rat (1 brain)	Initial protocol used from Abbott et al., 1992 see Section 2.1.1 in methods for full details.	No cell/ vessel yield.
2	Rat (1 brain)	Percoll centrifuged at a higher speed using ultracentrifuge, 20000 ×g to 39700 ×g.	Low yield of vessel fragments, no disassociation.
3	Rat (3 brain)	Adapted protocol based on Rosas-Hernandez et al., 2017: see Section 2.1.2 in methods for full details.	Low yield of vessel fragments, no disassociation.
4	Rat (3 brain)	Changed enzymatic digestion mix to collagenase/dispase at 0.55 mg/g brain tissue for 1st digestion and added dispase II at 10 mg/g brain tissue for 2nd digestion.	Single endothelial cells present, but in very low numbers. Vessels still present but no disassociation.
5	Rat (3 brain)	Enzyme digestion compositions remained the same but changed density dependent centrifugation to 13% (w/v)150,000 MW dextran solution rather than 25% (w/v) BSA.	No further improvement.
6	Rat (10 brain)	Added mechanical disassociation step with filtering brains through mesh initially, and through a 70 µm cell strainer before plating.	Single endothelial cells present in low numbers, only smaller vessel fragments present. No disassociation.
7	Pig (1 brain)	**Changed species to pig.** Each brain is 90-fold heavier and has a higher proportion of grey to white matter. Methods kept the same but total amount of enzyme added increased due to increased brain mass.	Capillary fragments and individual endothelial cells present upon plating. Cells were confluent by 72 hours.
8	Pig (1 brain)	Enzyme dissociation mix based on Rosas-Hernandez et al., 2017 protocol was unsustainably expensive due to amount required per gram of tissue. Switched to Nielsen et al., 2017 protocol to reduce cost, (see Section 2.1.3)	Many large capillaries present upon plating, within 24 hours they have disassociated into clusters of cells.
9	Pig (1 brain)	Addition of a smaller filter mesh (70 µm alongside 140 µm) increased yield of smaller capillaries. Addition of ECGS to cell media (see Table 2.1).	Increased total cell yield.
10	Pig (8 brains)	Nielsen et al. 2017 protocol used as before, but number of brains were scaled up for bulk isolation.	Cells were stored in liquid nitrogen and thawed when ready with little reduction in viability.

Table 3.1– *A chronological listing of changes made to early isolation protocols, from the first attempt at isolating cells from a single rodent brain to bulk isolations of porcine brains. Three main published protocols were used to develop these techniques, Abbott et al., 1992, Rosas-Hernandez et al., 2017, and Nielsen et al., 2017.*

Initial studies used rodent brains from lab-reared Sprague-Dawley rats. However, early isolations determined that a high number of brains (>10) would be required to obtain even a small and limited cell yield (Table 3.1). This was not sustainable and does not fulfil the 3Rs principles (replacement, reduction, and refinement of animals in research). Porcine brain isolations benefitted from an increased brain volume and higher proportion of grey matter. Moreover, initial methodologies using Percoll gradients to isolate the different cell types were deemed problematic as they frequently produced varying cell yields and required a high number of reagents (Table 3.1). However, refined methods, based on those published by Nielsen et al. (2017), which use mechanical homogenisation and physical isolation of complete cerebral microvessels were consistently more reliable and cost-effective.

3.2.2.2 Porcine BEC culture

The isolated porcine microvessels were seeded upon a T75 cell culture flask coated with fibronectin (Section 2.2). The morphology of the PBECs was examined using an upright light microscope (Leica DM5000) over time in culture. On the day of seeding, the capillaries were observed as branched, tubule-like structures, occasionally containing red blood cells in the central lumen, and were surrounded by isolation debris.

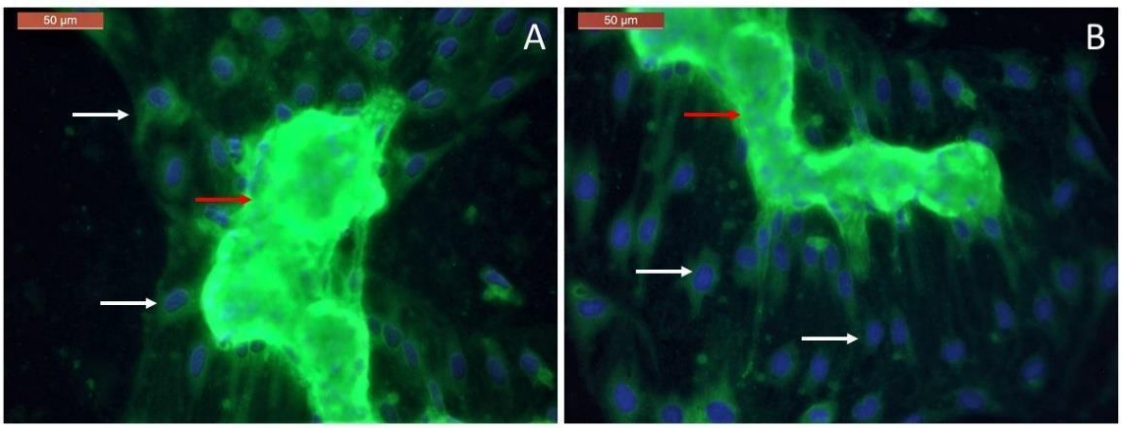

Figure 3.2 - *Immunoflourescent staining for ZO-1 in disassociating porcine vessels. Red arrows indicate vessel fragments; disassociating cells are indicted by white arrows. ZO-1 primary antibody (Abcam, ab221547; 1:100), secondary antibody goat anti-rabbit IgG Alexa Fluor 488 (Abcam, ab150077; 1:800) (green) and DAPI nuclear stain (blue). Images were captured using Leica upright microscope DM5000, at 40X magnification and processed using Leica Image software. Scale bar represents 50 µm. Control immunofluorescence was blank.*

The microvessel fragments adhered to the plate within 6 hours and were not removed in the 24-hour PBS wash. Staining for ZO-1 revealed that, within the 24 hours, capillary fragments had started to disassociate into islands of PBECs. Large central microvessel fragments (red arrows, Fig. 3.2) were observed surrounded by closely associated clusters of individual PBECs (white arrows, Fig 3.2) that appeared to grow away from the vessel along of the base of the flask.

At 72 hours post-seeding, the microvessel fragments had completely disassociated and cells had formed a confluent, tightly packed, and uniform monolayer (Fig. 3.3). These cells were typically spindle-shaped, elongated and had fusiform morphology, which is characteristic of an endothelial cell culture, and this morphology was consistent between isolations. Puromycin was added for the first 72 hours of culture to aid for selection of BECs. One porcine brain yielded sufficient capillary fragments for one T75 cell culture flask to be confluent after approximately 72 hours. Further investigation was undertaken to validate the purity of the PBECs and to characterise the expression of other markers of the BBB phenotype.

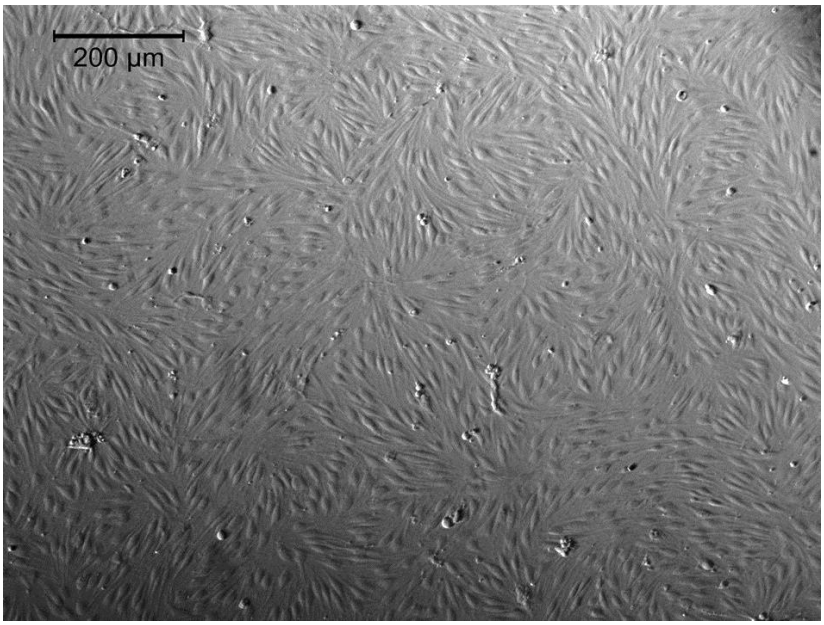

Figure 3.3 - *Confluent primary porcine brain endothelial cells (PBECs) after 72 hours of culture in standard endothelial growth media. The PBECs showed typical spindle-shaped fusiform morphology in a uniform tightly packed monolayer. Images captured using Leica inverted microscope. Scale bar is 200µm.*

3.2.3 Selection for PBECs in the primary culture

It is typical that when isolating primary cells from whole tissue, like brain, cultures will be contaminated with other cell types. One of the most effective purification methods is to culture BECs with low concentrations puromycin over the first three days of culture (Methods Section 2.2) (Perrière et al., 2005).

3.2.3.1 PCR for contaminating cell types

Initially, PCR was performed to identify the presence of astrocytes in the cell culture. PBECs were cultured for 72 hours in a 12-well plate with 4 µg/ml puromycin, followed by RNA extraction (Section 2.6). Expression of glial fibrillary acidic protein (GFAP, astrocyte) alongside VE-Cadherin (BEC) was investigated in the cultured PBECs alongside homogenised cerebral cortex (positive control) (Fig. 3.4). VE-Cadherin is an adherens junction protein that is highly enriched in endothelial cells. GAPDH was used as an endogenous control gene.

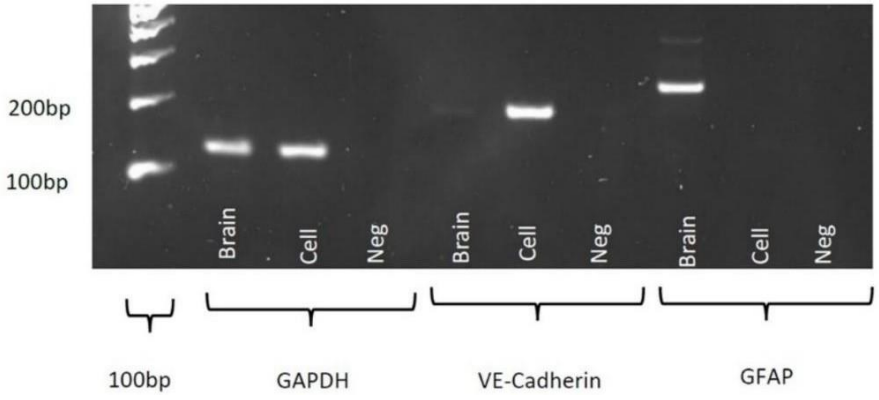

Figure 3.4 – *PCR for glial fibrillary acidic protein (GFAP) mRNA and VE-Cadherin mRNA in confluent porcine brain endothelial cells and porcine brain cortex. PCR product sizes for each lane as indicated are: GAPDH – 123bp, VE-Cadherin – 179bp, GFAP – 219bp. No template control lanes (neg) with no cDNA added showed no bands. Agarose gel was imaged using BioRad ChemiDoc Imaging System. PCR results as replicated across three experiments.*

VE-cadherin mRNA expression was detected in both whole brain cortex and PBECs, with an enriched expression in the cultured cells (Fig. 3.4). However, *GFAP* mRNA was only present in the RNA extracted from homogenised brain, with a faint non-specific band at an incorrect molecular weight for the GFAP PCR product. This indicated that the cultured PBECs contained no astrocyte contamination. The PCR negative controls were blank and endogenous control gene *GAPDH* was expressed in both PBECS and brain cortex.

Similarly, PCR was performed to examine whether puromycin treatment was effective in eliminating pericytes. PBECs were cultured for 72 hours after thawing either with or without 4 µg/ml puromycin treatment (Section 2.2). Perivascular pericytes express contractile protein alpha smooth muscle actin (aSMA), and this was used as the marker for pericytes while beta-2-microglobulin (B2M) was used as an endogenous control gene.

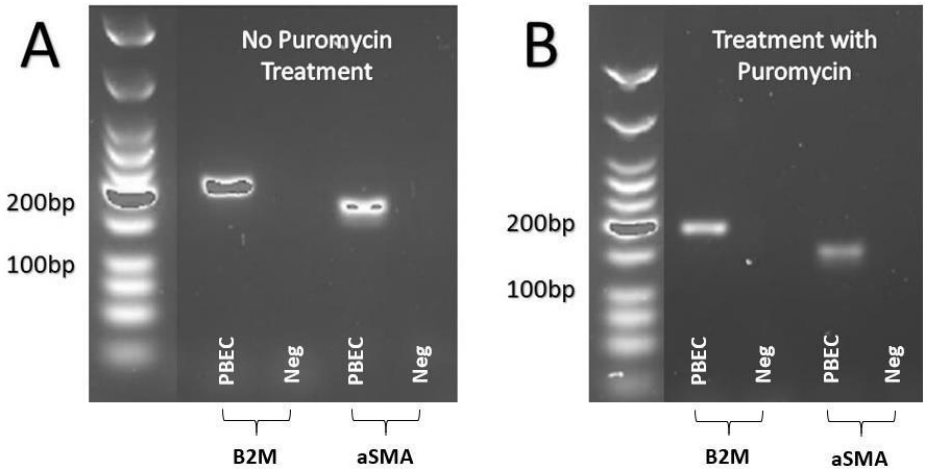

Figure 3.5 – *PCR for smooth muscle actin (aSMA) in mRNA extracted from confluent porcine BECs. PCR product sizes for each lane as indicated are: aSMA – 194bp, B2M – 161bp. No template control lanes with no cDNA added (Neg) showed no bands. Agarose gel was imaged using BioRad ChemiDoc Imaging System. PCR results as replicated across three experiments.*

Following electrophoresis, a clear band for aSMA at the expected size for the PCR product was observed in both the presence and absence of puromycin. Indicating that pericytes are present in both treatment regimes, however, as conventional PCR is a highly sensitive method, it is feasible that a low level of pericyte contamination was being detected.

3.2.3.2 Immunofluorescence for contaminating pericytes

To further investigate the apparent presence of pericytes in PBEC cultures, immunofluorescence for aSMA was performed on PBECS cultured with and without puromycin (Fig. 3.6). Cells were grown for 72-hours either with or without 4 µg/ml puromycin, before being fixed for immunofluorescence.

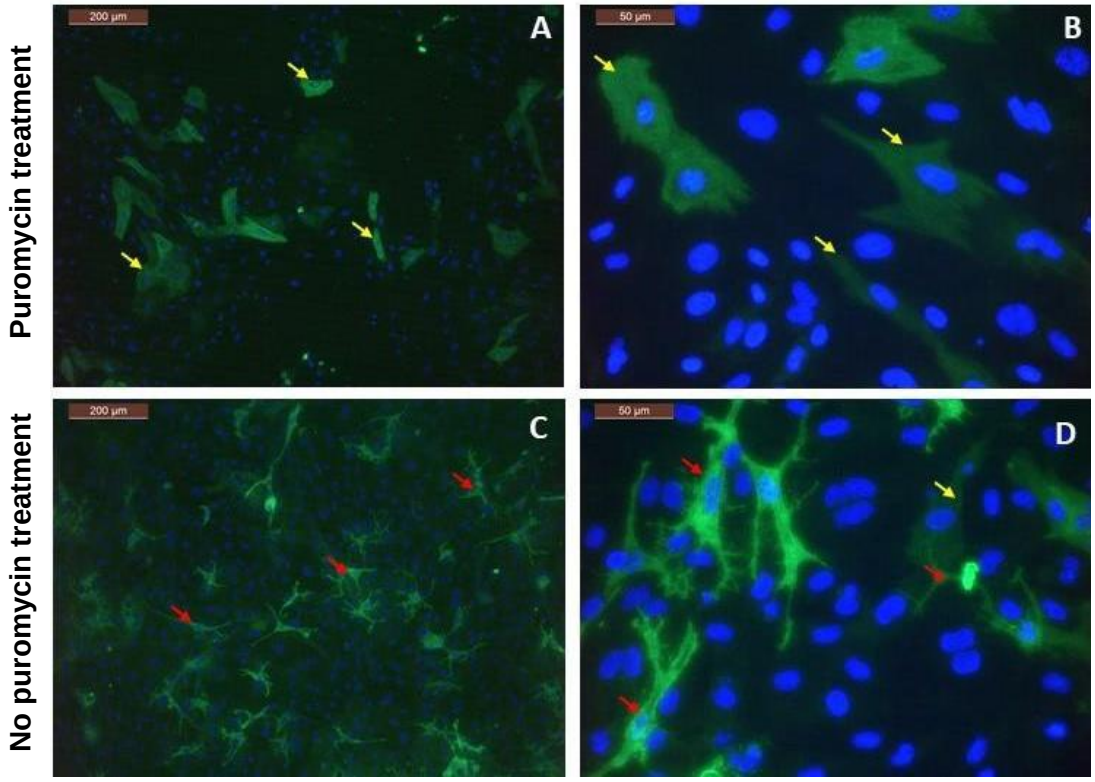

Figure 3.6 - *Immunofluorescent staining for alpha smooth muscle actin (aSMA) in confluent porcine brain endothelial cells. Figures A & B show cultures which have been treated with 4 µg/ml puromycin for 72 hours while Figures C & D show cultures which have not been treated with puromycin. Yellow arrows indicate epithelial-like morphology, red arrows indicate dendritic morphology. aSMA primary antibody ab5694 (Abcam, 1:100), goat anti-rabbit IgG Alexa Fluor 488 (ab150077 Abcam 1:800, green) and DAPI nuclear stain (blue). Images were captured using Leica upright microscope DM5000, at 20X/40X magnification and processed using Leica Image software. Scale bar represents 50 or 200 µm as indicated. Control immunofluorescence was blank, images representative of five fields of vision Negative control in Appendix 6.*

With no puromycin treatment, there were large populations of stained cells with a dendritic morphology (Fig. 3.6C&D). However, in the puromycin-treated cells (Fig. 3.6A&B), the stained cells had an epithelial-like polygonal morphology and were less populous. This indicates that puromycin treatment affected the morphology, and number, of cells present.

3.2.4 Identification of tight junctions between BECs

The presence of tight junctions in primary PBEC cultures was assessed using PCR, Western blotting, immunofluorescence, and SEM imaging for critical tight junction proteins. Furthermore, transendothelial electrical resistance (TEER)

experiments were performed as functional measure of the dynamic junctional adherence, while an FITC-conjugated dextran permeability assay was used to determine restriction of large molecules by the tight junctions.

3.2.4.1 PCR for tight junction associated proteins in BECs

Expression of VE-Cadherin (CDH5, adherens junction forming) and occludin (OCLN, tight junction forming) was assessed using PCR in confluent PBECs (Fig. 3.7) cultured in the presence of puromycin. Beta-2-Microglobulin (B2M) was used as an endogenous control gene.

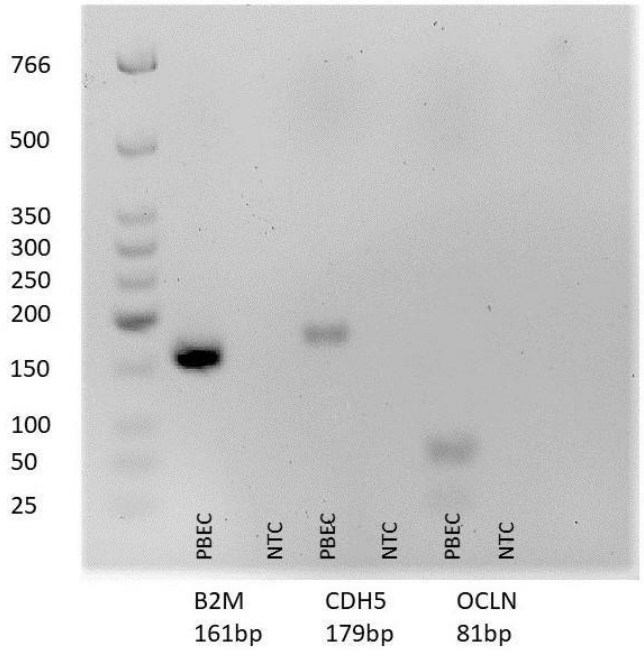

Figure 3.7 – *PCR for tight junctional adherence mRNA products extracted from porcine brain endothelial cells. PCR product sizes for each lane as indicated are: B2M (Beta-2-Microglobulin) - 161bp, CDH5 (VE-Cadherin) - 179bp, OCLN (Occludin) - 81bp. No template control lanes (NTC) show samples with no cDNA added. Agarose gel was imaged using BioRad ChemiDoc Imaging System.*

Single bands were observed for both genes examined at the correct product size for each gene. This showed that the isolated PBECs expressed occludin and VE-cadherin (Fig. 3.7), indicating that tight junctions and adherens junctions are present in the PBEC cultures.

3.2.4.2 Western Blot for adherens junction protein, VE-Cadherin, in BECs

Presence of adherens junction forming protein, VE-Cadherin, was confirmed by Western blotting to show that the mRNA was being translated.

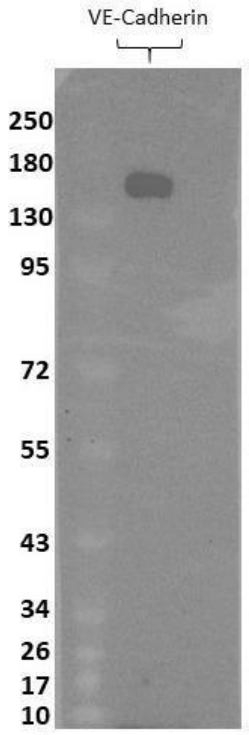

Figure 3.8 - *Western blot for VE-Cadherin in porcine brain endothelial cells. 20 µg of protein was loaded into each well. VE-Cadherin primary - D87F2 Cell Signalling 1:1000, secondary - A9169 from Sigma 1:5000. Chemiluminescence was detected using Bio-Rad ChemiDoc Imaging System.*

After immunoblotting, a single band at the expected size (140 kDa) was observed for VE-cadherin in the PBECs, thus indicating the presence of VE-cadherin protein in a similar manner to that for mRNA (Fig. 3.8).

3.2.4.3 Immunofluorescence for tight junction protein ZO-1 in BECs

ZO-1 is a critical component of the tight junction complex and should be present at the border of all cells in a continuous monolayer of BECs. Immunoflourescent staining was conducted to investigate the presence of ZO-1 between confluent PBECs after 72 hours of culture (Fig. 3.9).

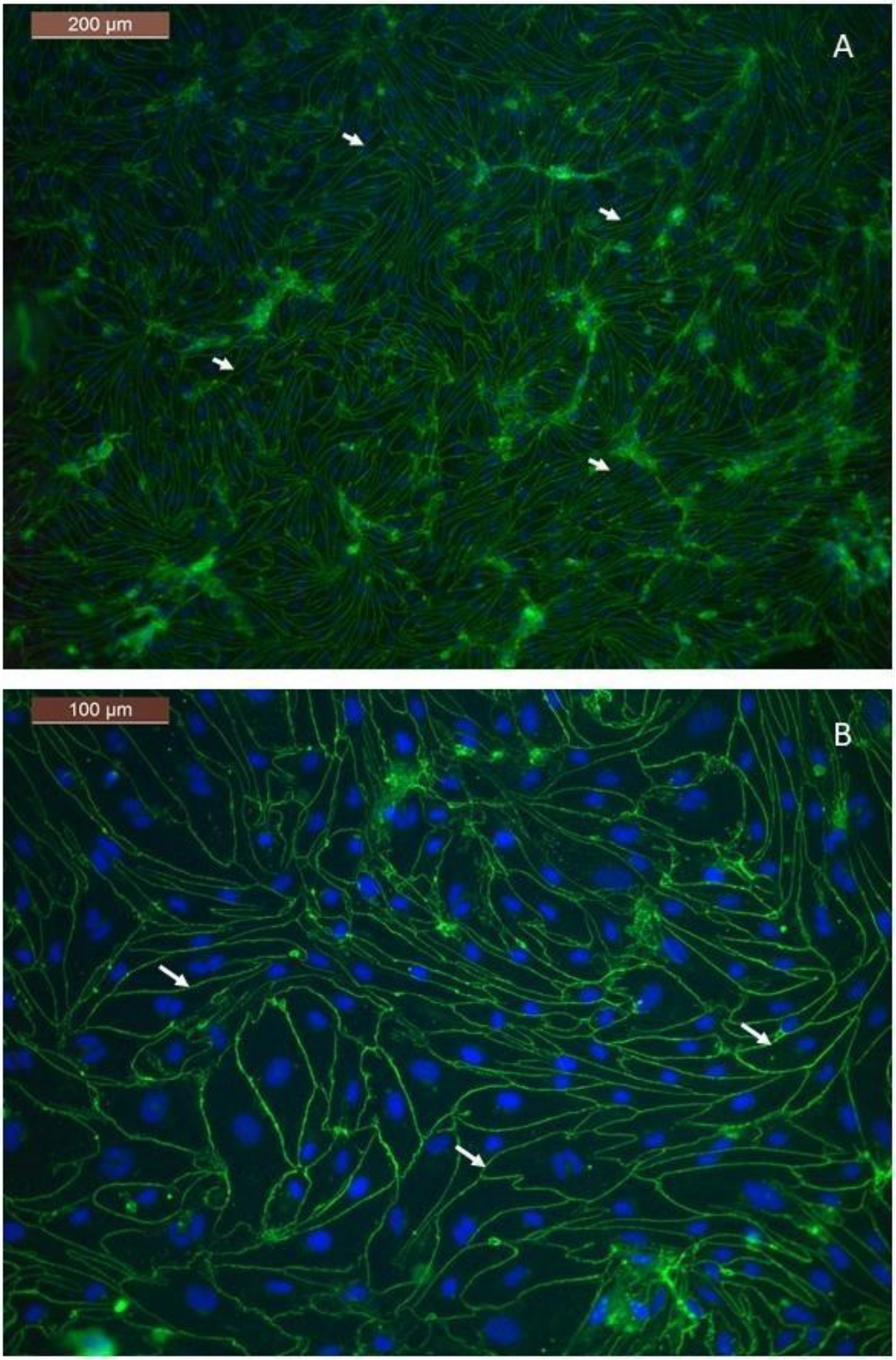

Figure 3.9 - *Immunoflourescent staining for ZO-1 in PBECs. ZO-1 (green) was detected using primary antibody ab221547 (Abcam 1:100), and secondary antibody goat anti-rabbit IgG Alexa Fluor 488 conjugated ab150077 (Abcam 1:800) and DAPI nuclear stain (blue). White arrows indicate example tight junctions. Images were captured using Leica upright microscope DM5000, at 20X (Figure A) or40X (Figure B) or magnification and processed using Leica Image software. Scale bar represents 100 or 200 µm as indicated. Controlwas blank, representative of five fields of vision. Negative control in Appendix 6.*

The primary PBECs formed a confluent monolayer with the mosaic morphology commonly observed in BECs; immunoflourescent staining of ZO-1 showed localisation exclusively at the cell membrane, indicating that the tight junctions are present between all PBECs (Figs. 3.9A and 3.9B). This demonstrates that PBECs are forming a continuous BBB monolayer spontaneously in culture.

3.2.4.4 Scanning Electron Microscopy Images of PBEC Tight Junctions

Detailed surface structure of the PBECs was investigated using scanning electron microscopy (SEM) imaging. Samples were prepared and SEM imaging was carried out by the University of Nottingham Nanoscale & Microscale Research Centre.

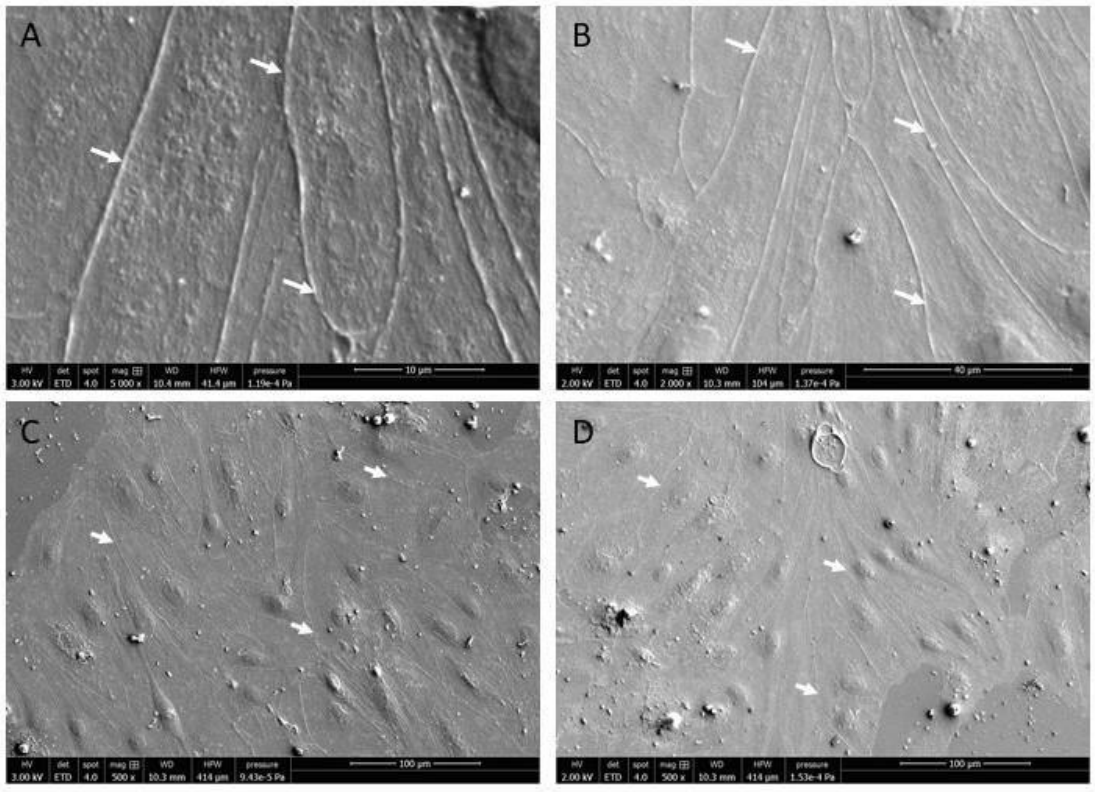

Figure 3.10 – *Scanning Electron Microscopy (SEM) images of primary porcine BECs, following fixation and dehydration. White arrows indicate example tight junctions in the culture. Parameters for microscopy are indicated individually on each image, and scale bars represent 10 µm (image A), 40 µm (image B), and 100 µm (image C & D) respectively. Images representative of five fields of vision*

The surface structure of the PBECs in culture showed distinct, raised, and overlapping areas at the cell-cell borders. This strongly suggested the formation

of tight junctions between the cells (Fig. 3.10). This supports the findings of the immunofluorescence study, indicating that the PBECs are forming a confluent monolayer which is connected by tight junctions at cell-cell borders.

3.2.4.5 Transendothelial electrical resistance in Transwell cultures of BECs

TEER values indicate the electrical resistance across a cell culture monolayer when an alternating current (AC) is applied, which reflects the junctional adhesion between the cells and clearly indicates the ability of the cells to form a tight BBB-like monolayer (Elbrecht et al., 2016). PBECs were cultured to confluence before the cells were passaged onto Transwell culture inserts. TEER values were measured using the EVOM2 voltmeter and ENDOM-6 voltmeter cup every 24 hours for 4 days.

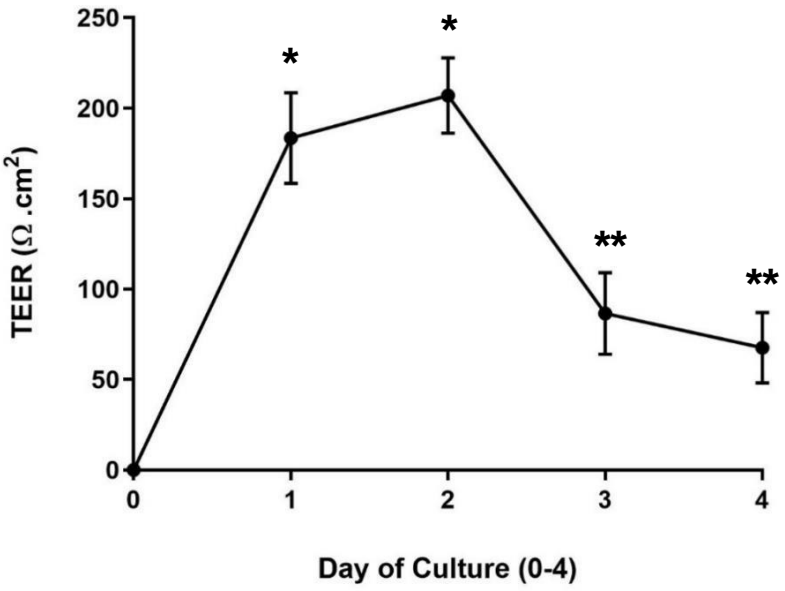

Figure 3.11 *-The effect of time in culture on TEER in PBECs. All TEER measurements were performed in triplicate for each individual insert, with 3 independent inserts in each experiment. Day 0 represents passage of PBECs to Transwell inserts. Data are expressed as mean TEER ± SEM. Statistical significance is indicated as: (*) statistically significant from Day 3 & Day 4 (**) statistically different from Day 1 & Day 2 (two-way ANOVA).*

TEER measurements over the 4 days of culture revealed an increase in the resistance per unit area across Day 1 and 2 (peaking at 207 ± 21 Ω.cm^2) after which the resistance reduced across Day 3 and 4 to below 100 Ω.cm^2. Day 3

and Day 4 were statistically different from Day 1 and Day 2 (P<0.001 Day 2 compared to Day 3) (Fig. 3.11). These results indicate the dynamic movement of junctional adhesion between the cells that make up the monolayer over that period. Furthermore, this gives a distinct time at which cells plated upon transwell inserts display optimum junctional adhesion for drug transport studies.

3.2.4.6 Measurement of FITC-dextran permeability in Transwell cultures of BECs

The restrictive nature of the PBEC monolayer was further examined through 4 kDa fluorescein conjugated dextran (FITC-dextran) transport studies. The TEER experiments determined that PBECs reached maximum junctional adherence after 48 hours in Transwell culture. Therefore, FITC-dextran permeability studies were performed at this time point. FITC-dextran permeability studies were undertaken in apical to basal (A-B) and basal to apical (B-A) directions at 60- and 120-minute time points. The transport of FITC-dextran across the PBEC barrier is presented as a percentage of the no cell control which represents free diffusion between the two compartments.

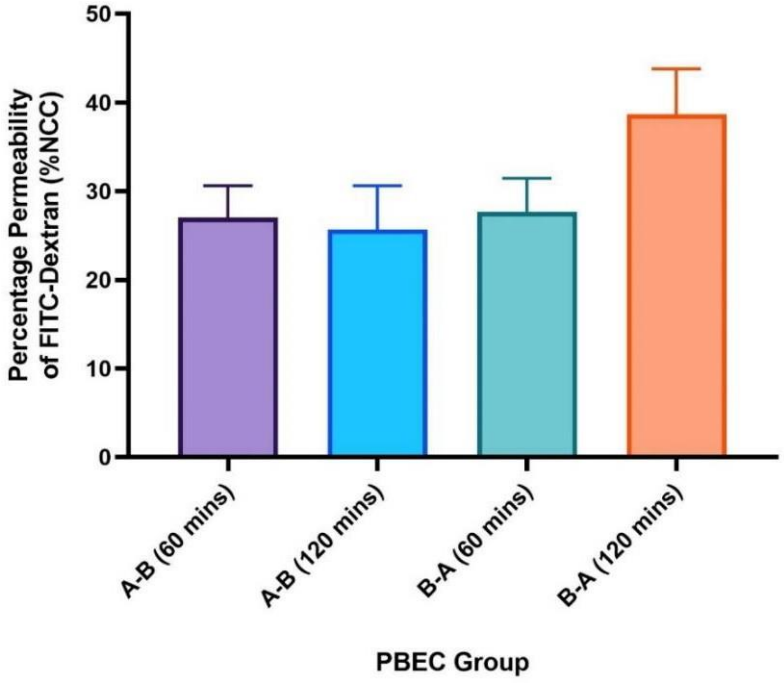

Figure 3.12 - *The percentage of FITC-dextran transport across PBECs from apical to basal (A-B) and basal to apical directions (B-A) at 60 minutes or 120 minutes. Data is presented as a percentage of FITC-dextran across a no cell control Transwell. Values shown are a mean average of 3 well replicates (n=3) ± SEM.*

FITC-dextran is restricted across the membrane in A-B (27%) and B-A (25%) directions at 60 minutes (Fig. 3.12). However, after 120 minutes, the amount of FITC-dextran across the monolayer is maintained in the A-B direction, yet in the B-A direction, this increased to 39%. This shows that the monolayer is restricting the flow of FITC-dextran, however, a significant amount of FITC-dextran is still able to pass from A-B and B-A compartments across the monolayer.

3.2.5 Identification of multidrug efflux transporters in BECs

ABC transporters including P-glycoprotein (P-gp), BCRP and MRPs, are responsible for the efflux of wide-range of common drugs (Mahringer & Fricker, 2016). PCR and Western blot analysis were used to confirm the expression of these critical transporters in isolated PBEC cultures.

3.2.5.1 qPCR for multidrug efflux transporter expression in BECs

The expression of multidrug efflux ABC transporters, P-gp (ABCB1), BCRP (ABCC1) and MRP1 (ABCG2), was investigated using qPCR TaqMan gene expression assay in confluent PBECs after 72 hours *in vitro*.

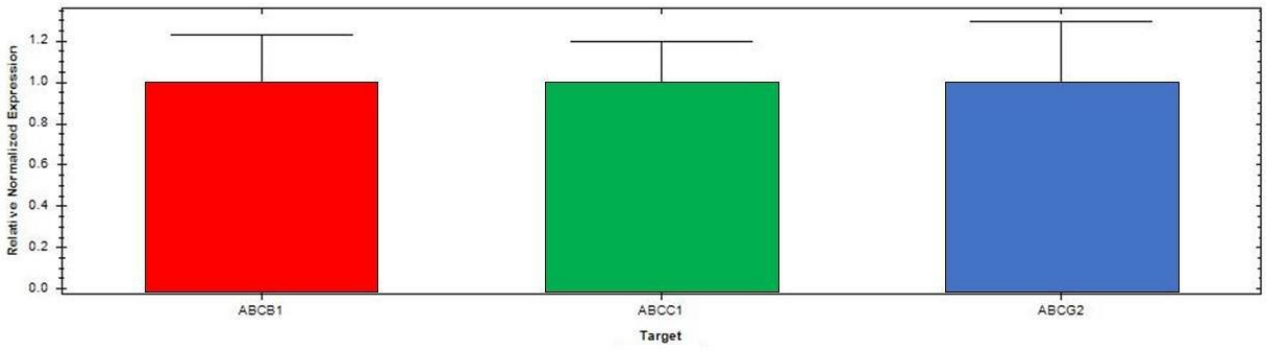

Figure 3.13 – *qPCR for ABC transporters ABCB1 (P-glycoprotein), ABCC1 (MRP1), and ABCG2 (BCRP). qPCR was carried out using TaqMan Gene Expression Assays for each gene, and results are presented as relative normalised expression to endogenous control, GAPDH. Data are Mean +/- SEM from 3 independent cultures*

As previously stated, P-gp, BCRP and MRP1 have been identified as crucial efflux transporters at the BBB. qPCR TaqMan assays showed that ABCB1 (P-gp), ABCC1 (MRP1) and ABCG2 (BCRP) were all expressed in PBECs after 72 hours in culture, and that the expression level was similar to that for the endogenous control gene, GAPDH (Fig. 3.13).

3.2.5.2 Western Blot for P-glycoprotein in BECs

P-gp is widely recognised as the most important protein involved in drug efflux at the BBB (Rauch, 2011). The presence of P-gp in PBECs cultured for 72 hours was examined using Western blot analysis.

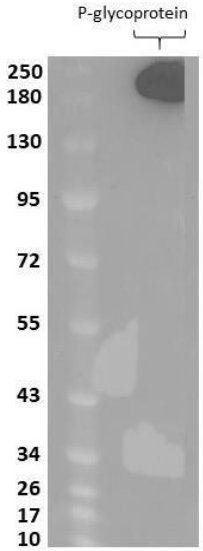

Figure 3.14 - *Western blot for P-glycoprotein in confluent porcine brain endothelial cells. Protein (20 µg) was loaded into each well and proteins were separated by SDS-polyacrylamide gel electrophoresis. (P-glycoprotein - ab170904 Abcam 1:1000 & secondary - A9169 Sigma 1:5000). Chemiluminescence was detected using Bio-Rad ChemiDoc Imaging System.*

Immunoblotting for P-gp produced a broad band at 180 kDa, the expected molecular weight of P-gp on the blot is 141 kDa, however, P-gp has three potential glycosylation sites which can affect the migration of the protein, often producing a higher molecular weight of 180 kDa (Abcam, 2021). Thus, the band present on the blot indicated that P-glycoprotein was expressed by the PBECs after 72 hours in culture

3.2.5.3 Assessment of γ-glutamyl transpeptidase activity in PBECs

The activity of GGT was assessed by quantifying the production of p-nitroanilide substrate from a γ-glutamyl-p-nitroanilide precursor added to the PBECs in a 96-well plate.

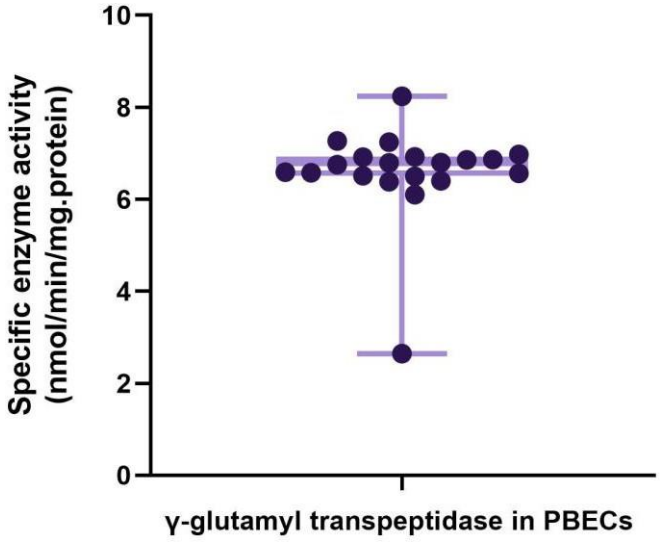

Figure 3.15 – *Specific enzyme activity of γ-glutamyl-transpeptidase in PBECs after 72 hours of culture. Specific enzyme activity was calculated as the production of p-nitroanilide from precursor γ-glutamyl-p-nitroanilide per unit time, per total cell protein as calculated by a Bradford assay. Results are shown as a box and whisker plot of all data points, with whiskers showing max and min values.*

Cultures of PBECs produced a consistent amount of p-nitroanilide per unit time (Figure 3.15). Two cultures were anomalous in their enzyme activity (one greater and one much reduced relative to the remainder) these cultures were not unusual in any other respect and the explanation of these results remain undefined. Outliers aside, this suggests that all the PBEC cultures tested express functional levels of GGT enzyme and have retained this phenotype in *in vitro* culture.

3.3 Discussion

The primary focus of this Chapter was to establish a robust and reliable isolation method to culture PBECs, to determine the purity of the cell cultures, and to characterise the BBB phenotype of the isolated cells when cultured *in vitro.*

Multiple isolation techniques were attempted during the development process to determine the optimal methodology for the project. Initially, it was intended that cultures of both murine and porcine BECs would be isolated and cultured, as BECs isolated from lab-reared rats would allow direct comparison of the collected *in vitro* data to the abundant *in viv*o drug permeability data from rodents, while porcine cerebral tissue has a higher homology with humans (Patabendige et al., 2013; Thomsen et al., 2015). However, the initial isolations which used a singular brain from Sprague-Dawley rats in the protocol from Abbott et al., 1992, resulted in an extremely low yield of vessels that did not disassociate. Endothelial cells grow in a continuous monolayer *in vivo* and *in vitro*, enabling communication through gap junctions, it was, therefore, hypothesised that the low cell/vessel yield restricted cell-cell communication within the population, and consequently reduced the growth and health of the cells (Dora, 2001). Therefore, the number of brains used in the isolation was increased from one to three, alongside an increase in enzyme concentration and digestion times to encourage vessel disassociation. This approach is supported by the protocol published by Rosas-Hernandez et al. 2018. Although, this did result in the presence of individual BECs alongside the vessel fragments, these cells did not survive past 24 hours and vessels did not disassociate. Thus, an isolation was then attempted with 10 Sprague-Dawley brains; however, it was apparent at this time that maintaining housing, food, and transport costs for this number of animals would make the model unsustainable in the long term. While using 10 brains did further increased the yield of cells and vessels, the cells still did not multiply, and vessels did not disassociate. Other groups including Rosas-Hernandez et al. 2018 and Abbott et al., 1992 did not have the same issues with primary BEC isolations from rat brains; however,

the failure of this methodology could be attributed to both limited resources and discrepancies with interpretation of protocols between laboratories.

The issue of low cell yield was not encountered when using porcine tissue, as porcine brains are significantly larger and have a higher proportion of grey matter. An added benefit of using porcine tissue is the availability, at negligible cost and in abundance, from the local abattoir. The use of porcine cerebral tissue also aligns the aims of this project to the 3Rs framework for the replacement, reduction, and refinement of animals in research as no animals are slaughtered solely for the research purposes. An increasing number of studies within the last decade have used primary PBECS for *in vitro* BBB modelling (Nielsen et al., 2017; Patabendige et al., 2013). In all these published studies, cultured primary PBECs have expressed key efflux transporters and consistently produced tight cell-cell junctions. Furthermore, results from a protein BLAST search demonstrate a high level of homology between human and porcine transporters (see Appendix 1). Coupled with results published by Warren et al., 2009, which demonstrate similar expression levels of key ABC transporters, porcine cells were considered a very appropriate contender for BBB modelling. The first isolation, using the isolation method developed by Rosas-Hernandez et al., 2018, in pig brain was effective, and cells from a single brain were confluent within a T75 flask with 72 hours. The disadvantage in using porcine tissue, however, was that with the increase in grey matter, there was an increased use of tissue weight dependent enzymes (as required by the Rosas-Hernandez et al. 2018 methodology). This would make the system progressively more costly. Therefore, the methodology was substituted to that described by Nielsen et al. 2017, in which the enzymes were more cost-effective by comparison to earlier methodologies.

Published isolation methods use either one of two fundamental isolation techniques for BECs. The protocols employed by Abbott et al., 1992, and Rosas-Hernandez et al., 2018, were based upon homogenising the cerebrum in an enzyme digest, followed by a density dependent centrifugation to separate endothelial cells from myelinated cells. However, the subsequent method, based on that developed by Nielsen et al., 2017, used filtration to separate

microvessels from the brain homogenate, which are then subjected to an enzyme digest before plating. This method, when paired with the increased grey matter of porcine brains, consistently produced robust cultures with high cell purity, as well as being more time/cost-efficient. This method was eventually scaled up to produce approximately eight vials of cells (stored in liquid nitrogen before use) from a bulk isolation of eight brains. The BBB vessels, once isolated using the methods discussed above, were plated upon fibronectin-coated cell culture plates in specialised growth media and left to disassociate. The BECs produced using this method had the spindle-shaped elongated fusiform morphology which is typical of endothelial cells and was consistent with the images of BEC cultures presented in published methods (Nielsen et al., 2017; Rosas-Hernandez et al., 2018).

When isolating whole capillaries from the cerebrum, it is logical to assume that both astrocytes and pericytes adhered to the blood vessel may also be present in the cell culture. To avoid growth of these contaminating cell types, puromycin was added to purify to the culture for the first 72 hours, in line with results from other studies (Perrière et al., 2005) (Nielsen et al., 2017). Puromycin is a substrate for P-gp, an ABC transporter that is highly expressed in BECs. Thus, puromycin will be effluxed from the BECs while causing cytotoxicity to other cell types (e.g., pericytes and astrocytes) which do not express this transporter at high levels. However, an examination of the cell types present in the isolated cultures that had been treated with puromycin, revealed that the puromycin did not remove all contaminating pericytic cells based on PCR for aSMA (pericyte marker). In order to further investigate the localisation of aSMA expression in PBEC cultures, immunofluorescence was performed for aSMA. This revealed distinct changes in the morphology and number of aSMA-positive cells with and without puromycin treatment. Namely, aSMA-positive cells in the absence of puromycin purification appear to be smaller, dendritic-like, with elongated processes from the cell body. However, cells treated with puromycin showed fewer stained cells and those were larger, and had spindle shaped fusiform morphology. The morphology of pericytes is known to be highly heterogenous, with variations in cell size and the projection of cell processes due to their wide

range of roles within the CNS (Dore-Duffy & Cleary, 2011). However, this discrepancy in cell morphology due to puromycin treatment was unexpected and has not currently been reported in the published literature. The dendritic cells in the non-puromycin treated cells extend long processes, these projections would wrap around the blood vessel to signal to endothelial cells *in vivo* (Bergers & Song, 2005; Orlidge & D'Amore, 1987). However, the morphology present in the puromycin treated cells show no projections and seem to have adopted a fusiform morphology. It has been proposed that pericytes have stem-cell like properties and consequently can differentiate into other cell types (Dore-Duffy & Cleary, 2011). It was therefore hypothesised that the pericytes in the puromycin treated cells could have a more endothelial-like phenotype, possibly upregulating transporters to ensure survival during the puromycin treatment. Further investigation of this cell type using immunoflourescent co-staining for BEC markers alongside aSMA would be required to test this hypothesis. In summary, puromycin treatment appears to eliminate astrocytic cells but does not fully eliminate pericyte contamination, although puromycin treatment does reduce overall pericyte number and results in morphological changes.

It is imperative to ensure that BEC cultures used for *in vitro* BBB modelling have functional tight junctions, as tight junction proteins, and adherens junction proteins, form the basis for limited paracellular permeability across the BBB (Wolburg & Lippoldt, 2002). The results presented in this Chapter suggest the expression and presence of both tight and adherens junction proteins in the isolated PBECs. Immunoflourescent staining of PBEC cultures for ZO-1 shows clearly defined staining at cell-cell borders, which is in line with immunoflourescent staining of ZO-1 in PBEC cultures presented by Neilsen et al., 2017 and Cantrill et al., 2012. Thus, indicating that tight junctions are present within the culture and that PBECs are creating a confluent monolayer *in vitro*. Similarly, the expression of both occludin in the isolated PBEC cultures is akin to the results presented by Cantrill et al., 2012 and Gericke et al., 2020, further highlighting the maintenance of the BBB phenotype. The finding of VE-cadherin expression from PCR and western blotting within the PBECs also supports this

statement, however, to the best of this author's knowledge, this is the first time that VE-cadherin expression has been identified within primary PBEC cultures. Therefore, demonstrating the presence of adherens junction proteins alongside the presence of the more commonly characterised tight junction proteins. The investigation of the surface structure of PBEC cultures using SEM imaging is also novel and reveals detailed structure of the PBECs. Zhang et al., 2006 and Cantrill et al., 2012 use transmission electron microscopy (TEM) to analyse the presence of tight junctions within the intracellular structure. However, investigation using SEM shows that tight junction structures between endothelial cells can also be viewed extracellularly as raised, overlapping junctions. In conclusion, the evidence for the presence of both tight junction proteins and adherens proteins, which are localised at the cell-cell junctions within the PBEC cultures, is robust.

Alongside examining the expression and localisation of tight junction proteins, it was also necessary to establish that the tight junctions were functional and created a restrictive barrier in the *in vitro* studies. TEER is often used as a comparable measure of junctional adhesion in BEC monolayers (Wilhelm et al., 2011). According to previous studies, the physiological value of TEER in the *in vivo* blood brain barrier could be as high as 6000 $\Omega.cm^2$ (Srinivasan et al., 2015). However, current BBB models vary widely in TEER values; with immortalised cell lines reporting values typically around 30 $\Omega.cm^2$, primary models between 100-2000 $\Omega.cm^{2,}$ and human induced pluripotent stem cells of more than 4000 $\Omega.cm^2$ (Czupalla et al., 2014; Wang et al., 2017). The protocol published by Neilsen et al., in 2017 shows that PBECs with no supporting cells will reach TEER values between 500-2000 $\Omega.cm^2$. In the present Chapter, TEER values varied over the 4-day span, showing the dynamic nature of junctional adhesion in the BBB model. TEER reached maximum at day 2, where junctional tightness reaches an average value of over 200 $\Omega.cm^2$. These TEER readings align with those shown by primary cells isolated in other laboratories (Patabendige et al., 2013). However, Neilsen et al., 2017 stated that their cultures routinely achieved TEER values of >1000 $\Omega.cm^2$. Nonetheless, during the early stages of practising the protocol, the authors state that inexperience handling these cells can result

in a reduced TEER value of 100-900 Ω.cm^2 (Nielsen et al., 2017). Although the TEER values achieved are not as high as TEER values reported in publications from other laboratories, these values are still approximately 10-fold greater than those measured in most immortalised cell lines, and results from other laboratories indicate that these values may increase with methodological experience (Nielsen et al., 2017; Rahman et al., 2016).

TEER results are commonly supported by tracer molecule permeability studies within published literature. Commonly used molecules include sucrose, mannitol, lucifer yellow and dextrans (Thomsen et al., 2015; Zhang et al., 2006). In this study, the permeability of 4 kDa FITC-conjugated dextran across the PBEC monolayer was quantified. At 60 minutes, approximately 27% of the FITC had passed from apical to basal, and from basal to apical compartments. After a further 60 minutes, the apical to basal compartment showed no further permeability. However, in the basal to apical compartment, this increased to 39%. It is likely that the discrepancy in the basal to apical, and apical-basal, directions at 120 minutes is due to biological variability between the models, as although all Transwell models showed over 100 Ω.cm^2 TEER before the experiment, biological variation between samples did result in small fluctuations in TEER between the groups and in this experiment each value was a mean value of n=3. Although it is evident that the cell monolayer is restricting the permeability of the FITC-dextran between compartments, this value is higher than usually accepted as an optimised value for permeability studies. For example, the standardised acceptable permeability of tracer compound is 3% across caco-2 cell monolayers for high-integrity studies (Yamashita et al., 2000). Furthermore, Gericke et al., 2020 reported the permeability of tracer compound mannitol as 3% per hour in PBECs. However, Gericke et al., 2020, also report 10-fold higher TEER values, thus this may suggest that the PBECs isolated in this chapter are not forming a complete barrier. In spite of this, Cantrill et al., 2012, showed that TEER values can be increased, and permeability can be reduced, with the co-culture of PBECs with CTX-TNA2 astrocytes. Thus, further optimisation of the culture protocols for the PBECs for BBB modelling and drug permeability screening will be examined in the following chapter.

In addition to tight junctions, which restrict permeability across the BBB, multidrug efflux transporters have an important role in restricting drug entry into the brain. Warren et al., 2009 analysed the expression levels of ABC transporters at the BBB in porcine and human, normalised to influx transporter GLUT1. It was established that both pig and human BECs have a high expression of P-gp, however, pig BECs have a significantly higher expression of BCRP and a low expression of MRP1 than human BECs. Many studies have shown that ABC transporter expression decreased during *in vitro* culture, due to dedifferentiation of the primary BECs, which leads to a loss of BBB phenotype (Sabbagh & Nathans, 2020). qPCR was used to demonstrate the expression of these three multidrug efflux transporters in PBECs after 72 hours in culture. Indeed, all three ABC transporters, P-gp (ABCB1), MRP1 (ABCC1) and BCRP (ABCG2), are present in the culture, at an approximately proportional ratio to the endogenous control, GAPDH. This differs from the results presented by Warren et al., 2009, which demonstrates negligible levels of MRP1 (ABCC1) within porcine capillaries. To our knowledge, this is the first instance of substantial expression of MRP1 in PBEC cultures, reinforcing the benefit of this cell type in BBB modelling. The expression levels of ABC transporters were also examined by Thomsen et al. 2015, who demonstrated that P-gp and BCRP were expressed at 1% and 2% of the endogenous control, β-actin, respectively. This is significantly lower than the results presented in this Chapter, although direct comparison cannot be made due to discrepancies in the endogenous control gene.

P-gp expression was also analysed using Western blotting which showed a single band for P-gp but at a higher molecular weight than the expected band size of 141 kDa. However, other studies using this antibody have also shown that bands are present at 180-200 kDa, due to the potential glycosylation sites on the protein (Abcam, 2021). Previous publications show that the expression of multidrug efflux transporters, including BCRP and P-gp, were induced by shear stress inducible receptors (Cucullo et al., 2011) and co-culture with astrocyte cells (Baello et al., 2016). Therefore, it is possible that expression of these transporters could be enhanced further by different culture methods.

γ-Glutamyl transpeptidase (GGT) is a metabolic enzyme which is highly expressed in brain capillaries and is often used as a BEC marker. It was determined that the isolated PBECs express the endothelial marker GGT, and also express the enzyme at a relatively consistent level between cultures. This indicates a consistent BEC phenotype between cultures. Cantrill et al., 2012, demonstrated that GGT expression is induced by co-culture with astrocytes, indicating that astrocyte co-culture aids in maintaining BBB phenotype and thus, demonstrating a further benefit of adapting the culture methods in BBB modelling, as will be examined in the following Chapter.

In conclusion, results confirm that a reliable method has been developed to isolate robust cultures of porcine BECs from pig cerebrum. This isolation method has been optimised to ensure that it is both repeatable and cost-effective, and reliably produces a high yield of PBEC cultures. The vessels isolated using this culture method rapidly disassociate into a confluent culture of PBECs, which can be effectively purified using puromycin purification. Molecular and microscopy techniques were employed to confirm the presence of mRNA and protein for key BBB phenotype markers: tight junction proteins, VE-cadherin, occludin, and ZO-1, ABC transporters, P-gp, MRP1, BCRP, and GGT. These cell cultures also demonstrate a restricted permeability across the membrane, as shown by TEER and FITC-dextran permeability studies, which is further indication of the BBB phenotype, however, the permeability is notably higher than that presented in other PBEC publications. In spite of this, the presence of efflux transporters and tight junction proteins *in vitro* indicates that the isolated cell cultures which have been characterised in this Chapter could be suitable for use in a BBB model for drug permeability testing within the pharmaceutical industry with further optimisation.

Chapter 4

Establishing Transwell and microfluidic models of the blood-brain barrier using PBECs

4.1 Background

A reliable method to isolate and culture primary porcine brain endothelial cells (PBECs) from pig cerebrum was established in the previous Chapter. As previously discussed, the majority of *in vitro* models which are widely used within the pharmaceutical industry have significant limitations, including limited genetic homology with humans in BEC phenotype, no representation of signalling from perivascular cell types within the neurovascular unit (NVU), or critical biophysical BBB properties (Gomes et al., 2016; Oddo et al., 2019). This Chapter presents the developments made in producing static and microfluidic cultures of PBECs and their potential use for drug permeability studies.

A number of primary PBEC Transwell models of the BBB have been previously established (Gericke et al., 2020; Patabendige et al., 2013; Thomsen et al., 2015). However, Transwell models of the BBB using immortalised cell lines are much more widespread within the field of drug discovery due to the ease of culture and availability of cells (Bicker et al., 2014). Immortalised Transwell models of the BBB consistently demonstrate reduced junctional adhesion, and while many uptake and efflux transporters are still expressed, their expression levels are decreased (Gericke at al., 2020; Rahman et al., 2016).

A major benefit of the Transwell system is the ability to co-culture BECs in a non-contact co-culture with supportive perivascular NVU cells (Bicker at al., 2014). The release of signalling molecules by astrocytes can increase or decrease vascular permeability (Cheslow & Alvarez, 2016). In Transwell models, the addition of astrocytes in co-culture with BECs has been shown to affect the expression of metabolic enzymes, tight junction proteins, and transporters including GLUT1 and P-gp (Cantrill et al., 2012; Gaillard et al., 2000; Toth et al., 2018). As soluble signalling molecules mediate the majority of astrocyte-endothelial interactions, many of the benefits of astrocyte co-culture can be mimicked by the addition of astrocyte-conditioned media (ACM) to BECs. Indeed, this has also been shown to decrease BBB permeability *in vitro* (Nielsen et al., 2017; Puech et al., 2018).

The Transwell model benefits from ease of use and the ability to co-culture cells, however, the system has a major limitation: Transwell models do not allow for the induction of shear stress. Studies using *in vitro* BBB models have demonstrated that induction of shear stress upon BECs upregulates the expression of tight junction proteins, multidrug efflux transporters, CYP enzymes and regulates carrier-mediated transport and immune cell invasion across the membrane (Partyka et al., 2018; Rochfort & Cummins, 2019; Santaguida et al., 2006). Thus, haemodynamic flow could be said to have a direct role in limiting the paracellular transport of large and hydrophilic molecules, reducing the diffusion of small and lipophilic molecules, increasing metabolism of xenobiotics, and regulating the disruptive barrier effects of inflammatory mediators at the BBB.

Recent advances in microfluidic technology, and a new understanding of the complex relationship between shear stress and cellular function, have laid the foundation for the generation of BBB on a chip (BBBoaC) models. This new and advanced group of BBB models are engineered to mimic the haemodynamic flow and biophysical environment of *in vivo* BECs within an *in vitro* culture system (Jiang et al., 2019). In these models, a continuous monolayer of endothelial cells lines the vascular microfluidic channel and cells are subjected to constant flow to mimic haemodynamic pressure, and thus shear stress, upon the cells (Oddo et al., 2019).

BBBoaC models have not yet been thoroughly evaluated for predicting human *in vivo* drug permeability across the BBB (Bagchi et al., 2019). The criteria for a BBBoaC model to be suitable for compound permeability testing include, real-time optical monitoring of cells, a separate vessel and CNS chamber, and individual inlet and outlet ports to allow compound collection. One such model incorporates these qualities is the “SynVivo” BBBoaC model, which has been used in multiple publications over the past decade (Brown et al., 2019; Prabhakarpandian et al., 2013; Deosarkar et al., 2015; Terrell-Hall et al., 2017). The SynVivo BBBoaC model has a parallel design consisting of two lateral outer vessel chambers, separated from one inner circular CNS chamber by 4 µm spaced micropillars. This model is made from oxygen-permeable and optically

clear PDMS and has built-in electrodes for real-time monitoring of TEER with no risk to cell viability in either chamber. The SynVivo microfluidic BBBoaC model has been established with immortalised BECs, HUVECs, and primary rat BECs (Brown et al., 2019; Prabhakarpandian et al., 2013; Deosarkar et al., 2015; Terrell-Hall et al., 2017). However, this model, nor any BBBoaC model, has been published using cultures of primary PBECs.

Therefore, the aim of this Chapter was to establish a static Transwell model of the BBB using PBECs to investigate the effect of astrocyte co-culture upon the BBB characteristics of the BECs. This primary PBEC Transwell model will be compared to immortalised human BEC line, HBEC-5i. Furthermore, the isolated primary PBECs will also be used to establish and optimise the first primary porcine BBBoaC model within the SynVivo microfluidic system.

4.2 Results

4.2.1 Induction of junctional adhesion by astrocytes and astrocyte conditioned media

Astrocytes outnumber neurons in the brain 10-fold and have myriad roles in maintaining the neuronal microenvironment, including signalling to BECs, and controlling BBB permeability (Davson & Oldendorf, 1967; Zonta et al., 2003). However, only astrocytes which have been harvested from neonatal mammals proliferate easily *in vitro,* making primary astrocytes difficult to obtain (Schildge et al. 2013). For this reason, immortalised astrocyte cell lines, such as the CTX-TNA2 line, are often used in BBB modelling (Wilhelm & Krizbai, 2014). The CTX-TNA2 cell line was created from primary astrocytes isolated from brain frontal cortex tissue of 1-day old Sprague-Dawley rats and has been shown to maintain the *in vivo* phenotype of primary porcine BECs (Cantrill et al., 2012). In addition, spent media from primary or immortalised astrocytes (known as ACM) has been proven to increase junctional adhesion and reduced permeability in BECs (Puech et al., 2018). This section assesses the effect of co-culture with CTX-TNA2 immortalised astrocytes, or CTX-TNA2 generated ACM, with primary PBECs in a non-contact Transwell culture to examine their effects on TEER values and FITC-dextran permeability.

4.2.1.2 TEER values across astrocyte treated PBECs

It was previously shown that TEER values of PBECs are highest on day 2, across a 4-day PBEC culture (Section 3.2.4.5). This experiment was repeated to determine the effect of astrocytes upon the electrical resistance across the membrane. PBECs were cultured on Transwell inserts for 24 hours, in either astrocyte co-culture, ACM treatment, or grown in monoculture. In the astrocyte co-culture group, CTX-TNA2 astrocytes were seeded in non-contact co-culture on the bottom of the Transwell plate, with PBECs suspended on the semi-permeable Transwell insert. In the ACM group, the medium in the bottom compartment was replaced with identical medium (DMEM :Ham's F12 1:1 with 10% FBS and supplements) which had previously been cultured with CTX-TNA2 astrocytes for 48 hours. The third group (monoculture) were cultured as previously shown (Section 3.2.4.5). TEER was measured in triplicate using the same methodology over a period of 4 days.

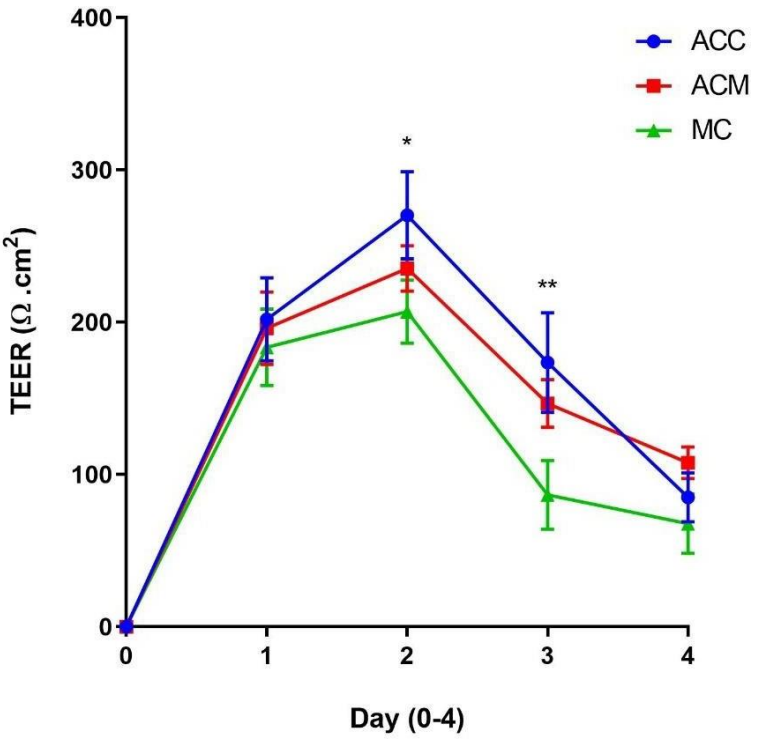

Figure 4.1 - *TEER values of Transwell PBEC cultures over a time course of 4 days (day 0 = day of seeding), in astrocyte co-culture, ACM treatment, or monoculture. Astrocytes or ACM media were added 24 hours prior to first measurement. All TEER measurements were taken in triplicate for each individual insert, and 3 independent inserts were included in each experiment. Data are expressed as mean TEER ± SEM. Data was analysed with two-way ANOVA where * (P<0.05) and ** (P<0.01) indicating time points where Astrocyte co-culture was different from PBEC monoculture.*

In all groups the highest TEER was recorded on Day 2, with the highest recorded TEER values measured for co-culture at 270 ± 26 Ω.cm^2, followed by ACM treatment at 235 ± 25 Ω.cm^2, and finally, PBEC monoculture at 207 ± 21 Ω.cm^2 (mean ± SEM). It is evident that both addition of ACM and astrocyte co-culture increased tight junction integrity and provided higher TEER values. However, only the astrocyte co-culture group (on days 2 and 3) was significantly different from the PBEC monoculture group ($P<0.05$ and $P<0.01$, respectively).

4.2.1.3 Permeability of FITC-Dextran in astrocyte treated PBECs

To further explore the effect of astrocytes upon tight junctions, FITC-dextran permeability experiments were conducted in Transwell at the day 2 time point, at which time peak TEER values were achieved for all treatment groups. The same treatment groups as previous sections were used: PBEC astrocyte co-culture (ACC), PBECs with ACM treatment (ACM), and PBECs in monoculture (MC). The PBECs in co-culture and ACM groups were cultured with astrocytes or ACM for 24 hours prior to the experiment.

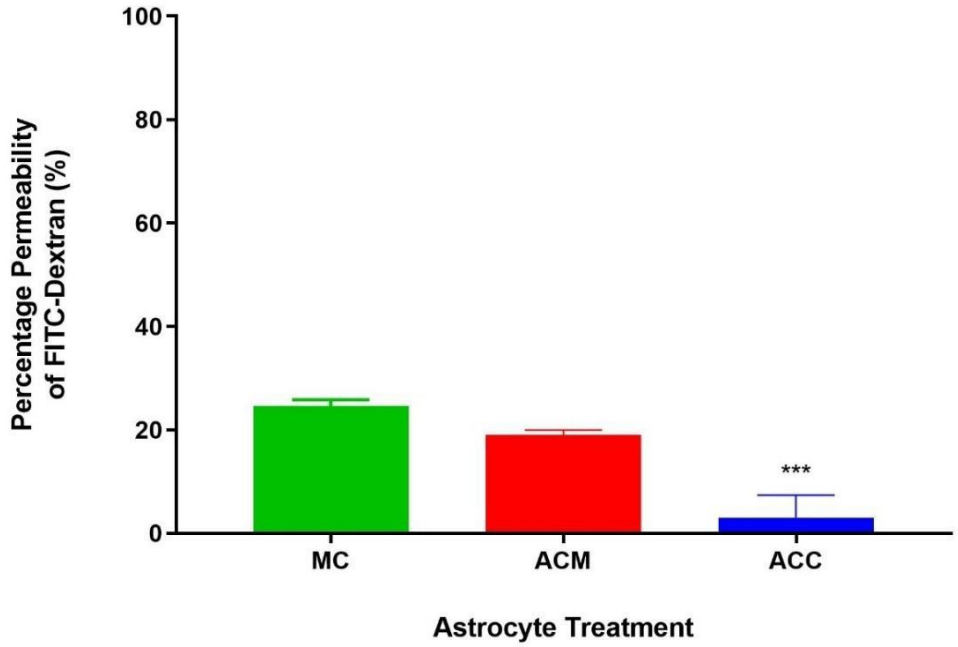

Figure 4.2 *- The effect of different astrocyte treatment groups on permeability of FITC-dextran across a PBEC monolayer in Transwell. The 3 groups were: No contact CTX-TNA2 astrocyte co-culture (ACC), treatment with astrocyte conditioned media (ACM), or PBECs in monoculture (MC). The PBEC permeability values are taken as a percentage of the no PBEC control value in each group to account for the restriction in permeability from the Transwell insert alone. Values shown for each group are a mean average of 3 well replicates ± SEM. Data were compared with one-way ANOVA and *** (P<0.001) indicates significance difference to both ACM and MC groups.*

FITC-dextran permeability experiment showed that, of the three groups, co-culture with astrocytes reduced permeability to the greatest extent (3 ± 2.5%) (Fig. 4.2). Although FITC-dextran permeability was lower following treatment with ACM (19 ± 0.6 %) than in the monocultures (25 ± 0.7 %), this difference was not significant. Therefore, the FITC-dextran permeability study supports the TEER data in confirming that astrocyte co-culture is the most effective means of in increasing tight junctional adhesion between PBECs.

4.2.2 Variance in junctional adhesion between primary and immortalised BECs

Immortalised BECs offer some of the benefits of primary BECs without the limitation of complex isolation methodologies and low passage numbers (Oddo et al., 2019). In spite of this, some studies have demonstrated that immortalised BECs have leaky cell-cell junctions (Gericke et al., 2020; Urich et al., 2012). In this section, the junctional adhesion of the PBEC cultures will be compared to a commercially available human cell line, HBEC-5i cells, to determine the differences in TEER values and FITC-dextran permeability and how these are affected by astrocyte co-culture.

4.2.2.1 TEER measurements in immortalised and primary BECs

HBEC-5i cells were cultured in a 12-well Transwell plate with the same three treatment groups used previously (Section 4.2.1.2): astrocyte co-culture (ACC), ACM treatment (ACM) and monoculture (MC). HBEC-5i cells in all groups were cultured with the same transport media constituents as PBECs for the duration of the experiment. CTX-TNA2 astrocytes or ACM were added to the Transwell basal compartments for 24-hours before measurements were taken.

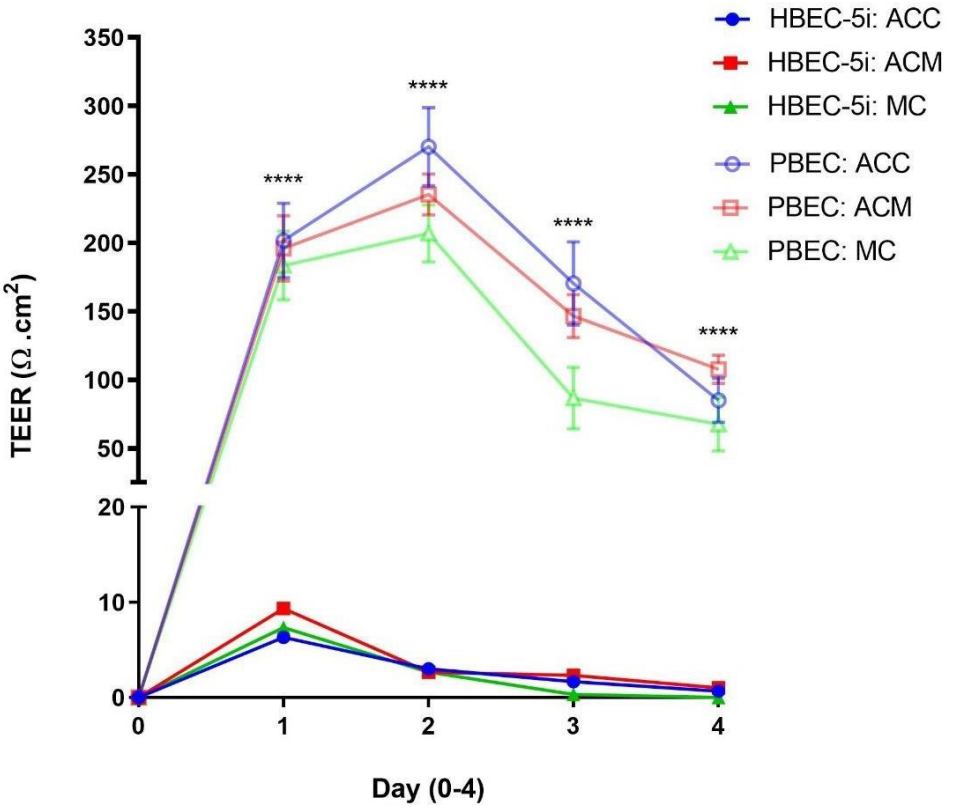

Figure 4.3 *- TEER values of Transwell PBEC and HBEC-5i cultures over a time course of 4 days, either in astrocyte co-culture, ACM treatment, or monoculture. Astrocytes or ACM media were added 24 hours prior to first measurement. All TEER measurements were taken in triplicate for each group, and 3 independent inserts were included in each experiment. Data are expressed as mean TEER ± SEM. On all days, the TEER values for all HBEC-5i treatment groups were significantly different to the PBEC treatment groups. Data were compared using two-way ANOVA and significance (P > 0.0001) is indicated on the figure as ****.*

TEER measurements show significant differences between primary and immortalised cells in all treatment groups over the time period (Fig. 4.3) (P>0.0001, two-way ANOVA). Unlike PBEC cultures, immortalised HBEC-5i cells reach their peak TEER value on day 1, with values of 6.3 ± 0.33 Ω.cm^2 for the astrocyte co-culture group, 9.3 ± 0.33 Ω.cm^2 for the ACM treated group, and 7.3 ± 0.33 Ω.cm^2 for the monoculture group. This was considerably lower than all PBEC groups, which had a TEER of greater than 200 Ω.cm^2 at their peak (day 2 of culture) in all three treatment groups. Furthermore, no response to astrocyte co-culture can be observed in HBEC-5i cultures, as TEER in monocultures was greater than the TEER in astrocyte co-cultured cells. The significantly lower TEER across the endothelial monolayer in HBEC-5i cultures, relative to the PBECs, across the entire time course indicates lower junctional adhesion between the immortalised cells.

4.2.2.2 FITC-Dextran permeability assay in immortalised and primary BECs

An FITC-dextran permeability assay was performed to further evaluate the differences in permeability between primary PBECs and immortalised HBEC-5i cells. HBEC-5i cells were cultured on a Transwell plate under the same conditions and same the three astrocyte treatment groups. Based on the TEER peak, the FITC-dextran permeability assay for HBEC-5i cells was conducted on day 1 of culture. This was compared to PBEC permeability values which were taken at their maximum TEER value on day 2 of culture.

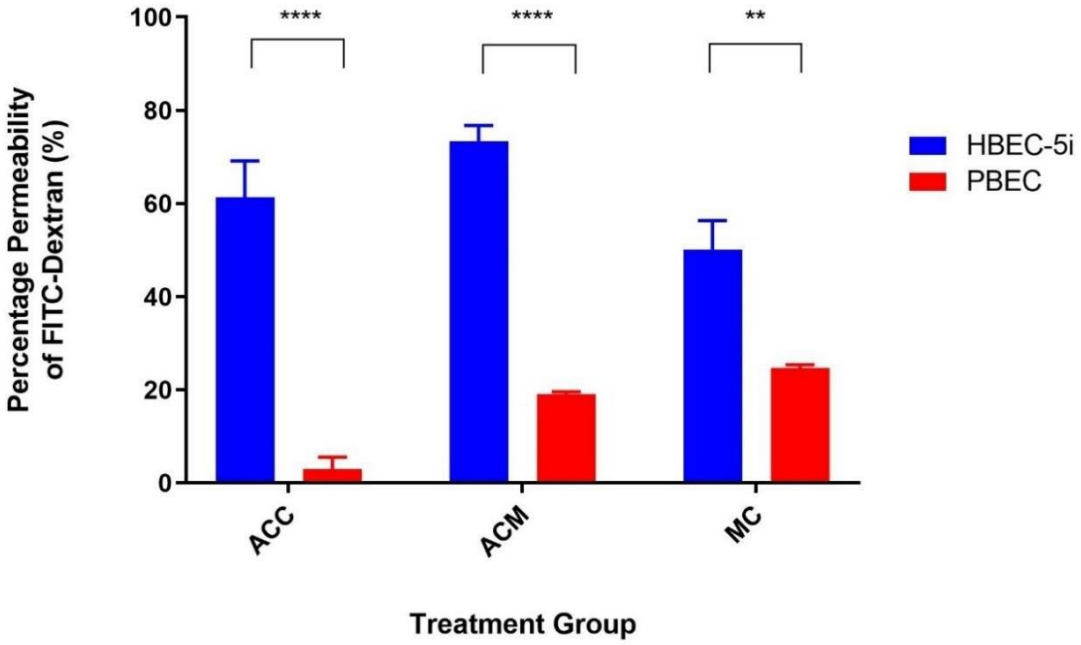

Figure 4.4 *- The permeability of FITC-dextran across HBEC-5i and PBEC monolayers in Transwell in three astrocyte treatment groups. No contact CTX-TNA2 astrocyte co-culture (ACC), treatment with astrocyte conditioned media (ACM), or PBECs / HBEC-5i cells in monoculture (MC). The cell permeability values were taken as a percentage of the no cell value to account for the restriction in permeability from the Transwell insert alone. Values shown for each group are a mean average of 3 well replicates ± SEM. Data were analysed by 2way ANOVA with ** = P = <0.01 and **** = P < 0.0001 indicating significance difference between the cell types.*

The permeability of FITC-dextran was significantly greater across HBEC-5i monolayers compared to PBEC monolayers across all treatment groups ($P<0.001$, two-way ANOVA) (Fig. 4.4). Across all 3 astrocyte treatment groups, the mean permeability across HBEC-5i cells ranged from 50 to 73%. This was unaffected by astrocyte treatment and was at least 2-fold greater than the permeability observed across all PBEC treatment groups. Furthermore, the percentage permeability values for the HBEC-5i cells do not correlate with astrocyte treatment in line with the PBEC permeability values. Therefore, the FITC-dextran permeability results further support the TEER values and indicate reduced tight junctional integrity of the immortalised HBEC-5i cell line.

4.2.3 Cell culture in the SynVivo chip

The SynVivo microfluidic idealised chip has been used with a wide range of cells to model the BBB and mimics shear stress by the infusion of media across the endothelial monolayer (Brown et al., 2019; Prabhakarpandian et al., 2013; Deosarkar et al., 2015; Terrell-Hall et al., 2017). Currently, no BBBoaC model has been developed, in the SynVivo chip or otherwise, using primary PBECs. Therefore, this section will detail the development of a protocol to culture PBECs within the SynVivo idealised chip.

4.2.3.1 Cell seeding in SynVivo chip

Protocols were developed and optimised for the culture of primary PBECs and immortalised HBEC-5i cells in the SynVivo chip. Within an extensive literature search, this has not been reported before and, given the novelty of the work, many optimisation steps were required to establish the protocols for the culturing of the cells within the microfluidic chip. This included changes in cell seeding density, basement membrane proteins, and flow conditions (Table 4.1).

Table 4.1 – Optimisation of seeding protocols for the SynVivo microfluidic chip.

Condition	HBEC-5i Protocol	PBEC Protocol
Optimisation of Cell Seeding Density	Concentration used as recommended by SynVivo, majority of cells seeded & survived, 2×10^7 cells/ml of cells used per chip. Cells take 24 hours to become confluent.	Higher concentration of cells required due to high rates of cell death; 4×10^7 cells/ml (2x pig brains per injection). Cells take 96 hours to become confluent.
Optimisation of Cell Seeding Time	Cell survival in chip was high after 1st seeding, no further seeding needed. High cell survival & density meant cells would adhere to all 3D surfaces in channel.	Cell survival was low after first seeding, two cell seedings required and must be seeded ~8 hours apart. Low density meant chip was rotated to ensure cells seed on all 3D surfaces in channel.
Optimisation of Flow during Seeding Procedure	Cells could survive infusion flow into chip during seeding of up to 10 µl/min.	High flow rates during infusion of cells into chip caused higher rates of cell death, must be <3 µl/min.
Changes to Basement Membrane Proteins	No changes to basement membrane proteins required from Transwell protocol (100 µg/ml fibronectin & 500 µg/ml collagen IV).	Increased concentrations of fibronectin & collagen IV required for seeding of cells, increased to 1 mg/ml fibronectin & 1 mg/ml collagen IV.
Prevention of Air Bubble Formation within Channels	SynVivo recommends pneumatic priming the microfluidic chip with inert gas using their pneumatic priming device at 7.5 psi for 20 mins to prevent trapped air from PDMS leaking into channel. This was not found to be sufficient to prevent air leakage. Empty & closed microfluidic chips were additionally pressurised with coating solution at 5 µl/min for 3 mins to ensure removal of air from PDMS.	
Cell Extravasation	HBEC-5i cells are significantly smaller than primary PBECs, this caused many cells to travel through 4 µm pores in the microfluidic chip into central	The larger size of PBECs caused less cells to extravasate through the pores into outer and central chambers, but some extravasation is present.

	& outer chambers where they seeded down.	
Media Flow Conditions	Cells must be kept at 37°c 5% CO2, however, the syringe pump containing media must be kept in atmospheric conditions to prevent damage. Flowing media loaded in the external syringe pump into the chip caused media to be warmed quickly to 37°c while passing through the tubing, this generated air bubbles which caused cell detachment. Media was withdrawn through the microfluidic chip from a 37°c media reservoir inside the incubator to a syringe loaded outside the incubator.	
Optimisation of Shear Stress	Cells were subjected to shear stress of 1 µl/min 24 hours post seeding. Cells could survive under shear stress for 48 hours.	Cells did not survive any shear stress within 72 hours of seeding, including levels down to 100 nl/min. Cells had to grow to confluency over 92 hours with daily media changes. After this change, cells could withstand shear stress of 3 µl/min for 48 hours.

Table 4.1 – *Workflow to optimise seeding protocols for HBEC-5i and PBEC cultures within the SynVivo microfluidic chip.*

Changes to the seeding protocols for HBEC-5i and primary PBECs, shown in Table 4.1, demonstrate the numerous cell type specific differences that were required to establish a microfluidic culture. Aside from alterations to media flow conditions and the prevention of air bubble formation, all other modifications required optimisation specifically to that cell type. The more resilient nature of the immortalised HBEC-5i cells resulted in a higher proportion of the cells which were injected into the chip successfully adhering to the coated PDMS. The majority of HBEC-5i cells injected into the chip after one injection at the recommended seeding density (2×10^7 cells/ml) would adhere to the PDMS and resulted in a near confluent monolayer of cells on all 3D surfaces in the outer channel of the microfluidic chip. However, the smaller cell size of the HBEC-5i cells resulted in high levels of cell extravasation out of the permeable pores, resulting in cell seeding in lateral chip compartments. There were no

optimisations, beyond that used for Transwell, to basement membrane coating proteins or infusion flow rates required for HBEC-5i cells.

In contrast, the seeding of the primary PBECs required further optimisation due to their sensitivity to the microfluidic environment. For example, after a single injection of PBECs into the outer channel of the microfluidic chip only a small proportion of cells would adhere to the PDMS, with the majority of cells shrinking and appearing to undergo apoptosis. The proportion of cells attaching to the PDMS was enhanced by increasing the concentration of basement membrane coating proteins, increasing the seeding concentration to 4×10^7 cells/ml, and decreasing the initial infusion flow rate of cells into the chip during seeding. As discussed, (Section 3.3), primary BECs are known to be adversely affected by low seeding densities, and without cell-to-cell contact they can undergo cell death. Therefore, a second cell injection step (at 4×10^7 cells/ml) was introduced to increase the number of viable cells in the channels. After two cell infusions, the cells within the channel would be 20-30% confluent. The cells would continue to grow during the 24-hour incubation period recommended by SynVivo before haemodynamic flow was started. However, cell growth would cease with as little as 100 nl/min of shear stress applied, which would ultimately result in cell death. Thus, the initial incubation period was increased to 96 hours with a daily media change enabled the PBECs to reach confluency. Once the primary PBECs had reached confluency within the channel, the cells could withstand levels of shear stress up to 3 µl/min.

4.2.3.2 Seeding of HBEC-5i cells in SynVivo chip

HBEC-5i cells were seeded into the SynVivo microfluidic chip, (Section 2.7.5 and Table 2). After 24 hours of incubation, HBEC-5i cells were subjected to flow at rates of 1 µl/min.

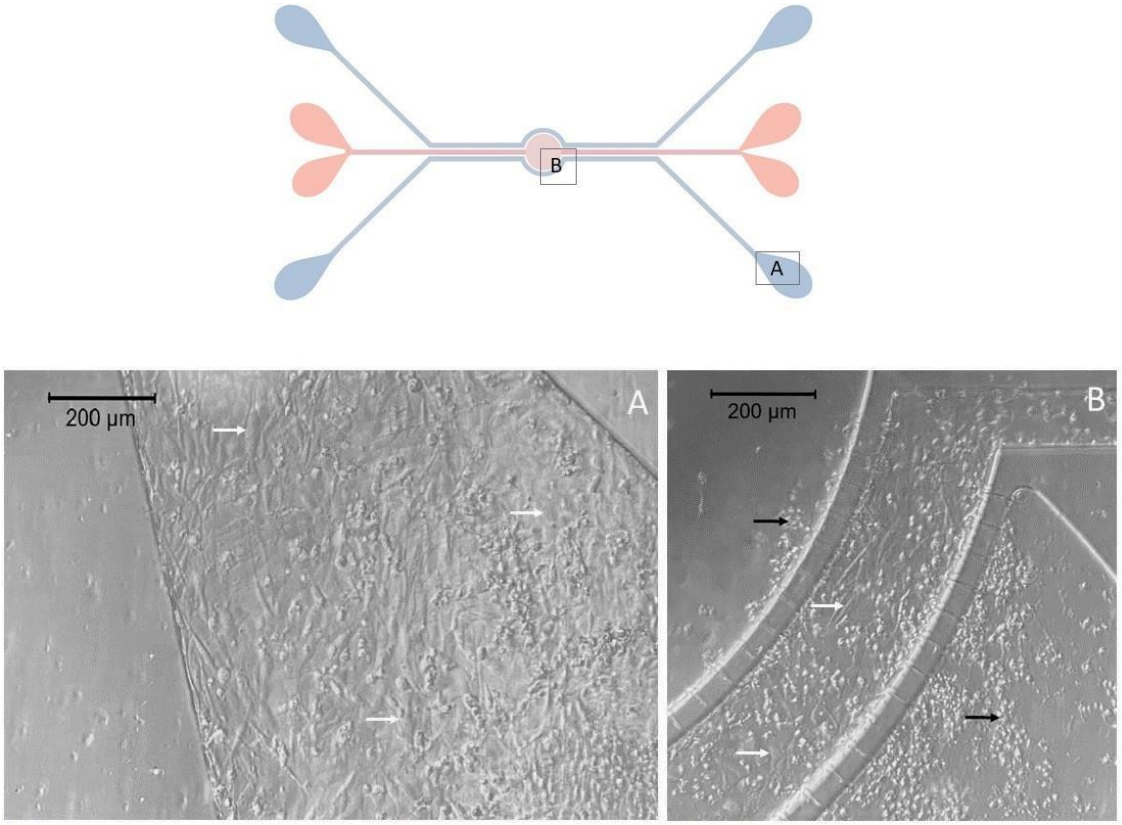

Figure 4.5 – *Light microscopy representative images of HBEC-5i cells captured 24 hours post seeding. Schematic indicates location of images on SynVivo chip. (A) shows cells at the outer channel inlet, and (B) shows cells in the central porous outer channel area. White arrows highlight seeded HBEC-5i cells, and black arrows show clusters of cells which have extravasated through channel pores. Images were captured using Leica microscope DM5000. Scale bar is 200µm. Images representative of five fields of vision.*

Fusiform HBEC-5i cells were observed in both the outer channel inlet (Fig. 4.5A), and the central porous channel area of the chip (Fig. 4.5B, indicated by black arrows). Clusters of dead cells which have not survived the seeding process were also observed inside the channel and in the lateral chambers (Fig. 4.5B, white arrows) where cells have extravasated through the 4 µm pores.

4.2.3.3 Cell seeding of PBECs in SynVivo chip

Primary PBECs were seeded into the SynVivo microfluidic chip (Table 4.1). After 96 hours of incubation, with daily media changes, cells would achieve confluence and withstand shear stress of 3 µl/min for 48 hours.

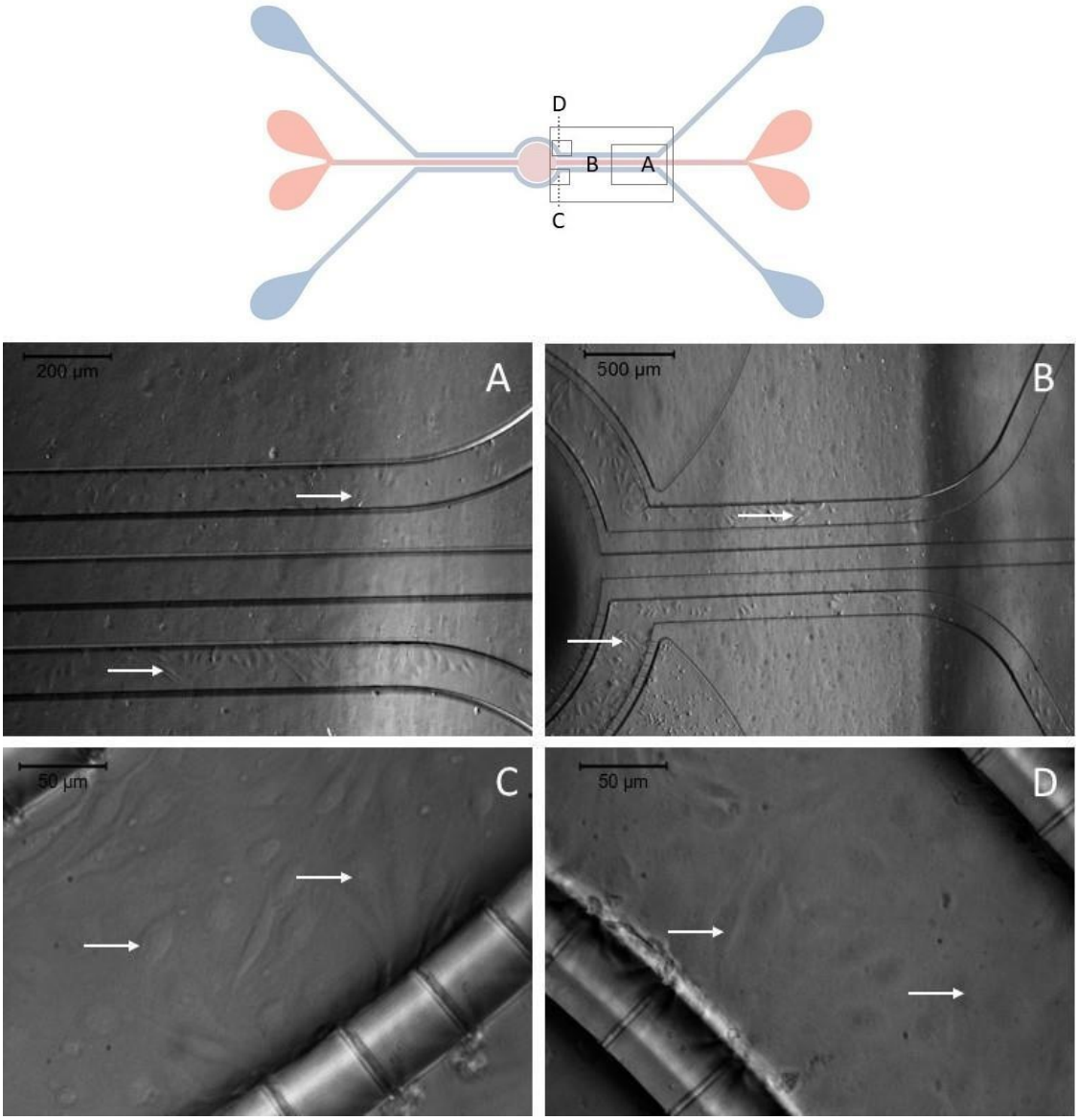

Figure 4.6 – *Light microscopy images of PBECs taken 96 hours post seeding. Schematic indicates location of images on SynVivo chip. Images A & B show cells in the outer channels, and Images C & D show cells in the central porous outer channel area. White arrows demonstrate example seeded PBECs. Images were captured using Leica microscope DM5000. Scale bars are 500 µm, 200 µm or 50 µm, respectively. Images representative of five fields of vision.*

The network of PBECs were seeded in the chip channels and cultured under static conditions for 96 hours (Fig 4.6). The PBECs lined the central porous chamber (Fig. 4.6 C&D), and the PBECs were also present in the outer channels but are less confluent (Fig. 4.6 A&B). Seeded PBECs are indicated by white arrows.

4.2.4 Evaluating tight junction formation in SynVivo chip culture of PBECs

The formation of tight junctions between primary PBECs in the SynVivo microfluidic chip was evaluated using an identical approach to that for Transwell cultures, namely FITC-dextran permeability assays and TEER measurements.

4.2.4.1 Measurement of FITC-dextran permeability in SynVivo microfluidic culture of PBECs

The ability of the primary PBECs to form a restrictive barrier within the SynVivo microfluidic chip was assessed using FITC-conjugated 4 kDa dextran. The FITC-dextran solution was infused into an empty microfluidic chip and a microfluidic chip containing PBECs which had been cultured for 96 hours. The permeability of FITC-dextran in the empty and cultured chip was assessed using fluorescence microscopy at 0-, 15-, and 30-minutes post-infusion.

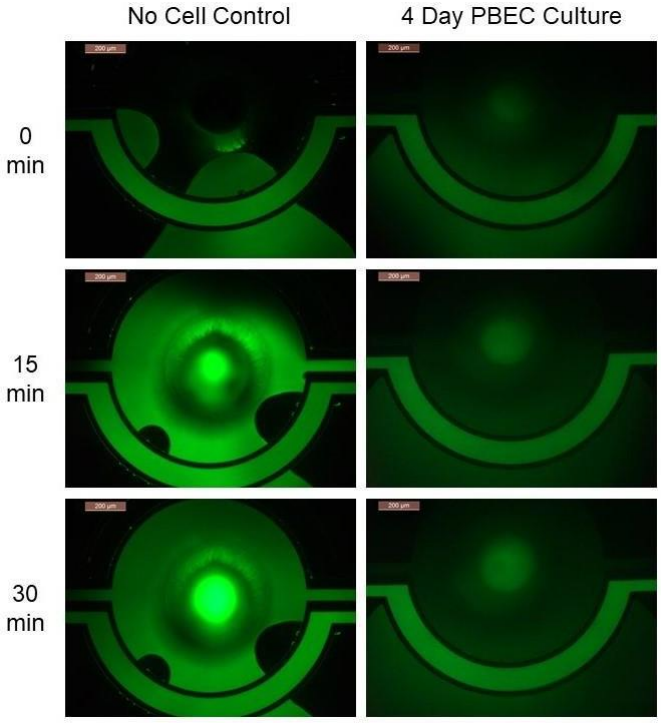

Figure 4.7 *- Permeability of conjugated 4 kDa FITC-dextran (green) from the bottom outer channel of the SynVivo microfluidic chip, in a chip containing no cell cultures (left) and a chip containing PBEC cultures (right). Images were captured using Leica upright microscope DM5000 and processed using Leica Image software. Scale bar represents 200 µm.*

In a SynVivo chip which contained no cells, FITC-dextran perfused into the outer channel immediately began to flow through the 4 µm pores between the two compartments (Fig. 4.7, left). FITC-dextran had filled the entirety of the central chamber within 30-minutes. Whereas upon infusion of FITC-dextran to the PBEC cultures, flow is greatly restricted between the compartments, and this was maintained for the 30-minute time period (Fig. 4.7, right). Therefore, this suggested that the PBECs formed a barrier that restricted the flow FITC-dextran between the two compartments of the SynVivo chip.

4.2.4.2 Measurement of PBEC TEER in the SynVivo chip

SynVivo have developed a unique electrode system to measure TEER with appropriate SynVivo microfluidic chips (SynVivo impedance analyser). The SynVivo impedance analyser measures tight junction integrity as impedance, rather than resistance, and can generate AC current of varying frequencies from 500 Hz to 10 kHz. In contrast, the EVOM2 TEER meter, used for Transwell systems, measures resistance values using an AC current with a set frequency of 12.5 Hz. It should be noted that, in the initial publication of the SynVivo BBB model by Deosarkar et al., 2015, it was stated that due to the novel method of impedance measurement and differences in surface area and pore density, the impedance values generated in the SynVivo microfluidic chip cannot be compared to the resistance values in a Transwell model.

Impedance measurements were taken in the SynVivo microfluidic chip for both HBEC-5i cell and primary PBECs (Table 4.2). It should be noted that this data is reported as raw impedance values without subtraction of blank values and is not normalised to surface area. For comparison of the SynVivo impedance analyser to the EVOM2 TEER meter, the impedance analyser was also used to measure impedance in Transwell cultures of HBEC-5i cells and PBECs (Table 4.3). These values for Transwell impedance measured using the SynVivo analyser are presented alongside EVOM2 measurements of resistance in the same Transwell cultures for both cell types (Table 4.3). These data are also raw values, which are not normalised to blank values or surface area.

Table 4.2 – Impedance measurements in SynVivo chip

Cell type	Impedance measurement of chip (kΩ)
Blank (no cell control)	220.5 ± 3.5
HBEC-5i	231.5 ± 2.5
PBECs	243 ± 19

Table 4.2 – *Impedance measurements taken in SynVivo microfluidic chips with the SynVivo impedance analyser at 10 kHz. Values are shown for blank (no cell culture present), HBEC-5i cells, and primary PBECs. All measurements were taken when cells were confluent. Data are not normalised to blank or surface area. Each value represents mean ± SEM with n=2 for each group.*

Table 4.3 – Resistance & impedance measures in Transwell

Cell type	Impedance measurement of Transwell (kΩ)	Resistance measurement of Transwell (Ω)
Blank (no cell control)	220 ± 7	90.5 ± 0.5
HBEC-5i	224.5 ± 7.5	113.5 ± 0.5
PBECs	237.5 ± 6.5	712 ± 19.5

Table 4.3 – *Resistance & impedance measurements taken in Transwell cultures with either SynVivo impedance analyser at 10 kHz (impedance measurement) or EVOM2 TEER meter and Endohm-6G electrode cup (resistance measurement). Values are shown for blank (no cell culture present), HBEC-5i cells, and primary PBECs. All measurements were taken when cells were confluent. Data are not normalised to blank or surface area. Each value represents mean ± SEM with n=2 for each group.*

There was no meaningful difference between the blank values measured and values measured for both cell types in the SynVivo chip cultures (Table 4.2). Transwell cultures of the same cell types measured using the SynVivo impedance analyser also showed no meaningful difference (Table 4.3). However, when Transwell cultures of HBEC-5i and PBEC cultures were measured using the EVOM2 TEER meter, resistance values across the same cell model were strikingly different, particularly in the PBECs. It should also be noted that these values also have differing units, as the SynVivo impedance analyser displays data in kΩ, whereas the EVOM2 meter displays data in Ω.

4.3 Discussion

The overarching aims of this Chapter were to establish a static Transwell model of the BBB using primary PBECs which could be used to investigate the effect of astrocyte co-culture upon BBB characteristics, as well comparing the primary PBECs to an immortalised cell line. Additionally, this Chapter aimed to optimise and implement a protocol to seed the isolated primary PBECs into the SynVivo microfluidic system to create a BBBoaC model. The results shown in this Chapter demonstrate that, in Transwell culture, the formation of tight junctions by PBECs was increased by the addition of astrocyte signalling (CTX-TNA2 cell line). Furthermore, the tight junctions formed by the primary PBECs superseded the junctional adhesion of the human immortalised cell line HBEC-5i. In addition to Transwell culture, this Chapter presented a novel methodology to culture primary PBECs within the SynVivo microfluidic chip system, while identifying clear differences in culture requirements between immortalised and primary BECs.

In order to establish a static model of the BBB, PBECs were cultured upon 24-well semi-permeable Transwell membrane inserts. The Transwell PBEC model was supported by the addition of a supplemented media. Transwell studies in PBEC cultures undertaken by Cantrill et al., 2012 demonstrated that without the addition of these signalling factors, PBECs were unable to reach optimal TEER values. The supplemented media did not contain vascular endothelial growth factor A (VEGFA) but was supplemented with cyclic adenosine monophosphate (cAMP), hydrocortisone and RO 20-1724, a selective inhibitor of cAMP-specific phosphodiesterase. VEGFA was omitted as its signalling has been shown to promote vascular permeability and to decrease tight junctional adhesion (Wang et al., 2001). Whereas cAMP signalling has been shown to promote the function of tight junctions in the BBB and increase the expression of tight junction protein, claudin-5 (Ishizaki et al., 2003). Additionally, hydrocortisone can induce tighter junctional adhesion in BECs as well as inducing claudin-5 and occludin expression (Förster et al., 2008). Cell-cell signalling by hydrocortisone, and increased the cellular availability of cAMP, have been suggested as mechanism of actions for astrocyte-endothelial signalling (Abbott, 2002).

TEER analysis was used as a measure of barrier resistance in the PBEC Transwell model. As previously indicated, *in vivo* TEER values for the BBB are between 1000 and 6000 Ω.cm^2 in rats (Howarth et al., 1992). This Chapter has demonstrated that TEER values in PBECs increased by 30% from 207 Ω.cm^2 to 270 Ω.cm^2 with astrocyte co-culture. Additionally, ACM alone increased the average TEER value to 235 Ω.cm^2. Astrocyte treatment also prolonged the viability of the PBECs, maintaining TEER values to over 180 Ω.cm^2 on day 3 of culture in both ACM and no-contact co-culture groups. The resistance data achieved through TEER measurements is supported by the permeability data for the diffusion of 4 kDa FITC-conjugated dextran across the membrane under the same astrocyte treatments. The tight junctions present between the PBECs should restrict the paracellular transport of large molecules (>500 Da), thus restricting the permeability of the FITC-dextran to transport via the transcellular pathway. In line with TEER results, treatment of primary PBECs with no-contact astrocyte co-culture reduced the permeability of FITC-dextran across the PBEC monolayer in line with the generally accepted level (<3%) within drug discovery permeability assays, for cell lines such as Caco-2 (Yamashita et al., 2000).

In the present study, it was evident that astrocyte co-culture increased functional tight junction formation in the Transwell BBB model. Comparative studies in other laboratories using Transwell systems are in broad agreement with astrocyte contributions stimulating the BBB phenotype of BECs and overall increasing barrier tightness (Cantrill et al., 2012; Nielsen et al., 2017; Puech et al., 2018). Furthermore, the results agree with previous studies in which astrocytes from one species can induce barrier properties in BECs from another species. For example, a critical study from Janzer & Raff, 1987, demonstrated that rat astrocytes are capable of inducing barrier properties in chick BECs. Additionally, in PBEC Transwell studies undertaken by Thomsen et al., 2015, there was no difference in barrier tightness induction between co-culture with astrocytes from rat or pig origin. It is also recognised that there is no difference between the use of primary or immortalised astrocytes in the induction of barrier pathways (Cantrill et al., 2012). Thus, results shown in this Chapter reinforce the concept that immortalised rat astrocytes can induce barrier properties in

PBECs. Although the mechanism of action of astrocyte signalling upon BECs has yet to be fully elucidated, evidence suggests that the Wnt signalling pathway and upregulation of alkaline phosphatase play major roles in induction of barrier tightness (Liebner & Plate, 2010; Meyer & Galla, 1991). This therefore suggests high levels of conservation of these BEC-astrocyte signalling pathways between species.

The co-culture of astrocytes in the PBEC Transwell model presented in this Chapter extended the viable period of the PBECs, however, the number of viable days taken to reach maximum TEER were significantly less than reported in similar studies. For example, many studies report maximum TEER after 6 days in Transwell culture (Cantrill et al., 2012; Gericke et al., 2020; Zhang et al., 2006), whereas some report culturing PBECs on Transwell for up to 2 weeks before TEER assays began (Thomsen et al., 2015). It was determined, in this study, that PBECs would reach maximum TEER and lowest permeability 48 hours after passage to Transwell and would be viable with astrocyte co-culture for a 2–3-day period. This discrepancy could be due to a difference in the cell growth area on the Transwell plate. In all of studies with a longer growth period, Transwell inserts with a growth area of 1.12 cm^2 were used, whereas in the present study, PBECs were seeded on Transwell inserts with a smaller area of 0.33 cm^2. Although TEER values are normalised to surface area, it is possible that with a reduced growth area, PBECs could become overconfluent, and multi-layering of cells could result in pre-mature cell death or detachment. Further investigation would need to be undertaken using confocal microscopy to determine the effect of Transwell insert sizing upon cell growth and density. However, the smaller growth area used in this study allows for a high-throughput assay format, which is critical within drug discovery permeability studies, so the benefits and disadvantages of the Transwell system used must be evaluated for the study purpose.

The technical skill, cost, and low throughput nature of primary BECs could make them less favourable candidates for BBB modelling than their immortalised counterparts (He et al. 2014). Immortalised BECs have the benefit of being stable for a number of passages, producing highly replicable results and

requiring less characterisation than freshly isolated cells (Helms et al., 2015). In spite of these benefits, many studies have consistently demonstrated lower levels of junctional adhesion in immortalised BECs. In a systematic review of immortalised BECs for BBB modelling, Rahman et al., 2016, examined the TEER values produced by different immortalised BEC lines (not including HBEC-5i cells). A range of 17 TEER values were obtained for human immortalised BECs, of which 13 are less than 100 $\Omega.cm^2$ and the median TEER value was 40 $\Omega.cm^2$. However, different culture methods and TEER measurement equipment leads to a large variability in the assessment of immortalised BECs and there is a lack of studies which directly compare these two cell types under the same culture conditions.

Within this study, TEER analysis revealed that in monoculture, the resistance across the HBEC-5i cells was 25-fold less than PBECs. Furthermore, unlike PBECs, TEER in the HBEC-5i cells did not respond to astrocyte treatment in co-culture or ACM treatment. These results were further supported by FITC-dextran permeability data, in which more 4 kDa molecules passed across the HBEC-5i cell monolayer than across the PBEC monolayer. This is further indication that the junctions between HBEC-5i cells could be considered “leaky”, with a phenotype which has more similarity to peripheral endothelial cells than BECs. This is in contrast to results from Puech et al., 2018, where a HBEC-5i Transwell model showed TEER values of the HBEC-5i cells alone to be 35.8 $\Omega.cm^2$, which is 5-fold higher than those from the present study. Furthermore, HBEC-5i TEER values were increased, and permeability values were decreased, with the addition of human ACM (Puech et al., 2018). Asides the species difference in ACM treatment, all other culture methodology was identical, including equipment used to measure TEER values, which demonstrates a level of variability present in analysis of BBB models between laboratories. In spite of these discrepancies, it is evident from these results and those presented by Puech et al., 2018, that the primary PBECs form tighter junctions than HBEC-5i cells and would therefore be a better candidate for BBB modelling for drug permeability testing.

Advancements in microfluidic technology have led to significant developments in the field of Organ-on-a-Chip modelling, with a range of BBB-on-a-Chip models being published within the past decade (Wilhelm & Krizbai, 2014). This includes BBBoaC models with a vast array of applications from examination of cell extravasation to drug permeability studies (Jiang et al., 2019; Oddo et al., 2019). However, the majority of BBBoaC models developed use immortalised cell lines, which are often not representative of the BBB. Currently, no BBBoaC model has been published using PBECs, in spite of many studies demonstrating their viability in static models (Nielsen et al., 2017; Patabendige et al., 2013; Thomsen et al, 2015). As previously discussed, the SynVivo microfluidic system was selected due to the characterisation of the system in other BBBoaC publications and advantages of the design for drug transport studies, including real-time cell imaging, separate inlet and outlet ports, and a separate chamber for co-culture (Deosarkar et al. 2015; Prabhakarpandian et al., 2013). The SynVivo BBBoaC system is inclusive of a generic endothelial cell seeding protocol, and this, alongside methodology from previous SynVivo publications was used to develop a seeding protocol for the primary PBECs. A seeding protocol was also developed for the immortalised HBEC-5i cell line for comparison.

A major impediment in the development of the seeding protocol for PBECs was the slower replication time by comparison to HBEC-5i cells, which resulted in the PBECs not reaching confluency before shear stress was applied. It was determined that an extension in growth period resulted in more cell division, and as cells reached a high population density, cells were consequently able to withstand shear stress for 48 hours with little death or detachment. It is, therefore, evident that the nature of the primary cells results in a need for further optimisation by comparison to immortalised BECs. However, despite the increased technical requirements for seeding, once established, the primary cells can withstand higher levels of shear stress. Thus, suggesting that a more robust and stable barrier has been formed. This phenomenon was also shown in the two initial SynVivo papers (Deosarkar et al., 2015; Prabhakarpandian et al., 2013). The BBBoaC model established by Prabhakarpandian et al. used

immortalised rat BECs (RBE4) whereas that published by Deosarkar et al. used primary rat BECs (RBECs). Comparing these publications, the model using RBE4 cells required a lower seeding density and a shorter time before shear stress is introduced than the RBECs. However, RBE4 cells were capable of withstanding 10-fold higher shear stress than their primary counterparts. This is, though, in disagreement with the findings in this Chapter, which suggest that both HBEC-5i cells and primary PBECs require between 24-96 hours to grow to confluence before the cells could withstand shear stress.

Two further BBBoaC models using the SynVivo system have been published. Firstly, Terrell-Hall et al., 2015, published a neonatal BBBoaC model using HUVECs, which used a seeding density similar to that used by Deosarkar at al., 2013. However, a growth period of 24 hours was required for cell growth before shear stress was applied. Secondly, Brown et al., 2019, published the μHub BBBoaC model using the SynVivo device with the human immortalised BEC line, hCMEC/d3. Brown et al. determined that hCMEC/d3 cells required two seedings at high density and a longer incubation period for growth. This suggests that the hCMEC/D3 cell line required a similar seeding protocol to that established to be required by PBECs than HBEC-5i cells in this Chapter. Moreover, Brown et al., 2019, suggested that the hCMEC/D3 cell line is unable to proliferate under shear stress, and this resulted in detachment after premature exposure. This is also in line with the findings for PBECs, which exhibited the same phenomenon of being unable to withstand shear stress until fully confluent. This has also been reported in microfluidic studies in other peripheral cell types, where the application of shear stress on endothelial cells was shown to down-regulate ERK1/2 and P38 MAPK pathways, and consequently reduce the rate of endothelial cell proliferation (Ji et al., 2019). Therefore, although there is abundant evidence for shear stress upregulating beneficial BBB proteins, such as transporters and tight junctions, it is evident that application of shear stress can also be detrimental to endothelial cell growth. Thus, protocol optimisation for each cell type cannot be omitted during methodological development.

Alongside cell-type specific optimisation of the SynVivo BEC seeding protocol, overall changes to improve the system were made. Firstly, the pneumatic priming system suggested by SynVivo was insufficient for removing air bubbles from the PDMS in their entirety. Using gas to remove trapped air in the PDMS presented issues, as the inert gas itself would leech into the channel. Other microfluidic protocols suggest removing air bubbles from PDMS by pressuring the closed chip system or by using a bubble trap (Wang et al., 2012). It was found that air bubbles could be removed from the PDMS efficiently by pressuring the closed chip system with coating solution at 5 µl/min. Air bubbles could also result in disruption and detachment when infused into the chip via the culture media while inducing shear stress.

As the Harvard syringe pump cannot be housed within a humidified cell incubator, previous SynVivo publications have pre-warmed the cell media by flowing through a 75 cm length of tubing which is housed in the 37°C incubator between the syringe pump and the chip. However, it was found that warming the media quickly using this method resulted in the formation of air bubbles within the liquid which would then be infused into the chip. In the absence of a media bubble trap within the system, an alternative method was developed, where media was housed in a reservoir inside the incubator and withdrawn through the chip in reverse into a syringe depository in the Harvard pump. This reduced the incidence of bubbles and consequently reduced cell death and detachment.

Although the use of PDMS in the microfluidic chip allows for real-time imaging with light microscopy, the fusiform endothelial morphology of the PBECs presents with extremely flat and thin outer edges (as shown by SEM imaging), consequently cell cultures cannot be accurately observed through light microscopy. Therefore, the PBECs within the microfluidic chip need further characterisation using staining techniques such as immunofluorescence for tight junction proteins. However, the optimisation of immunofluorescent staining techniques within the microfluidic chip caused further issues which were not able to be resolved due to the impact of pandemic-related time constraints on the project.

In addition to Transwell studies, the permeability of the microfluidic cultures of primary PBECs was measured using 4 kDa FITC-dextran. Unsurprisingly, the compound immediately leaked into the central compartment in the empty chip, which was filled with fluorescent compound within 30 minutes. However, with a culture of PBECs present, the flow of FITC-dextran into the central compartment was significantly reduced. This agrees with Deosarkar et al., 2015, in which RBEC cells restricted the flow of 40 kDa conjugated Texas Red from the outer channel into the central compartment after 120 minutes. The difference in permeability rates is likely due to the 10-fold increase in compound size between these two experiments. In spite of the lower molecular weight of the FITC (4 kDa) by comparison to the Texas Red (40 kDa), the amount of permeated compound appears to be slightly less in the PBECs compared to the RBECs. However, Deosarkar et al., 2015, demonstrate that barrier permeability can also be reduced by co-culture with astrocytes or ACM. Considering the effect of astrocyte co-culture upon tight junction formation in the PBECs, as shown in Transwell studies, it would be logical to assume that co-culture would also improve the restrictive nature of the PBECs in the SynVivo culture. This will be a key point for further investigation into the viability of this PBEC BBBoaC model.

In order to further investigate the ability of the SynVivo microfluidic cell cultures to form a functional barrier, TEER measurements were obtained using the SynVivo impedance analyser system. The values measured in the SynVivo microfluidic chip cultures for both HBEC-5i cells and PBECs show no difference between either cell type as well as between the cells and no cell control. This data does not replicate that presented using the same system and the same equipment (Deosarkar et al. 2015). In the supplementary data of this publication, Deosarkar et al., 2015, presented a baseline value of 101 kΩ using the same chip model and coating proteins. In spite of the differences in baseline measurements, the impedance values for HBEC-5i and PBEC microfluidic cultures could be considered of the same order as the impedance data presented in Deosarkar et al., 2015. To further investigate the values generated by the impedance analyser in the microfluidic chip, the system was used to investigate impedance values in Transwell, enabling comparison with readings

from the EVOM2 TEER meter. The impedance measurements taken in Transwell showed similar results to those observed in the microfluidic chip, with the same blank measurement and similar impedance values for both cell types. However, when investigated using the EVOM2 TEER meter, a different blank reading and non-proportional resistance values were measured. Furthermore, the readings taken using the SynVivo impedance analyser were 1000-fold higher than those measured using the EVOM2 TEER meter. The extreme differences in measurement between the two pieces of equipment, the high blank impedance value, and the magnitude of the reading calls in to question the validity of this measurement. Thus, no firm conclusions can be drawn from the impedance data measured in the SynVivo microfluidic system. It should be noted that, Deosarkar et al., 2015, state that as the methodology and instrumentation of the SynVivo impedance analyser is different to that of the Transwell resistance TEER meter, and consequently, the values cannot be compared. Furthermore, as impedance values by Deosarkar et al., 2015, are not presented as a proportion of surface area, they cannot be considered to be TEER values. This phenomenon raises questions about the methods used to evaluate and compare BBB systems, and calls into question whether the inability to measure barrier resistance in a non-disruptive assay could be considered an inconvenience, or indeed, a major limitation that could prevent the widespread use of BBBoaC models (Kaisar et al., 2017).

To conclude, the overarching aims of this Chapter were achieved, as in a static Transwell model, PBECs were responsive to the addition of astrocytes in co-culture. Additionally, this Chapter has demonstrated that immortalised BEC lines, HBEC-5i, has major limitations for BBB modelling. However, the HBEC-5i immortalised cell line required significantly simpler methodology and fewer optimisations to culture in the SynVivo chip than the primary PBECs. The methodology for culturing primary PBECs within the SynVivo microfluidic chip required numerous optimisations to cell seeding density and growth times to ensure adequate cell growth. Furthermore, PBECs were still not present in as high numbers as HBEC-5i cells even after these significant protocol changes. However, the primary PBECs formed a restrictive barrier to FITC-conjugated

dextran within the SynVivo chip. In spite of efforts to further characterise the permeability of the monolayer using TEER measurements, limitations with the equipment and inconclusive measurements rendered the data generated to be invalid for analysis. Although this is the first time that a primary PBEC BBBoaC model has been developed, much characterisation is still required to validate this model, which has been limited due to Covid-19 circumstances surrounding this study. These studies would include immunoflourescent staining studies to determine true cell confluence in the microfluidic chip, the examination of the effect of shear stress and astrocyte culture upon the translocation and function of key BBB proteins, and the evaluation of the microfluidic model for use in drug discovery using drug permeability and transport assays.

Chapter 5

Assessing drug transport in the Transwell PBEC model

5.1 Background

A major issue in the development of novel centrally acting drugs is the absence of a reliable and well-characterised model of blood-brain barrier (BBB) permeability (Bicker et al., 2014). Although the porcine brain endothelial cell (PBEC) blood-brain barrier on-a-chip (BBBoaC) model established in Chapter 4 showed promise as a novel BBB model in early studies, the time restraints placed on this study due to the Covid-19 pandemic meant that drug transport studies had to be undertaken in the earlier established PBEC Transwell model. Furthermore, astrocyte co-cultures were omitted from the PBEC Transwell model used in these drug transport studies due to the limited time available, consequently, astrocyte conditioned media (ACM) was used as a replacement. Therefore, this Chapter will examine the transport of a selection of test drugs across a Transwell model of the BBB created from PBECs cultured with ACM and supplemented media in a 24-well insert layout.

Multiple methods have been established to assess the permeability of a novel compound and its interactions with drug transporters at the BBB using *in vitro* studies. Apparent permeability (P_{app}) is a longstanding quantifier of the rate of permeability of a compound across an *in vitro* model of the BBB. P_{app} is calculated using Equation 1.3, which remains accurate while drug transport between *in vitro* compartments is in the linear phase and where less than 10% of the drug has passed between the compartments, and also where there is inappreciable backflow and a good mass balance (Tran et al., 2004). An alternative to P_{app}, defined as P_{exact} (Equation 1.4 & 1.5), has consequently been derived to provide a mathematical solution for the entirety of the drug transport curve, and is thus applicable when there is more than 10% of drug permeated and when mass balance issues occur (Tran et al., 2004). In this Chapter, both P_{app} and P_{exact} were calculated for a range of test drugs to examine the rate of permeability of the drugs across the monolayer of PBECs to give an indication of drug permeability and any multidrug efflux transporter interactions taking place.

Alongside examining the effect of multidrug efflux transporter interactions upon the rate of test drug permeability, it was also necessary to validate the Transwell PBEC model through comparison to *in vivo* data available in published literature. In order to select the appropriate test drugs, a database of drug characteristics and quantifiers of drug permeability was created for over 160 compounds. From these compounds, 10 test drugs were selected for transport studies in the porcine Transwell model; these selections were based on molecular weight, lipophilicity, known drug-transporter interactions, and availability of *in vivo* brain penetration data. The most widely available *in vivo* data parameters for BBB permeability are K_p, which represents the blood to brain concentration ratio, and $K_{p,uu}$, which represents the unbound blood to unbound brain concentration ratio. $K_{p,uu}$ is widely regarded as a more useful measure than K_p, as in the free drug hypothesis, only drug which is unbound is available to cross the BBB (Chen et al., 2020). Consequently, $K_{p,uu}$ values were predicted for all of the test drugs selected using permeability coefficient values measured during drug transport studies in the PBEC Transwell model, and rapid equilibrium dialysis in porcine plasma and brain to measure drug-tissue binding. The predicted *in vitro* values for $K_{p,uu}$ for the test drugs in the PBEC Transwell model were thus compared to published *in vivo* $K_{p,uu}$ values from the established database.

Therefore, results presented in this Chapter evaluate the rate of permeability of selected test drugs across the Transwell PBEC model as an indication of drug transporter interaction. Furthermore, the blood-brain concentration ratio (both bound and unbound) was calculated for the selected test drugs and compared to *in vivo* data to evaluate the accuracy of the PBEC model.

5.2 Results

5.2.1 Creation of a drug database for BBB permeability

In order to select the most appropriate drugs for use in transport studies, a database of permeability parameters for centrally and non-centrally acting drugs was created using Microsoft Excel. Values in the database were obtained from published sources following a literature search. The data obtained for each drug was as follows: LogP and molecular weight, compound target, known BBB

transporter interactions, permeability characteristics including fraction unbound (F_u), volume unbound (V_u), K_p and $K_{p,uu}$. The drug target, LogP, and molecular weight information were obtained from existing online databases listed in Methods Section 2.8.1. Quantified permeability values listed in the database were obtained from individual published sources as described in the database. Drug values for K_p and $K_{p,uu}$ were listed alongside species and methodology used to obtain the data, thus allowing for examination of experimental differences. Test drugs were selected based upon the number of values for *in vivo* permeability data (particularly $K_{p,uu}$) present in the database, to cover different known transporter interactions, and to cover a range of LogP values and molecular weights. The full database is recorded in Appendix 2.

Table 5.1 – Selected test drugs

Drug	Target	LogP	MW	Transporter	Kp,uu	Species
Amprenavir	Non-CNS	2.9	505.6	MDR1 substrate	0.076 0.087	Rat Mouse
Carbamazepine	CNS	2.5	236.7	None listed	1.05 0.094 0.771 1.02 0.27	Rat Rat Rat Rat Mouse
Chlorpromazine hydrochloride	CNS	5.4	355.3	MDR1 inhibitor	2.77 0.49	Rat Mouse
Donepezil hydrochloride	CNS	4.2	416.0	MDR1 inhibitor	2.7	Rat
Haloperidol	CNS	3.2	375.9	MDR1 inhibitor	1.1	Mouse
Levodopa	CNS	-2.7	197.2	LAT1 uptake	None	None
Loperamide hydrochloride	Non-CNS	4.7	513.5	MDR1 substrate	0.009 0.007 0.110 0.019	Rat Rat Mouse Mouse
Primidone	CNS	0.9	218.3	None listed	0.420	Rat
Thiopental	CNS	2.9	242.3	None listed	1.530 0.100 0.911 0.170 0.090	Rat Rat Rat Rat Rat
Topiramate	CNS	-0.8	339.4	MDR1 substrate	0.330	Rat

Table 5.1 – *Example drug parameters and permeability values for the selected 10 test drugs from the database created. Full database available in Appendix 2.*

As previously stated, the 10 test drugs were chosen based upon a defined selection criteria. Firstly, all drugs selected have a logP value of less than 5.5, to ensure that the effect of non-specific binding by highly lipophilic drugs is limited. The drugs chosen, unless under exceptional circumstances, have at least one literature value for $K_{p,uu}$ in rodent studies for comparison. Furthermore, amprenavir, topiramate, and loperamide are all substrates for MDR1/P-gp, which should mean that drugs are actively effluxed from the brain to the blood compartment. This can be observed in the $K_{p,uu}$ values for these drugs recorded in the database. In contrast, chlorpromazine, donepezil, and haloperidol, are inhibitors of MDR1/P-gp, which suggests that $K_{p,uu}$ values should be equal to or more than one, unless unknown transporter interactions have an effect on permeability. This is supported by the majority of recorded $K_{p,uu}$ values for these drugs in the database. Alongside examining MDR1/P-gp efflux and inhibition, levodopa is a substrate for LAT1 uptake transporter. Consequently, it would be anticipated that levodopa would have a $K_{p,uu}$ value of more than 1, although this is the only drug selected that does not have *in vivo* $K_{p,uu}$ data available. Primidone and carbamazepine have no listed transporter interactions, and thus were included as passive diffusion controls. Although thiopental also has no known transporter interactions, it has been recorded that some volatile anaesthetics can act to disrupt the BBB *in vivo*, consequently increasing brain penetration of the anaesthetic compound and co-administered drugs.

5.2.2 Transport studies

Transport studies were conducted in *in vitro* Transwell cultures of PBECs cultured with ACM using the range of 10 drugs selected from the database. Permeability of compounds was measured in triplicate for each drug, and from apical-to-basal (A-B) and from basal-to-apical (B-A) directions. Transwell PBEC cultures were incubated with drug for 120 minutes, with samples taken at 30-minute, 60-minute, and 120-minute time points. Permeability parameters were calculated using Equations 1.3-1.5 & 2.7-2.10. Due to poor mass spectrometry sensitivity samples for levodopa could not be accurately analysed, and consequently, levodopa results have been omitted from this Chapter. Drug

sample chromatograms are included in Appendix 4, and standard curves used to calculate drug concentrations are available in Appendix 3.

5.2.2.1 Apparent and exact permeability of test drugs across PBEC Transwell model

As previously stated, apparent permeability (P_{app}) and exact permeability (P_{exact}) values represent the rate of drug transport across a cell monolayer. P_{app} and P_{exact} values were calculated for each of the 9 successful test drugs at 30-minute, 60-minute and 120-minute time points, in both A-B and B-A directions.

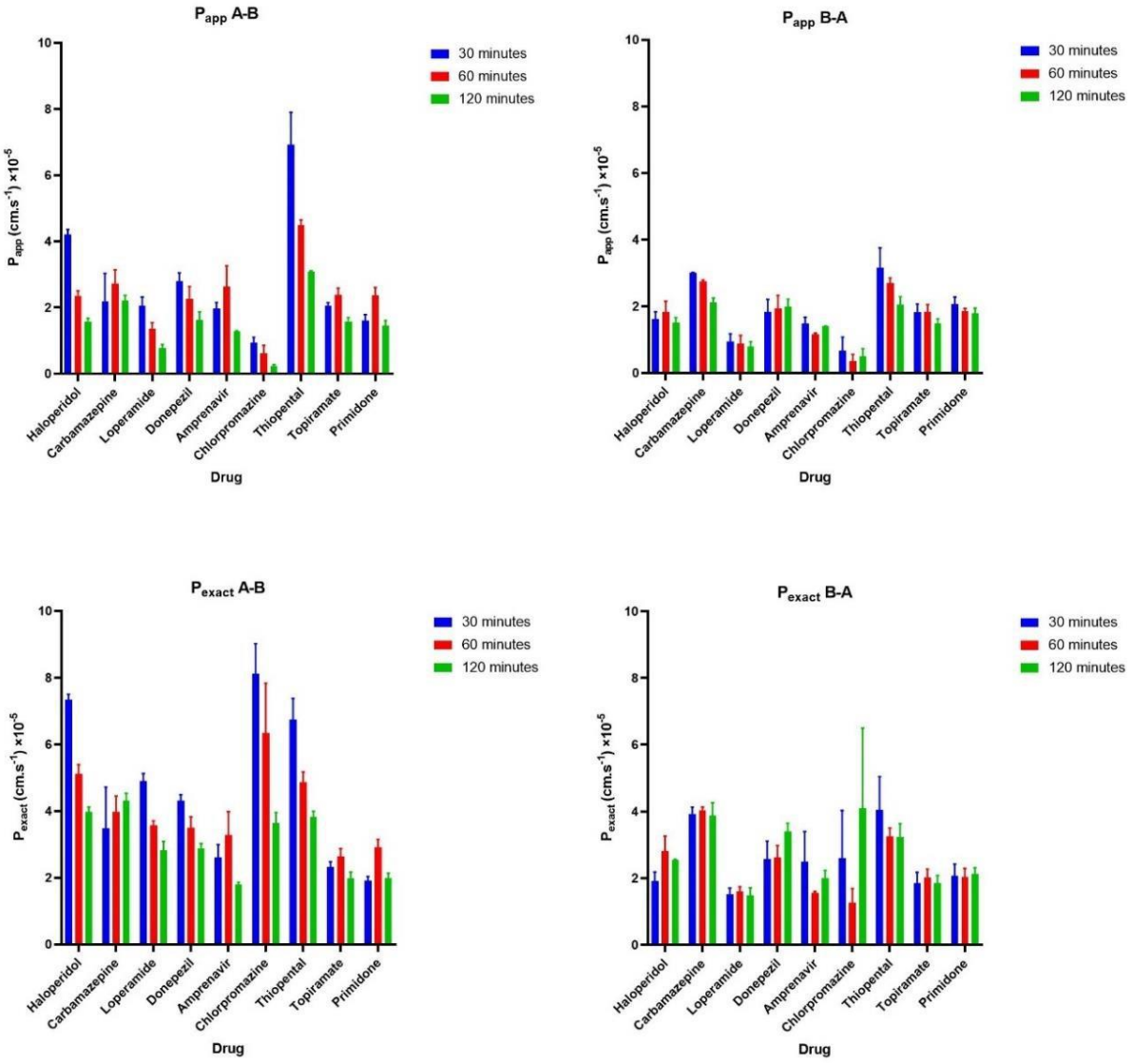

Figure 5.1 – *P_{app} and P_{exact} values for test drugs across a PBEC Transwell monolayer at 3 time points, in apical-to-basal (A-B) and basal-to-apical (A-B) directions. Each bar represents mean ± SEM where n=3. Further P_{app} and P_{exact} calculations can be found in detail in Appendix 5.*

Table 5.2 - P_{app} and P_{exact} values

	30 minutes			
	P_{app}		**P_{exact}**	
	A-B	*B-A*	*A-B*	*B-A*
Haloperidol	4.21 ± 0.24	1.63 ± 0.36	7.33 ± 0.29	1.92 ± 0.46
Carbamazepine	2.18 ± 1.47	3.01 ± 0.01	3.48 ± 2.14	3.92 ± 0.36
Loperamide	2.07 ± 0.43	0.94 ± 0.40	4.89 ± 0.41	1.52 ± 0.32
Donepezil	2.81 ± 0.42	1.84 ± 0.64	4.31 ± 0.32	2.58 ± 0.93
Amprenavir	1.97 ± 0.32	1.48 ± 0.33	2.60 ± 0.68	2.50 ± 1.56
Chlorpromazine	0.95 ± 0.27	0.66 ± 0.72	8.12 ± 1.56	2.60 ± 2.48
Thiopental	6.92 ± 1.71	3.16 ± 1.02	6.74 ± 1.09	4.05 ± 1.73
Topiramate	2.07 ± 0.14	1.81 ± 0.44	2.33 ± 0.26	1.85 ± 0.57
Primidone	1.61 ± 0.31	2.06 ± 0.37	1.92 ± 0.20	2.07 ± 0.62
	60 minutes			
	P_{app}		**P_{exact}**	
	A-B	*B-A*	*A-B*	*B-A*
Haloperidol	2.36 ± 0.25	1.83 ± 0.56	5.12 ± 0.47	2.83 ± 0.76
Carbamazepine	2.72 ± 0.73	2.75 ± 0.07	3.98 ± 0.81	4.03 ± 0.20
Loperamide	1.37 ± 0.31	0.89 ± 0.42	3.57 ± 0.25	1.61 ± 0.23
Donepezil	2.27 ± 0.64	1.93 ± 0.69	3.50 ± 0.57	2.61 ± 0.64
Amprenavir	2.63 ± 1.10	1.16 ± 0.06	3.28 ± 1.21	1.56 ± 0.07
Chlorpromazine	0.63 ± 0.41	0.36 ± 0.33	6.34 ± 2.60	1.27 ± 0.73
Thiopental	4.50 ± 0.27	2.69 ± 0.27	4.87 ± 0.52	3.26 ± 0.44
Topiramate	2.38 ± 0.36	1.83 ± 0.38	2.64 ± 0.40	2.02 ± 0.44
Primidone	2.37 ± 0.42	1.84 ± 0.17	2.91 ± 0.42	2.04 ± 0.44
	120 minutes			
	P_{app}		**P_{exact}**	
	A-B	*B-A*	*A-B*	*B-A*
Haloperidol	1.59 ± 0.16	1.51 ± 0.26	3.97 ± 0.27	2.54 ± 0.04
Carbamazepine	2.21± 0.27	2.11 ± 0.23	4.31 ± 0.39	3.89 ± 0.65
Loperamide	0.78 ± 0.18	0.79 ± 0.26	2.83 ± 0.46	1.48 ± 0.41
Donepezil	1.62 ± 0.43	1.99 ± 0.39	2.88 ± 0.25	3.40 ± 0.43
Amprenavir	1.29 ± 0.02	1.40 ± 0.02	1.79 ± 0.12	2.00 ± 0.39
Chlorpromazine	0.24 ± 0.06	0.51 ± 0.38	3.64 ± 0.55	4.10 ± 4.16
Thiopental	3.09 ± 0.04	2.05 ± 0.42	3.82 ± 0.30	3.24 ± 0.69
Topiramate	1.59 ± 0.20	1.48 ± 0.26	1.98 ± 0.33	1.86 ± 0.39
Primidone	1.46 ± 0.26	1.79 ± 0.28	2.00 ± 0.24	2.14 ± 0.31

Table 5.2 – *P_{app} and P_{exact} values from PBEC drug transport studies in A-B and B-A directions across 30-, 60-, and 120-minute time points (units for all datapoints are $cm.s^{-1}$ and values are reported as $\times 10^{-5}$). Data shown are mean ± SEM for n=3 replicates for each compound and timepoint. Further P_{app} and P_{exact} calculations and concentrations can be found in detail in Appendix 5.*

The two parameters, P_{app} and P_{exact}, generate values which are significantly different from each other in both directions and across time points (one-way ANOVA, $P < 0.05$) (Fig. 5.1). This includes for the drug chlorpromazine, where the rate of permeability across the PBECs is up to 8-fold higher in P_{exact} calculations compared to P_{app} calculations in both directions. Furthermore, P_{app} and P_{exact} values for drugs including haloperidol, loperamide, donepezil, amprenavir, and thiopental, are higher in the A-B than the B-A directions at multiple time points. This difference in transport rates between directions is also significant ($P<0.01$, one-way ANOVA). Alongside variability between transport parameters and directions, differences in the rate of drug transport can also be observed between time points for most compounds, with the rate of permeability increasing between 30- and 120-minutes for multiple compounds.

5.2.2.2 Efflux ratios of test drugs across PBEC monolayer

Efflux ratios, calculated from P_{app} and P_{exact} values, describe the ratio of the rates of permeability in between transport directions for each drug (B-A/A-B). Assuming that, in the Transwell model, the PBECs orientate such that the basal cell membrane is adherent to the basement membrane proteins, as *in vivo*, the apical compartment will represent the plasma compartment and the basal compartment will represent the brain compartment. Consequently, it would be expected that a drug which is a substrate for efflux transporters expressed on the apical membrane will have a reduced A-B transport by comparison to B-A. In this light, any compound with an efflux ratio of greater than 2 could be considered a substrate for multidrug efflux transport.

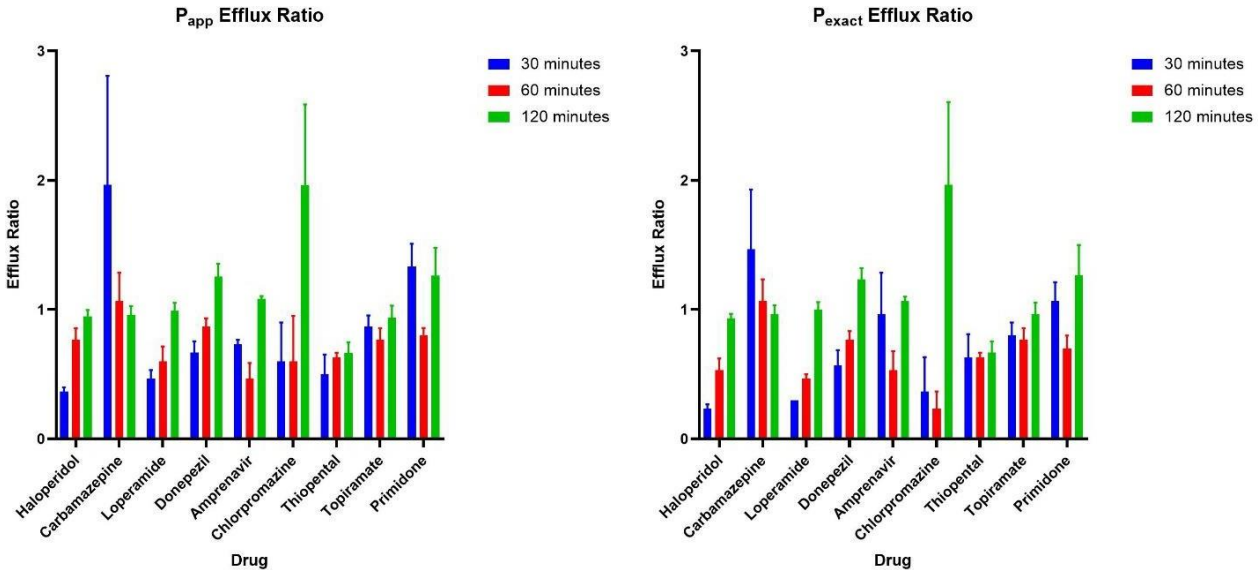

Figure 5.2 – *Efflux ratios (ER) from P_{app} and P_{exact} values for test drugs across a PBEC Transwell monolayer at 30-, 60-, and 120-minute time points. ER data values are available in Appendix 5. Each bar represents mean ± SEM where n=3.*

Firstly, no compound measured had a mean ER value higher than 2 using either P_{app} or P_{exact}, suggesting that compounds have not undergone significant efflux from multidrug efflux transporters (Fig. 5.2). Values for carbamazepine at 30-minutes and chlorpromazine at 120-minutes, with mean values of 1.99 and 1.96, respectively, could be considered inconclusive due to the large standard error of means and low ER values across other time points. Efflux ratios showed a significant difference with time across the compounds (P = 0.0005, two-way ANOVA). The efflux ratio of many drugs, such as haloperidol, loperamide, donepezil, and thiopental increased between the 30-minute and 120-minute time points. Indicating a reduced flow from A-B, or an increased flow from B-A, between time points.

5.2.2.3 Drug permeability of PBECs compared to no cell controls

Alongside the drug transport studies across the PBEC Transwell model, a no cell control experiment was carried out in empty Transwell inserts at the 120-minute time point in A-B and B-A directions. P_{exact} values for the 9 selected compounds in both conditions and directions in PBECs were compared to the no cell control at the same time point. It should be noted that Thiopental is

omitted in the A-B direction due to an error with sample analysis in the no cell control.

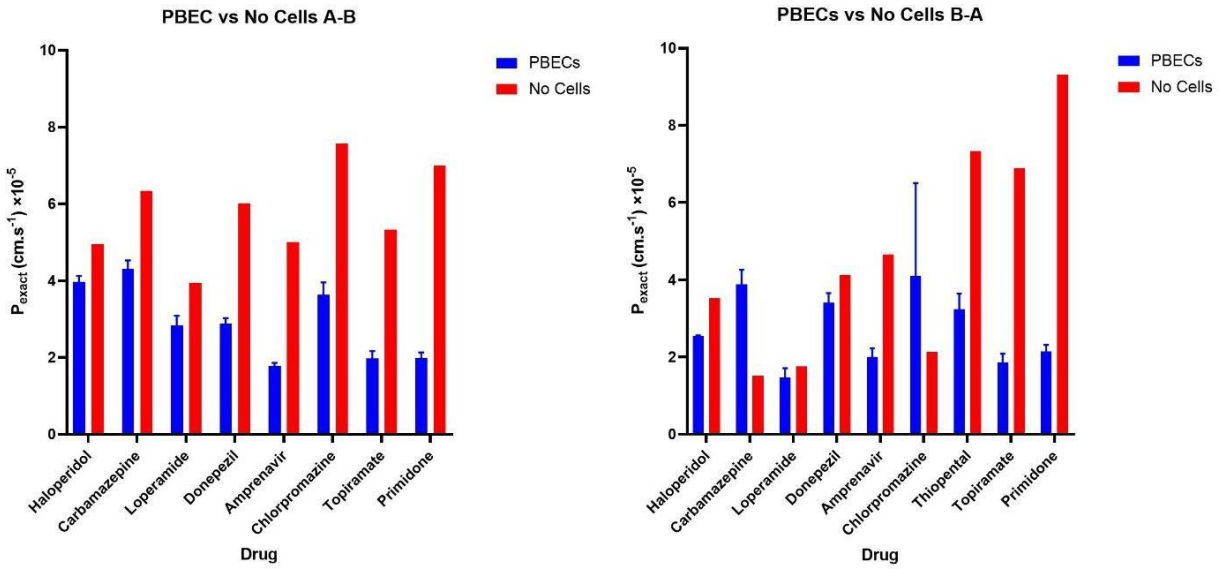

Figure 5.3 – *P_{exact} values for test drugs across PBEC Transwell models and Transwell inserts with no cells at the 120-minute time point. P_{exact} data values are available in Appendix 5. Each bar represents mean ± SEM where n=3 for PBECs and n=1 for no cell controls.*

PBECs restrict the flow of all drugs between compartments by comparison to the no cell control in the A-B direction, with maximum of 4-fold (primidone) (Fig. 5.3). However, in the B-A directions, this is to less of an extent than in the A-B directions for many drugs, and carbamazepine and chlorpromazine have a faster permeability across the PBEC monolayer than in the no cell control group. However, it is possible that the low recovery rates of these drugs, and the small sample number for the no cell control group, has resulted in an inflated response.

5.2.2.4 Comparison of measured PBEC efflux ratios to literature

In order to evaluate the ability of the PBECs to restrict drug transport across the monolayer, P_{app} values, P_{exact} values, and efflux ratios were compared to data from another PBEC Transwell model for a range of drugs which were included in both studies (Bentham, 2010).

Table 5.3 – A comparison of P_{app} and P_{exact} values

A-B	**P_{app}**				**P_{exact}**			
	Measured		**Literature**		**Measured**		**Literature**	
Haloperidol	2.4E-05	±2.5E-06	7.1E-06	±3.2E-06	5.1E-05	±4.7E-06	6.6E-06	±3.0E-06
Carbamazepine	2.7E-05	±7.3E-06	4.9E-06		4.0E-05	±8.1E-06	4.5E-06	
Donepezil	2.3E-05	±6.4E-06	4.1E-06		3.5E-05	±5.7E-06	3.9E-06	
Amprenavir	2.6E-05	±1.1E-05	3.5E-06	±1.7E-06	3.3E-05	±1.2E-05	3.4E-06	±1.6E-06
Chlorpromazine	6.3E-06	±4.1E-06	5.6E-06	±2.0E-06	6.3E-05	±2.6E-05	9.2E-06	±1.4E-06
B-A	**P_{app}**				**P_{exact}**			
	Measured		**Literature**		**Measured**		**Literature**	
Haloperidol	1.8E-05	±5.6E-06	1.1E-05	±3.1E-06	2.8E-05	±7.6E-06	6.8E-06	±1.4E-06
Carbamazepine	2.8E-05	±6.9E-07	2.0E-05		4.0E-05	±2.0E-06	1.6E-05	
Donepezil	1.9E-05	±6.9E-06	3.8E-05		2.6E-05	±6.4E-06	3.8E-05	
Amprenavir	1.2E-05	±6.0E-07	2.1E-05	±4.1E-06	1.6E-05	±6.9E-07	1.9E-05	±4.5E-06
Chlorpromazine	3.6E-06	±3.4E-06	1.8E-06	±6.5E-07	1.3E-05	±7.3E-06	1.7E-06	±6.1E-07

Table 5.3 – *A comparison of P_{app} and P_{exact} values in both B-A and A-B directions at 60 minutes across PBEC monolayers in Transwell. Measured values represent values from this experimental study, while literature values represent those by Bentham, 2010. Values shown are mean ± SD where n=3 for measured studies and n=2 for literature values.*

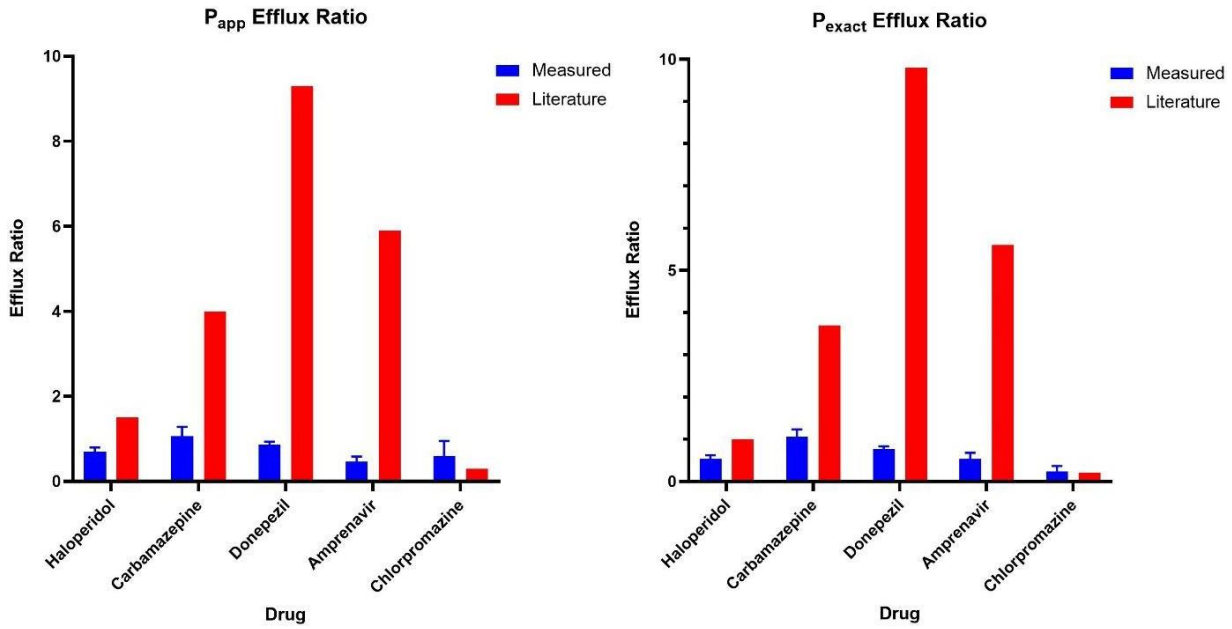

***Figure* 5.4** *- Efflux ratios (ER) from P_{app} and P_{exact} values for test drugs across PBEC Transwell monolayers measured in this study and from literature values (Bentham, 2010). Data are from the 60-minute time point to compare with published values. Raw data values are available in Appendix 5. Each bar represents mean ± SEM where n=3 for measured values.*

In spite of similarities in experimental design between the two studies, the permeability coefficients measured show distinct differences (Fig. 5.4). Across both P_{app} and P_{exact} parameters, chlorpromazine shows the least variation. In this light, donepezil demonstrates the largest variation between datasets, with a 10-fold difference between efflux ratios from both P_{app} and P_{exact}. Furthermore, within the dataset from Bentham, 2010, carbamazepine, donepezil, and amprenavir all show an efflux ratio of greater than 2, which is indicative of active efflux of the compounds. This is not reflected in the datasets from the current study, where the efflux ratio is less than 2 for all compounds. The P_{app} and P_{exact} values also vary between studies, as shown in Table 5.3, where the measured values determined in this Chapter appear to have a rate of permeability approximately 10-fold faster across all compounds in the A-B direction. Furthermore, the rate of permeability in the A-B direction shown in this PBEC Transwell model is faster than that shown in the Bentham PBEC Transwell model when a selective P-gp inhibitor is added (Bentham, 2010). Results from this study show also faster transport in the B-A direction (using P_{exact} data) than measured by Bentham, 2010, for haloperidol, carbamazepine, and chlorpromazine. This suggests that compounds are also passing the monolayer via paracellular transport in the B-A direction. However, values for P_{exact} in the B-A directions for donepezil and amprenavir show that the rate of drug flow is within 2-fold of those measured by Bentham, 2010. This discrepancy the A-B and B-A transport rates for amprenavir and donepezil could suggest a downregulation or lack of function in multidrug efflux transporters.

5.2.2.5 Fraction unbound in porcine plasma and brain from rapid equilibrium dialysis

Rapid equilibrium dialysis was used to measure the fraction unbound of drug in both porcine plasma and porcine brain for the selected test drugs. The measured values for fraction unbound in plasma and brain were compared to values from Bentham, 2010.

Table 5.4 – Fraction unbound in porcine plasma and brain

	Measured			Literature	
	$F_{,u\ Brain}$	**$F_{,u\ Plasma}$**	**K_b**	***$F_{,u\ Brain}$***	***$F_{,u\ Plasma}$***
Amprenavir	0.034	0.24	0.15	*0.17*	*0.19*
Carbamazepine	0.19	0.30	0.65	*0.18*	*0.21*
Chlorpromazine	0.0045	0.027	0.17	*0.0020*	*0.016*
Loperamide	0.0033	0.045	0.074		
Haloperidol	0.020	0.11	0.17	*0.036*	*0.069*
Donepezil	0.059	0.26	0.23	*0.12*	*0.28*
Topiramate	0.34	0.55	0.62		
Thiopental	0.12	0.44	0.26		
Primidone	0.56	0.61	0.92	*0.45*	*0.64*

Table 5.4 – *Fraction unbound values obtained from rapid equilibrium dialysis in porcine brain and plasma. Measured values represent values obtained experimentally from this study, whereas literature values were obtained from Bentham, 2010. Values are expressed as a mean where n=3 for both measured and literature values.*

Fraction unbound values for porcine plasma and brain were successfully obtained for the 9 selected test drugs using rapid equilibrium dialysis (Table 5.4). As shown, the fraction unbound values between the drugs in brain vary between 0.0033 and 0.56, while the fraction unbound in plasma varies between 0.027 and 0.61, with the fraction unbound in plasma being marginally larger across all compounds. K_b values were defined as the ratio of fraction unbound in brain to the fraction unbound in plasma. Compared to values for fraction unbound in porcine plasma and brain presented by Bentham, 2010, the measured values all fall within 2-fold other than amprenavir in brain, with a 6-fold difference.

5.2.2.6 Blood-to-brain concentration ratios of test drugs across PBEC monolayer

Using data obtained from drug transport studies (P_{exact}) and rapid equilibrium dialysis studies ($F_{u,\ brain}$ and $F_{u,\ blood}$), blood-to-brain concentration ratios were predicted for the selected test drugs. As the Transwell PBEC model used in the

transport studies does not contain protein for drug binding, Equations 2.7-2.10 were used to predict an unbound blood to unbound brain concentration ratio value ($K_{p,uu,predicted}$) for each compound. Fraction unbound ratios (K_b) were used as a representation of *in vivo* drug-protein binding, and consequently, can be used to make a prediction of the blood-to-brain concentration ratio ($K_{p,predicted}$) as detailed in Equation 2.10. As previously described, a K_p or $K_{p,uu}$ value of less than 1 is indicative of drug efflux, whereas a value of more than 1 is indicative of uptake. The $K_{p,predicted}$ and $K_{p,uu,predicted}$ values were determined using P_{exact} efflux ratios across the 30-, 60-, 120-minute time points for the 9 selected test drugs.

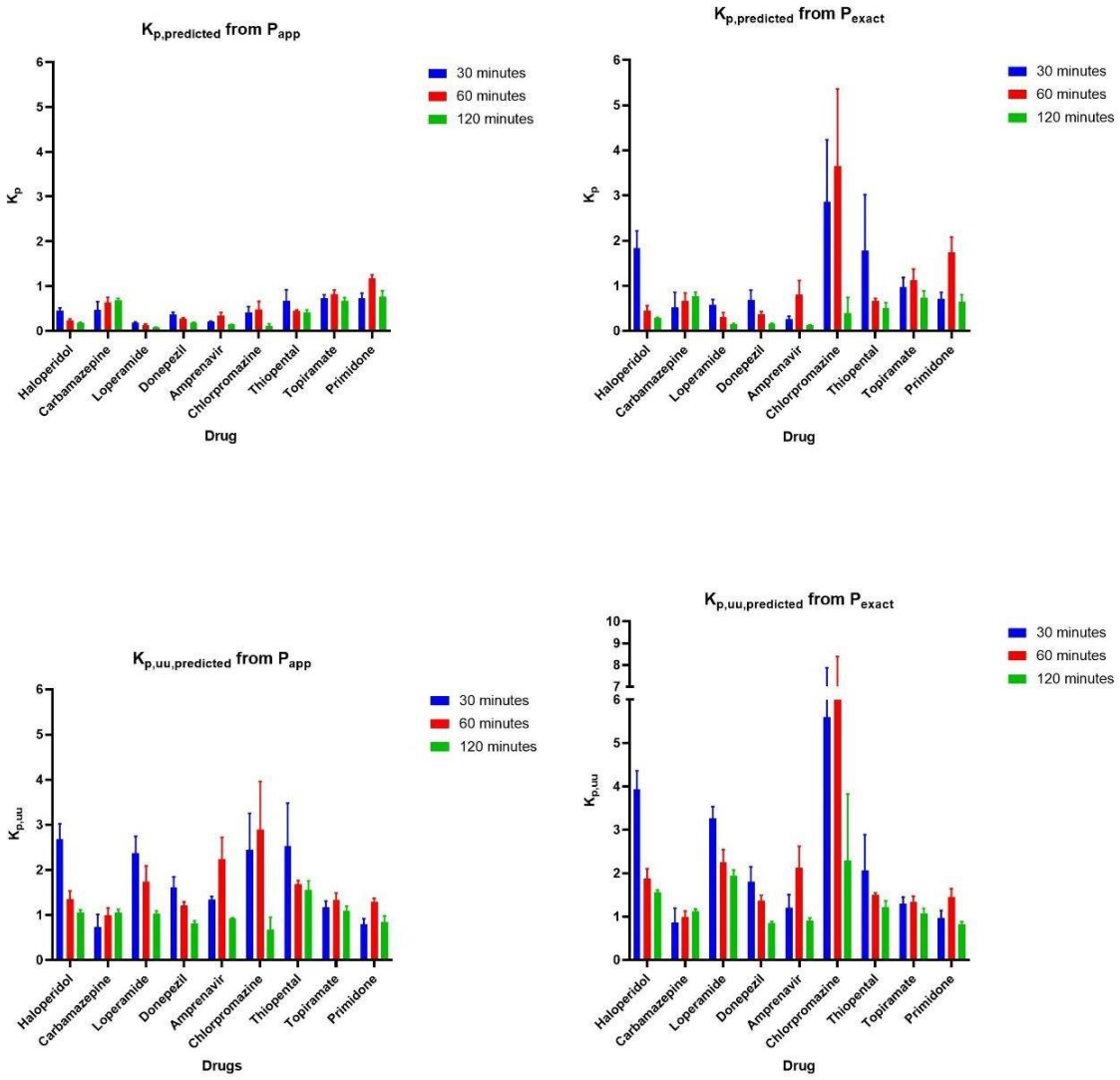

Figure 5.5 - *$K_{p,predicted}$ and $K_{p,uu,predicted}$ values calculated using P_{exact} efflux ratios across the 30-, 60-, 120-minute time points for the 9 selected test drugs. Bars show mean ± SEM where n=3 for each drug.*

It can be observed that different values are produced for $K_{p,predicted}$ and $K_{p,uu,predicted}$ using both P_{app} and P_{exact} (Fig. 5.5), these differences are significant, where P<0.0001 (analysed using two-way ANOVA). The differences observed between the two graphs demonstrate a substantial increase in K_p ratio when taking drug binding into account, where most values see at least a 2-fold increase in the ratio when only free drug is considered. There are also noticeable fluctuations in both values with time, however, this does not appear to follow a distinct trend across the compounds. For example, the $K_{p,predicted}$ value for carbamazepine is shown to increase across time points, whereas haloperidol, loperamide, donepezil and thiopental all decrease in K_p over the time period. Of all compounds tested, carbamazepine has the highest $K_{p,uu,predicted}$ and $K_{p,predicted}$ ratios by a significant margin, with means of 4.6 and 3.5 across all time points, respectively. However, the large error rate of this drug could have an effect upon the ratios calculated.

5.2.2.7 Comparison of measured PBEC $K_{p,uu}$ to database

In order to evaluate the unbound blood to unbound brain concentration values predicted from the experimental data, the $K_{p,uu,predicted}$ results were compared to *in vivo* $K_{p,uu}$ values from rodent studies which were recorded in the database used to select the test compounds (Appendix 2). The *in vivo* rodent data for $K_{p,uu}$ recorded within the database was averaged for each compound selected.

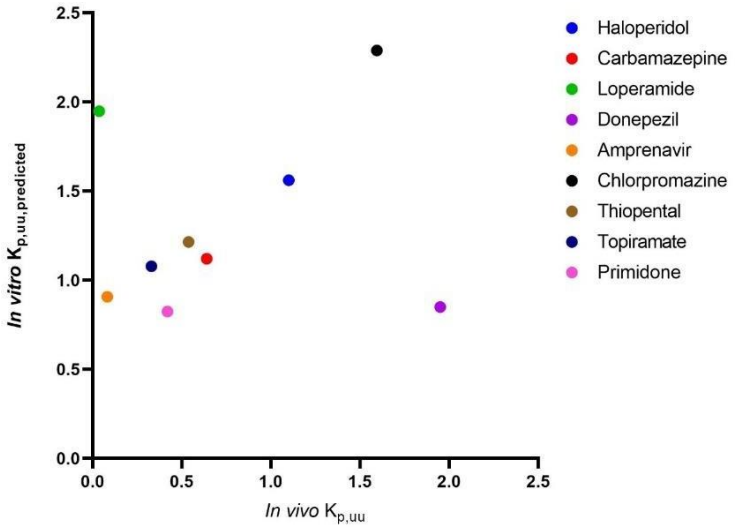

Figure 5.6 – *Predicted unbound blood to unbound brain concentration ratio ($K_{p,uu,predicted}$) (*in vitro*) compared to* in vivo *rodent $K_{p,uu}$ values (*in vivo*). Each data point represents mean where n=3 for in vitro, and n=1-5 for in vivo (data located in Table 5.1).*

The *in vitro* $K_{p,uu,predicted}$ values from this study are higher across the majority of compounds than the *in vivo* values obtained from the database (Fig. 5.6). In some cases, for example, carbamazepine, the *in vitro* value is less than 1-fold that of the *in vivo* value (1.1±0.1 to 0.6±0.4, mean ± SD, respectively). However, in the case of loperamide, the *in vitro* model has over predicted the $K_{p,uu}$ by over 50-fold (2.0±0.2 to 0.03±0.05, respectively). The only drug in which the *in vitro* $K_{p,uu}$ has underpredicted the database value is donepezil. However, there is a large range of *in vivo* $K_{p,uu}$ values in the database which may have resulted in an inaccurate mean *in vivo* value for this compound.

5.2.2.8 Correlation of apparent permeability with TEER values

TEER values of each *in vitro* PBEC Transwell model were taken before all drug transport studies to ensure the minimum value of 100 Ω.cm^2 was achieved. These values were recorded, and the value of individual wells taken in each experimental replicate were compared to the P_{exact} value achieved for the corresponding well to examine for a negative correlation.

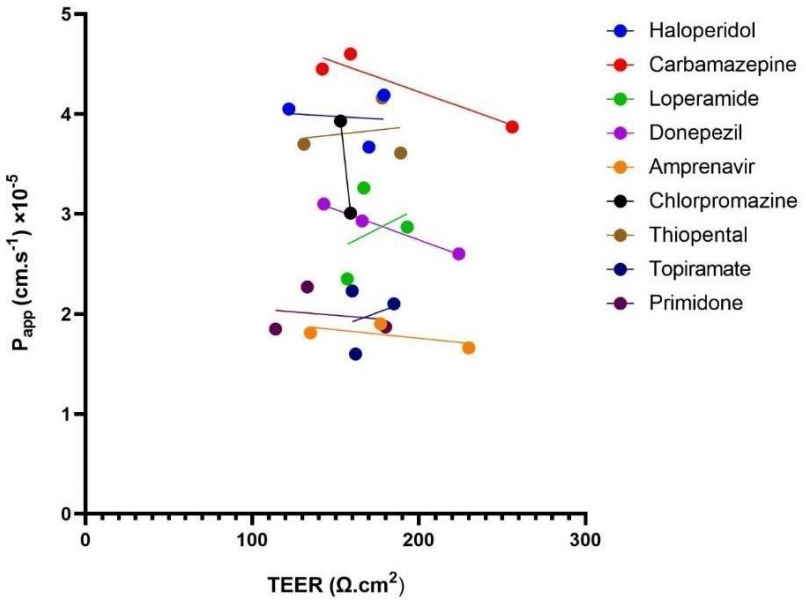

Figure 5.7 – *Plot of TEER value for PBECs cultured on Transwell insert on day of study against Pexact. Lines of best fit were generated using linear regression.*

As demonstrated by the line of best fit for each plot (Fig. 5.7), there is a minor negative correlation between the TEER value of the individual PBEC Transwell

insert and the P_{exact} value for certain compounds, including carbamazepine, donepezil and amprenavir. The plot displays a wide range of TEER values were varying between 114 Ω.cm^2 and 230 Ω.cm^2.

5.3 Discussion

Within this Chapter, an *in vitro* Transwell PBEC model of the BBB was evaluated with a series of test drugs. The test drugs were selected from a database which was created to include both chemical and experimental parameters relevant to compound permeability at the BBB. Drug transport studies were conducted using 10 compounds, across 3 time points, in both A-B and B-A directions, and sample concentrations were analysed using LC-MS/MS. Compound permeability was evaluated using a selection of pharmacokinetic parameters, including P_{app}, P_{exact}, ER, F_u, $K_{p,predicted}$ and $K_{p,uu,predicted}$, all of which allowed comparison of this model to other *in vitro* and *in vivo* data for evaluation.

P_{app} and P_{exact} values were calculated for the drug transport studies across time points and directions. Overall trends in this data suggest that P_{app} underpredicts the rate of permeability of compounds, demonstrated by a lower P_{app} than P_{exact} value across all compounds, with particular emphasis at the 120-minute time point. This is due to the limitations present in the calculation of P_{app}, which is only valid when drug transport is in the linear phase and when less than 10% of compound has crossed the membrane. As P_{exact} accounts for the back flow of compound after the linear phase of drug transport has passed, this parameter gives a more accurate estimation of the rate of drug permeability, particularly at the later stages of the study, where compound across the membrane is more likely to be reaching an equilibrium phase. Furthermore, it can also be observed that in both parameters and across all compounds, there is variability in the rate of drug flow between the compartments with time. Although this could be anticipated with the P_{app} parameter, as this calculation does not make an allowance for the backflow of drug present at later time points, the fluctuation of P_{exact} values with time was not expected. A similar phenomenon was observed by Tran et al., 2004, who hypothesised that variability of P_{exact} with time is due to structural changes in one or both of the polarised cell membranes with time.

However, it could also be possible that the variability of P_{exact} over time observed is due to slow rates of drug binding in the Transwells throughout the study, as the P_{exact} calculation only accounts for fast non-specific drug binding (Tran et al., 2004). In addition to the trends described, it can also be observed that there is a higher rate of flow of compound from A-B than B-A across many compounds, including haloperidol, loperamide, donepezil, amprenavir, chlorpromazine and thiopental. This is an unexpected result, as drugs which are known substrates for efflux transporters, including amprenavir and loperamide, would be expected to have a lower flow rate from A-B than B-A due to efflux on the apical side of the PBEC membrane. The other compounds, according to details from the drug database, are either MDR1 inhibitors or passive diffusion controls, so would be expected to have an equal flow rate between compartments.

Results from this study show that the efflux ratios calculated do not significantly vary between P_{app} and P_{exact} parameters, however, the efflux ratios do vary with time. Multiple compounds, including haloperidol, loperamide, donepezil, and topiramate increase in efflux ratio over the three time points. However, carbamazepine is observed to decrease over the time period. In spite of the variation across earlier time points, one notable commonality between compounds is that at the final time point, all compounds have an ER value of between 0.94 and 1.96. This, therefore, implies that there is no significant active transport of compounds taking place across the PBEC membrane at the end of the study. Consequently, it can be hypothesised that at the earlier time points, the efflux ratios are being differentially affected by issues such as membrane structural changes and slow rates of drug binding, and no significant uptake or efflux is taking place in the overall time period.

This hypothesis is supported by comparing data from this study to that obtained by Bentham, 2010, in a similar *in vitro* primary PBEC Transwell model. Comparing the efflux ratios obtained in the two studies, it is evident that strong efflux is taking place for the compounds carbamazepine, donepezil, and amprenavir in results from Bentham, 2010. However, in the present study, the strong efflux ratio is not reflected in the data obtained; haloperidol and

carbamazepine are the sole compounds with an efflux ratio within 2-fold of those from Bentham, 2010, and these compounds were not predicted to have efflux transporter interactions. Additionally, it can be observed that P_{app} and P_{exact} values obtained by Bentham, 2010, are 10-fold slower in the A-B direction than in the current study, reinforcing the notion that compounds which are transporter substrates are not being effluxed across the apical membrane in the current study. In the B-A direction, P_{exact} values from this study show a faster rate of permeability for haloperidol, carbamazepine, and chlorpromazine. Although this difference is not as exaggerated as in the A-B direction, this could suggest overall higher rates of paracellular transport in the current model than that presented by Bentham, 2010. However, as donepezil and amprenavir have similar rates of transport in the B-A direction between the current study and that by Bentham, 2010, despite having different values in the A-B direction, this suggests that there is also a lack of expression or function of multidrug efflux transporters in the current PBEC model.

By comparing P_{exact} values across the PBEC monolayer to a no cell control, it can be observed that the PBEC monolayer does slow the rate of permeability between the two compartments in both directions. However, two compounds, chlorpromazine, and carbamazepine, have a faster rate of permeability across the PBECs than in a no cell control. Although it is unknown whether this difference is statistically significant due the sample size of n=1 for the no cell control samples.

P_{exact} and P_{app} parameters were also used to predict an *in vitro* ratio of unbound drug in blood to brain compartments ($K_{p,uu,predicted}$). Values of $K_{p,uu,predicted}$ and F_u values for plasma and brain were used to predict values for *in vitro* blood to brain concentration ratio ($K_{p,predicted}$). The values of $K_{p,uu,predicted}$ which were calculated using P_{exact} and P_{app} parameters show distinct differences, with the 30- and 60-minute time points having higher ratios when calculated with P_{exact}. However, this phenomenon is not observed at the 120-minute time point. Thus, this indicates that the initial difference in K_p prediction is due to different binding rates at the earlier study time points, which has been accounted for in the P_{exact} calculation, but not in the P_{app} calculation. Additionally, the *in vitro* calculations

predict significant differences between K_p and $K_{p,uu}$ values, which demonstrates the importance of considering the proportion of free drug able to cross the membrane in the *in vivo* system.

In order to evaluate the predicted values, *in vitro* $K_{p,uu,predicted}$ data calculated from P_{exact} at the 120-minute time point was compared to *in vivo* $K_{p,uu}$ data from rodents compiled in the database. From the database values, it can be seen that loperamide, amprenavir and topiramate are effluxed *in vivo*. Database values also suggest that passive controls, carbamazepine and primidone, and BBB disrupting compound, thiopental, are substrates for efflux. Furthermore, database values suggest that MDR1 inhibitors donepezil and chlorpromazine may be substrates for uptake *in vivo*. It must be noted that due to species differences in transporter expression, it is possible that the *in vivo* values presented may not accurately reflect the *in vivo* transporter mechanisms in pig or human. However, it is evident, when comparing the *in vitro* predicted $K_{p,uu}$ to the *in vivo* $K_{p,uu}$, that the *in vitro* model has over predicted $K_{p,uu}$ in almost all compounds. The only $K_{p,uu}$ value which is underpredicted by the model is donepezil, which has previously been shown by Bentham, 2010, to be a substrate of multidrug efflux transporters in porcine. It could consequently be hypothesised that this disparity is due to species differences. Otherwise, in the *in vitro* model, the majority of $K_{p,uu}$ values predicted are ~1, indicating no uptake or efflux mechanisms are present. Thus, supporting the other datasets presented in this Chapter. However, a $K_{p,uu,predicted}$ value of note is loperamide, which has been widely shown to be strongly effluxed across many species (Fridén et al., 2009; Uchida et al., 2011). However, the results from the *in vitro* model may be indicative of uptake across the PBEC monolayer, with a value of ~2. A possible explanation for this phenomenon is that the PBECs have disorientated in the Transwell insert, so the apical membrane containing major efflux transporters is facing the Transwell insert, resulting in reverse efflux from basal to apical, which would need further investigation using confocal microscopy.

It is, therefore, apparent that there are many differences in drug transport between the PBEC model evaluated in this Chapter, and both *in vivo* data and

other PBEC Transwell *in vitro* data. However, when comparing the PBEC model generated to a wider range of Transwell BBB models using other cell types, different conclusions can be drawn. Firstly, when comparing the permeability co-efficients obtained from the PBEC model in this Chapter to those of cell lines, hCMEC/D3, MDR1-MDCKII, and MDCK wild-type (wt), the overall rates of transport for overlapping compounds in the study are faster in cell lines than in the primary PBECs (Bentham, 2010). For example, comparing the P_{app} value in A-B direction for carbamazepine at 60 minutes for PBECs calculated in this study (27.2×10^{-6} cm.s^{-1}) to hCMEC/d3 human BBB cell line (38.5×10^{-6} cm.s^{-1}) and MDCK cell lines (MDR1 MDCKII = 91.1×10^{-6} cm.s^{-1}, MDCKwt = 78.8×10^{-6} cm.s^{-1}) reported by Bentham, 2010, there is evidence of a reduced flow rate of compound across the PBECs by comparison to common cell lines. Furthermore, in another study of a PBEC Transwell model by Franke et al., 2000, the reported P_{app} value in A-B direction for haloperidol is almost identical to that reported in this study (Franke et al., 2000 = 20.1×10^{-6} cm.s^{-1}, current study = 23.6×10^{-6} cm.s^{-1}). Additionally, the P_{app} value in A-B direction for donepezil at 60 minutes in this study (22.7×10^{-6} cm.s^{-1}) is lower than that reported for both MDCK lines (MDR1 MDCKII = 64.6×10^{-6} cm.s^{-1}, MDCKwt = 66.3×10^{-6} cm.s^{-1}, Bentham, 2010), for rat primary BECs (63×10^{-6} cm.s^{-1}, Veszelka et al., 2018), and for human iPSC derived BECs (40.5×10^{-6} cm.s^{-1}, Mantle et al., 2016). However, in spite of the reduced flow rates across the PBEC monolayer by comparison to other cell types, the data could be interpreted as to suggest that the expression of multidrug efflux transporters by the PBECs isolated in this study is distinct to that of other BBB cell types. For example, the efflux ratios for amprenavir presented in Bentham, 2010, for MDR1-MDCKII (8.6) and MDCK (2) indicate that amprenavir is a strong substrate for multidrug efflux transporter MDR1. However, results presented in this study for the corresponding time point of 60-minutes (0.5) may suggest that amprenavir is being shunted across the PBEC monolayer. This result, alongside the $K_{p,uu,predicted}$ value for loperamide, could provide further evidence for the expression of multidrug efflux transporters being present on the basal, rather than the apical membrane in the Transwell PBEC cultures.

The data presented in this Chapter show that the PBEC Transwell model generated allows for more paracellular transport across the membrane than a similar PBEC Transwell model (Bentham, 2010). However, PBECs isolated in this study are more restrictive than other frequently used BBB cell types (MDCK and hCMEC/d3, Bentham 2010) (rat primary BECs, Veszelka et al., 2018) (human iPSCs, Mantle, 2016). The permeability data from drug transport studies in the PBEC Transwell model may suggest that the expression of key BBB multidrug efflux transporters (such as P-gp) is either down regulated or not as functional as other PBEC cultures or in MDR1 over-expression cell lines (Bentham, 2010). Yet there has been evidence to suggest that the PBEC model presented in this study may be expressing drug efflux transporters in an inverse manner, with apical transporters present on the basolateral cell membrane. However, firm conclusions upon this hypothesis cannot be drawn, as significant levels of paracellular transport may be masking any efflux transporter function present, and inhibitor studies and confocal microscopy studies would need to be carried out in order to determine the location of the transporters within the cells. These conclusions can be corroborated from the TEER results presented in Chapter 4. In the 2016 publication by Mantle et al., it was concluded that transport properties of an *in vitro* BBB membrane remain unchanged above a threshold TEER value, which the author suggests being at 500 $\Omega.cm^2$. Indeed, results presented in this Chapter may suggest that there is some slight correlation between rate of permeability and TEER across a limited number of compounds. In Chapter 4 of the current study, the mean TEER values presented for PBECs in Transwell culture with ACM is 235 ± 25 $\Omega.cm^2$. However, in the PBEC Transwell model presented by Bentham, 2010, the mean TEER value presented for PBECs cultured with CTX-TNA2 astrocytes was 10-fold higher, at 2132 ± 169 $\Omega.cm^2$. Whereas immortalised cell lines, such as MDCK and hCMEC/d3, also have reported TEER values below 300 $\Omega.cm^2$ (Kim Kit Lee, 2014; Rahmen et al., 2016). This suggests that the PBECs isolated in this study, like immortalised cell lines, are not meeting the minimum required TEER values for representative BBB transport studies. Therefore, the paracellular permeability of compounds will be higher than expected, and the ability to observe the effect of efflux transporters will be reduced.

It can thus be concluded that the PBECs isolated in this study, although showing expression of key BBB tight junction proteins and efflux transporters using molecular techniques, do not meet the minimum threshold for BBB drug transport studies. Further investigation is needed into the cause of different TEER levels reported between the PBEC model presented in the Chapter and others which have been previously published (Bentham, 2010; Franke, 2000). Additionally, inhibition studies must also be conducted to examine whether the permeability co-efficient values presented are being affected by the presence of multidrug efflux transporters.

Chapter 6

Discussion

6.1 Introduction

This purpose of this study was to establish if porcine brain endothelial cells (PBECs) could be used to create a viable blood-brain barrier on-a-chip (BBBoaC) model for permeability screening in the drug discovery process. Initially, a method was established to isolate PBECs from porcine brains obtained from the local abattoir. These cells were thoroughly characterised to ensure retention of blood-brain barrier (BBB) phenotype, including the expression of tight junctional adhesion proteins and multidrug efflux transporters. It was demonstrated that in static culture, the BBB phenotype of PBECs was closer to *in vivo* physiology than the immortalised BEC line, HBEC-5i, and the PBEC phenotype could be further improved through co-culture with immortalised murine astrocytes. However, drug transport studies in Transwell showed that the PBECs isolated in this study are leakier and have a lower level of multidrug efflux than previous publications which isolated PBECs using the same methodology. This could therefore indicate that that phenotype of the PBECs isolated in this study could be enhanced using different culture conditions. From the static Transwell models, two microfluidic BBBoaC models were developed from PBEC and HBEC-5i cultures, respectively. Comparison of the seeding protocols for PBECs and for the immortalised cell line, HBEC-5i, showed that PBECs required significantly more adaptations to BBBoaC seeding protocols to allow for cell growth and maintenance under shear stress. In spite of more complex technical requirements, PBECs grown in the microfluidic chip showed an increased ability to withstand shear stress by comparison to the immortalised cell line. Although significant characterisation would be required to compare the microfluidic and static models, and to evaluate the effect of microfluidic flow upon drug transport, results presented in this study provide promise that a PBEC BBBoaC model could be of use within the drug discovery process.

6.2 Junctional adhesion

The retention of proteins associated with junctional adhesion at the BBB, and the localisation of these proteins at cell-cell junctions, within PBEC cultures has

been demonstrated numerous times across this study. Previous studies have demonstrated that PBECs retain expression of tight junction proteins, including ZO-1, claudin-5, and occludin, *in vitro* and that these proteins are localised at cell-cell junctions within the culture (Cantrill et al., 2012; Gericke et al., 2020; Patabendige et al., 2013; Thomsen et al., 2015). In line with these studies, results demonstrate that PBECs isolated in this research retain expression of tight junctions, as ZO-1 is expressed and localised in the same location. Furthermore, novel identification of VE-cadherin mRNA and protein in PBECs within this work confirms retention of adherens junctions within the cultures. The application of SEM imaging to investigate the detailed surface structure of PBECs in static culture for the first time, revealed distinct raised areas at cell-cell junctions, which are believed to be tight junctions. This would consequently mean that tight junctions can be viewed using extracellular microscopy methods without the use of immunostaining techniques.

Similarly, many studies have demonstrated that PBECs in static BBB models are capable of achieving high levels of TEER in monoculture, with maximal values of between 370 – 1650 $\Omega.cm^2$ (Cantrill et al., 2012; Gericke et al., 2020; Patabendige et al., 2013; Thomsen et al., 2015). In this study, PBECs in monoculture achieved an average TEER value of 207 $\Omega.cm^2$ in monoculture. This value is significantly higher than average TEER values reported for immortalised cell lines in the literature, with a median value of 40 $\Omega.cm^2$ reported in one systematic review, and in this study, with a maximum value of 7 $\Omega.cm^2$ (Rahman et al., 2016). However, it is evident that the PBEC TEER values reported in this study are lower than those reported in previous publications. This could be due to methodological differences in the Transwell plates used, as discrepancies in surface area of the growth area used can accentuate inaccuracies in TEER measurements during calculations, and smaller Transwell inserts, such as those used in this study could result in over-confluence, resulting in poor cell survival. The differences in TEER values reported could also be due to the presence of pericytes with a polygonal morphology surviving puromycin purification in the PBEC culture. Although many studies use puromycin to purify cultures, the level of pericyte contamination remaining in

PBEC cultures in these studies is poorly characterised (Gericke et al., 2020; Patabendige et al., 2013; Thomsen et al., 2015). Thus, direct comparison of TEER values between studies should be done with caution due to underlying and unanalysed discrepancies. Further impediments to the interpretation of TEER values were revealed during impedance spectroscopy in the PBEC BBBoaC model. Analysis with the specialised electrode system, the SynVivo impedance analyser, in both Transwell and in the BBBoaC model resulted in unexpected baseline values which were significantly different to those reported in previous publications (Deosarkar et al., 2015). Thus, rendering the data inconclusive.

Previous studies have demonstrated that co-culture of PBECs with astrocytes has a significant effect upon the expression and function of tight junctions in *in vitro* culture (Nielsen et al., 2017; Thomsen et al., 2015). Indeed, in this study, astrocyte co-culture significantly increased TEER levels of PBECs, and decreased permeability of large molecule fluorescent marker FITC-dextran, suggesting an increase in tight junctional adhesion between the PBECs. Although the mechanism behind astrocytic modulation of tight junctions is yet to be fully elucidated, it has been hypothesised that astrocytes exert this function through the release a range of soluble factors which act to induce barrier function through increasing intracellular cAMP and inducing Wnt signalling pathways (Abbott, 2006; Gonzalez-Mariscal et al., 2008).

Although molecular studies validated the expression and localisation of tight junction proteins within the isolated PBEC cultures, transport studies across Transwell monolayers of PBECs demonstrated paracellular leakage of compounds. Indeed, drug permeability rates demonstrated in this study show drug permeability rates up to 10-fold higher in both directions than those seen in parallel studies reported in the literature (Bentham, 2010). In spite of this, it is evident that the PBEC Transwell model is significantly more restrictive in terms of permeability than immortalised cell lines. This was demonstrated against HBEC-5i cells using FITC-dextran in Chapter 4, but also against published cell line drug permeability rates (Bentham, 2010). In summary, it can be assumed that the PBECs are forming a monolayer but are not as tightly bound at cell-cell

junctions as other PBEC cultures reported in the literature. This phenomenon was also observed in TEER values, where the values recorded for PBECs in this study were up to 10-fold lower than those reported in the literature (Bentham, 2010; Cantrill et al., 2012; Gericke et al., 2020; Zhang et al., 2006). The higher rates of permeability observed in this study could be due to the methodological and pericyte contamination issues as previously described. In conclusion, these results support the statement made by Mantle et al., 2016, that TEER values must reach a threshold of 500 $\Omega.cm^2$ to express BBB transport properties. Consequently, in order to develop PBEC cultures for drug transport studies, the TEER values must first be elevated to above 500 $\Omega.cm^2$.

6.3 Multidrug efflux transporters

The many structurally heterogenous substrates of multidrug efflux transporters at the BBB, including P-glycoprotein (P-gp), BCRP and MRPs, make ABC transporters a major challenge in drug development (Rauch, 2011). It is for this reason that the expression of multidrug efflux transporters by BECs are widely investigated, with P-gp being renowned as the most well characterised BBB transporter. Previous studies have shown expression of P-gp and BCRP in PBEC *in vitro* cultures (Cantrill et al., 2012; Gericke et al., 2020; Patabendige et al., 2013; Thomsen et al., 2015). Indeed, results presented here show that PBECs isolated for this study express both P-gp and BCRP, however, these cultures also expressed MRP1 which was previously thought to be expressed at negligible levels in PBECs (Warren et al., 2009). Results suggest that the three multidrug efflux transporters examined in this study are expressed at comparable levels to endogenous control, GAPDH. This is within a one-fold range to that of BCRP expression levels in cultured PBECs in a study by Patabendige et al., 2013.

Drug transport studies carried out in the PBEC Transwell model, however, indicate a reduced level of efflux of known transporter substrates by comparison to other PBEC and MDR1-MDCKII models (Bentham, 2010). Although expression of multidrug efflux transporters was shown using qPCR, the presence of mRNA does not directly translate to functional transporters, and

consequently, P-gp function assays would need to be undertaken to validate function in the model. However, it is also possible that expression of transporters could be downregulated during the drug transport studies, and thus qPCR on PBECs should be done immediately after the drug transport studies have taken place. It is also possible that high levels of paracellular transport, as a result of leaky cell-cell junctions, could be masking some of the drug efflux taking place. With this in mind, there is also some indication of reverse active efflux of drugs, where compounds expected to have a reduced flow in the apical to basal direction, instead show a lower rate of transport in the B-A direction. It is, therefore, evident that further drug transport studies are needed to fully elucidate the function of multidrug efflux transporters in the Transwell model. Confocal microscopy in conjunction with immunoflourescent staining for P-gp could also elucidate the position of the transporters on the PBEC membrane.

Multiple studies have demonstrated that multidrug efflux transporter expression can be altered by co-culture with astrocytes or by induction of BECs with shear stress (Cucullo et al., 2011; Gaillard et al., 2000; Garcia-Polite et al., 2017; Wang et al., 2018). PBECs isolated in this study demonstrated increased tight junctional adhesion in response to co-culture with astrocytes in line with previous studies, and it is thus logical to presume that astrocyte co-culture could significantly affect the upregulation of multidrug efflux transporter expression. In this light, it is also possible that the PBECs subjected to 48 hours of shear stress in microfluidic culture have higher levels of multidrug efflux transporters, which could impact drug transport. This clearly shows two avenues for further study into the optimisation and adaption of the work presented in this study.

6.4 The neurovascular unit

The NVU plays a critical role in maintaining function of BECs in *in vitro* culture. The NVU consists of pericytes, astrocytes, other supportive glial cell types, and basement membrane proteins, with neurons sometimes being considered (Duport et al., 1998). Despite being a supportive cell type, the presence of pericytes within primary cultures can be considered a problematic contaminant. This is because pericytes can rapidly out-compete BECs in growth time,

becoming the major component of the primary culture, and as pericytes do not express tight junctions, they can have an adverse effect on paracellular permeability (Perrière et al. 2005). Puromycin purification is widely used to reduce the number of pericytes in culture and has been reported to remove up to 98% of pericytes from BEC cultures (Nielsen et al., 2017; Perrière et al. 2005). However, novel results within this study show that puromycin purification results in a phenotypic change in the pericytes present as well as reducing overall number. To the extent of this author's knowledge, this phenomenon has not been reported in published literature and, thus, the cellular changes taking place remain poorly characterised. It could, however, be hypothesised that the plastic nature of pericytes has caused the cells to undergo a phenotypic change to take on an endothelial-like morphology (Dore-Duffy & Cleary, 2011). It is also possible that the presence of these pericytes have resulted in lower levels of junctional adhesion in this PBEC model by comparison to other published Transwell models. However, as these studies did not investigate the presence of pericytes without astrocyte treatment, no firm conclusions could be drawn (Cantrill et al., 2012; Patabendige et al., 2013; Thomsen et al., 2015). Consequently, further investigation into the aSMA-expressing cells present following puromycin is needed, including an immunoflourescent co-stain of ZO-1 and aSMA to elucidate the spatial interaction of endothelial and pericytic cells in the culture.

The ability of astrocytes to maintain the expression of the BBB phenotype of PBECs has been long established and this is further reinforced by the results presented in this study, which show that astrocytes significantly increase TEER values and decrease permeability in PBECs (Duport et al., 1998) (Nielsen et al., 2017). However, it was also demonstrated that astrocytes did not have the same induction effect upon the human immortalised cell line, HBEC-5i, suggesting that the cell line does not express the astrocyte signalling receptors associated with the BBB phenotype (Gaillard et al., 2000; Puech et al., 2018).

The drug transport studies undertaken in the PBEC Transwell model demonstrated that the PBEC monolayer has reduced junctional adhesion compared to other models (Cantrill et al., 2012; Patabendige et al., 2013;

Thomsen et al., 2015). It should be noted that in drug transport study protocols used in this study, ACM was used as a replacement for astrocyte co-culture due to Covid-199 related time restrictions on the study. However, other PBEC models, which showed increased junctional adhesion, used co-culture with astrocytes as standard (Bentham, 2010; Cantrill et al., 2012; Thomsen et al., 2015). Although it is likely that co-culture with astrocytes would induce tighter junctions in the PBEC Transwell model (as shown in Chapter 4), resulting in reduced paracellular transport of compounds, the TEER values recorded in this study for astrocyte co-culture were still below the suggested threshold for drug transport studies of 500 $\Omega.cm^2$ (Mantle et al., 2016). Thus, it is likely that additional changes to the model will be needed to reduce paracellular transport to negligible levels.

The basement membrane, formed of a deposition of basement membrane proteins around the blood vessels of the CNS, is an often-neglected part of the NVU (Yao et al., 2014). However, these proteins play a significant role in regulating gene transcription in endothelial cells (Abbott et al., 2010). Within this study, fibronectin and collagen IV were used to culture PBECs in Transwell and HBEC-5i cells within the microfluidic chip. However, it was determined that this was insufficient for the microfluidic culture of PBECs, and the amount of basement membrane proteins applied for culture was consequently increased to allow increased cell adhesion. Thus, demonstrating the critical nature of these proteins in complex cell culture conditions such as microfluidic systems.

6.5 Drug transport & quantification

The movement of drugs across the BBB is a net flux from many different transport mechanisms, including passive diffusion, transcytosis, carrier and receptor mediated transport, and drug efflux (Pardridge, 2012). Compared to peripheral endothelial cells, BECs have a reduced level of passive diffusion and transcytosis, while having a higher expression of multidrug efflux transporters and select receptor and carrier mediated transport systems. In order to examine the BBB phenotype of the BECs, a database of drugs and the associated uptake and efflux mechanisms was created, and a range of drugs were selected to be

used in transport studies (Appendix 2). Compounds able to cross the BBB by transcellular passive diffusion and uptake transporters were selected, alongside compounds which were subject to efflux by multidrug efflux transporters. Drug transport studies across PBEC monolayers in Transwell showed higher than expected levels of paracellular transport, which is negligible across the *in vivo* BBB. Thus, with high levels of paracellular transport, other drug transport mechanisms, including transcellular passive diffusion, uptake, and efflux become difficult to elucidate.

Apparent and exact permeability coefficients (P_{app} and P_{exact}) were calculated to show the rate of transport of a compound across the PBEC monolayer. It could be seen from these values that, on average, there was a higher transport rate for most compounds in the apical to basal direction than the basal to apical direction, and that P_{app} calculations underestimated the rate of permeability, particularly at later time points. Furthermore, both P_{app} and P_{exact} values showed a higher rate of transport than other PBEC models and of the same order as other immortalised BEC models (Bentham, 2010). Using the permeability coefficients in both directions, an efflux ratio was calculated for each compound. An efflux ratio value demonstrates whether the compound has been subject to significant uptake or efflux across the membrane; it was, consequently, evident that none of the test drugs in this study underwent significant uptake or efflux across the PBEC monolayer. As permeability coefficients can be considered a rate of clearance across the PBEC monolayer, and as the unbound blood to unbound brain concentration ratio ($K_{p,uu}$) is a ratio of the clearances in apical to basal and basal to apical directions, the reciprocal of the efflux ratio can be considered to be a predicted value of $K_{p,uu}$ (Tran et al., 2004). As expected from the efflux ratios, the predicted $K_{p,uu}$ values showed no significant uptake or efflux of compounds across the PBEC monolayer. The predicted values of $K_{p,uu}$ can also be used to predict a value for K_p, which represents the total blood-to-brain concentration ratio using the fraction unbound (F_u) values from porcine brain and plasma. The predicted K_p values were significantly lower than the predicted $K_{p,uu}$ values, and ratios predicted using P_{exact} were higher than those calculated using P_{app}. This, therefore, demonstrates the importance in the careful selection

of parameters chosen to quantify drug transport across *in vitro* BBB, especially when comparing to *in vivo* values.

6.6 The Transwell model of the BBB

The Transwell model of the BBB is commonly utilised in the drug discovery process, and many models using PBECs have been published thus far (Cantrill et al., 2012; Gericke et al., 2020; Patabendige et al., 2013; Thomsen et al., 2015). A major benefit of the Transwell culture system is the ease of use; in agreement with this statement, this study found that no further cell culture method adaptations were required to culture PBECs upon Transwell inserts.

The PBEC Transwell model developed in this study, however, lacks some of the critical BBB characteristics observed in other Transwell BBB models. For example, the maximum TEER value recorded is up to 10-fold less than that published from previous static PBEC models, and permeability of the tracer compound (4 kDa FITC-dextran) compared to the no cell control shows substantial paracellular transport which is higher than that observed in previous BBB models (Bentham, 2010; Cantrill et al., 2012; Nielsen et al., 2017; Patabendige et al., 2013; Thomsen et al., 2015). The high levels of paracellular transport and the leakiness of the tight junctions, by comparison to other PBEC models, was reflected in faster rates of compound permeability in drug transport studies, which made multidrug efflux transport activity difficult to elucidate. The cause of the discrepancy in results could be due to methodological differences in Transwell culture, including the size of the Transwell insert used, the length of culture time, and supporting NVU cell types, as previously discussed.

It can consequently be concluded that the PBEC Transwell model created within this study needed little refinement in order to develop a protocol, was simple to use in high throughput drug trials, and benefitted from plentiful literature works for comparison. However, the resulting model could not be considered an accurate *in vitro* model of the BBB for drug permeability testing due to inconsistencies with previous literature and high levels of compound permeability. Consequently, further investigation and development of this model

is required in order to create a model which would be suitable for permeability screening.

6.7 The BBB-on-a-chip model

By comparison to Transwell models, BBBoaC models offer a complex and realistic cellular environment which mimics haemodynamic flow upon the apical membrane of BECs. Multiple BBBoaC models have been published within the past decade using different cell types and designs, but few have been fully evaluated for use within the drug discovery process, and none thus far have been developed using primary PBECs (Bagchi et al., 2019; Jiang et al., 2019).

Within this study, two BBBoaC models were generated using the commercially available SynVivo idealised microfluidic chip (Deosarkar et al., 2015). Firstly, HBEC-5i immortalised human BECs were cultured within the microfluidic chip. Although the protocol published by SynVivo for cell seeding within the chip required minor adaptations for this cell type, the cell seeding protocol remained much the same to the Transwell system. However, the seeding for PBECs required multiple significant changes, including increased cell density, infusions, and growth time. Therefore, demonstrating significant differences in the culture methodology required between cell types within the same BBBoaC system. This was in line with methodologies developed in previous publications, which demonstrated that primary and immortalised cell lines required different culture conditions (Brown et al., 2015; Deosarkar et al., 2015; Prabhakarpandian et al., 2013).

Once cells were seeded in the SynVivo chip, PBECs were able to withstand a greater shear stress than the immortalised HBEC-5i cell line, indicating that the primary cells would be better candidates for microfluidic culture. After being subjected to shear stress for 48 hours, tight junctions in the cells were assessed using FITC-dextran permeability and TEER analysis. Although TEER analysis was rendered unsuccessful due to issues with the SynVivo impedance analyser, FITC-dextran permeability showed some restriction across the PBEC monolayer by comparison to the no cell control in a similar pattern to that previously observed in the SynVivo model (Deosarkar et al., 2015).

Therefore, it can be concluded that a protocol has been established to successfully culture the primary PBECs within a BBBoaC model, in which early indications demonstrate a restrictive barrier is formed. However, neither TEER data nor FITC-dextran transport data can be directly compared to that obtained from the Transwell model, and thus no conclusions can be drawn about the differences between the two models. This could be considered a limitation within the system. Additionally, the extensive technical skill required to set up this model with primary cells, alongside the cost of individual microfluidic chips, indicate that BBBoaC models of this nature may not be suitable for high-throughput drug screening like the Transwell system (Bagchi et al., 2019; Jiang et al., 2019).

6.8 Summary & project implications

In conclusion, this study has demonstrated that PBECs show many molecular indications of the retention of BBB phenotype within *in vitro* culture, including multidrug efflux transporters and tight junctions. However, it is also evident that the technical skill required for the development and implication of primary PBEC isolation techniques could be considered a limitation of the cell type. Furthermore, permeability studies of the PBECs isolated in this study showed that there is substantial paracellular transport of markers and compounds, resulting in a lower TEER than has been previously reported for this cell type. However, TEER values and permeability of compounds indicates that the PBEC barrier is still more restrictive than immortalised cell lines, HBEC-5i and MDCK. Additionally, the Transwell model generated in this study required little protocol adaptation and benefits from ease of use for high throughput screening of compounds. In contrast, development of the static Transwell PBEC model into a dynamic microfluidic PBEC BBBoaC model required significant microfluidic methodological development and numerous adaptations to cell culture protocols. Although, once established, PBECs show early indications of forming a restrictive cell barrier within the microfluidic chip. More analysis is required to draw conclusions on the success of the microfluidic PBEC model; however, this study has highlighted the advanced technical requirements for microfluidic culture of primary cells. These advanced technical requirements show that

primary microfluidic models would not meet the criteria for high throughput compound screening in the drug development process. However, this is not to say that primary microfluidic models have no place in the drug development pipeline, and this microfluidic PBEC model could be more suited to the replacement of animals in the later stages of drug development (where there are only 1-3 test drugs) once further characterisation has taken place.

6.9 Future directions

The impact of the Covid-19 pandemic on this project restricted the work that could be undertaken to evaluate the PBEC models developed. Firstly, further investigation into the cause of the lower-than-expected TEER values and paracellular permeability of small drug compounds in the Transwell PBEC model would be required. This would involve using confocal microscopy to image the PBECs on the Transwell inserts to examine if cell multi-layering and over-confluency is taking place, alongside immunoflourescent staining of P-gp coupled with confocal microscopy to examine the presence of transporters on the apical membrane. This would be aided by investigation into cell death in Transwells, which might be caused as a result of over-confluence, using trypan blue. Additionally, further investigation into the presence of aSMA expressing cells in the PBEC cultures would be required to determine if this is a potential cause of the “leaky” tight junctions within the Transwell system. This would require an immunoflourescent co-stain for ZO-1 and aSMA, to determine if the aSMA cells are integrated into the monolayer, where they could cause disruption to tight junctional adhesion. Furthermore, the expression of multidrug efflux transporters following drug transport studies must be undertaken using qPCR, to ensure that efflux transporters are not being downregulated in the duration of the study. Finally, the major difference between the PBEC Transwell model used in the current study, and those used in published PBEC Transwell models, is the co-culture with CTX-TNA2 astrocytes. This study demonstrated that CTX-TNA2 co-culture reduced paracellular permeability of marker compound 4 kDa FITC-dextran to ~3% of the no cell control, however, time constraints placed on the drug transport studies meant that only ACM was used to support the PBECs in culture. Therefore, the drug studies would need to be

repeated with CTX-TNA2 astrocyte co-culture to examine the effect on paracellular permeability of the compounds and the function of multi-drug efflux transporters, ideally in the presence and absence of a selective P-gp inhibitor so that the function of P-gp in the studies can be fully elucidated.

With regard to the PBEC BBBoaC model, further characterisation studies are necessary to further investigate the effect of shear stress upon the phenotype of the PBECs, but time constraints placed on the project prevented further analysis. This would firstly involve immunofluorescent staining for ZO-1 in the PBEC BBBoaC model to visualise the tight junction formation of cells within the microfluidic chip, the use of qPCR to assess the effect of shear stress upon multidrug efflux transporters, alongside the application of confocal microscopy to examine cell morphology in the chip and the localisation of transporters on the apical membrane, including any resulting changes from the induction of shear stress upon the PBECs. Investigation and adaptation of the TEER methodology used for the SynVivo chip is also necessary, particularly the cause of the high baseline readings which need to be investigated by calibration of the impedance analyser. Finally, the protocol for PBEC BBBoaC development would need to be adapted to include seeding of CTX-TNA2 astrocytes in the central chip compartment. The drug transport studies could then be repeated using the same compounds as in Transwell model to directly compare the permeability and efflux of compounds within the two models.

If the PBEC BBBoaC model was successful in the drug transport studies, there are many adaptations which could be performed to make the model more physiologically relevant. Firstly, a limitation of the current SynVivo BBBoaC model is that the lumen of the synthetic vessels does not accurately mimic the shape or structure of an *in vivo* brain microvessel. This would result in an adverse effect on the flow media through the system, affecting shear stress by resulting in uneven and non-physiological force being applied to the apical membrane. Consequently, using advances in 3D-printing, hyper realistic vessels could be created from PDMS, which would increase the overall physiological relevance of the study. Additionally, the current PBEC model would only be viable for testing drug permeability in a healthy non-diseased

BBB. Subsequently, this model could be used to mimic various CNS disease states with the addition of microglia, reactive astrocytes, or patient-derived neurons from disease-states, including multiple sclerosis, Alzheimer's disease, or glioblastoma. In summary, once fully validated, the microfluidic PBEC model has the potential to be developed to include the latest advancements in technology and cell culture to become more physiologically relevant than BBBoaC models that are currently available.

Bibliography

Abbott, N. J. (2002). Astrocyte-endothelial interactions and blood-brain barrier permeability. *Journal of Anatomy*, *200*(6), 629–638. https://doi.org/10.1046/j.1469-7580.2002.00064.x

Abbott, N. J. (2004). Prediction of blood-brain barrier permeation in drug discovery from in vivo, in vitro and in silico models. *Drug Discovery Today:Technologies*, *1*(4), 407–416. https://doi.org/10.1016/j.ddtec.2004.11.014

Abbott, N. J., Hughes, C. C. W., Revest, P. A., & Greenwood, J. (1992). Development and characterisation of a rat brain capillary endothelial culture:towards an in vitro blood-brain barrier. *Journal of Cell Science*, *103*, 23–37.

Abbott, N. J., Patabendige, A. A. K., Dolman, D. E. M., Yusof, S. R., & Begley, D. J. (2010). Structure and function of the blood-brain barrier. *Neurobiology of Disease*, *37*(1), 13–25. https://doi.org/10.1016/j.nbd.2009.07.030
Abbott, N. J., Rönnbäck, L., & Hansson, E. (2006). Astrocyte-endothelial interactions at the blood-brain barrier. *Nature Reviews Neuroscience*, *7*(1),41–53. https://doi.org/10.1038/nrn1824

Abcam. (2021). *P Glycoprotein antibody [EPR10364-57] KO Tested (ab170904)*. Recombinant Anti-P Glycoprotein Antibody [EPR10364-57] KOTested (Ab170904). https://www.abcam.com/p-glycoprotein-antibody- epr10364-57-ab170904.html

Armulik, A., Genové, G., Mäe, M., Nisancioglu, M. H., Wallgard, E., Niaudet, C., He, L., Norlin, J., Strittmatter, K., Johansson, B. R., & Christer Betsholtz, &.(2010). Pericytes regulate the blood-brain barrier. *Nature.*, *468*(7323), 557–561. https://doi.org/10.1038/nature09522

Baello, S., Iqbal, M., Gibb, W., & Matthews, S. G. (2016). Astrocyte-mediated regulation of multidrug resistance P-glycoprotein in fetal and neonatal brain endothelial cells: age-dependent effects. *Physiological Reports*, *4*(16). https://doi.org/10.14814/phy2.12853

Bagchi, S., Chhibber, T., Lahooti, B., Verma, A., Borse, V., & Jayant, R. D. (2019). In-vitro blood-brain barrier models for drug screening and permeationstudies: An overview. *Drug Design, Development and Therapy*, *13*, 3591– 3605. https://doi.org/10.2147/DDDT.S218708

Baker, D. E. (2007). Loperamide: A pharmacological review. *Reviews in Gastroenterological Disorders*, *7*(3), S11-8.

Beconi, M. G., Howland, D., Park, L., Lyons, K., Giuliano, J., Dominguez, C.,Munoz-Sanjuan, I., & Pacifici, R. (2012). Pharmacokinetics of memantine in rats and mice. *PLoS Currents*, *3*. https://doi.org/10.1371/currents.RRN1291

Bentham, L. (2010). *The Use of In Vitro Unbound Drug Fraction and Permeability in Predicting Central Nervous System Drug Penetration*. University of Manchester, Faculty of Medical & Human Sciences, Doctor ofPhilosophy.

Berezowski, V., Landry, C., Dehouck, M.P., Cecchelli, R., Fenart, L. (2004). Contribution of glial cells and pericytes to the mRNA profiles of P-glycoprotein and multidrug resistance-associated proteins in an in vitro model of the blood-brain barrier. *Brain Res,* 1018(1),1-9. doi: 10.1016/j.brainres.2004.05.092.

Bergers, G., & Song, S. (2005). The role of pericytes in blood-vessel formationand maintenance. *Neuro-Oncology*, *7*(4), 452–464. https://doi.org/10.1215/s1152851705000232

Bickel, U. (2005). How to measure drug transport across the blood-brainbarrier. *NeuroRx*, *2*(1), 15–26. https://doi.org/10.1602/neurorx.2.1.15

Bicker, J., Alves, G., Fortuna, A., & Falcão, A. (2014). Blood-brain barrier models and their relevance for a successful development of CNS drug deliverysystems: A review. *European Journal of Pharmaceutics and Biopharmaceutics*, *87*(3), 409–432. https://doi.org/10.1016/j.ejpb.2014.03.012

Blomstrand, F., Khatibi, S., Muyderman, H., Hansson, E., Olsson, T., Rönnbäck, L. (1999) 5-Hydroxytryptamine and glutamate modulate velocity and extent of intercellular calcium signalling in hippocampal astroglial cells in primary cultures. *Neuroscience*, 88(4), 1241-53. doi: 10.1016/s0306-4522(98)00351-0

Booth, R., & Kim, H. (2014). Permeability Analysis of Neuroactive Drugs Through a Dynamic Microfluidic In Vitro Blood–Brain Barrier Model. *Annals ofBiomedical Engineering*, *42*(12), 2379–2391. https://doi.org/10.1007/s10439-014-1086-5

Booth, Ross, & Kim, H. (2012). Characterization of a microfluidic in vitro modelof the blood-brain barrier (μBBB). *Lab on a Chip*, *12*(10), 1784–1792. https://doi.org/10.1039/c2lc40094d

Borst, P., & Schinkel, A. H. (2013). P-glycoprotein abcb1: A major player in drug handling by mammals. *Journal of Clinical Investigation*, *123*(10), 4131–4133. https://doi.org/10.1172/JCI70430

Brown, J. A., Codreanu, S. G., Shi, M., Sherrod, S. D., Markov, D. A., Neely, M. D., Britt, C. M., Hoilett, O. S., Reiserer, R. S., Samson, P. C., McCawley, L.J., Webb, D. J., Bowman, A. B., McLean, J. A., & Wikswo, J. P. (2016). Metabolic consequences of inflammatory disruption of the blood-brain barrier in an organ-on-chip model of the human neurovascular unit. *Journal of Neuroinflammation*, *13*(1). https://doi.org/10.1186/s12974-016-0760-y

Brown, T. D., Nowak, M., Bayles, A. v., Prabhakarpandian, B., Karande, P., Lahann, J., Helgeson, M. E., & Mitragotri, S. (2019). A microfluidic model of human brain (μHuB) for assessment of blood brain barrier. *Bioengineering &Translational Medicine*, *4*(2). https://doi.org/10.1002/btm2.10126

Butt, A. M., Jones, H. C., & Abbott, N. J. (1990). Electrical resistance acrossthe blood-brain barrier in anaesthetized rats: a developmental study. *The Journal of Physiology*, *429*(1), 47–62. https://doi.org/10.1113/jphysiol.1990.sp018243

Campisi, M., Shin, Y., Osaki, T., Hajal, C., Chiono, V., & Kamm, R. D. (2018).3D self-organized microvascular model of the human blood-brain barrier with

endothelial cells, pericytes and astrocytes. *Biomaterials*, *180*, 117–129. https://doi.org/10.1016/j.biomaterials.2018.07.014

Cantrill, C. A., Skinner, R. A., Rothwell, N. J., & Penny, J. I. (2012). An immortalised astrocyte cell line maintains the in vivo phenotype of a primaryporcine in vitro blood-brain barrier model. *Brain Research*, *1479*, 17–30. https://doi.org/10.1016/j.brainres.2012.08.031

Cecchelli, R., Berezowski, V., Lundquist, S., Culot, M., Renftel, M., Dehouck,M.-P., & Fenart, L. (2007). Modelling of the blood–brain barrier in drug discovery and development. *Nature Reviews Drug Discovery 2007 6:8*, *6*(8),650–661. https://doi.org/10.1038/nrd2368

Chen, C., Zhou, H., Guan, C., Zhang, H., Li, Y., Jiang, X., Dong, Z., Tao, Y., Du, J., Wang, S., Zhang, T., Du, N., Guo, J., Wu, Y., Song, Z., Luan, H., Wang, Y., Du, H., Zhang, S., … Wang, T. (2020). Applicability of free drug hypothesis to drugs with good membrane permeability that are not efflux transporter substrates: A microdialysis study in rats. *Pharmacology Research& Perspectives*, *8*(2). https://doi.org/10.1002/PRP2.575

Cheslow, L., & Alvarez, J. I. (2016). Glial-endothelial crosstalk regulates blood-brain barrier function. *Current Opinion in Pharmacology*, *26*, 39–46. https://doi.org/10.1016/j.coph.2015.09.010

Christensen J., Højskov C.S., Dam M., & Poulsen J.H. (2001). Plasma concentration of topiramate correlates with cerebrospinal fluid concentration.*Therapeutic Drug Monitoring*, *23*(5), 529–535. https://doi.org/10.1097/00007691-200110000-00006

Cucullo, L., Hossain, M., Puvenna, V., Marchi, N., & Janigro, D. (2011). Therole of shear stress in Blood-Brain Barrier endothelial physiology. *BMC Neuroscience*, *12*(1), 40. https://doi.org/10.1186/1471-2202-12-40

Czupalla, C. J., Liebner, S., & Devraj, K. (2014). In Vitro Models of the Blood–Brain Barrier. *Methods in Molecular Biology (Clifton, N.J.)*, *1135*, 415–437. https://doi.org/10.1007/978-1-4939-0320-7_34

Daneman, R., & Prat, A. (2015). The blood–brain barrier. *Cold Spring Harbor Perspectives in Biology*, *7*(1). https://doi.org/10.1101/cshperspect.a020412

Davson, H., Oldendorf, W.H., (1967). Symposium on membrane transport: Transport in the central nervous system. *Proc R Soc Med*, 60(4), 326-9.

Deguchi, Y. (2002). Application of In Vivo Brain Microdialysis to the Study ofBlood-Brain Barrier Transport of Drugs. *Drug Metabolism and Pharmacokinetics*, *17*(5), 395–407. https://doi.org/10.2133/dmpk.17.395

Deosarkar, S. P., Prabhakarpandian, B., Wang, B., Sheffield, J. B., Krynska,B., & Kiani, M. F. (2015). A novel dynamic neonatal blood-brain barrier on a chip. *PLoS ONE*, *10*(11). https://doi.org/10.1371/journal.pone.0142725

di Salle, E., Pacifici, G. M., & Morselli, P. L. (1974). Studies on plasma proteinbinding of carbamazepine. *Pharmacological Research Communications*, *6*(2),193–202. https://doi.org/10.1016/S0031-6989(74)80028-7

Di, L., & Chang, C. (2015). Methods for Assessing Brain Binding. *Blood-BrainBarrier in Drug Discovery*, 274–283. https://doi.org/10.1002/9781118788523.ch12

Di, L., Kerns, E. H., & Carter, G. T. (2008). Strategies to assess blood-brainbarrier penetration. *Expert Opinion on Drug Discovery*, *3*(6), 677–687. https://doi.org/10.1517/17460441.3.6.677

Di, L., Kerns, E. H., Bezar, I. F., Petusky, S. L., & Huang, Y. (2009). Comparison of blood–brain barrier permeability assays: in situ brain perfusion,MDR1-MDCKII and PAMPA-BBB. *Journal of Pharmaceutical Sciences*, *98*(6),1980–1991. https://doi.org/10.1002/jps.21580

Dohgu, S., Takata, F., Yamauchi, A., Nakagawa, S., Egawa, T., Naito, M., Tsuruo, T., Sawada, Y., Niwa, M., & Kataoka, Y. (2005). Brain pericytes contribute to the induction and up-regulation of blood-brain barrier functionsthrough transforming growth factor-β production. *Brain Research*, *1038*(2), 208–215. https://doi.org/10.1016/j.brainres.2005.01.027

Dora, K. A. (2001). Cell-cell communication in the vessel wall. *VascularMedicine*, *6*(1), 43–50.

Dore-Duffy, P., & Cleary, K. (2011). Morphology and Properties of Pericytes.*Methods in Molecular Biology (Clifton, N.J.)*, *686*, 49–68. https://doi.org/10.1007/978-1-60761-938-3_2

Duport, S., Robert, F., Muller, D., Grau, G., Parisi, L., Stoppini, L. (1998). An in vitro blood-brain barrier model: cocultures between endothelial cells and organotypic brain slice cultures. *Proc Natl Acad Sci*, 95(4),1840-5. doi: 10.1073/pnas.95.4.1840

Elbrecht, D. H., Long, C. J., & Hickman, J. J. (2016). Transepithelial/endothelial Electrical Resistance (TEER) theory and ap- plications for microfluidic body-on-a-chip devices. *J Rare Dis Res Treat*, *1*(3),46–52.

Esser, L., Zhou, F., Pluchino, K. M., Shiloach, J., Ma, J., Tang, W. K., Gutierrez, C., Zhang, A., Shukla, S., Madigan, J. P., Zhou, T., Kwong, P. D., Ambudkar, S. v., Gottesman, M. M., & Xia, D. (2017). Structures of the Multidrug Transporter P-glycoprotein Reveal Asymmetric ATP Binding and theMechanism of Polyspecificity. *Journal of Biological Chemistry*, *292*(2), 446– 461. https://doi.org/10.1074/jbc.M116.755884

Förster, C., Burek, M., Romero, I. A., Weksler, B., Couraud, P. O., & Drenckhahn, D. (2008). Differential effects of hydrocortisone and TNFα ontight junction proteins in an in vitro model of the human blood-brain barrier.*Journal of Physiology*, *586*(7), 1937–1949. https://doi.org/10.1113/jphysiol.2007.146852

Franke, H., Galla, H.-J., Beuckmann, C. T., & Beuckmann. (2000). Primarycultures of brain microvessel endothelial cells: a valid and flexible model to

study drug transport through the blood-brain barrier in vitro. *Brain Research Protocols*, *5*(3), 248–256. https://doi.org/doi: 10.1016/s1385-299x(00)00020-9

Fridén, M., Ducrozet, F., Middleton, B., Antonsson, M., Bredberg, U., & Hammarlund-Udenaes, M. (2009). Development of a high-throughput brain slice method for studying drug distribution in the central nervous system. *DrugMetabolism and Disposition*, *37*(6), 1226–1233. https://doi.org/10.1124/dmd.108.026377

Gaillard, P. J., Cornelia, I., van der Sandt, J., Voorwinden, L. H., Vu, D., Nielsen, J. L., Gerrit De Boer, A., & Durk Breimer, D. (2000). Astrocytes Increase the Functional Expression of P-Glycoprotein in an In Vitro Model ofthe Blood-Brain Barrier. *Pharm Res.*, *17*(10), 1198–1205.

Garcia-Polite, F., Martorell, J., Rey-Puech, P. del, Melgar-Lesmes, P., O'Brien, C. C., Roquer, J., Ois, A., Principe, A., Edelman, E. R., & Balcells, M. (2017). Pulsatility and high shear stress deteriorate barrier phenotype in brain microvascular endothelium. *Journal of Cerebral Blood Flow & Metabolism*, *37*(7), 2614. https://doi.org/10.1177/0271678X16672482

Gericke, B., Römermann, K., Noack, A., Noack, S., Kronenberg, J., Blasig, I. E., & Löscher, W. (2020). A face-to-face comparison of claudin-5 transduced human brain endothelial (hCMEC/D3) cells with porcine brain endothelial cellsas blood-brain barrier models for drug transport studies. *Fluids and Barriers ofthe CNS*, *17*(1), 53. https://doi.org/10.1186/s12987-020-00212-5

Ghosh, C., Gonzalez-Martinez, J., Hossain, M., Cucullo, L., Fazio, V., Janigro,D., & Marchi, N. (2010). Pattern of P450 expression at the human blood-brain barrier: Roles of epileptic condition and laminar flow. *Epilepsia*, *51*(8), 1408– 1417. https://doi.org/10.1111/j.1528-1167.2009.02428.x

Ghosh, C., Puvenna, V., Gonzalez-Martinez, J., Janigro, D., & Marchi, N. (2011). Blood-Brain Barrier P450 Enzymes and Multidrug Transporters in DrugResistance: A Synergistic Role in Neurological Diseases. *Current Drug Metabolism*, *12*(8), 742.

Gomes, M. J., Mendes, B., Martins, S., & Sarmento, B. (2016). Cell-based in vitro models for studying blood-brain barrier (BBB) permeability. *Concepts andModels for Drug Permeability Studies: Cell and Tissue Based In Vitro Culture Models*, 169–188. https://doi.org/10.1016/B978-0-08-100094-6.00011-0

Gomez-Zepeda, D., Taghi, M., Scherrmann, J. M., Decleves, X., & Menet, M. C. (2020). ABC transporters at the blood–brain interfaces, their study models,and drug delivery implications in gliomas. *Pharmaceutics*, *12*(1), 20. https://doi.org/10.3390/pharmaceutics12010020

González-Mariscal L., Tapia R., & Chamorro D. (2008). Crosstalk of tight junction components with signaling pathways. *Biochimica et Biophysica Acta*,*1778*(3), 729–756. https://doi.org/10.1016/J.BBAMEM.2007.08.018

Griep, L. M., Wolbers, F., de Wagenaar, B., ter Braak, P. M., Weksler, B. B.,Romero, I. A., Couraud, P. O., Vermes, I., van der Meer, A. D., & van den Berg, A. (2013). BBB on CHIP: Microfluidic platform to modulate blood-brainbarrier function mechanically and biochemically. *Biomedical Microdevices*, *15*(1), 145–150. https://doi.org/10.1007/s10544-012-9699-7

Gustafsson, S., Sehlin, D., Lampa, E., Hammarlund-Udenaes, M., & Loryan, I. (2019). Heterogeneous drug tissue binding in brain regions of rats, Alzheimer's patients, and controls: impact on translational drug development. *Scientific Reports*, *9*(1), 1–15. https://doi.org/10.1038/s41598-019-41828-4

Hayashi, Y., Nomura, M., Yamagishi, S., Harada, S., Yamashita, J., Yamamoto, H. (1997). Induction of various blood-brain barrier properties in non-neural endothelial cells by close apposition to co-cultured astrocytes. *Glia*, 19(1), 13-26

He, Y., Yao, Y., Tsirka, S. E., & Cao, Y. (2014). Cell-Culture Models of theBlood–Brain Barrier. *Stroke*, *45*(8), 2514–2526. https://doi.org/10.1161/STROKEAHA.114.005427

Hellinger, É., Veszelka, S., Tóth, A. E., Walter, F., Kittel, Á., Bakk, M. L., Tihanyi, K., Háda, V., Nakagawa, S., Dinh Ha Duy, T., Niwa, M., Deli, M. A., & Vastag, M. (2012). Comparison of brain capillary endothelial cell-based and epithelial (MDCK-MDR1, Caco-2, and VB-Caco-2) cell-based surrogate blood-brain barrier penetration models. *European Journal of Pharmaceutics and Biopharmaceutics*, *82*(2), 340–351. https://doi.org/10.1016/j.ejpb.2012.07.020

Helms, H. C., Abbott, N. J., Burek, M., Cecchelli, R., Couraud, P. O., Deli, M. A., Förster, C., Galla, H. J., Romero, I. A., Shusta, E. v., Stebbins, M. J., Vandenhaute, E., Weksler, B., & Brodin, B. (2015). In vitro models of the blood-brain barrier: An overview of commonly used brain endothelial cell culture models and guidelines for their use. *Journal of Cerebral Blood Flow and Metabolism*, *36*(5), 862–890. https://doi.org/10.1177/0271678X16630991

Heymans, M., Sevin, E., Gosselet, F., Lundquist, S., & Culot, M. (2018). Mimicking brain tissue binding in an in vitro model of the blood-brain barrier illustrates differences between in vitro and in vivo methods for assessing therate of brain penetration. *European Journal of Pharmaceutics and Biopharmaceutics*, *127*, 453–461. https://doi.org/10.1016/j.ejpb.2018.03.007

Howarth, A. G., Hughes, M. R., & Stevenson, B. R. (1992). Detection of the tight junction-associated protein ZO-1 in astrocytes and other nonepithelial celltypes. *American Journal of Physiology - Cell Physiology*, *262*(2 31-2). https://doi.org/10.1152/ajpcell.1992.262.2.c461

Hu, C., Tao, L., Cao, X., & Chen, L. (2020). The solute carrier transporters andthe brain: Physiological and pharmacological implications. In *Asian Journal of Pharmaceutical Sciences* (Vol. 15, Issue 2, pp. 131–144). Shenyang Pharmaceutical University. https://doi.org/10.1016/j.ajps.2019.09.002

Hu, Y., Rip, J., Gaillard, P. J., de Lange, E. C. M., & Hammarlund-Udenaes, M. (2017). The Impact of Liposomal Formulations on the Release and Brain Delivery of Methotrexate: An In Vivo Microdialysis Study. *Journal of Pharmaceutical Sciences*, *106*(9), 2606–2613. https://doi.org/10.1016/J.XPHS.2017.03.009

Ishizaki, T., Chiba, H., Kojima, T., Fujibe, M., Soma, T., Miyajima, H., Nagasawa, K., Wada, I., & Sawada, N. (2003). Cyclic AMP induces phosphorylation of claudin-5 immunoprecipitates and expression of claudin-5gene in blood-brain-barrier endothelial cells via protein kinase A-dependent and -independent pathways. *Experimental Cell Research*, *290*(2), 275–288. https://doi.org/10.1016/S0014-4827(03)00354-9

Jahnsen, E. D., Trindade, A., Zaun, H. C., Lehoux, S., Duarte, A., & Jones, E. A. V. (2015). Notch1 Is pan-endothelial at the onset of flow and regulated byflow. *PLoS ONE*, *10*(4). https://doi.org/10.1371/journal.pone.0122622

Ji, Q., Wang, Y. L., Xia, L. M., Yang, Y., Wang, C. S., & Mei, Y. Q. (2019). High shear stress suppresses proliferation and migration but promotes apoptosis of endothelial cells co-cultured with vascular smooth muscle cells via down-regulating MAPK pathway. *Journal of Cardiothoracic Surgery*, *14*(1),1–10. https://doi.org/10.1186/s13019-019-1025-5

Jiang, L., Li, S., Zheng, J., Li, Y., & Huang, H. (2019). Recent progress inmicrofluidic models of the blood-brain barrier. *Micromachines*, *10*(6). https://doi.org/10.3390/mi10060375

Kaisar, M. A., Sajja, R. K., Prasad, S., Abhyankar, V. v., Liles, T., & Cucullo, L.(2017). New experimental models of the blood-brain barrier for CNS drug discovery. *Expert Opinion on Drug Discovery*, *12*(1), 89. https://doi.org/10.1080/17460441.2017.1253676

Kalvass, J. C., Maurer, T. S., & Pollack, G. M. (2007). Use of Plasma and Brain Unbound Fractions to Assess the Extent of Brain Distribution of 34 Drugs: Comparison of Unbound Concentration Ratios to in Vivo P- Glycoprotein Efflux Ratios. *Drug Metabolism and Disposition*, *35*(4), 660–666. https://doi.org/10.1124/DMD.106.012294

Kim Kit Lee, M. (2014). Drug Development in Cell Culture: Crosstalk from the Industrial Prospects. *J Bioequiv Availab*, *6*(3), 3. https://doi.org/10.4172/jbb.1000188

Kodaira, H., Kusuhara, H., Fujita, T., Ushiki, J., Fuse, E., & Sugiyama, Y. (2011). Quantitative Evaluation of the Impact of Active Efflux by P- Glycoprotein and Breast Cancer Resistance Protein at the Blood-Brain Barrieron the Predictability of the Unbound Concentrations of Drugs in the Brain Using Cerebrospinal Fluid Concentration as a Surrogate. *Journal of Pharmacology and Experimental Therapeutics*, *339*(3), 935–944. https://doi.org/10.1124/JPET.111.180398

Kojima, T., Go, M., Takano, K. I., Kurose, M., Ohkuni, T., Koizumi, J. I., Kamekura, R., Ogasawara, N., Masaki, T., Fuchimoto, J., Obata, K., Hirakawa,S., Nomura, K., Keira, T., Miyata, R., Fujii, N., Tsutsumi, H., Himi, T., & Sawada, N. (2013). Regulation of tight junctions in upper airway epithelium. *BioMed Research International*, *2013*. https://doi.org/10.1155/2013/947072

Kreisl, W. C., Liow, J. S., Kimura, N., Seneca, N., Zoghbi, S. S., Morse, C. L., Herscovitch, P., Pike, V. W., & Innis, R. B. (2010). P-glycoprotein function at the blood-brain barrier in humans can be quantified with the substrate radiotracer 11C-N-desmethyl-loperamide. *Journal of Nuclear Medicine*, *51*(4),559–566. https://doi.org/10.2967/jnumed.109.070151

Liebner, S., & Plate, K. H. (2010). Differentiation of the brain vasculature: theanswer came blowing by the Wnt. *Vascular Cell*, *2*(1), 1. https://doi.org/10.1186/2040-2384-2-1

Linville, R. M., DeStefano, J. G., Sklar, M. B., Xu, Z., Farrell, A. M., Bogorad, M. I., Chu, C., Walczak, P., Cheng, L., Mahairaki, V., Whartenby, K. A., Calabresi, P. A., & Searson, P. C. (2019). Human iPSC-derived blood-brainbarrier microvessels: validation of barrier function and endothelial cell behavior. *Biomaterials*, *190–191*, 24–37. https://doi.org/10.1016/j.biomaterials.2018.10.023

Lippmann, E. S., Azarin, S. M., Kay, J. E., Nessler, R. A., Wilson, H. K., Al- Ahmad, A., Palecek, S. P., & Shusta, E. v. (2012). Derivation of blood-brainbarrier endothelial cells from human pluripotent stem cells. *Nature Biotechnology*, *30*(8), 783–791. https://doi.org/10.1038/nbt.2247

Lisa Iorio, A., da Ros, M., Fantappiè, O., Lucchesi, M., Facchini, L., Stival, A., Becciani, S., Guidi, M., Favre, C., de Martino, M., Genitori, L., & Sardi, I. (2016). Blood-Brain Barrier and Breast Cancer Resistance Protein: A Limit tothe Therapy of CNS Tumors and Neurodegenerative Diseases. *Anti-Cancer Agents in Medicinal Chemistry*, *16*(7), 810–815. https://doi.org/10.2174/1871520616666151120121928

Liu X., van Natta K., Yeo H., Vilenski O., Weller P.E., Worboys P.D., & Monshouwer M. (2009). Unbound drug concentration in brain homogenate andcerebral spinal fluid at steady state as a surrogate for unbound concentration in brain interstitial fluid. *Drug Metabolism and Disposition: The Biological Fate of Chemicals*, *37*(4), 787–793. https://doi.org/10.1124/DMD.108.024125

Liu, W. Y., Wang, Z. bin, Zhang, L. C., Wei, X., & Li, L. (2012). Tight Junctionin Blood-Brain Barrier: An Overview of Structure, Regulation, and Regulator Substances. *CNS Neuroscience & Therapeutics*, *18*(8), 609–615. https://doi.org/10.1111/j.1755-5949.2012.00340.x

Liu, X., Tu, M., Kelly, R. S., Chen, C., & Smith, B. J. (2004). Development of a computational approach to predict blood-brain barrier permeability. *Drug Metabolism and Disposition*, *32*(1), 132–139. https://doi.org/10.1124/dmd.32.1.132

Lochhead, J. J., Yang, J., Ronaldson, P. T., & Davis, T. P. (2020). Structure, Function, and Regulation of the Blood-Brain Barrier Tight Junction in CentralNervous System Disorders. In *Frontiers in Physiology* (Vol. 11, p. 914). Frontiers Media S.A. https://doi.org/10.3389/fphys.2020.00914

Loryan, I., Fridén, M., & Hammarlund-Udenaes, M. (2013). The brain slice method for studying drug distribution in the CNS. *Fluids and Barriers of theCNS*, *10*(1), 6. https://doi.org/10.1186/2045-8118-10-6

Löscher, W., & Potschka, H. (2005). Blood-brain barrier active efflux transporters: ATP-binding cassette gene family. *NeuroRx*, *2*(1), 86–98. https://doi.org/10.1602/neurorx.2.1.86

Lucchetti, J., Fracasso, C., Balducci, C., Passoni, A., Forloni, G., Salmona, M.,& Gobbi, M. (2019). Plasma and brain concentrations of doxycycline after single and repeated doses in wild-type and APP23 mices. *Journal of Pharmacology and Experimental Therapeutics*, *368*(1), 32–40. https://doi.org/10.1124/jpet.118.252064

Luissint, A. C., Artus, C., Glacial, F., Ganeshamoorthy, K., & Couraud, P. O. (2012). Tight junctions at the blood brain barrier: Physiological architecture and disease-associated dysregulation. In *Fluids and Barriers of the CNS* (Vol.9, Issue 1, p. 23). BioMed Central. https://doi.org/10.1186/2045-8118-9-23

Lundquist, S., & Renftel, M. (2002). The use of in vitro cell culture models for mechanistic studies and as permeability screens for the blood-brain barrier in the pharmaceutical industry - Background and current status in the drug discovery process. In *Vascular Pharmacology* (Vol. 38, Issue 6, pp. 355–364).Elsevier Inc. https://doi.org/10.1016/S1537-1891(02)00203-3

Mader, S., & Brimberg, L. (2019). Aquaporin-4 Water Channel in the Brain andIts Implication for Health and Disease. *Cells*, *8*(2), 90. https://doi.org/10.3390/cells8020090

Mahringer, A., & Fricker, G. (2016). ABC transporters at the blood-brain barrier. *Expert Opinion on Drug Metabolism and Toxicology*, *12*(5), 499–508. https://doi.org/10.1517/17425255.2016.1168804

Mantle, J. L., Min, L., & Lee, K. H. (2016). *Minimum Transendothelial Electrical Resistance Thresholds for the Study of Small and Large Molecule Drug Transport in a Human in Vitro Blood−Brain Barrier Model*. https://doi.org/10.1021/acs.molpharmaceut.6b00818

Mastorakos, P., & McGavern, D. (2019). The anatomy and immunology ofvasculature in the central nervous system. *Science Immunology*, *4*(37). https://doi.org/10.1126/sciimmunol.aav0492

Maurer, T. S., DeBartolo, D. B., Tess, D. A., & Scott, D. O. (2005). RELATIONSHIP BETWEEN EXPOSURE AND NONSPECIFIC BINDING OFTHIRTY-THREE CENTRAL NERVOUS SYSTEM DRUGS IN MICE. *Drug Metabolism and Disposition*, *33*(1), 175–181. https://doi.org/10.1124/DMD.104.001222

Meyer J., Rauh J., & Galla H.J. (1991). The susceptibility of cerebral endothelial cells to astroglial induction of blood-brain barrier enzymes depends

on their proliferative state. *Journal of Neurochemistry*, *57*(6), 1971–1977. https://doi.org/10.1111/J.1471-4159.1991.TB06411.X

Meyer, J., Mischeck, U., Veyhl, M., Henzel, K., & Galla, H. J. (1990). Blood-brain barrier characteristic enzymatic properties in cultured brain capillary endothelial cells. *Brain Research*, *514*(2), 305–309. https://doi.org/10.1016/0006-8993(90)91425-G

Miller, D. S. (2010). Regulation of P-glycoprotein and other ABC drug transporters at the blood-brain barrier. *Trends in Pharmacological Sciences*,*31*(6), 246–254. https://doi.org/10.1016/j.tips.2010.03.003

Morris, M. E., Rodriguez-Cruz, V., & Felmlee, M. A. (2017). SLC and ABC Transporters: Expression, Localization, and Species Differences at the Blood- Brain and the Blood-Cerebrospinal Fluid Barriers. *AAPS Journal*, *19*(5), 1317–1331. https://doi.org/10.1208/s12248-017-0110-8

Nielsen, S. S. E., Siupka, P., Georgian, A., Preston, J. E., Tóth, A. E., Yusof, S. R., Abbott, N. J., & Nielsen, M. S. (2017). Improved method for the establishment of an in Vitro Blood-Brain barrier model based on porcine brainendothelial cells. *Journal of Visualized Experiments*, *2017*(127). https://doi.org/10.3791/56277

Niven, J. E., & Chittka, L. (2016). Current Biology Evolving understanding ofnervous system evolution. *Current Biology*, *26*, 937–980. https://doi.org/10.1016/j.cub.2016.09.003

Oddo, A., Peng, B., Tong, Z., Wei, Y., Tong, W. Y., Thissen, H., & Voelcker, N. H. (2019). Advances in Microfluidic Blood–Brain Barrier (BBB) Models. In*Trends in Biotechnology* (Vol. 37, Issue 12, pp. 1295–1314). Elsevier Ltd. https://doi.org/10.1016/j.tibtech.2019.04.006

Orlidge, A., & D'Amore, P. A. (1987). Inhibition of capillary endothelial cell growth by pericytes and smooth muscle cells. *Journal of Cell Biology*, *105*(3),1455–1462. https://doi.org/10.1083/jcb.105.3.1455

Orlowski, M., Sessa, G., & Green, J. P. (1974). γ-Glutamyl transpeptidase inbrain capillaries: Possible site of a blood-brain barrier for amino acids. *Science*, *184*(4132), 66–68. https://doi.org/10.1126/science.184.4132.66

Palumbo, P., Picchini, U., Beck, B., van Gelder, J., Delbar, N., & DeGaetano, A. (2008). A general approach to the apparent permeability index. *Journal of Pharmacokinetics and Pharmacodynamics*, *35*(2), 235–248. https://doi.org/10.1007/s10928-008-9086-4

Pardridge, W. M. (1983). Brain metabolism: a perspective from the blood-brainbarrier Biologic Drug Development for the CNS View project. *Physiol Rev.*, *63*(4), 1481–1535. https://doi.org/doi: 10.1152/physrev.1983.63.4.1481

Pardridge, W. M. (2005). The blood-brain barrier: Bottleneck in brain drug development. *NeuroRx*, *2*(1), 3–14. https://doi.org/10.1602/neurorx.2.1.3

Pardridge, W. M. (2007). Blood-brain barrier delivery of protein and non-viralgene therapeutics with molecular Trojan horses. *Journal of Controlled Release*, *122*(3), 345–348. https://doi.org/10.1016/j.jconrel.2007.04.001

Pardridge, W. M. (2012). Drug transport across the blood-brain barrier. *Journalof Cerebral Blood Flow and Metabolism*, *32*(11), 1959–1972. https://doi.org/10.1038/jcbfm.2012.126

Partyka, P. P., Godsey, G. A., Galie, J. R., Kosciuk, M. C., Acharya, N. K., Nagele, R. G., & Galie, P. A. (2017). Mechanical stress regulates transport in acompliant 3D model of the blood-brain barrier. *Biomaterials*, *115*, 30–39. https://doi.org/10.1016/j.biomaterials.2016.11.012

Patabendige, A., Skinner, R. A., & Abbott, N. J. (2013). Establishment of a simplified in vitro porcine blood-brain barrier model with high transendothelialelectrical resistance. *Brain Research*, *1521*, 1–15. https://doi.org/10.1016/j.brainres.2012.06.057

Perrière, N., Demeuse, PH., Garcia, E., Regina, A., Debray, M., Andreux, J.- P., Couvreur, P., Scherrmann, J.-M., Temsamani, J., Couraud, P.-O., Deli, M.A., & Roux, F. (2005). Puromycin-based purification of rat brain capillary endothelial cell cultures. Effect on the expression of blood-brain barrier- specific properties. *Journal of Neurochemistry*, *93*(2), 279–289. https://doi.org/10.1111/j.1471-4159.2004.03020.x

Phan, D. T. T., Bender, R. H. F., Andrejecsk, J. W., Sobrino, A., Hachey, S. J., George, S. C., & Hughes, C. C. W. (2017). Blood–brain barrier-on-a-chip: Microphysiological systems that capture the complexity of the blood–central nervous system interface. *Experimental Biology and Medicine*, *242*(17), 1669–1678. https://doi.org/10.1177/1535370217694100

Prabhakarpandian, B., Shen, M. C., Nichols, J. B., Mills, I. R., Sidoryk-Wegrzynowicz, M., Aschner, M., & Pant, K. (2013). SyM-BBB: A microfluidicblood brain barrier model. *Lab on a Chip*, *13*(6), 1093–1101. https://doi.org/10.1039/c2lc41208j

Public Health England. (2018). *Deaths associated with neurological conditionsin England 2001 to 2014: Data analysis report*. https://www.gov.uk/government/publications/deaths-associated-with- neurological-conditions

Puech, C., Hodin, S., Forest, V., He, Z., Mismetti, P., Delavenne, X., & Perek, N. (2018). Assessment of HBEC-5i endothelial cell line cultivated in astrocyte conditioned medium as a human blood-brain barrier model for ABC drug transport studies. *International Journal of Pharmaceutics*, *551*(1–2), 281–289. https://doi.org/10.1016/j.ijpharm.2018.09.040

Pulgar, V. M. (2019). Transcytosis to cross the blood brain barrier, new advancements, and challenges. *Frontiers in Neuroscience*, *13*(JAN). https://doi.org/10.3389/fnins.2018.01019

Rahman, N. A., Rasil, A. N. A. H. M., Meyding Lamade, U., Craemer, E. M., Diah, S., Tuah, A. A., & Muharram, S. H. (2016). Immortalized endothelial celllines for in vitro blood-brain barrier models: A systematic review. *Brain Research*, *1642*, 532–545. https://doi.org/10.1016/j.brainres.2016.04.024

Rauch, C. (2011). The "Multi" of Drug Resistance Explained by OscillatingDrug Transporters, Drug-Membrane Physical Interactions and Spatial Dimensionality. *Cell Biochemistry and Biophysics*, *61*(1), 103–113. https://doi.org/10.1007/s12013-011-9166-8

Ribatti, D., Nico, B., Crivellato, E., & Artico, M. (2006). Development of the blood-brain barrier: A historical point of view. *Anatomical Record - Part B NewAnatomist*, *289*(1), 3–8. https://doi.org/10.1002/ar.b.20087

Rochfort, K. D., & Cummins, P. M. (2019). In Vitro Cell Models of the Human Blood-Brain Barrier: Demonstrating the Beneficial Influence of Shear Stress onBrain Microvascular Endothelial Cell Phenotype. *Neuromethods*, *142*, 71–98. https://doi.org/10.1007/978-1-4939-8946-1_5

Römermann, K., Fedrowitz, M., Hampel, P., Kaczmarek, E., Töllner, K., Erker,T., Sweet, D. H., & Löscher, W. (2017). Multiple blood-brain barrier transport mechanisms limit bumetanide accumulation, and therapeutic potential, in the mammalian brain. *Neuropharmacology*, *117*, 182–194. https://doi.org/10.1016/j.neuropharm.2017.02.006

Rosas-Hernandez, H., Cuevas, E., Lantz, S. M., Paule, M. G., & Ali, S. F. (2018). Isolation and culture of brain microvascular endothelial cells for in vitroblood-brain barrier studies. *Methods in Molecular Biology*, *1727*, 315–331. https://doi.org/10.1007/978-1-4939-7571-6_23

Sabbagh, M. F., & Nathans, J. (2020). A genome-wide view of the dedifferentiation of central nervous system endothelial cells in culture. *Elife*,*9*(e51276). https://doi.org/10.7554/eLife.51276

Santaguida, S., Janigro, D., Hossain, M., Oby, E., Rapp, E., & Cucullo, L. (2006). Side by side comparison between dynamic versus static models of blood-brain barrier in vitro: A permeability study. *Brain Research*, *1109*(1), 1–13. https://doi.org/10.1016/j.brainres.2006.06.027

Schildge, S., Bohrer, C., Beck, K., & Schachtrup, C. (2013). Isolation and culture of mouse cortical astrocytes. *Journal of Visualized Experiments : JoVE*,*71*, 50079. https://doi.org/10.3791/50079

Sharif, Y., Jumah, F., Coplan, L., Krosser, A., Sharif, K., & Tubbs, R. S. (2018). Blood brain barrier: A review of its anatomy and physiology in health

and disease. *Clinical Anatomy*, *31*(6), 812–823.https://doi.org/10.1002/ca.23083

Sivandzade, F., & Cucullo, L. (2018). In-vitro blood–brain barrier modeling: A review of modern and fast-advancing technologies. *Journal of Cerebral BloodFlow and Metabolism*, *38*(10), 1667–1681. https://doi.org/10.1177/0271678X18788769

Srinivasan, B., Kolli, A. R., Esch, M. B., Abaci, H. E., Shuler, M. L., & Hickman, J. J. (2015). TEER Measurement Techniques for In Vitro Barrier ModelSystems. *Journal of Laboratory Automation*, *20*(2), 107–126. https://doi.org/10.1177/2211068214561025

Stamatovic, S. M., Johnson, A. M., Keep, R. F., & Andjelkovic, A. v. (2016).Junctional proteins of the blood-brain barrier: new insights into function anddysfunction. *Tissue Barriers*, *4*(1). https://doi.org/10.1080/21688370.2016.1154641

Stewart, P. A., & Wiley, M. J. (1981). Developing nervous tissue induces formation of blood-brain barrier characteristics in invading endothelial cells: Astudy using quail-chick transplantation chimeras. *Developmental Biology*, *84*(1), 183–192. https://doi.org/10.1016/0012-1606(81)90382-1

Stone, N. L., England, T. J., & O'Sullivan, S. E. (2019). A novel transwell bloodbrain barrier model using primary human cells. *Frontiers in Cellular Neuroscience*, *13*, 230. https://doi.org/10.3389/fncel.2019.00230

Summerfield, S. G., Read, K., Begley, D. J., Obradovic, T., Hidalgo, I. J., Coggon, S., Lewis, A. v., Porter, R. A., & Jeffrey, P. (2007). Central Nervous System Drug Disposition: The Relationship between in Situ Brain Permeabilityand Brain Free Fraction. *Journal of Pharmacology and Experimental Therapeutics*, *322*(1), 205–213. https://doi.org/10.1124/JPET.107.121525

Syvänen, S., Lindhe, Ö., Palner, M., Kornum, B. R., Rahman, O., Långström, B., Knudsen, G. M., & Hammarlund-Udenaes, M. (2009). Species Differencesin Blood-Brain Barrier Transport of Three Positron Emission Tomography Radioligands with Emphasis on P-Glycoprotein Transport. *Drug Metabolism and Disposition*, *37*(3), 635–643. https://doi.org/10.1124/DMD.108.024745

Terrell-Hall, T. B., Ammer, A. G., Griffith, J. I. G., & Lockman, P. R. (2017). Permeability across a novel microfluidic blood-tumor barrier model. *Fluids and Barriers of the CNS*, *14*(1). https://doi.org/10.1186/s12987-017-0050-9

The Neurological Alliance. (2019). *Neuro Numbers 2019: A Report by The Neurological Alliance*. https://www.neural.org.uk/assets/pdfs/neuro-numbers-2019.pdf

Thomsen, L. B., Burkhart, A., & Moos, T. (2015). A triple culture model of theblood-brain barrier using porcine brain endothelial cells, astrocytes and pericytes. *PLoS ONE*, *10*(8). https://doi.org/10.1371/journal.pone.0134765

Tietz, S., & Engelhardt, B. (2015). Brain barriers: Crosstalk between complextight junctions and adherens junctions. *Journal of Cell Biology*, *209*(4), 493– 506. https://doi.org/10.1083/jcb.201412147

Toth, A. E., Siupka, P., Thomas, T. J., Venø, S. T., Thomsen, L. B., Moos, T., Lohi, H. T., Madsen, P., Lykke-Hartmann, K., & Nielsen, M. S. (2018). The Endo-Lysosomal System of Brain Endothelial Cells Is Influenced by AstrocytesIn Vitro. *Molecular Neurobiology*, *55*(11), 8522–8537. https://doi.org/10.1007/s12035-018-0988-x

Tran T.T., Mittal A., Gales T., Maleeff B., Aldinger T., Polli J.W., Ayrton A., Ellens H., & Bentz J. (2004). Exact kinetic analysis of passive transport acrossa polarized confluent MDCK cell monolayer modeled as a single barrier. *Journal of Pharmaceutical Sciences*, *93*(8), 2108–2123. https://doi.org/10.1002/JPS.20105

Tsuji, A. (2005). Small molecular drug transfer across the blood-brain barriervia carrier-mediated transport systems. *NeuroRx*, *2*(1), 54–62. https://doi.org/10.1602/neurorx.2.1.54

Tunblad, K., Ederoth, P., Gärdenfors, A., Hammarlund-Udenaes, M., & Nordström, C.-H. (2004). Altered brain exposure of morphine in experimentalmeningitis studied with microdialysis. *Acta Anaesthesiologica Scandinavica*, *48*(3), 294–301. https://doi.org/10.1111/J.0001-5172.2003.0311.X

Uchida, Y., Ohtsuki, S., Kamiie, J., & Terasaki, T. (2011). Blood-Brain Barrier (BBB) Pharmacoproteomics: Reconstruction of In Vivo Brain Distribution of 11P-Glycoprotein Substrates Based on the BBB Transporter Protein Concentration, In Vitro Intrinsic Transport Activity, and Unbound Fraction in Plasma and Brain in Mice. *Journal of Pharmacology and Experimental Therapeutics*, *339*(2), 579–588. https://doi.org/10.1124/JPET.111.184200

Urich, E., Lazic, S. E., Molnos, J., Wells, I., & Freskgård, P. O. (2012). Transcriptional profiling of human brain endothelial cells reveals key propertiescrucial for predictive in vitro blood-brain barrier models. *PLoS ONE*, *7*(5). https://doi.org/10.1371/journal.pone.0038149

van der Helm, M. W., van der Meer, A. D., Eijkel, J. C. T., van den Berg, A., & Segerink, L. I. (2016). Microfluidic organ-on-chip technology for blood-brain barrier research. *Tissue Barriers*, *4*(1). https://doi.org/10.1080/21688370.2016.1142493

van Itallie, C. M., Lidman, K. F., Tietgens, A. J., & Anderson, J. M. (2019). Newly synthesized claudins but not occludin are added to the basal side of thetight junction. *Molecular Biology of the Cell*, *30*(12), 1406–1424. https://doi.org/10.1091/mbc.E19-01-0008

Veszelka, S., Tóth, A., Walter, F. R., Tóth, A. E., Gróf, I., Mészáros, M., Bocsik, A., Hellinger, É., Vastag, M., Rákhely, G., Deli, M. A., Guizzetti, M., & Rosas-Hernandez, H. (2018). Comparison of a Rat Primary Cell-Based Blood-

Brain Barrier Model with Epithelial and Brain Endothelial Cell Lines: GeneExpression and Drug Transport. *Front Mol Neurosci.*, *11*(166). https://doi.org/10.3389/fnmol.2018.00166

Wang X., Huang S., Jiang Y., Liu Y., Song T., Li D., & Yang L. (2018). Reactive astrocytes increase the expression of P-gp and Mrp1 via TNF-α andNF-κB signaling. *Molecular Medicine Reports*, *17*(1), 1198–1204. https://doi.org/10.3892/MMR.2017.7939

Wang X., Xu B., Xiang M., Yang X., Liu Y., Liu X., & Shen Y. (2020). Advanceson fluid shear stress regulating blood-brain barrier. *Microvascular Research*, *128*. https://doi.org/10.1016/j.mvr.2019.103930

Wang, W., Dentler, W. L., & Borchardt, R. T. (2001). VEGF increases BMEC monolayer permeability by affecting occludin expression and tight junction assembly. *American Journal of Physiology - Heart and Circulatory Physiology*,*280*(1 49-1). https://doi.org/10.1152/ajpheart.2001.280.1.h434

Wang, Y. I., Abaci, H. E., & Shuler, M. L. (2017). Microfluidic blood–brainbarrier model provides in vivo-like barrier properties for drug permeabilityscreening. *Biotechnology and Bioengineering*, *114*(1), 184–194. https://doi.org/10.1002/bit.26045

Wang, Y., Lee, D., Zhang, L., Jeon, H., Mendoza-Elias, J. E., Harvat, T. A., Hassan, S. Z., Zhou, A., Eddington, D. T., & Oberholzer, J. (2012). Systematicprevention of bubble formation and accumulation for long-term culture of pancreatic islet cells in microfluidic device. *Biomedical Microdevices*, *14*(2), 419–426. https://doi.org/10.1007/s10544-011-9618-3

Wang, Z., Yang, H., Wu, Z., Wang, T., Li, W., Tang, Y., & Liu, G. (2018). In Silico Prediction of Blood–Brain Barrier Permeability of Compounds by Machine Learning and Resampling Methods. *ChemMedChem*, *13*(20), 2189–2201. https://doi.org/10.1002/cmdc.201800533

Warren, M. S., Zerangue, N., Woodford, K., Roberts, L. M., Tate, E. H., Feng,B., Li, C., Feuerstein, T. J., Gibbs, J., Smith, B., de Morais, S. M., Dower, W. J., & Koller, K. J. (2009). Comparative gene expression profiles of ABC transporters in brain microvessel endothelial cells and brain in five species including human. *Pharmacological Research*, *59*(6), 404–413. https://doi.org/10.1016/j.phrs.2009.02.007

Weidman, E. K., Foley, C. P., Kallas, O., Dyke, J. P., Gupta, A., Giambrone, A.E., Ivanidze, J., Baradaran, H., Ballon, D. J., & Sanelli, P. C. (2016). Evaluating permeability surface-area product as a measure of blood-brain barrier permeability in a murine model. *American Journal of Neuroradiology*,*37*(7), 1267–1274. https://doi.org/10.3174/ajnr.A4712

Wevers, N. R., Kasi, D. G., Gray, T., Wilschut, K. J., Smith, B., van Vught, R., Shimizu, F., Sano, Y., Kanda, T., Marsh, G., Trietsch, S. J., Vulto, P., Lanz, H. L., & Obermeier, B. (2018). A perfused human blood-brain barrier on-a-chip for

high-throughput assessment of barrier function and antibody transport Fluidsand Barriers of the CNS. *Fluids Barriers CNS*, *15*, 23. https://doi.org/10.1186/s12987-018-0108-3

Wilhelm, I., & Krizbai, I. A. (2014). In vitro models of the blood-brain barrier forthe study of drug delivery to the brain. In *Molecular Pharmaceutics* (Vol. 11, Issue 7, pp. 1949–1963). American Chemical Society. https://doi.org/10.1021/mp500046f

Wilhelm, I., Fazakas, C., & Krizbai, I. A. (2011). In vitro models of the blood-brain barrier. *Acta Neurobiologiae Experimentalis*, *71*(1), 113–128.

Wolburg, H. & Lippoldt, A. (2002). Tight junctions of the blood–brain barrier: development, composition and regulation. *Vasc. Pharmacol.* **38**, 323–337

Wolf, S., & Gassen, H. G. (1997). γ-glutamyl transpeptidase, A blood-brainbarrier associated membrane protein: Splitting peptides to transport aminoacids. *Advances in Experimental Medicine and Biology*, *421*, 37–45. https://doi.org/10.1007/978-1-4757-9613-1_6

Workman, M. J., & Svendsen, C. N. (2020). Recent advances in human iPSC-derived models of the blood-brain barrier. *Fluids Barriers CNS*, *17*(30). https://doi.org/10.1186/s12987-020-00191-7

Yamashita, S., Furubayashi, T., Kataoka, M., Sakane, T., Sezaki, H., & Tokuda, H. (2000). Optimized conditions for prediction of intestinal drug permeability using Caco-2 cells. *European Journal of Pharmaceutical Sciences*, *10*(3), 195–204. https://doi.org/10.1016/S0928-0987(00)00076-2

Yao, Y., Chen, Z.L., Norris, E.H., Strickland, S. (2014). Astrocytic laminin regulates pericyte differentiation and maintains blood brain barrier integrity. *Nat Commun*, 5:3413. doi: 10.1038/ncomms4413

Yu, F., Nivasini, Kumar, S., Foo, L. C., Sum, |, Ng, H., Hunziker, | Walter, & Choudhury, D. (2020). A pump-free tricellular blood-brain barrier on-a-chip model to understand barrier property and evaluate drug response. *Biotechnology and Bioengineering*, *117*, 1127–1136.https://doi.org/10.1002/bit.27260
Zhang, W. (2010). ABC Transporters and Drug Efflux at the Blood-BrainBarrier. *Reviews in the Neurosciences*, *21*, 29–53. https://doi.org/10.1515/REVNEURO.2010.21.1.29

Zhang, Y. Y., Liu, H., Summerfield, S. G., Luscombe, C. N., & Sahi, J. (2016). Integrating in Silico and in Vitro Approaches to Predict Drug Accessibility to the Central Nervous System. *Molecular Pharmaceutics*, *13*(5), 1540–1550. https://doi.org/10.1021/acs.molpharmaceut.6b00031

Zhang, Y., Li, C. S. W., Ye, Y., Johnson, K., Poe, J., Johnson, S., Bobrowski,W., Garrido, R., & Madhu, C. (2006). Porcine brain microvessel endothelial cells as an in vitro model to predict in vivo blood-brain barrier permeability. *Drug Metabolism and Disposition*, *34*(11), 1935–1943. https://doi.org/10.1124/DMD.105.006437

Zobel, K., Hansen, U., & Galla, H. J. (2016). Blood-brain barrier properties invitro depend on composition and assembly of endogenous extracellular

matrices. *Cell and Tissue Research*, *365*(2), 233–245. https://doi.org/10.1007/s00441-016-2397-7

Zonta, M., Angulo, M. C., Gobbo, S., Rosengarten, B., Hossmann, K. A., Pozzan, T., & Carmignoto, G. (2003). Neuron-to-astrocyte signaling is centralto the dynamic control of brain microcirculation. *Nature Neuroscience*, *6*(1), 43–50. https://doi.org/10.1038/nn980

Appendix 1

BLAST gene sequence comparison between humans and pigs for key blood-brain barrier transporters, p-glycoprotein (MDR1), MRP1, and BCRP.

Pig vs human P-glycoprotein (ABCB1)
86% SEQUENCE IDENTITY

```
   1 MENSERAEEMQDSFQRNVKLQEHLLKVRKQVVGPIEIFRFADRLDITLMILGLLASLLNG     60
   1 ||||||||||||   |||    |   | ||  || ||||||||| ||||||||| |||| ||     60
   1 MENSERAEEMQENYQRNGTAEEQP-KLRKEAVGSIEIFRFADGLDITLMILGILASLVNG     60

  61 ACLPVMSLILGEMSDNLIGGCLVKTNTTNFRNCTQSQEKINEDVIVLTLYYVAIGISALV    120
  61 |||| | | ||||||||| |||| |||||  |||||||| |||   |||||| ||  ||    120
  61 ACLPLMPLVLGEMSDNLISGCLVQTNTTNYQNCTQSQEKLNEDMTLLTLYYVGIGVAALI    120

 121 FGYMQISFWVMTAARQTKRIRKQFFHSILAQDISWFDSCGIGELNTRMTDDINKINDGIG    180
 121 ||| ||| |  ||||||||||||||| ||||| ||||| ||||||||||| || ||||    180
 121 FGYIQISLWIITAARQTKRIRKQFFHSVLAQDIGWFDSCDIGELNTRMTDDIDKISDGIG    180

 181 DKIALLFQNMSTFSIGLVIGLAKGWKLTLVTLSTSPLIIASAAMFSRIVISLSSKELNAY    240
 181 ||||||||||||||||  || |||||||||||||||| ||||  || |||| |||| ||    240
 181 DKIALLFQNMSTFSIGLAVGLVKGWKLTLVTLSTSPLIMASAAACSRMVISLTSKELSAY    240

 241 SKAGAVAEEVLSSIRTVIAFGAQEKEIQRYTQNLKDAKDVGIKKAIASKLSLGAVYFFMN    300
 241 |||||||||||||||||||| ||||| |||||||||||| |||  |||| ||||||||||    300
 241 SKAGAVAEEVLSSIRTVIAFRAQEKELQRYTQNLKDAKDFGIKRTIASKVSLGAVYFFMN    300

 301 GTYGLAFWYGTFLILSGEPDYTIGTVLAVFFSVIHSSYCIGAAAPNFESFAIARGAAFNI    360
 301 |||||||||||| ||| ||| |||||||||||||||||||||||| | || ||||||||| |    360
 301 GTYGLAFWYGTSLILNGEPGYTIGTVLAVFFSVIHSSYCIGAAVPHFETFAIARGAAFHI    360

 361 FHIIDKKPTIDNFSTTGCKLECIEGTVEFKNVSFSYPSRPSVKILKGLSLKIKSGETVAL    420
 361 |  ||||| |||||| | | | |||||||||||| |||||| |||||| | |||||||||    420
 361 FQVIDKKPSIDNFSTAGYKPESIEGTVEFKNVSFNYPSRPSIKILKGLNLRIKSGETVAL    420

 421 VGPSGSGKSTAVQLLQRLYDPDDGFITVDGKDIRTLNVQHYREHFGVVSQEPVLFGTTIN    480
 421 ||  |||||| ||||||||||||||| ||  ||| ||| ||| | |||||||||||||    480
 421 VGLNGSGKSTVVQLLQRLYDPDDGFIMVDENDIRALNVRHYRDHIGVVSQEPVLFGTTIS    480

 481 NNIKYGRDSVTDEDIENAAKEANAYDFIMEFPKKFNTLVGEKGAQMSGGQKQRIAIARAL    540
 481 |||||||| ||||  | || |||||||||||| |||||||||||||||||||||||||||    540
 481 NNIKYGRDDVTDEEMERAAREANAYDFIMEFPNKFNTLVGEKGAQMSGGQKQRIAIARAL    540

 541 IRNPKILILDEATSALDTESESVVQAALEKASKGRTTIVIAHRLSTIRSADMIVTLKDGM    600
 541  |||||||||||||||| || | ||||||||||||||| |||||||||| ||||||||    600
 541 VRNPKILILDEATSALDSESKSAVQAALEKASKGRTTIVVAHRLSTIRSADLIVTLKDGM    600

 601 VVEKGTHAELMAKQGPYYSLAISQDIKKADEQMESMAYSTEKNTSSTPLCSMNSINPD-T    660
 601   ||| ||||||| | ||||  |||||||||||||| ||||  | | || |  ||  |     660
 601 LAEKGAHAELMAKRGLYYSLVMSQDIKKADEQMESMTYSTERKTNSLPLHSVKSIKSDFI    660

 661 DKSEDSIQYKKTSLPEVSLLKIFKLNKSEWPSVVLGTLASVLNGSVHPVFSIIFAKIVTM    720
 661 || | | | |  |||||||||| |||| ||| |||||||||||| |||||||||||  ||    720
 661 DKAEESTQSKEISLPEVSLLKILKLNKPEWPFVVLGTLASVLNGTVHPVFSIIFAKIITM    720

 721 FENDDKTTLKHDAEIYSMIFVILGIICFVSYFIQGLFYGRAGEILTMRLRHLAFKAMLYQ    780
 721 | | ||||||||||||||||||||| ||||||| |||||||||||||||||||||||||||    780
 721 FGNNDKTTLKHDAEIYSMIFVILGVICFVSYFMQGLFYGRAGEILTMRLRHLAFKAMLYQ    780

 781 DISWFDEKENSTGALTTILAIDIAQIQGATGSRVGVLTQNATNMGLSVIISFIYGWEMTL    840
```

```
 781 ||  |||||||||| |||||||||||||||||| |||||||||||||||||||||||||     840
 781 DIAWFDEKENSTGGLTTILAIDIAQIQGATGSRIGVLTQNATNMGLSVIISFIYGWEMTF    840

 841 LILSIAPVLALAGMIETAAMTGFANKDKQELERAGKIATEAVENIRTIVSLTREKAFEQM    900
 841 ||||||||||  |||||||||||||||||||  |||||||| ||||||||||||||||||    900
 841 LILSIAPVLAVTGMIETAAMTGFANKDKQELKHAGKIATEALENIRTIVSLTREKAFEQM    900

 901 YEETLQTQHRNTLKKAQIIGICYAFSHAFVYFAYAAGFLFGTHLIQAGRMTPEGMFIVFT    960
 901 |||  ||||||||  |||||||  ||||||||  ||||||||  ||  ||||||||||||||    960
 901 YEEMLQTQHRNTSKKAQIIGSCYAFSHAFIYFAYAAGFRFGAYLIQAGRMTPEGMFIVFT    960

 961 AVAYGAMAIGETLVLAPEYSRAKSGAAHLFALLEKKPTIDSHSQEGTKTDIFEGNIEFRE   1020
 961 |  ||||||||||||||||  ||||||||||||||  |||  ||||  |  |  |||  ||||   1020
 961 AIAYGAMAIGETLVLAPEYSKAKSGAAHLFALLEKKPNIDSRSQEGKKPDTCEGNLEFRE   1020

1021 VSFFYPCRPDVLILRNLSLSIEKGKTVAFVGSSGCGKSTSVQLMQRFYDPVKGQVLFDGV   1080
1021 ||||||||||| |||  ||||||  ||||||||||||||||||||  ||  ||||  ||||||||   1080
1021 VSFFYPCRPDVFILRGLSLSIERGKTVAFVGSSGCGKSTSVQLLQRLYDPVQGQVLFDGV   1080

1081 DAKELNVQWLRSQIAIVSQEPVLFNCSIAENIAYGDNSRVVPLHEIKEVADAANIHSFIE   1140
1081 ||||||||||||||||  |||||||||||||||||||||||||  ||||  |  |||||||||   1140
1081 DAKELNVQWLRSQIAIVPQEPVLFNCSIAENIAYGDNSRVVPLDEIKEAANAANIHSFIE   1140

1141 GLPEKYNTQVGPKGTQLSGGQKQRLAIARALLRKPKILLLDEATSALDNESEKVVQHALD   1200
1141 ||||||||||| ||  ||||||||||||||||  ||||||||||||||||  ||||||||||   1200
1141 GLPEKYNTQVGLKGAQLSGGQKQRLAIARALLQKPKILLLDEATSALDNDSEKVVQHALD   1200

1201 KASKGRTCLMVAHRLSTIQNADLIVVLHNGKIKEQGTHQELLKNRDIYFKLVNAQSVQ     1258
1201 ||  |||||  |  ||||  |||||||||||||||||||||||||  ||||||||||||||     1258
1201 KARTGRTCLVVTHRLSAIQNADLIVVLHNGKIKEQGTHQELLRNRDIYFKLVNAQSVQ     1258
```

Pig vs human MRP1 (ABCC1)
88.9% SEQUENCE IDENTITY

```
1 MTHLNKAKTALGFLLWIVCWADLFYSFWERSLGKLLAPVFLVSPTLLGVTMLLATFLIQI     60

  1 ||  |||  |||||||||||||||||||||||  |  ||||||||||||  ||||||||||      60
  1 MTPLNKTKTALGFLLWIVCWADLFYSFWERSRGIFLAPVFLVSPTLLGITMLLATFLIQL     60

 61 ERRRGVQSSGIMLTFWLVALLCAIAILRSKIMTALKEPAPRPVQAASSKPSSLPPSPLPG    120
 61 |||  ||||||||||||||||  ||  ||||||||||||  |                      120
 61 ERRKGVQSSGIMLTFWLVALVCALAILRSKIMTALKEDAQ--------------------    120

121 QDAVVVDIFRNVTFYIYFALVLIQLVLSCFSDRSPLFSETIHDPNPCPESSASFLSRITF    180
121      ||  ||  |||  ||  |  ||||||||||||||||||||||||||||||||||||||    180
121 -----VDLFRDITFYVYFSLLLIQLVLSCFSDRSPLFSETIHDPNPCPESSASFLSRITF    180

181 WWITGLMVQGYRQPLEITDLWSLNKEDMSEQVVPVLVKNWKKECAKSRKQPVRIVYSSKD    240
181 ||||||  |  |||||||  |||||||||  ||||||||||||||||||  |||||  ||||||    240
181 WWITGLIVRGYRQPLEGSDLWSLNKEDTSEQVVPVLVKNWKKECAKTRKQPVKVVYSSKD    240

241 PAKPKGGSKVDVNEEAEALIVKSPQKERDPSLFKVLYKTFGPYFLMSFLFKALHDLMMFA    300
241 ||  ||  ||||  |||  ||||||||||  ||||||||||||||||||  |||  ||||||     300
241 PAQPKESSKVDANEEVEALIVKSPQKEWNPSLFKVLYKTFGPYFLMSFFFKAIHDLMMFS    300

301 GPEILKLLINFVNDKKAPDWQGYFFTALLFISACLQTLVLHQYFHICFVSGMRIKSAVIG    360
301 ||  ||||||  ||||  |||||||||  |  |||  ||||||||||||||||||||||  ||||    360
```

```
 301 GPQILKLLIKFVNDTKAPDWQGYFYTVLLFVTACLQTLVLHQYFHICFVSGMRIKTAVIG    360
 361 AVYRKALVITNSARKSSTVGEIVNLMSVDAQRFMDLATYINMIWSAPLQVILALYLLWLN    420
 361 ||||||||||||||||||||||||||||||||||||||||||||||||||||||||||||    420
 361 AVYRKALVITNSARKSSTVGEIVNLMSVDAQRFMDLATYINMIWSAPLQVILALYLLWLN    420
 421 LGPSVLAGVAVMIFMVPLNAMMAMKTKTYQVAHMKSKDNRIKLMNEILNGIKVLKLYAWE    480
 421 ||||||||||||  ||| || ||||||||||||||||||||||||||||||||||||||    480
 421 LGPSVLAGVAVMVLMVPVNAVMAMKTKTYQVAHMKSKDNRIKLMNEILNGIKVLKLYAWE    480
 481 LAFKEKVLAIRQEELKVLKKSAYLAAVGTFTWVCTPFLVALCTFAVYVTIDKNNILDAQK    540
 481 |||| |||||||||||||||||| |||||||||||||||||||||||| |||||||      540
 481 LAFKDKVLAIRQEELKVLKKSAYLSAVGTFTWVCTPFLVALCTFAVYVTIDENNILDAQT    540
 541 AFVSLALFNILRFPLNILPMVISSIVQASVSLKRLRIFLSHEELEPDSIQRLPIKDVGTT    600
 541 |||||||||||||||||||||||||||||||||||||||||||||||| | | || | |    600
 541 AFVSLALFNILRFPLNILPMVISSIVQASVSLKRLRIFLSHEELEPDSIERRPVKDGGGT    600
 601 NSITVKNATFSWARSDPPTLHGITFSIPEGSLVAVVGQVGCGKSSLLSALLAEMDKVEGH    660
 601 ||||| |||| ||||||||| ||||||||| |||||||||||||||||||||||||||||    660
 601 NSITVRNATFTWARSDPPTLNGITFSIPEGALVAVVGQVGCGKSSLLSALLAEMDKVEGH    660
 661 VAIKGSVAYVPQQAWIQNVSLRENILFGRQLQERYYKAVIEACALLPDLEILPSGDRTEI    720
 661 |||||||||||||||||| |||||||| || | ||  || ||||||||||||||||||    720
 661 VAIKGSVAYVPQQAWIQNDSLRENILFGCQLEEPYYRSVIQACALLPDLEILPSGDRTEI    720
 721 GEKGVNLSGGQKQRVSLARAVYCNSDIYLFDDPLSAVDAHVGKHIFENVVGPKGMLKNKT    780
 721 |||||||||||||||||||||| | |||||||||||||||||||||| ||||||||||    780
 721 GEKGVNLSGGQKQRVSLARAVYSNADIYLFDDPLSAVDAHVGKHIFENVIGPKGMLKNKT    780
 781 RLLVTHGLSYLPQVDVIIVMSGGKISEMGSYQELLARDGAFAEFLRTYASAEQEQGEPED    840
 781 | ||||  |||||||||||||||||||||||||||||||||||||||||| ||||   |    840
 781 RILVTHSMSYLPQVDVIIVMSGGKISEMGSYQELLARDGAFAEFLRTYASTEQEQDAEEN    840
 841 GLGGISSPGKEAKQMENGVLVTEAAGKHLQRQFSSSSSYSGDVGRHHTSTAELQKPGAQA    900
 841 |  | | |||||||||||| |||  ||| |||| |||||||||  ||| |||||||  |     900
 841 GVTGVSGPGKEAKQMENGMLVTDSAGKQLQRQLSSSSSYSGDISRHHNSTAELQKAEAKK    900
 901 EDTWKLMEADKAQTGQVKLSVYWDYMKAIGLFISFLSIFLFLCNHVAALVSNYWLSLWTD    960
 901 | |||||||||||||||||||||||||||||||||||||||||| |||| || ||||||||||    960
 901 EETWKLMEADKAQTGQVKLSVYWDYMKAIGLFISFLSIFLFMCNHVSALASNYWLSLWTD    960
 961 DPIVNGTQEHTKVRLSVYGALGISQGVTVFAYSMAVSIGGIFASRRLHLDLLHNVLRSPM   1020
 961 |||||||||||||||||||||||||  || |||||||||| ||| || ||||  |||||   1020
 961 DPIVNGTQEHTKVRLSVYGALGISQGIAVFGYSMAVSIGGILASRCLHVDLLHSILRSPM   1020
1021 SFFERTPSGNLVNRFSKELDTVDSMIPQVIKMFMGSLFNVVGACIIILLATPVAAVIIPP   1080
1021 |||||||||||||||||||||||||| |||||||||||| |||| |||||| || ||||   1080
1021 SFFERTPSGNLVNRFSKELDTVDSMIPEVIKMFMGSLFNVIGACIVILLATPIAAIIIPP   1080
```

```
1081 LGLIYFFVQRFYVASSRQLKRLESVSRSPVYSHFNETLLGVSVIRAFEEQERFIRQSDLK   1140
1081 ||||||||||||||||||||||||||||||||||||||||||||||||||||||| |||||   1140
1081 LGLIYFFVQRFYVASSRQLKRLESVSRSPVYSHFNETLLGVSVIRAFEEQERFIHQSDLK   1140
1141 VDENQKAYYPSIVANRWLAVRLEFVGNCIVLFAALFAVISRHNLSAGLVGLSVSYSLQIT   1200
1141 ||||||||||||||||||||||| |||||||||||||||| |||||||||||||| |   1200
1141 VDENQKAYYPSIVANRWLAVRLECVGNCIVLFAALFAVISRHSLSAGLVGLSVSYSLQVT   1200
1201 AYLNWLVRMSSEMETNIVAVERLKEYSDTEKEAPWRIPEVAPPSTWPQVGRVEFRDYGLR   1260
1201  |||||||||||||||||||||||| ||||||| | | |||| |||||||||| | ||   1260
1201 TYLNWLVRMSSEMETNIVAVERLKEYSETEKEAPWQIQETAPPSSWPQVGRVEFRNYCLR   1260
1261 YRDDLDLVLKHINVTIDGGEKVGIVGRTGAGKSSLTLGLFRINESAEGEIVIDDVNIAQI   1320
1261 || ||| || |||||| |||||||||||||||||||||||||||||| ||  ||| |   1320
1261 YREDLDFVLRHINVTINGGEKVGIVGRTGAGKSSLTLGLFRINESAEGEIIIDGINIAKI   1320
1321 GLHDLRFKITIIPQDPVLFSGSLRMNLDPFSQYSEEEVWTSLELAHLKGFVSALPDKLNH   1380
1321 |||||||||||||||||||||||||||||||| |||||||||||| ||||||||| |   1380
1321 GLHDLRFKITIIPQDPVLFSGSLRMNLDPFSQYSDEEVWTSLELAHLKDFVSALPDKLDH   1380
1381 ECAEGGENLSVGQRQLVCLARALLRKTKILVLDEATAAVDLETDDLIQSTIRTQFHDCTV   1440
1381 |||||||||||||||||||||||||||||||||||||||||||||||||||||| ||||   1440
1381 ECAEGGENLSVGQRQLVCLARALLRKTKILVLDEATAAVDLETDDLIQSTIRTQFEDCTV   1440
1441 LTIAHRLNTIMDYTRVIVLDKGEIREHGSPSELLQQRGLFYGMAKDAGLV             1490
1441 ||||||||||||||||||||||| | | || ||||||||| ||||||||             1490
1441 LTIAHRLNTIMDYTRVIVLDKGEIQEYGAPSDLLQQRGLFYSMAKDAGLV             1490
```

Pig vs human BCRP (ABCG2)
84.5% SEQUENCE IDENTITY

```
1 MSSNSYQVSIPMSKRNTNGLPGSSSNELKTSAGGAVLSFHDICYRVKVKSGFLFCRKTVE     60
    1 |||    | || |  |||| |   || ||    ||||||| |||||| ||||| ||| ||     60
    1 MSSSNVEVFIPVSQGNTNGFPATASNDLKAFTEGAVLSFHNICYRVKLKSGFLPCRKPVE     60
   61 KEILTNINGIMKPGLNAILGPTGGGKSSLLDVLAARKDPHGLSGDVLINGAPRPANFKCN    120
   61 |||| |||||||||||||||||||||||||||||||| ||||||||||||||||||||    120
   61 KEILSNINGIMKPGLNAILGPTGGGKSSLLDVLAARKDPSGLSGDVLINGAPRPANFKCN    120
  121 SGYVVQDDVVMGTLTVRENLQFSAALRLPTTMTNHEKNERINMVIQELGLDKVADSKVGT    180
  121 ||||||||||||||||||||||||||||| |||||||||||| ||||||||||||||||    180
  121 SGYVVQDDVVMGTLTVRENLQFSAALRLATTMTNHEKNERINRVIQELGLDKVADSKVGT    180
  181 QFIRGVSGGERKRTSIAMELITDPSILFLDEPTTGLDSSTANAVLLLLKRMSKQGRTIIF    240
  181 ||||||||||||||| |||||||||||||||||||||||||||||||||||||||||||    240
  181 QFIRGVSGGERKRTSIGMELITDPSILFLDEPTTGLDSSTANAVLLLLKRMSKQGRTIIF    240
  241 SIHQPRYSIFKLFDSLTLLASGRLMFHGPAREALGYFASIGYNCEPYNNPADFFLDVING    300
```

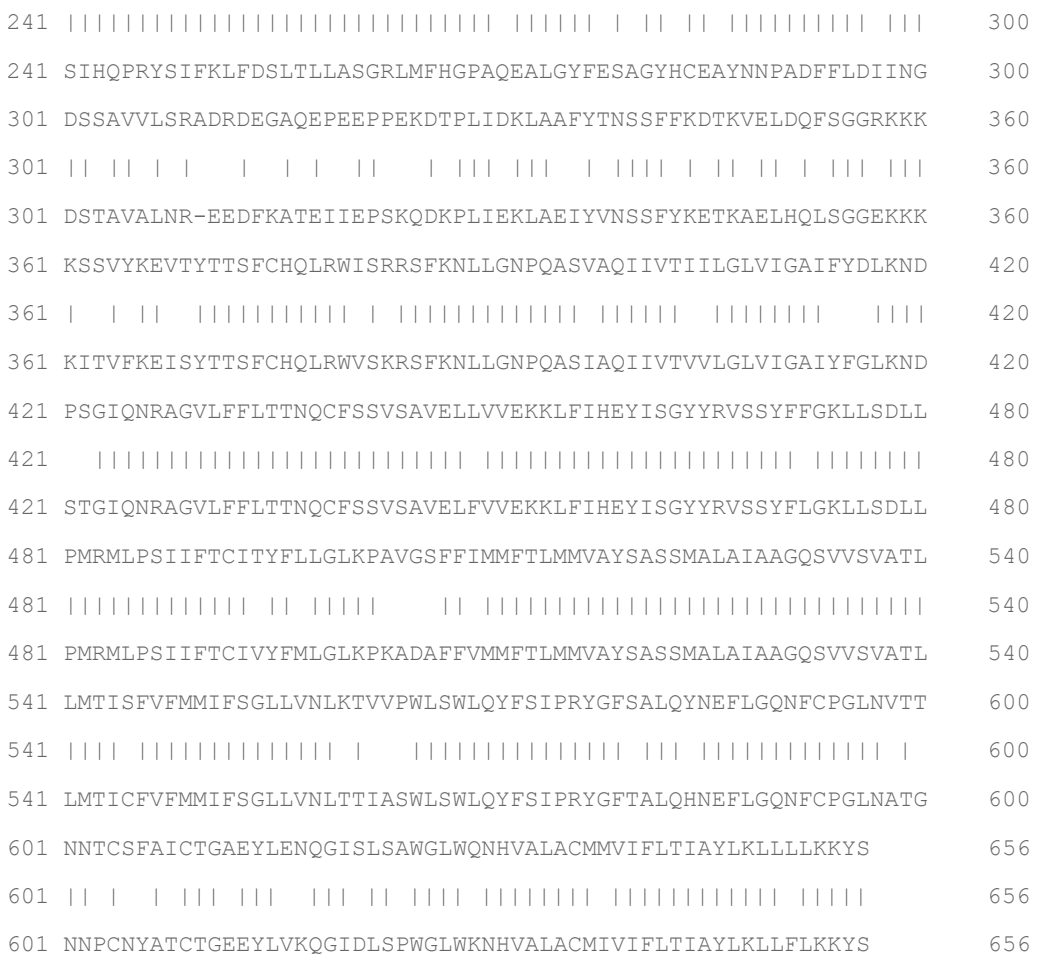

Appendix 2

A database of blood-brain barrier drug permeability values, in vivo and in vitro, across species was created for comparison to in vitro porcine brain endothelial cell drug transport studies. Reference key for the database is shown in Table A2.1.

Table A2.1 – Reference Key for Database

Database Number	Reference
1	Liu et al., 2009
2	Fridén et al., 2009
3	Syvanen et al., 2009
4	Bentham, 2010
5	Liu et al., 2003
6	Kodiara et al. 2011
7	Zhang et al. 2006
8	Tunblad et al., 2004
9	Coclough et al., 2016
10	Christensen et al., 2001
11	Di Salle et al., 1974
12	Kalvass et al., 2007
13	Loryan et al., 2013
14	Summerfield et al., 2007
15	Uchida et al., 2017
16	Hu et al., 2017
17	Maurer et al., 2005

Drug	CNS Drug?	LogP	MW	Transporter Interactions	Kp method	Species	Fu,brain	Fu,plasma	Kbb	Vu,brain	Kp,brain	Kp,uu (brain)	logKp,uu(B)	Kp,uu (CSF)	logKp,uu(C)	Reference
9-OH-Risperidone	Yes	2.32	426.5	Substrate for MDR1	Microdialysis	Rat						0.008	-2.07785632			1
Acetaminophen	Yes	0.31	151.16	Modulator of MDR1	Microdialysis	Rat						0.180	-0.74472749			2
Aciclovir		-1.56	225.2		Microdialysis	Rat						0.300	-0.52287875			2
Alfentanil	Yes	2.16	416.5	MDR1 inhibitor	Homogenate Binding	Mouse						0.230	-0.63827216			2
Alovudine		-0.3	224.22		Microdialysis	Rat						0.290	-0.537602			2
Altanserin	Yes	3.2	411.5		PET	Human					1.04					3
					PET	Pig					2.08					3
					PET	Rat					0.23					3
Alprenolol		3.1	249.35		Homogenate Binding	Rat		0.44		50	8.3	0.380	-0.4202164	0.33	-0.4814861	2
Amitriptyline	Yes	5	277.4	Substrate for MDR1	Homogenate Binding	Human								0.18	-0.7447275	2
					Homogenate Binding	Rat		0.088		310	20	0.730	-0.13667714	0.17	-0.7695511	2
Amprenavir		2.9	505.6	Substrate for MDR1		Pig	0.166	0.192	0.86458	6.65						4
						Dog	0.157	0.206	0.76214	7.11						4
						Rat	0.186	0.164	1.13415	5.66						4
					Microdialysis	Rat						0.076	-1.11918641			2
					Homogenate Binding	Mouse						0.087	-1.06048075			2
					Equilibrium Dialysis	Mouse	0.32	0.26								12
Antipyrine		0.4	188.23			Rat										5
					Microdialysis	Rat						0.708	-0.14996674			6
Apomorphine	Yes	2.3	267.32		Microdialysis	Rat						5.000	0.69897			2
					Homogenate Binding	Rat						11.000	1.04139269			2
Aricept (Donepezil Hydrochloride)	Yes		416	Uptake via OCT2	Homogenate Binding	Rat						1.200	0.07918125			2
Atenolol		0.2	266.34		Homogenate Binding	Rat		1		2.5	0.066	0.026	-1.58502665			2
					Microdialysis	Rat						0.038	-1.4202164			2
Baclofen	Yes	-1	213.66	Uptake via LAT1/2	Homogenate Binding	Human								0.17	-0.7695511	2
					Homogenate Binding	Rat		1		1.7	0.034	0.020	-1.69897			2
					Microdialysis	Rat						0.022	-1.65757732	0.027	-1.5686362	2
Baicalein	Yes	1.7	270.24	Interaction with MDR1	Microdialysis	Rat						0.023	-1.63827216			2
Benzylpenicillin		1.8	334.3	Efflux by MDR1, BCRP	Microdialysis	Rat						0.026	-1.57839607			6
Bisphenol		3.3	228.29	Decreased BCRP activity	Microdialysis	Rat						0.038	-1.4202164			2
Bupropion	Yes	3.2	239.74		Homogenate Binding	Human								2	0.30103	2
					Homogenate Binding	Rat		0.31		16	9.8	2.000	0.30103	0.49	-0.3098039	2
Buspirone	Yes	2.6	385.5	MDR1 inhibitor	Microdialysis	Rat						0.612	-0.21324858			6
					Homogenate Binding	Mouse						1.300	0.11394335			2
Caffeine	Yes	-0.1	194.4			Rat										5
					Microdialysis	Rat						0.584	-0.23358715			6
					Homogenate Binding	Mouse						0.460	-0.33724217			2
					Microdialysis	Rat						0.960	-0.01772877			2
Camptothecin		1	348.4		Microdialysis	Rat						0.270	-0.56863624			2
Carbamezapine	Yes	2.5	236.7			Dog	0.238	0.187	1.271	6.57						4
						Pig	0.182	0.211	1.159	6.32						4
					Equilibrium Dialysis	Rat	0.275	0.34	1.324	4.75	1.39	1.050	0.0211893			4
						Human		0.24								11
					Microdialysis	Rat						0.094	-1.02640023			1
					Microdialysis	Rat	0.697	0.917				0.771	-0.11294562	1.03		6
					Microdialysis	Rat						1.020	0.00860017			2
						MDCK										14
					Homogenate Binding	Rat	0.118									14
					Homogenate Binding	Mouse						0.270	-0.56863624			2
Carisopordol		1.9	260.33		Homogenate Binding	Mouse						0.340	-0.46852108			2
Cefazolin		-0.4	454.5		Microdialysis	Rat						0.060	-1.22184875			2
Cefotaxime		-1.4	455.5		Homogenate Binding	Human								0.17	-0.7695511	2
					Homogenate Binding	Rat		0.59						0.007	-2.154902	2
					Microdialysis	Rat						0.069	-1.16115091			2
Cefuroxime		-0.2	424.2		Microdialysis	Rat						0.042	-1.37675071			2
Celecoxib	Yes	3.4	381.4	MRP4 inhibitor	Homogenate Binding	Rat						0.420	-0.37675071			2
Cephalexin		0.6	347.4		Homogenate Binding	Rat						0.016	-1.79588002			2
					Microdialysis	Rat						0.015	-1.82390874			6
Cetirizine		1.7	388.9	MDR1 inhibitor	Homogenate Binding	Mouse						0.009	-2.04575749			2
					Microdialysis	Rat						0.170	-0.76955108			2

					Mlcrodl.i,lysas	•••						0.1"	o0..8S387196				2 S
ChlOfllrdludl		u	300.2			•••	0.002	0.018	0.11111	631.SS							●
								O.Ol	0.2	3...5							
Chlorp,Oft'Wlne	'ti	u	318.9	MDfll 'flhllllltor	E(tJlllbrll.ffl Chly51$	•••	0.002	0.014	0.0&333	535.S3	2731	WO	0.44247977				●
					H •••	Ml)Q(	0.002										
Ot'1.iiione		,··	133.4		H •••	•••						•••••	o0.30980391				2
O ldlne					H	•••							o0..16115091				2
		•••	251.14	'll.bm.l'IP£!!!!:!lbl1D!OIi.Tl	Mlcrodl.i,lysas	M W						0010	ol. OOS330'J9				
					H •••							0.022	·1.45757731				2
							0.0S2	O.lU	0.182'61	21.96							
							•••	0.25	032	16.15							●
~-	'ti	ll	324.4	Mllfll Inhibitor/substrate	E(tJlllbrll.ffl ()l.i,ly51$	•••	•••••	0.251	0.16295	2JJ	••••	1.810	0.15767857				●
					Mlcrodl.i,lysas							••••,	·1-34822545				l
					Mlcrodl.i,lysas	•••						•••••	oO.J0627lOS				
0-					H •••	M W						•••••	,0..16749109				2
							0.014	''''	0.11.818	9.,.							●
	'ti	u	326.8		E(tJlllbrll.ffl Chly51$	•••	0.014	0.199	0.07033	9U	22.&7	2.710	0.41296929				●
					•••	M W											
'''''''	'ti	2.3	303.35		H Mlcrodl.i,lysas	•••						L000	a				2
												0.370	o0.43179828				2
					H									0.79	·0.1023729		2
Codeine	'ti	1.1	299.4		H •••	•-m		0.95		''	2.7	•••••	o0.0S060999	o.s4	·0.2676062		2
					Mlcrodl.i,lysas	•••						L000	a				2
'''''-	'ti	''	399.4	MORI WIHtrae	Mlcrodl.i,lysas	•••						••••	·1-39794001				S 2
''''', _			275.4	& l!Hre·	•••	M W											
		2.S	254.14	BCB.Psubstr.111!'	Mlcrodl.i,lysas					● ●	0.027	L<00	0.10'11998				2
Euntrolcne		1.7	314.15	MM l Slt><ltilfr 'll:l	H Mlcrodl.i,lysas	•••						0.067	·1..17387417				
						•••		0.016				0.OlO	·1.S2724355				'
					•••								·1-36653154				
													,0..9'S860731				
					•••	•-m		0.11		20	23	0.110	0.02938378	0.23			
O:iu ln	'ti	1.8	527.5	MORI w!Htrae	Mlcrodl.i,lysas	•-m						1.020	,0.09'20412				S
					•••							••••,,	a	0.OS1			
IIIIIIIIIIIIII	'ti	2 1:9 3	456.6 392.S		Mlcrodl.i,lysas	•••						L000	o0.00S77191	0.79	·0.6382721		2
			284.74	Mllfll substr:rte,!!:mti>t«	H	M W						0.9S0	·1..0315110S	0.78			
			296.1	MOR! WIHtrKt:	H	•••						0093			·1...2924198		2
,,,,,,,,		•••	780.9		H	•••						•••••	·1.4202164		·0.1023729		2
Clc:b c	'ti			MORI WIHtrae	H			OAS		32	''	I.0S0	O.Ol.11893		·0.1079054		2
Oifioedn		1.3	25S.3S	MOR! WIHtrKt:	H •••	M W						L<00	0.10'11998				'
		''			H	•••	0.117	,,••	0.41197	•••							2
OOneperll	'ti		379.S	M!la.lsubstr.:itr& 'nh'111101		M W	0.1'5	0265	0.54717	&22							2
		•.3			E(tJlllbrll.ffl E)l.i,ly51$	'''	0.1'3	0.21S	0.66512	•••	3A3	2.710	0.41296929				2
						•••											S 2 2 2 ● ●
					•••							0.059					''
00=-		·l	153.18			MOO(						•••••					S
lkrlc,t,n	'ti	u	382.S		H	•••	0.1J$						·1-22914799				2
Uorkoldb	'ti		3S8.8			•••							o0.40S93SI9				2
Fenl.i,n'lf		●	136.S	MORI w!Htrae	H	M W							,0.00436481				2
•••				Mllfllsub51ntr& 'nh'·llltor	H •••												
					•••												

,0.02227639
•1..43179828
•1.1198407
,0..60205999
,0..60205999
,0..67178071
•1.74172749

2
2
2
2
2
$

'Auoriisu'

3 | SCl2.7 | NDfl:l Et!z:'irrrr | H

M W | 0.950

401.8 | MOR1 w!Htrae | Mlcrodl.i,lysas

MOIU substr.atr&IWl'.bllot

,0.1 | 369.14 | 0.037

Mlcrodl.i,lysas

<2 | 244.16

.u | 134.l | Mlcrodl.i,lysas | 0.053

H

Mlcrodl.i,lysas | 0.2S0

0.2S0

0.210

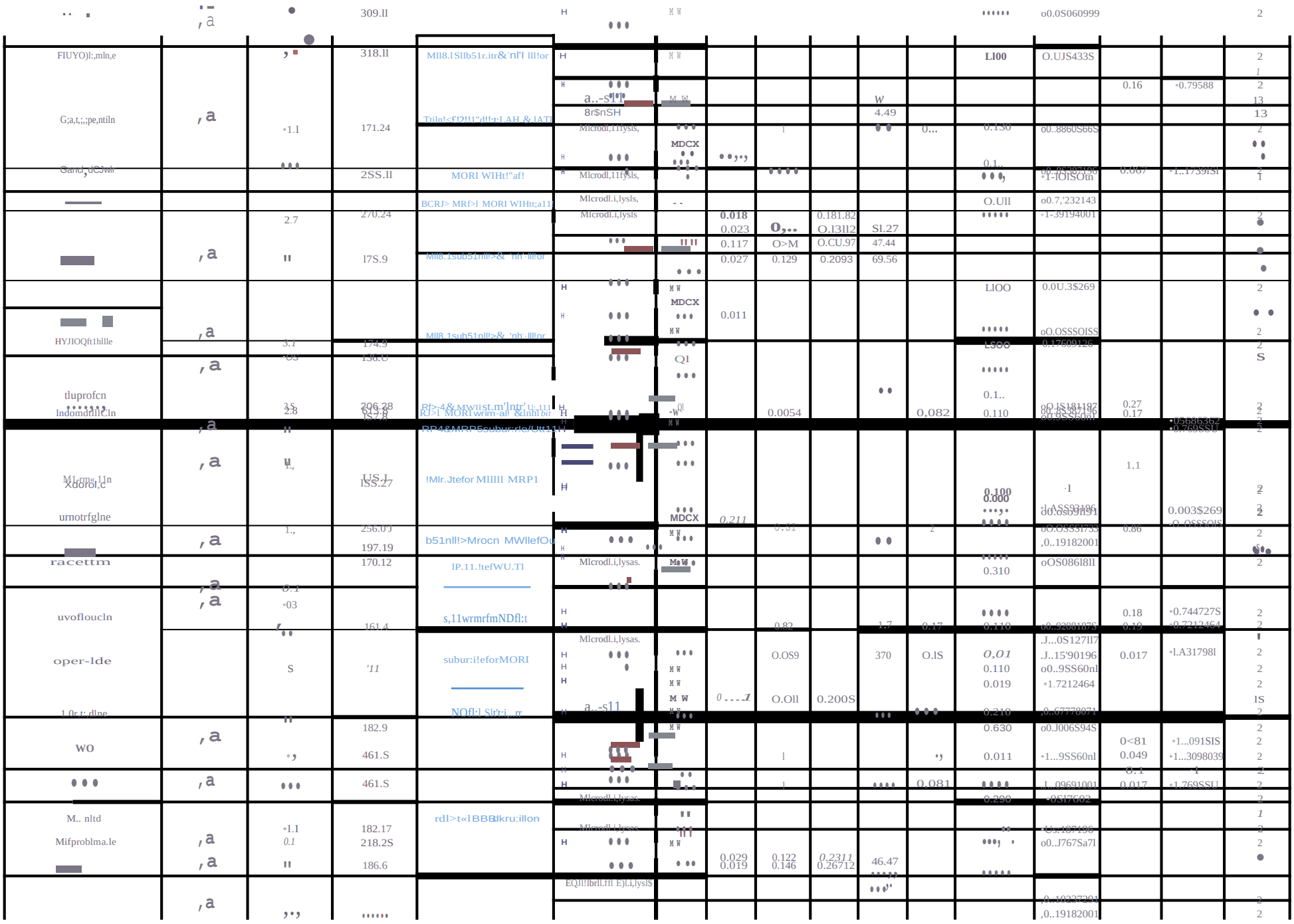

tMm:idone			Subur:i!e&11'1"ll"IDI'of MDfll	H H			0.0'1	0.195	0.21.026	1 ...	0.220 0.790	o0..6S7S7n2	
Mi:ttlottftlle	▫U	454.4	BCJCP. OATl-4. MRPl-4.MOR	H								O,W	·l...2076083 2

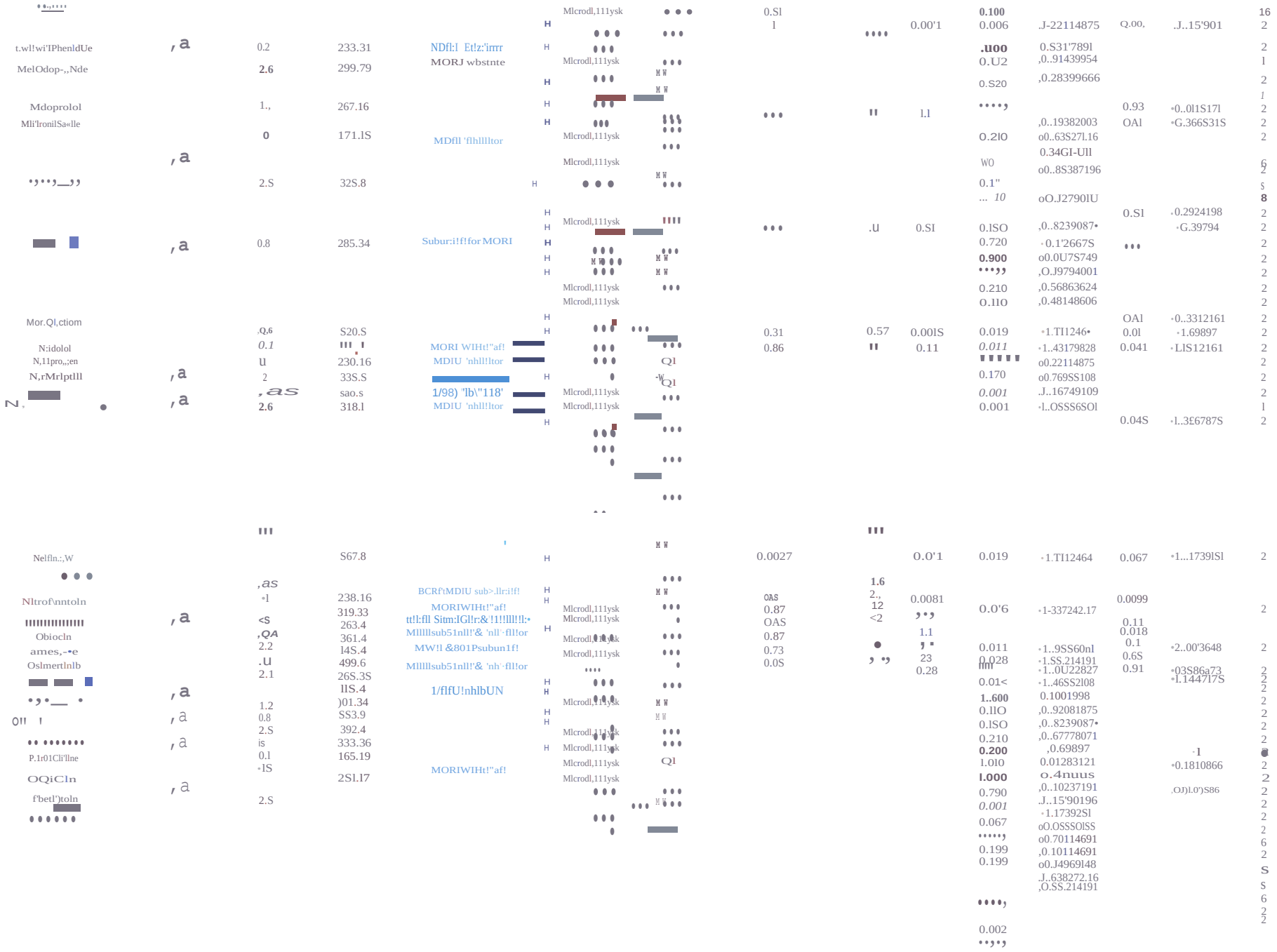

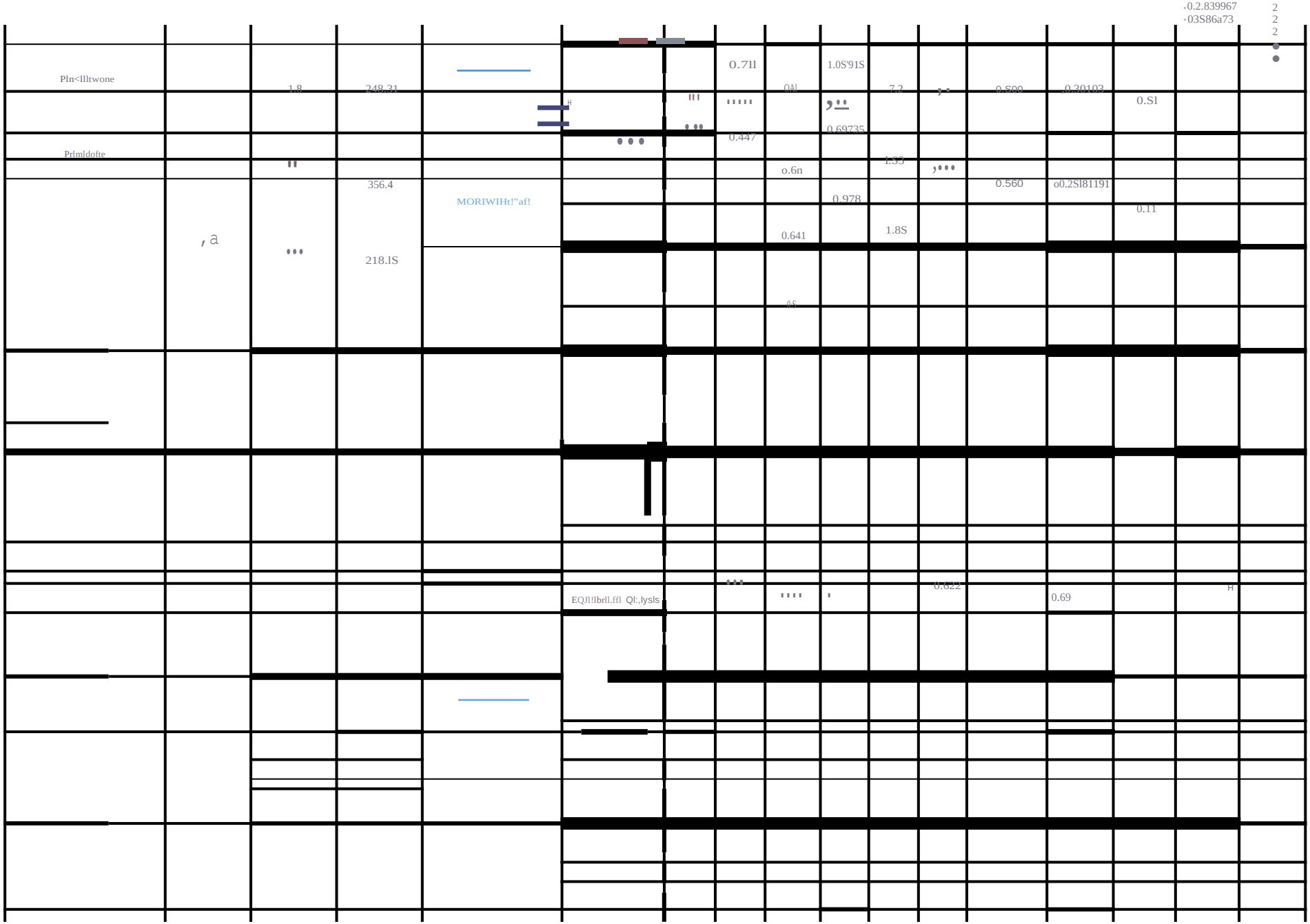
0.2.839967
03S86a73
Pln<llltwone
1.8
248.31
0.7ll
1.0S'91S
7.2
0.S90
0.30103
0.Sl
0.69735
0.447
Prlmldofte
o.6n
1.S3
356.4
0.560
o0.2Sl81191
MORIWIHt!"af!
0.978
0.11
0.641
1.8S
218.lS
0.622
0.69
EQJl!lbrll.ffl Ql:,lysls

0.78 ...20 o0.J7 71

"

67Sa

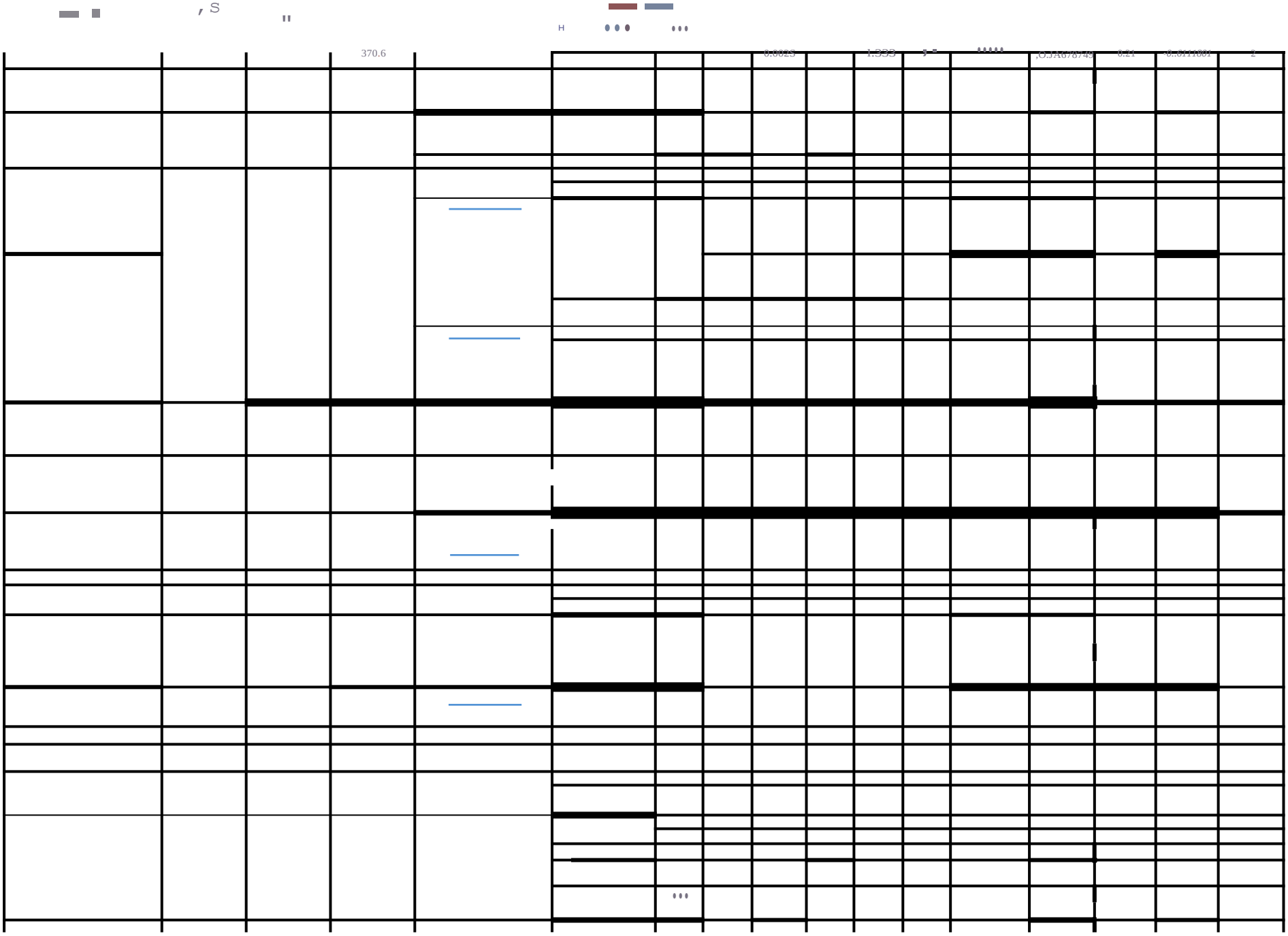

Topiramate	Yes	-0.8	339.36	MDR1 substrate	CSF sampling	Human								0.98	-0.0087739	10
					Homogenate Binding	Human								1	0	2
					Homogenate Binding	Rat						0.330	-0.48148606	0.63	-0.2006595	2
Tramadol	Yes	2.6	263.37	OAT substrate	Homogenate Binding	Human								1.44	0.15836249	2
					Homogenate Binding	Rat		0.79		3.2	0.84	1.460	0.16435286	0.71	-0.1487417	2
Trazodone	Yes	2.8	371.9	MDR1 inducer	Homogenate Binding	Mouse						0.560	-0.25181197			2
Triprolidine		3.9	278.4		Homogenate Binding	Mouse						1.800	0.25527251			2
Valdecoxib		2.6	314.4		Homogenate Binding	Rat						0.220	-0.65757732			2
Valproic acid	Yes	2.8	144.21			Rat										5
venlafaxine	Yes	2.9	277.4	MDR1 substrate & inhibitor	Homogenate Binding	Mouse						0.980	-0.00877392			2
Verapamil		3.8	454.6	MDR1 substrate & inhibitor	PET	Monkey					0.4					3
					PET	Rat					1.13					3
					Homogenate Binding	Human								1.13	0.05307844	2
					Homogenate Binding	Rat		0.12		54	0.34	0.053	-1.27572413	0.11	-0.9586073	2
					Microdialysis	Rat						0.079	-1.10457745			6
					Homogenate Binding	Mouse						0.100	-1			2
					Homogenate Binding	Mouse						0.130	-0.88605665			2
Vinblastine		3.7	811	DR1 substrate, inhibitor, induc	Homogenate Binding	Mouse						0.087	-1.06048075			2
Xanthine		-0.7	152.11			Rat										5
Zalcitabine		-1.3	211.22		Microdialysis	Rat						0.190	-0.7212464			2
Zidovudine		0	267.24	MDR1 substrate	Homogenate Binding	Human								1.04	0.01703334	2
					Homogenate Binding	Rat		0.64		1.1	0.065	0.090	-1.04575749	0.18	-0.7447275	2
					Microdialysis	Rat						0.150	-0.82390874			2
Ziprasidone	Yes	4	412.9			Pig	0.016	0.027	0.59259	74.56						4
						Dog	0.032	0.054	0.59259	49.66						4
					Equilibrium Dialysis	Rat	0.017	0.015	1.13333	80.78	1.51	1.810	0.25767857			4
Zolmitriptan	Yes	2.2	287.36		Homogenate Binding	Mouse						0.021	-1.67778071			2
Zolpidem	Yes	2.5	307.4		Microdialysis	Rat						0.447	-0.34969248			6
					Homogenate Binding	Mouse						0.240	-0.61978876			2

Appendix 3

Standard curves were developed from calibration line concentrations and measured response (ratio of area of drug peak to internal standard peak). This standard curve was used to generate sample concentrations for each drug. The standard curve for each drug as calculated is listed below.

Figure A3.1 - Haloperidol

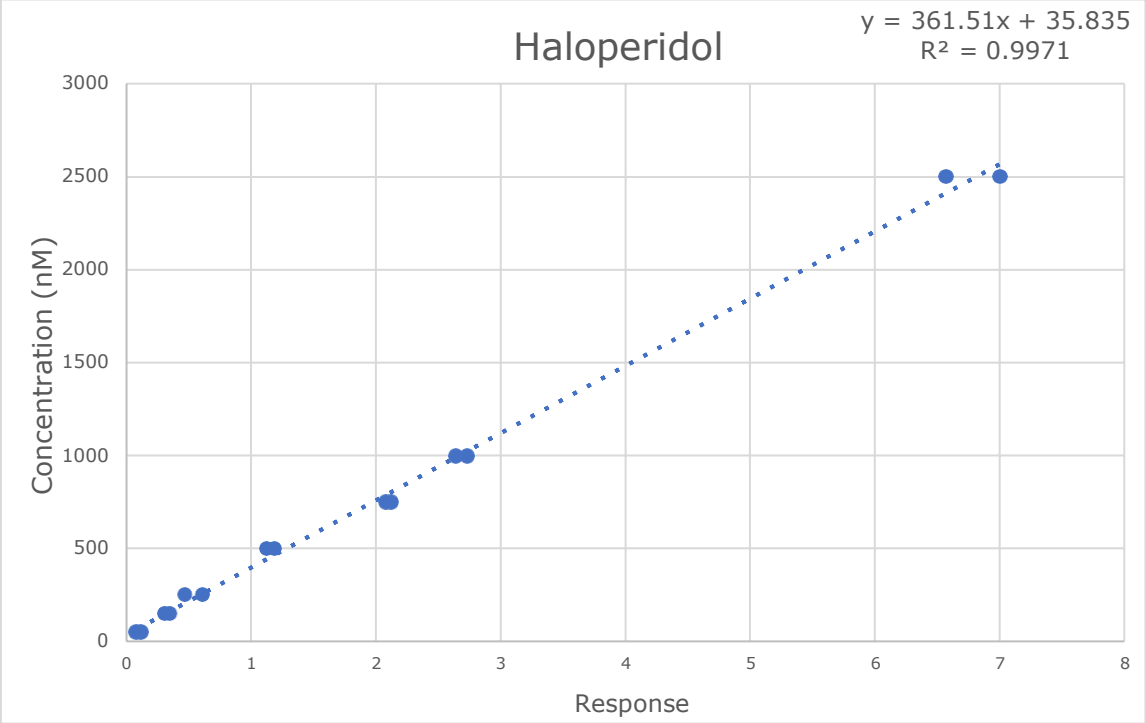

Figure A3.1 – Standard curve fit of Haloperidol calibration values for drug transport study. Response is shown on the X axis, sample concentration is shown on the Y axis. The graph shows the linear line of best fit equation used to calculate projected concentrations.

Figure A3.2 - Carbamazepine

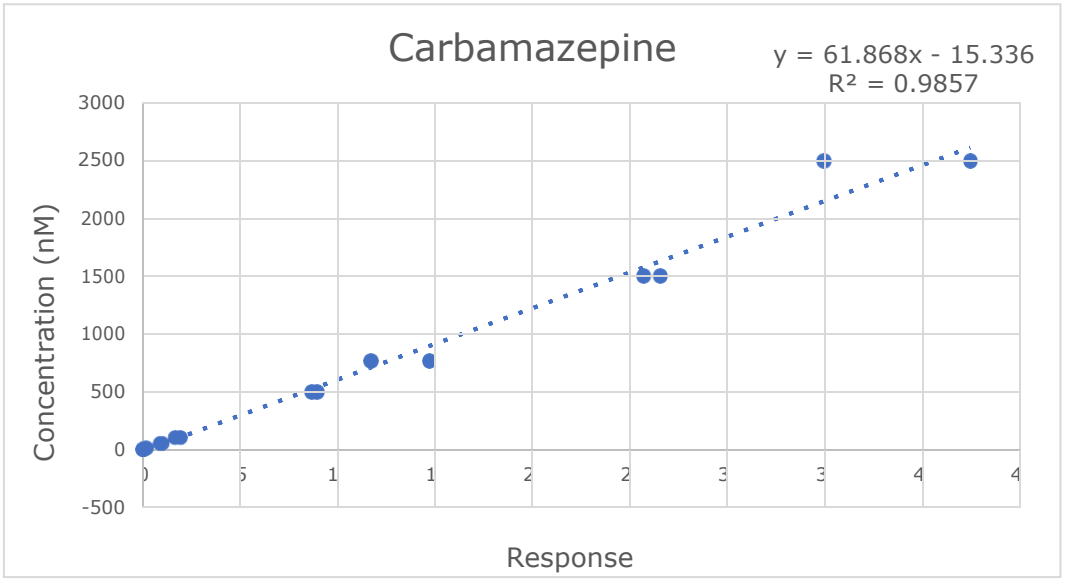

Figure A3.2 – Standard curve fit of Carbamazepine calibration values for drug transport study. Response is shown on the X axis, sample concentration is shown on the Y axis. The graph shows the linear line of best fit equation used to calculate projected concentrations.

Figure A3.3 - Loperamide

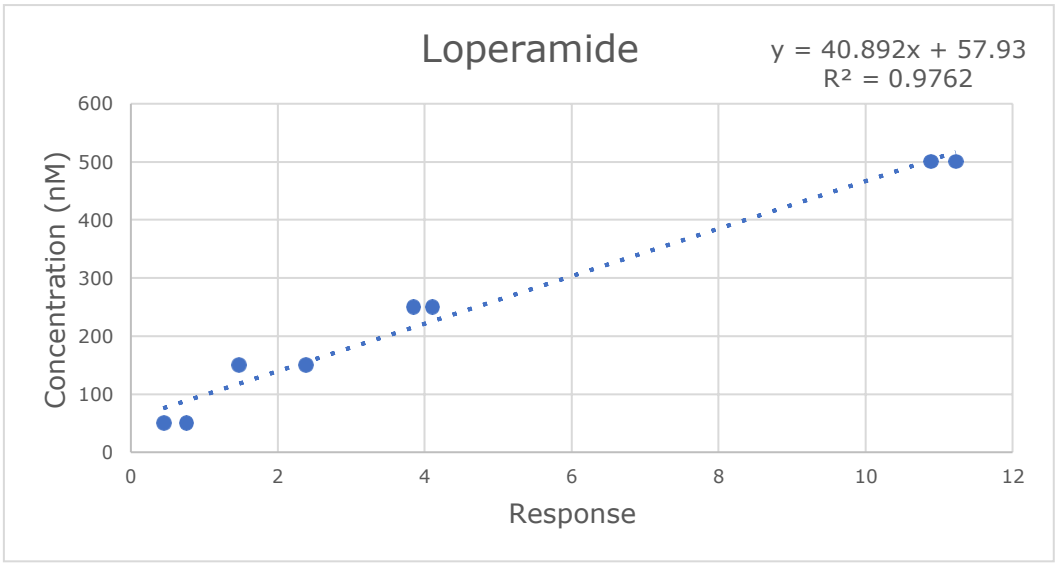

Figure A3.3 – Standard curve fit of Loperamide calibration values for drug transport study. Response is shown on the X axis, sample concentration is shown on the Y axis. The graph shows the linear line of best fit equation used to calculate projected concentrations.

Figure A3.4 - Donepezil

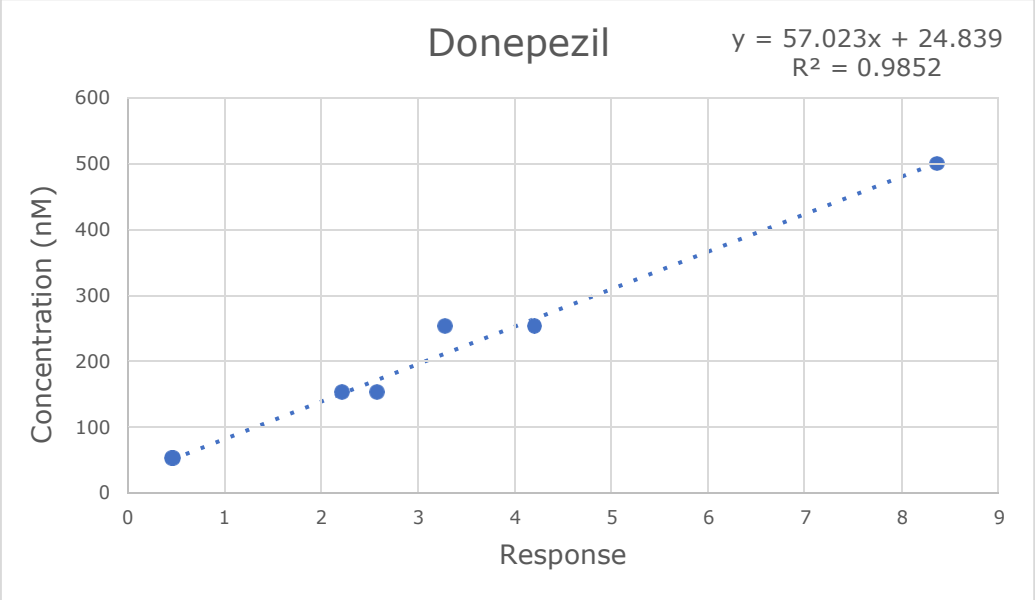

Figure A3.4 – Standard curve fit of Donepezil calibration values for drug transport study. Response is shown on the X axis, sample concentration is shown on the Y axis. The graph shows the linear line of best fit equation used to calculate projected concentrations.

Figure A3.5 – Amprenavir

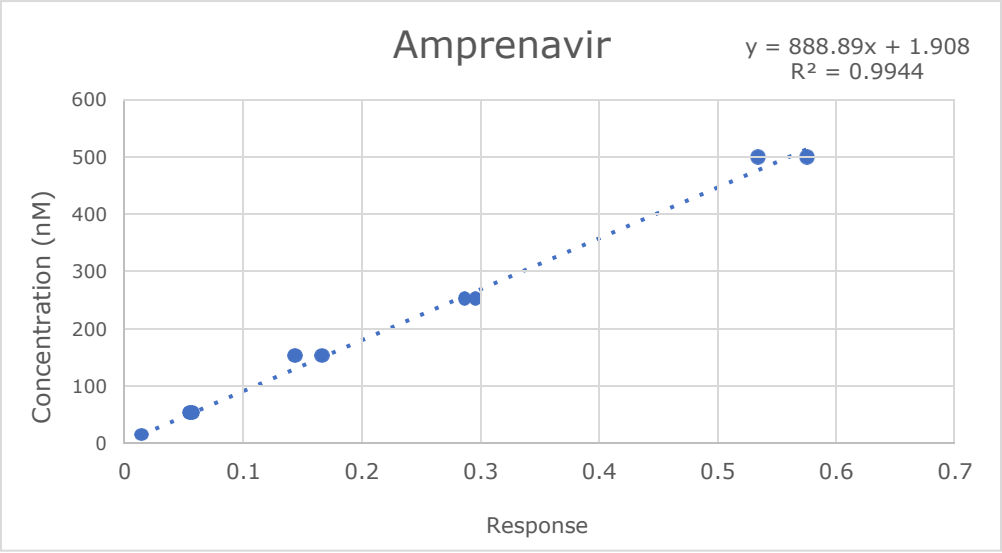

Figure A3.1 – Standard curve fit of Amprenavir calibration values for drug transport study. Response is shown on the X axis, sample concentration is shown on the Y axis. The graph shows the linear line of best fit equation used to calculate projected concentrations.

Figure A3.6 - Chlorpromazine

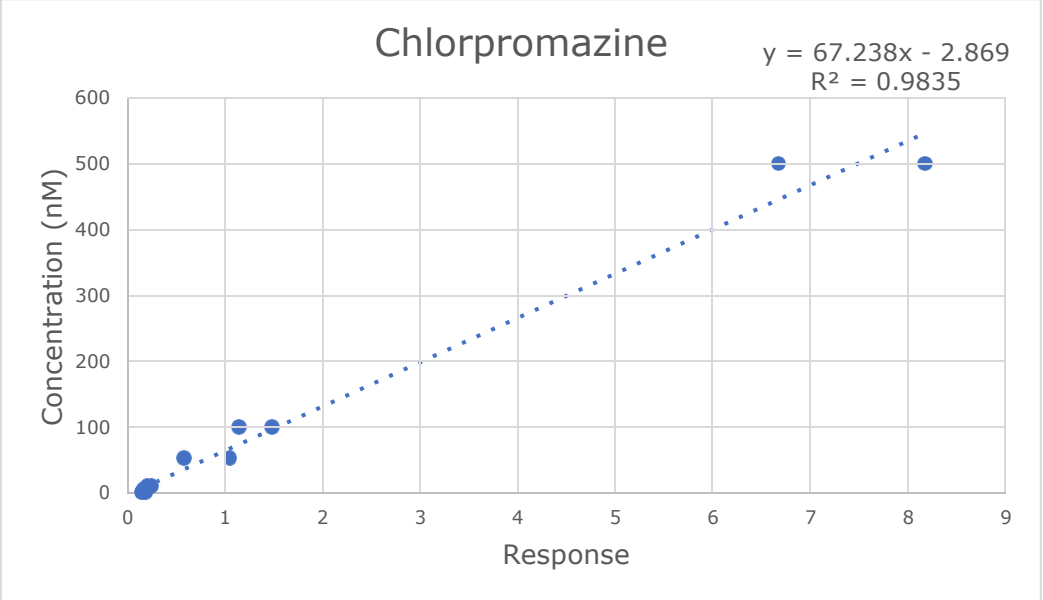

Figure A3.6 – Standard curve fit of Chlorpromazine calibration values for drug transport study. Response is shown on the X axis, sample concentration is shown on the Y axis. The graph shows the linear line of best fit equation used to calculate projected concentrations.

Figure A3.7 - Thiopental

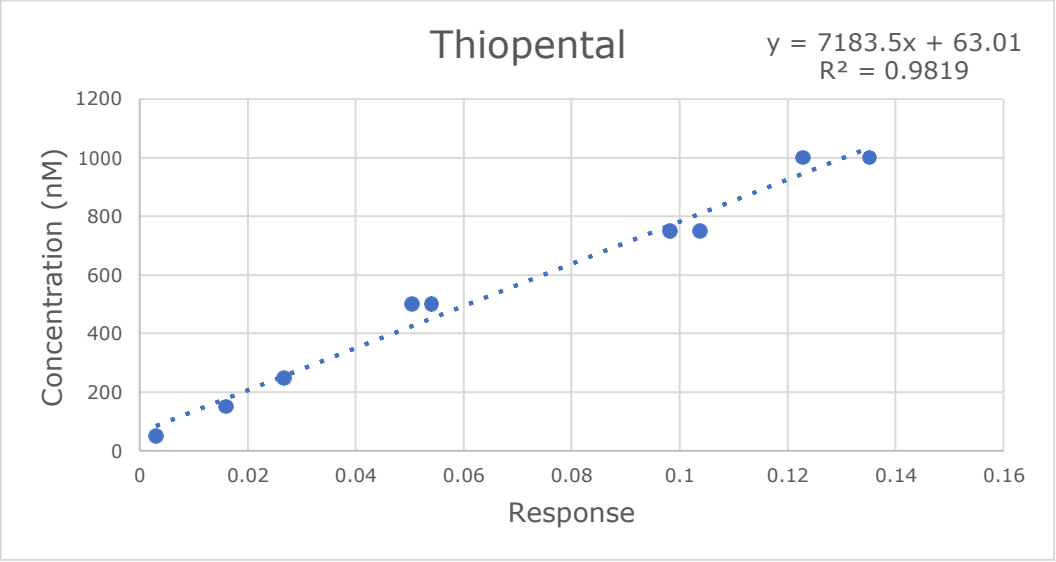

Figure A3.7 – Standard curve fit of Thiopental calibration values for drug transport study. Response is shown on the X axis, sample concentration is shown on the Y axis. The graph shows the linear line of best fit equation used to calculate projected concentrations.

Figure A3.8 - Topiramate

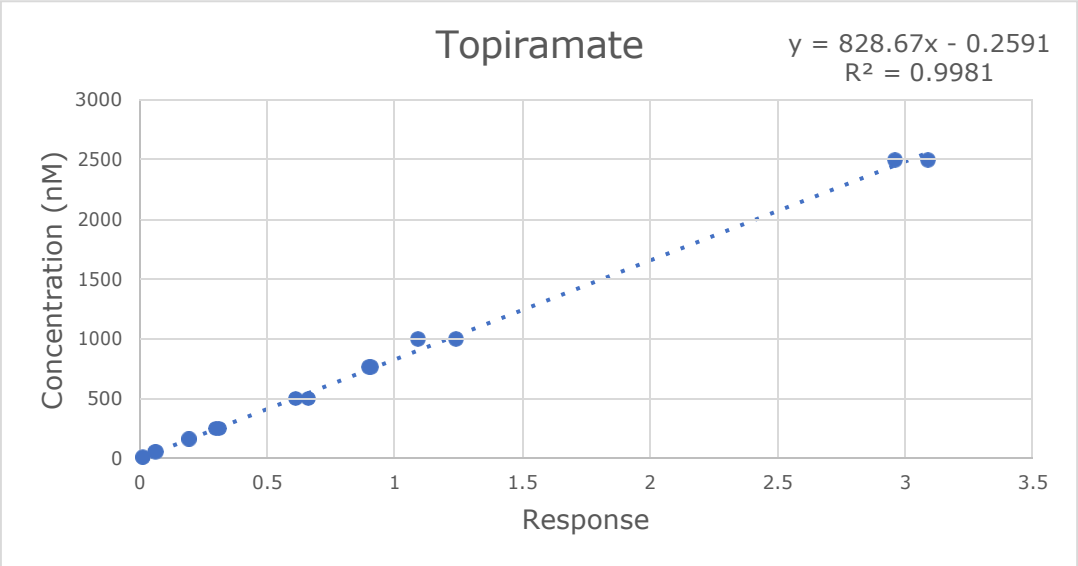

Figure A3.8 – Standard curve fit of Topiramate calibration values for drug transport study. Response is shown on the X axis, sample concentration is shown on the Y axis. The graph shows the linear line of best fit equation used to calculate projected concentrations.

Figure A3.9 - Primidone

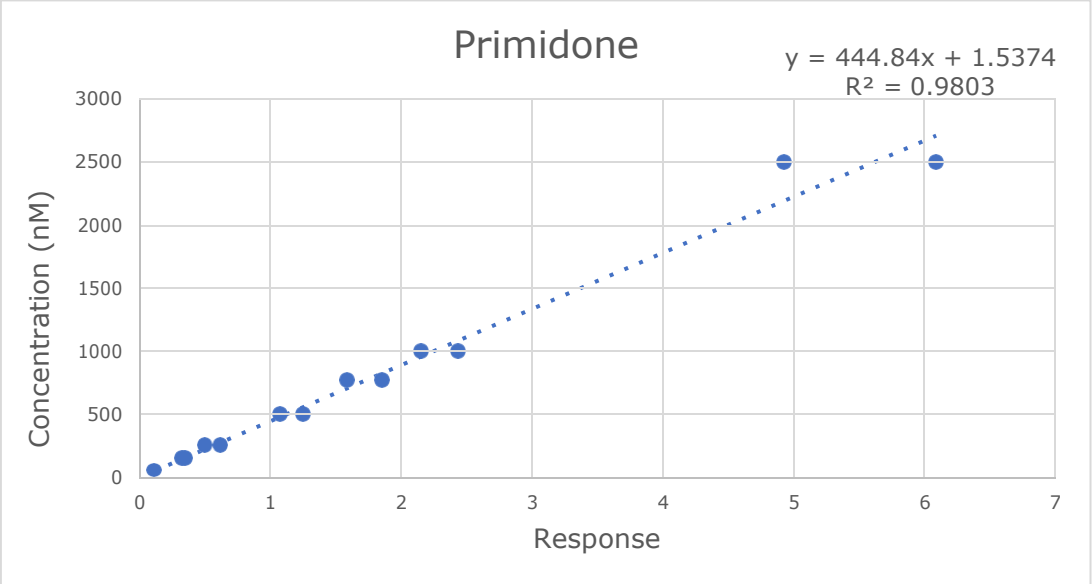

Figure A3.9 – Standard curve fit of Primidone calibration values for drug transport study. Response is shown on the X axis, sample concentration is shown on the Y axis. The graph shows the linear line of best fit equation used to calculate projected concentrations.

Appendix 4

Chromatography graphs for drug samples and internal standard from LC-MS/MS analysis.

Figure A4.1 - Haloperidol

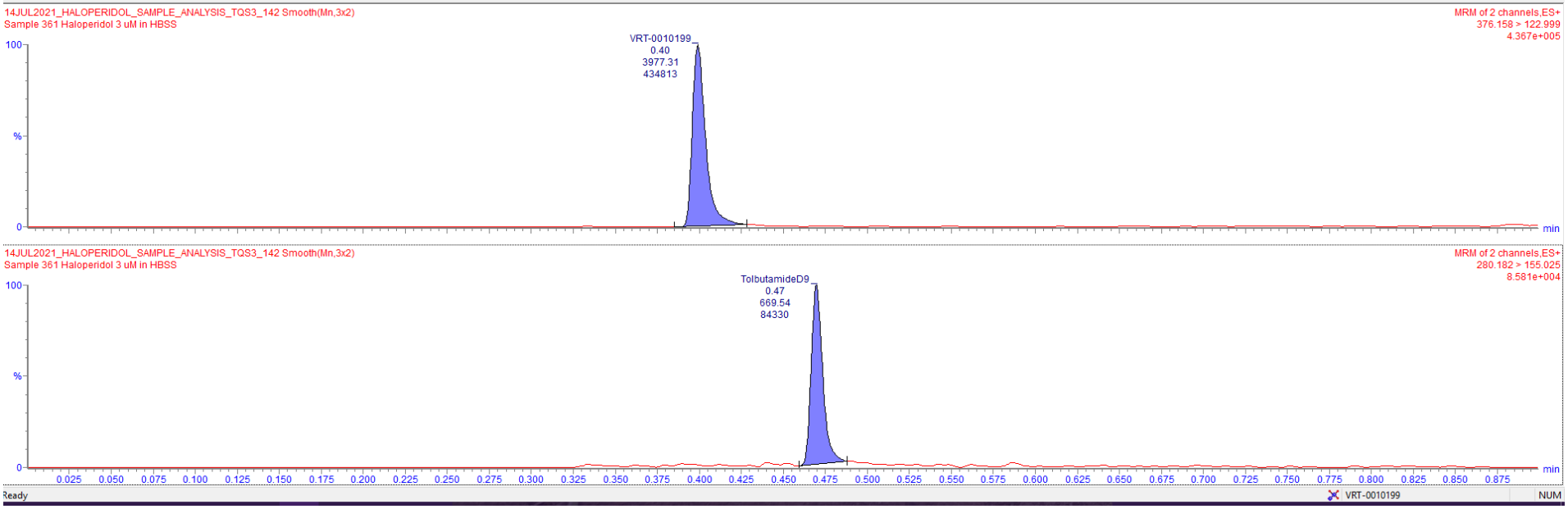

Figure A4.1 - Chromatograms produced for Haloperidol and internal standard (Tolbutamide-D9) for drug transport studies. Percentage response is shown (y axis) vs retention time (x axis, minutes). Retention time of Haloperidol was 0.40 minutes and Tolbutamide-D9 was 0.47 minutes.

Figure A4.2 - Carbamazepine

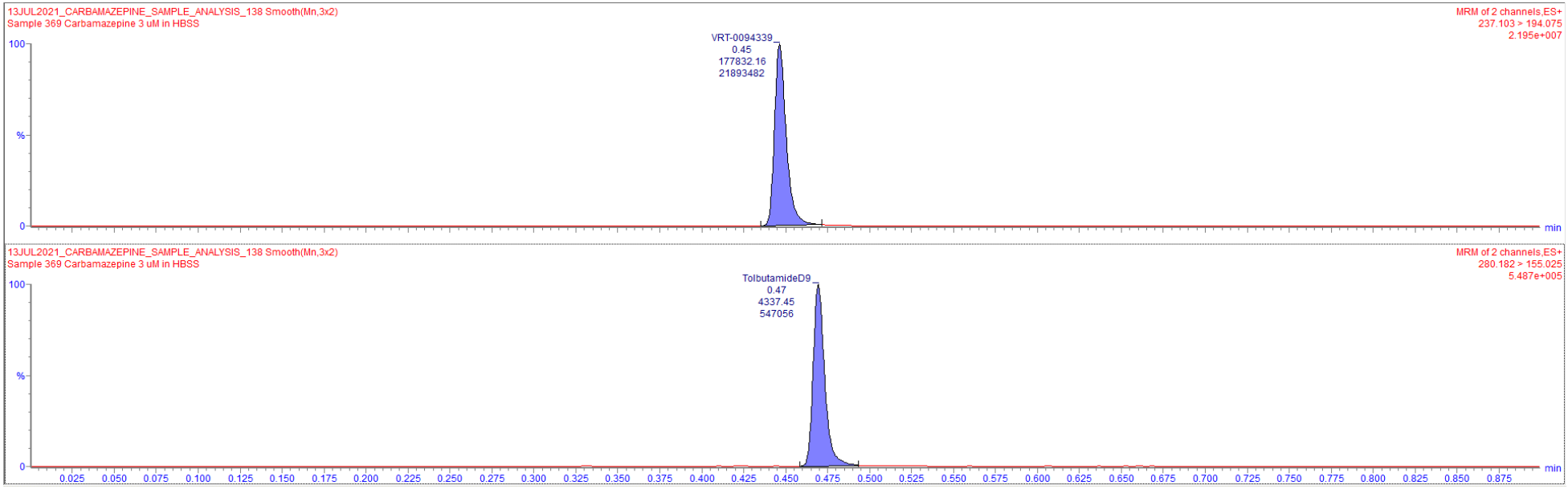

Figure A4.2 - Chromatograms produced for Carbamazepine and internal standard (Tolbutamide-D9) for drug transport studies. Percentage response is shown (y axis) vs retention time (x axis, minutes). Retention time of Haloperidol was 0.45 minutes and Tolbutamide-D9 was 0.47 minutes.

Figure A4.3 - Loperamide

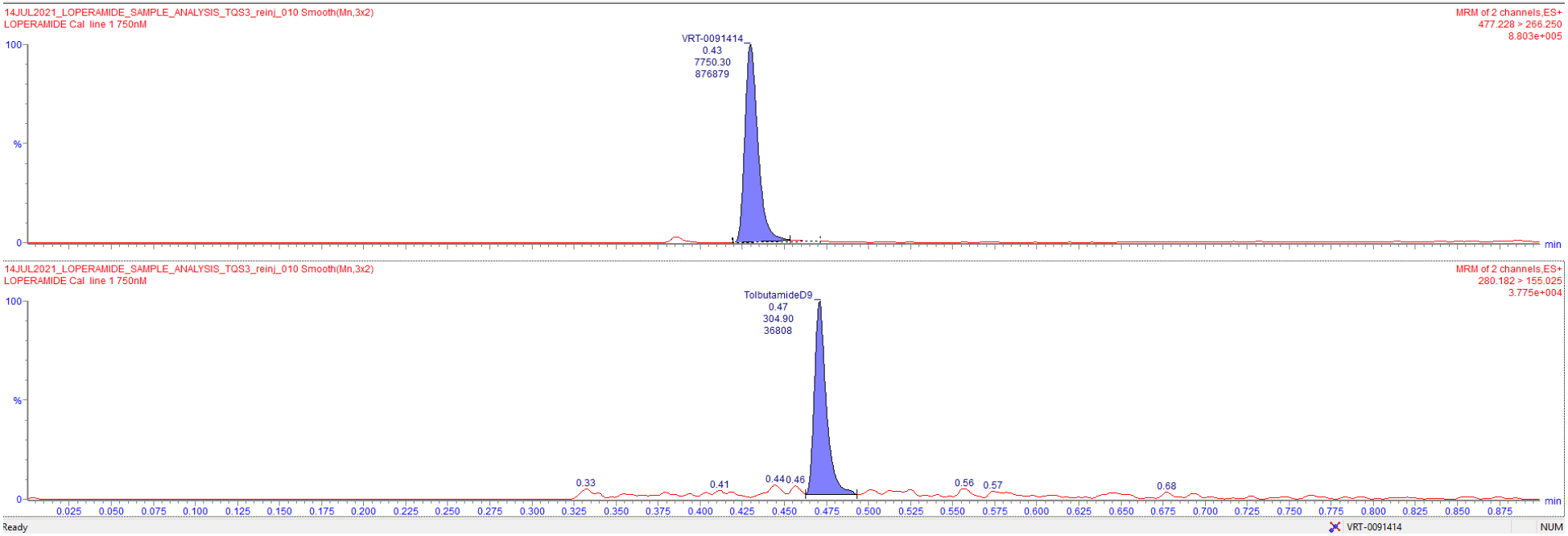

Figure A4.3 - Chromatograms produced for Loperamide and internal standard (Tolbutamide-D9) for drug transport studies. Percentage response is shown (y axis) vs retention time (x axis, minutes). Retention time of Loperamide was 0.43 minutes and Tolbutamide-D9 was 0.47 minutes.

Figure A4.4 - Donepezil

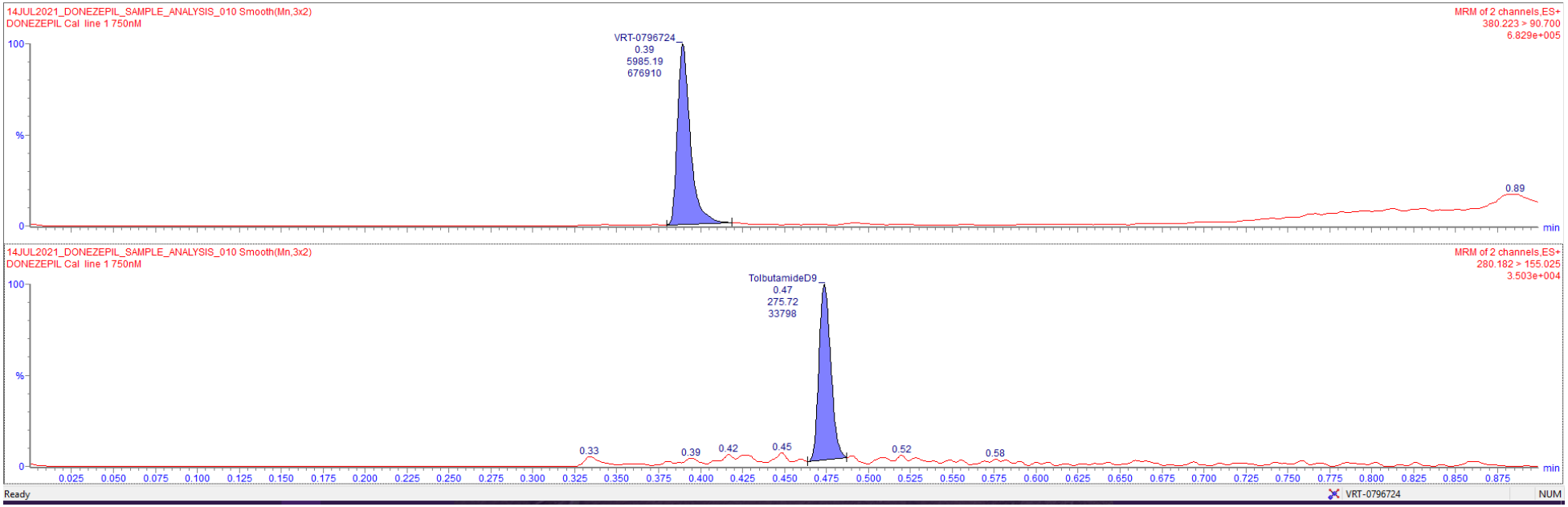

Figure A4.4 - Chromatograms produced for Donepezil and internal standard (Tolbutamide-D9) for drug transport studies. Percentage response is shown (y axis) vs retention time (x axis, minutes). Retention time of Haloperidol was 0.39 minutes and Tolbutamide-D9 was 0.47 minutes.

Figure A4.5 - Amprenavir

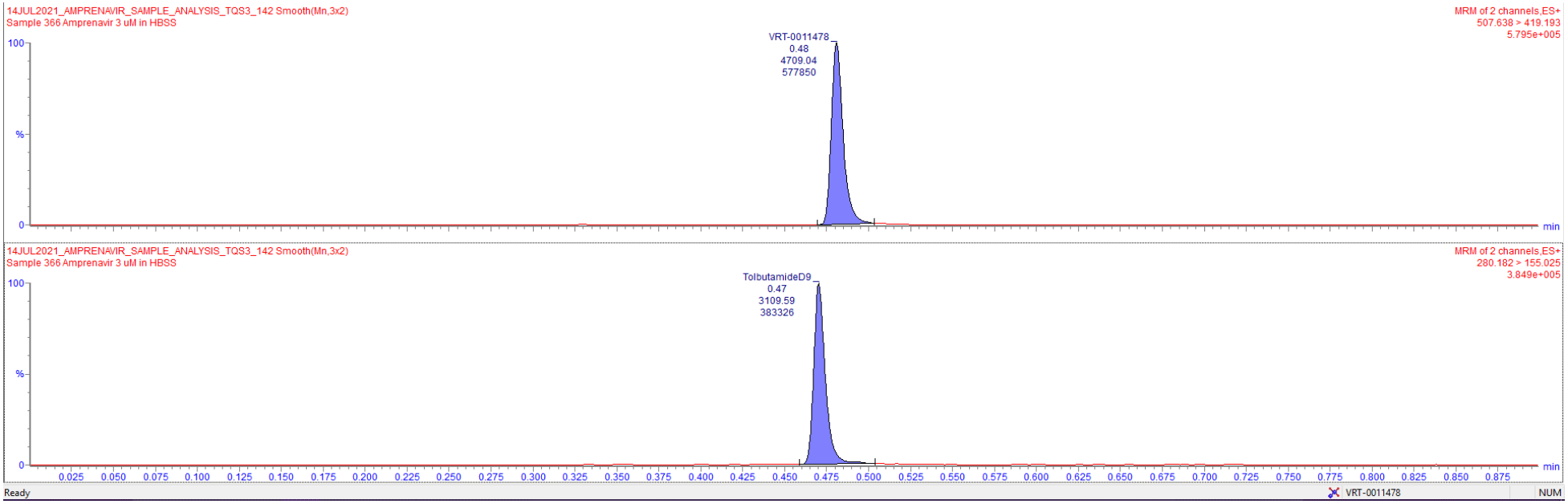

Figure A4.5 - Chromatograms produced for Amprenavir and internal standard (Tolbutamide-D9) for drug transport studies. Percentage response is shown (y axis) vs retention time (x axis, minutes). Retention time of Amprenavir was 0.48 minutes and Tolbutamide-D9 was 0.47 minutes.

Figure A4.6 - Chlorpromazine

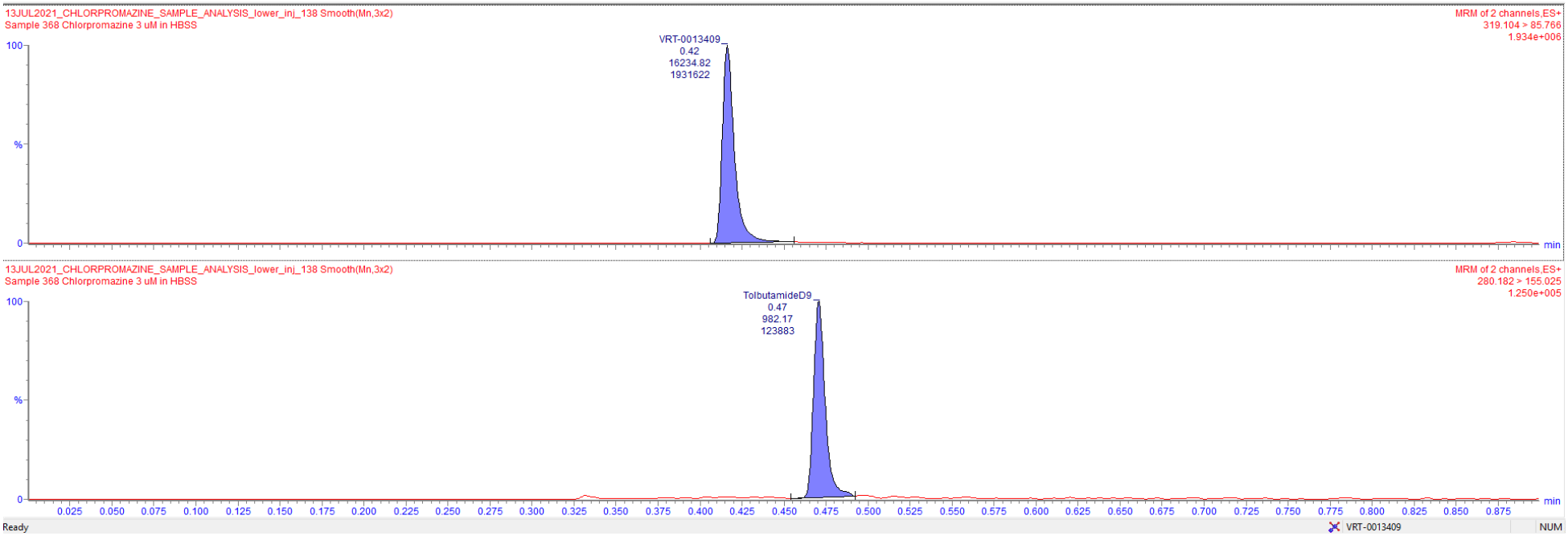

Figure A4.6 - Chromatograms produced for Chlorpromazine and internal standard (Tolbutamide-D9) for drug transport studies. Percentage response is shown (y axis) vs retention time (x axis, minutes). Retention time of Haloperidol was 0.42 minutes and Tolbutamide-D9 was 0.47 minutes.

Figure A4.7 - Thiopental

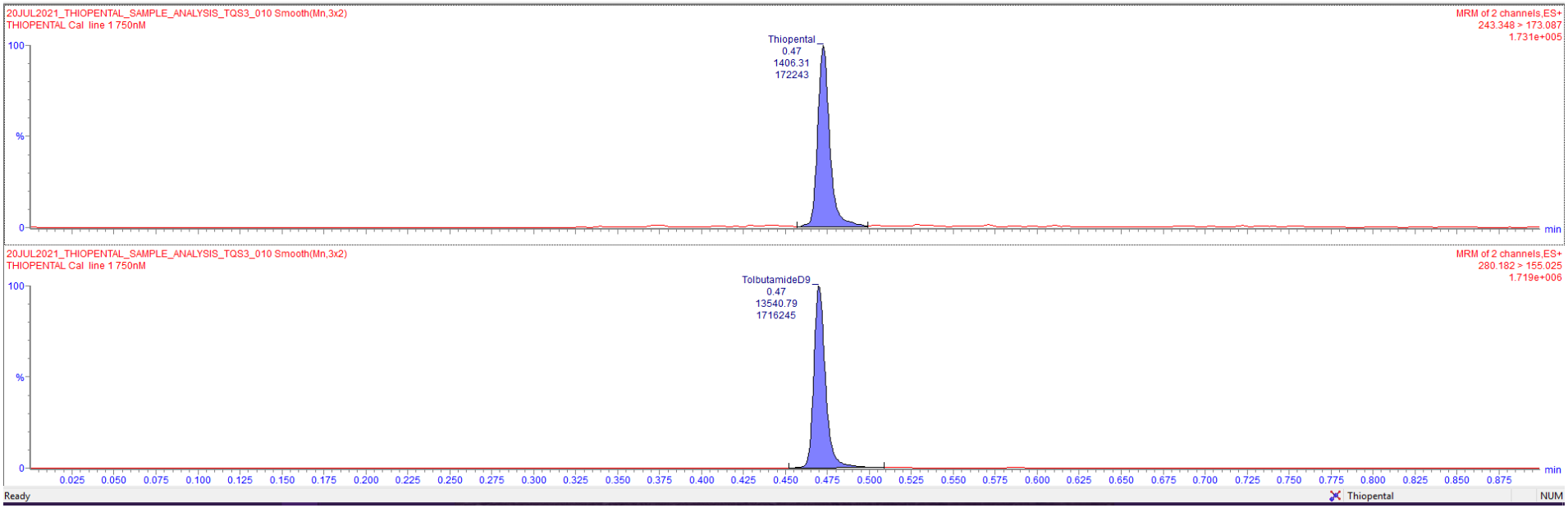

Figure A4.7 - Chromatograms produced for Thiopental and internal standard (Tolbutamide-D9) for drug transport studies. Percentage response is shown (y axis) vs retention time (x axis, minutes). Retention time of Haloperidol was 0.47 minutes and Tolbutamide-D9 was 0.47 minutes.

Figure A4.8 - Topiramate

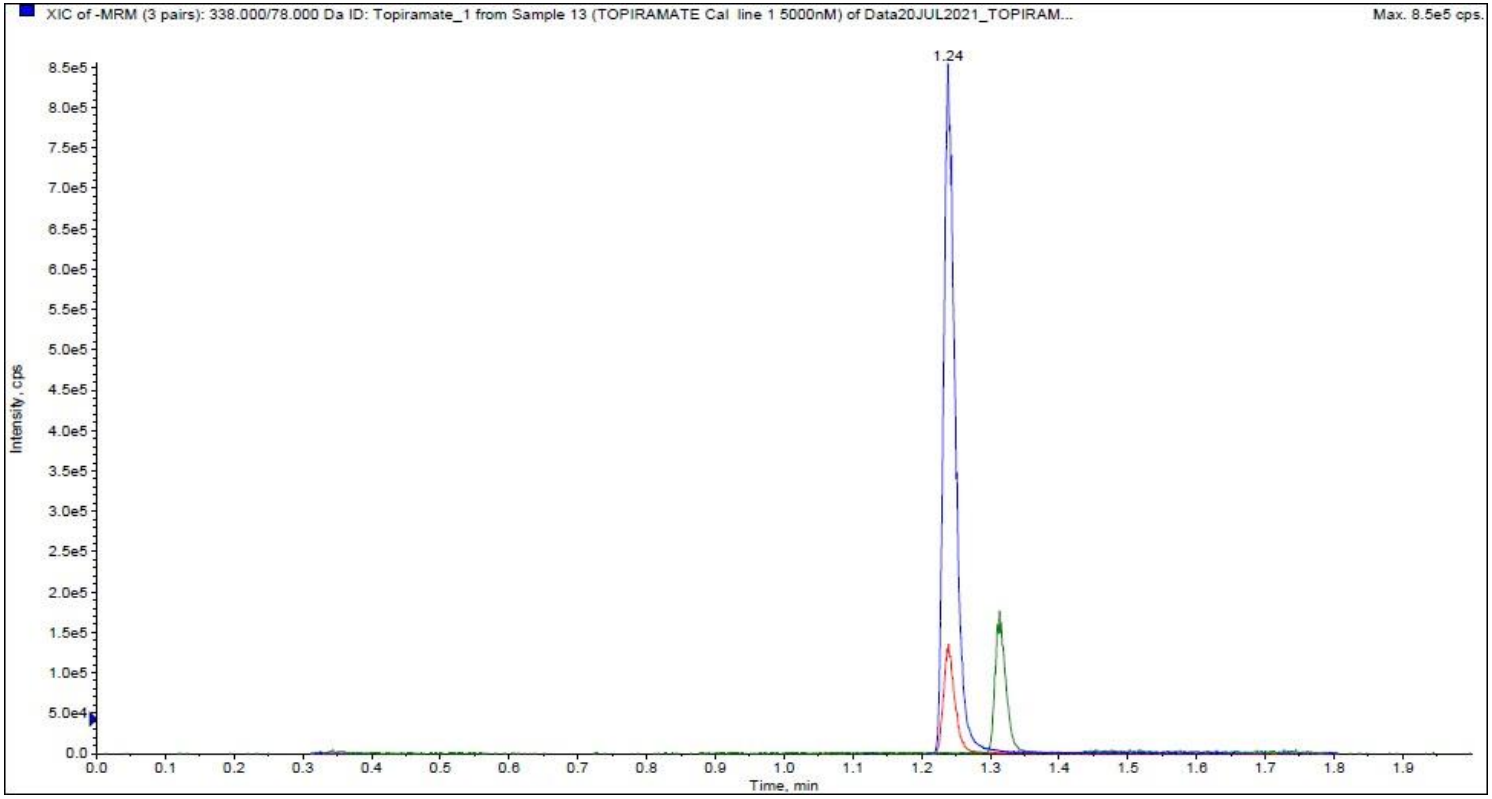

Figure A4.8 - Chromatogram produced for Topiramate for drug transport studies. Intensity is shown (y axis) vs retention time (x axis, minutes). Retention time of Topiramate was 1.24 minutes.

Figure A4.9 - Primidone

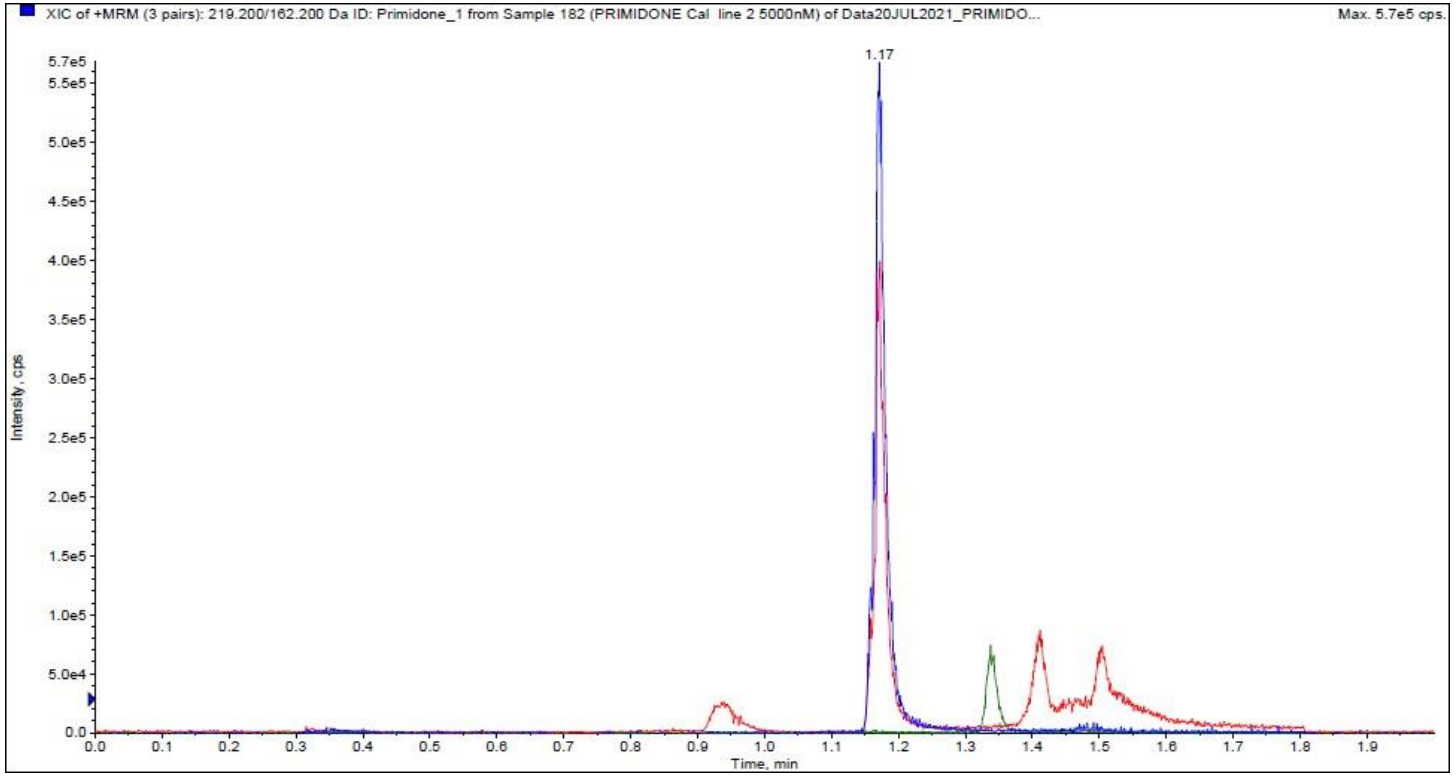

Figure A4.9 - Chromatogram produced for Primidone for drug transport studies. Intensity is shown (y axis) vs retention time (x axis, minutes). Retention time of Topiramate was 1.17 minutes.

Figure A4.10 - Levodopa

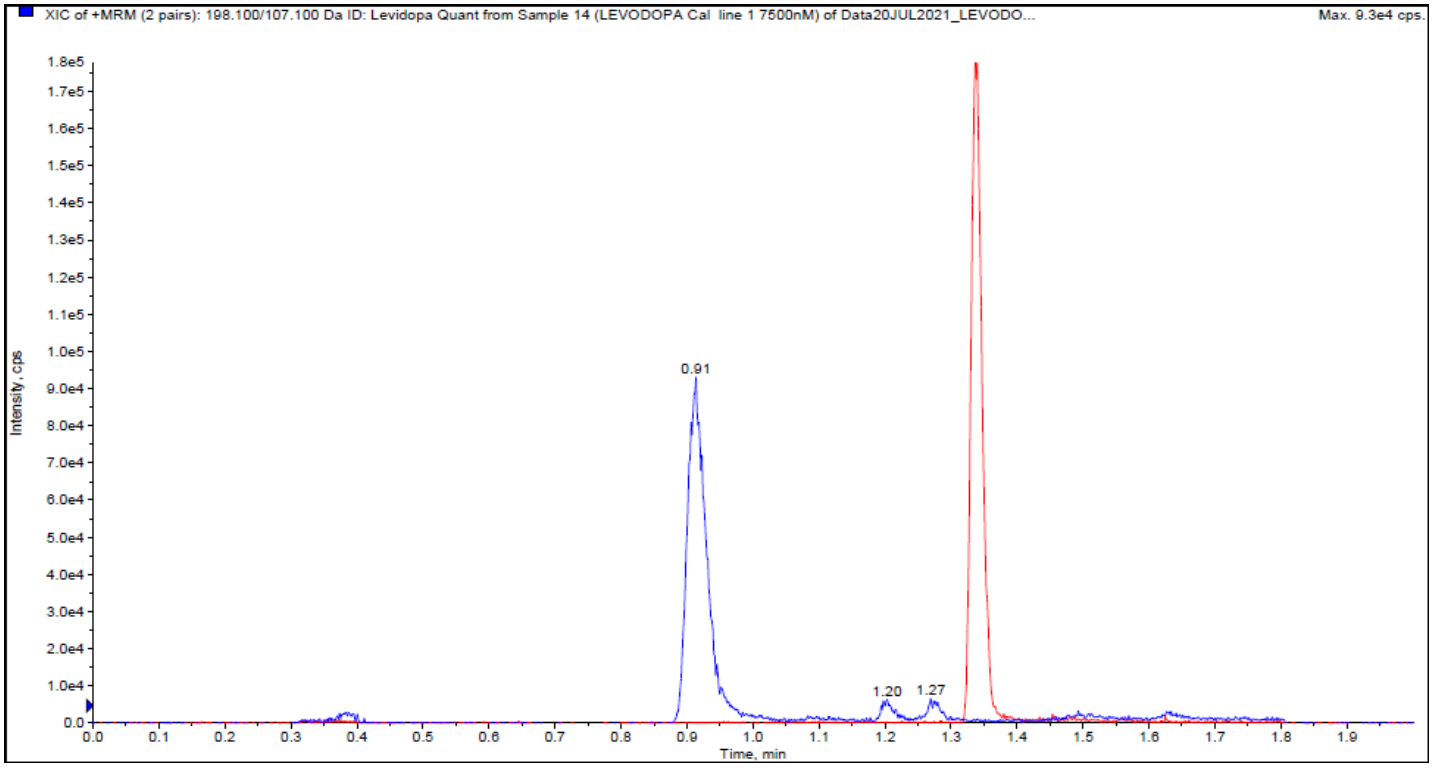

Figure A4.10 - Chromatogram produced for Levodopa for drug transport studies. Intensity is shown (y axis) vs retention time (x axis, minutes). Retention time of Levodopa was 0.91 minutes. Data for Levodopa was deemed void due to low detection levels.

Appendix 5

Additional data from LC-MS/MS analysis of drug transport studies.

Table A5.1 - Time Point 1 Replicate 1

Replicate	Compound (spiking)	Conc apical start (nM)	conc apical end (nM)	Conc basolateral start (nM)	Conc basolateral end (nM)	amount apical start (nmol)	amount apical end (nmol)	amount basolateral start (nmol)	amount basolateral end (nmol)	Total in well start (nmol)	Total in well end (nmol)	Recovery (%)
1	Haloperidol A-B	2183.0	1072.8	0.0	88.3	0.2	0.1	0.0	0.1	0.2	0.2	73.4
	Haloperidol B-A	0.0	236.1	2183.0	2475.9	0.0	0.0	1.3	1.5	1.3	1.5	115.2
	Carbamazepine A-B	2521.2	1496.0	0.0	49.4	0.3	0.1	0.0	0.0	0.3	0.2	71.1
	Carbamazepine B-A	0.0	451.6	2521.2	1984.7	0.0	0.0	1.5	1.2	1.5	1.2	81.7
	Loperamide A-B	6795.3	2550.5	0.0	150.3	0.7	0.3	0.0	0.1	0.7	0.3	50.8
	Loperamide B-A	0.0	552.7	6795.3	5599.2	0.0	0.1	4.1	3.4	4.1	3.4	83.8
	Donepezil A-B	5457.2	3662.9	0.0	157.9	0.5	0.4	0.0	0.1	0.5	0.5	84.5
	Donepezil B-A	0.0	649.8	5457.2	5341.5	0.0	0.1	3.3	3.2	3.3	3.3	99.9
	Amprenavir A-B	1348.0	979.6	0.0	28.5	0.1	0.1	0.0	0.0	0.1	0.1	85.4
	Amprenavir B-A	0.0	139.1	1348.0	611.4	0.0	0.0	0.8	0.4	0.8	0.4	47.1
	Chlorpromazine A-B	1108.6	182.5	0.0	13.5	0.1	0.0	0.0	0.0	0.1	0.0	23.7
	Chlorpromazine B-A	0.0	98.1	1108.6	347.6	0.0	0.0	0.7	0.2	0.7	0.2	32.8
	Thiopental A-B	1074.0	916.3	0.0	63.0	0.1	0.1	0.0	0.0	0.1	0.1	120.5
	Thiopental B-A	0.0	254.6	1074.0	880.3	0.0	0.0	0.6	0.5	0.6	0.6	85.9
	Topiramate A-B	1565.9	1309.0	0.0	34.2	0.2	0.1	0.0	0.0	0.2	0.2	96.7
	Topiramate B-A	0.0	207.7	1565.9	1507.9	0.0	0.0	0.9	0.9	0.9	0.9	98.5
	Primidone A-B	2581.6	2030.0	0.0	40.1	0.3	0.2	0.0	0.0	0.3	0.2	87.9
	Primidone B-A	0.0	381.4	2581.6	2697.3	0.0	0.0	1.5	1.6	1.5	1.7	106.9

Table A5.2 - Time Point 1 Replicate 2

Replicate	Compound (spiking)	Conc apical start (nM)	conc apical end (nM)	Conc basolateral start (nM)	Conc basolateral end (nM)	amount apical start (nmol)	amount apical end (nmol)	amount basolateral start (nmol)	amount basolateral end (nmol)	Total in well start (nmol)	Total in well end (nmol)	Recovery (%)
2	Haloperidol A-B	2183.0	1077.3	0.0	97.2	0.2	0.1	0.0	0.1	0.2	0.2	76.1
	Haloperidol B-A	0.0	239.4	2183.0	1751.7	0.0	0.0	1.3	1.1	1.3	1.1	82.1
	Carbamazepine A-B	2521.2	1420.2	0.0	93.5	0.3	0.1	0.0	0.1	0.3	0.2	78.6
	Carbamazepine B-A	0.0	448.8	2521.2	2103.6	0.0	0.0	1.5	1.3	1.5	1.3	86.4
	Loperamide A-B	6795.3	3296.3	0.0	161.4	0.7	0.3	0.0	0.1	0.7	0.4	62.8
	Loperamide B-A	0.0	356.0	6795.3	5315.4	0.0	0.0	4.1	3.2	4.1	3.2	79.1
	Donepezil A-B	5457.2	3526.6	0.0	170.8	0.5	0.4	0.0	0.1	0.5	0.5	83.4
	Donepezil B-A	0.0	773.0	5457.2	3912.2	0.0	0.1	3.3	2.3	3.3	2.4	74.1
	Amprenavir A-B	1348.0	846.6	0.0	28.9	0.1	0.1	0.0	0.0	0.1	0.1	75.7
	Amprenavir B-A	0.0	127.7	1348.0	1165.9	0.0	0.0	0.8	0.7	0.8	0.7	88.1
	Chlorpromazine A-B	1108.6	99.0	0.0	10.3	0.1	0.0	0.0	0.0	0.1	0.0	14.5
	Chlorpromazine B-A	0.0	19.3	1108.6	341.7	0.0	0.0	0.7	0.2	0.7	0.2	31.1
	Thiopental A-B	1074.0	881.7	0.0	63.0	0.1	0.1	0.0	0.0	0.1	0.1	117.3
	Thiopental B-A	0.0	221.4	1074.0	955.8	0.0	0.0	0.6	0.6	0.6	0.6	92.4
	Topiramate A-B	1565.9	1234.5	0.0	32.1	0.2	0.1	0.0	0.0	0.2	0.1	91.1
	Topiramate B-A	0.0	172.9	1565.9	1756.5	0.0	0.0	0.9	1.1	0.9	1.1	114.0
	Primidone A-B	2581.6	2239.1	0.0	49.6	0.3	0.2	0.0	0.0	0.3	0.3	98.3
	Primidone B-A	0.0	286.7	2581.6	2225.7	0.0	0.0	1.5	1.3	1.5	1.4	88.1

Table A5.3 - Time Point 1 Replicate 3

Replicate	Compound (spiking)	Conc apical start (nM)	conc apical end (nM)	Conc basolateral start (nM)	Conc basolateral end (nM)	amount apical start (nmol)	amount apical end (nmol)	amount basolateral start (nmol)	amount basolateral end (nmol)	Total in well start (nmol)	Total in well end (nmol)	Recovery (%)
3	Haloperidol A-B	2183.0	1010.7	0.0	87.7	0.2	0.1	0.0	0.1	0.2	0.2	70.4
	Haloperidol B-A	0.0	156.7	2183.0	1679.1	0.0	0.0	1.3	1.0	1.3	1.0	78.1
	Carbamazepine A-B	2521.2	1280.2	0.0	20.5	0.3	0.1	0.0	0.0	0.3	0.1	55.7
	Carbamazepine B-A	0.0	449.3	2521.2	2332.1	0.0	0.0	1.5	1.4	1.5	1.4	95.5
	Loperamide A-B	6795.3	1914.2	0.0	106.5	0.7	0.2	0.0	0.1	0.7	0.3	37.6
	Loperamide B-A	0.0	231.1	6795.3	2431.3	0.0	0.0	4.1	1.5	4.1	1.5	36.3
	Donepezil A-B	5457.2	2513.0	0.0	127.1	0.5	0.3	0.0	0.1	0.5	0.3	60.0
	Donepezil B-A	0.0	368.9	5457.2	3351.7	0.0	0.0	3.3	2.0	3.3	2.0	62.5
	Amprenavir A-B	1348.0	1119.5	0.0	882.7	0.1	0.1	0.0	0.5	0.1	0.6	475.9
	Amprenavir B-A	0.0	88.5	1348.0	1172.5	0.0	0.0	0.8	0.7	0.8	0.7	88.1
	Chlorpromazine A-B	1108.6	64.7	0.0	7.5	0.1	0.0	0.0	0.0	0.1	0.0	9.9
	Chlorpromazine B-A	0.0	13.6	1108.6	171.0	0.0	0.0	0.7	0.1	0.7	0.1	15.6
	Thiopental A-B	1074.0	987.9	0.0	94.5	0.1	0.1	0.0	0.1	0.1	0.2	144.8
	Thiopental B-A	0.0	128.4	1074.0	1043.4	0.0	0.0	0.6	0.6	0.6	0.6	99.1
	Topiramate A-B	1565.9	1416.8	0.0	29.9	0.2	0.1	0.0	0.0	0.2	0.2	101.9
	Topiramate B-A	0.0	125.7	1565.9	1623.9	0.0	0.0	0.9	1.0	0.9	1.0	105.0
	Primidone A-B	2581.6	1887.7	0.0	33.7	0.3	0.2	0.0	0.0	0.3	0.2	80.9
	Primidone B-A	0.0	279.6	2581.6	3546.9	0.0	0.0	1.5	2.1	1.5	2.2	139.2

Table A5.4 - Time Point 2 Replicate 1

Replicate	Compound (spiking)	Conc apical start (nM)	conc apical end (nM)	Conc basolateral start (nM)	Conc basolateral end (nM)	amount apical start (nmol)	amount apical end (nmol)	amount basolateral start (nmol)	amount basolateral end (nmol)	Total in well start (nmol)	Total in well end (nmol)	Recovery (%)
1	Haloperidol A-B	2183.0	775.5	0.0	108.8	0.2	0.1	0.0	0.1	0.2	0.1	65.4
	Haloperidol B-A	0.0	535.2	2183.0	1802.2	0.0	0.1	1.3	1.1	1.3	1.1	86.6
	Carbamazepine A-B	2521.2	1402.2	0.0	144.3	0.3	0.1	0.0	0.1	0.3	0.2	89.9
	Carbamazepine B-A	0.0	811.8	2521.2	2167.7	0.0	0.1	1.5	1.3	1.5	1.4	91.3
	Loperamide A-B	6795.3	2530.3	0.0	199.5	0.7	0.3	0.0	0.1	0.7	0.4	54.9
	Loperamide B-A	0.0	985.5	6795.3	4959.7	0.0	0.1	4.1	3.0	4.1	3.1	75.4
	Donepezil A-B	5457.2	3333.5	0.0	287.8	0.5	0.3	0.0	0.2	0.5	0.5	92.7
	Donepezil B-A	0.0	1680.7	5457.2	5118.6	0.0	0.2	3.3	3.1	3.3	3.2	98.9
	Amprenavir A-B	1348.0	917.0	0.0	40.6	0.1	0.1	0.0	0.0	0.1	0.1	86.1
	Amprenavir B-A	0.0	176.6	1348.0	985.5	0.0	0.0	0.8	0.6	0.8	0.6	75.3
	Chlorpromazine A-B	1108.6	114.0	0.0	12.5	0.1	0.0	0.0	0.0	0.1	0.0	17.0
	Chlorpromazine B-A	0.0	95.4	1108.6	424.9	0.0	0.0	0.7	0.3	0.7	0.3	39.8
	Thiopental A-B	1074.0	731.6	0.0	94.5	0.1	0.1	0.0	0.1	0.1	0.1	120.9
	Thiopental B-A	0.0	375.3	1074.0	1042.6	0.0	0.0	0.6	0.6	0.6	0.7	102.9
	Topiramate A-B	1565.9	1267.6	0.0	63.9	0.2	0.1	0.0	0.0	0.2	0.2	105.4
	Topiramate B-A	0.0	347.8	1565.9	1615.6	0.0	0.0	0.9	1.0	0.9	1.0	106.9
	Primidone A-B	2581.6	1696.4	0.0	130.5	0.3	0.2	0.0	0.1	0.3	0.2	96.0
	Primidone B-A	0.0	615.4	2581.6	2359.2	0.0	0.1	1.5	1.4	1.5	1.5	95.4

Table A5.5 - Time Point 2 Replicate 2

Replicate	Compound (spiking)	Conc apical start (nM)	conc apical end (nM)	Conc basolateral start (nM)	Conc basolateral end (nM)	amount apical start (nmol)	amount apical end (nmol)	amount basolateral start (nmol)	amount basolateral end (nmol)	Total in well start (nmol)	Total in well end (nmol)	Recovery (%)
2	Haloperidol A-B	2183.0	807.6	0.0	107.7	0.2	0.1	0.0	0.1	0.2	0.1	66.6
	Haloperidol B-A	0.0	581.9	2183.0	1648.8	0.0	0.1	1.3	1.0	1.3	1.0	80.0
	Carbamazepine A-B	2521.2	1469.7	0.0	167.0	0.3	0.1	0.0	0.1	0.3	0.2	98.0
	Carbamazepine B-A	0.0	812.8	2521.2	2070.5	0.0	0.1	1.5	1.2	1.5	1.3	87.5
	Loperamide A-B	6795.3	2680.4	0.0	216.2	0.7	0.3	0.0	0.1	0.7	0.4	58.5
	Loperamide B-A	0.0	821.1	6795.3	4571.6	0.0	0.1	4.1	2.7	4.1	2.8	69.3
	Donepezil A-B	5457.2	2968.3	0.0	281.6	0.5	0.3	0.0	0.2	0.5	0.5	85.4
	Donepezil B-A	0.0	1287.2	5457.2	4752.5	0.0	0.1	3.3	2.9	3.3	3.0	91.0
	Amprenavir A-B	1348.0	912.1	0.0	99.1	0.1	0.1	0.0	0.1	0.1	0.2	111.8
	Amprenavir B-A	0.0	195.2	1348.0	1169.6	0.0	0.0	0.8	0.7	0.8	0.7	89.2
	Chlorpromazine A-B	1108.6	85.4	0.0	23.3	0.1	0.0	0.0	0.0	0.1	0.0	20.3
	Chlorpromazine B-A	0.0	39.2	1108.6	352.4	0.0	0.0	0.7	0.2	0.7	0.2	32.4
	Thiopental A-B	1074.0	776.7	0.0	102.0	0.1	0.1	0.0	0.1	0.1	0.1	129.3
	Thiopental B-A	0.0	349.9	1074.0	1041.0	0.0	0.0	0.6	0.6	0.6	0.7	102.4
	Topiramate A-B	1565.9	1217.9	0.0	85.9	0.2	0.1	0.0	0.1	0.2	0.2	110.7
	Topiramate B-A	0.0	408.3	1565.9	1574.2	0.0	0.0	0.9	0.9	0.9	1.0	104.9
	Primidone A-B	2581.6	1749.8	0.0	96.7	0.3	0.2	0.0	0.1	0.3	0.2	90.3
	Primidone B-A	0.0	513.1	2581.6	2354.7	0.0	0.1	1.5	1.4	1.5	1.5	94.5

Table A5.6 - Time Point 2 Replicate 3

Replicate	Compound (spiking)	Conc apical start (nM)	conc apical end (nM)	Conc basolateral start (nM)	Conc basolateral end (nM)	amount apical start (nmol)	amount apical end (nmol)	amount basolateral start (nmol)	amount basolateral end (nmol)	Total in well start (nmol)	Total in well end (nmol)	Recovery (%)
3	Haloperidol A-B	2183.0	792.0	0.0	89.3	0.2	0.1	0.0	0.1	0.2	0.1	60.8
	Haloperidol B-A	0.0	312.5	2183.0	1429.1	0.0	0.0	1.3	0.9	1.3	0.9	67.9
	Carbamazepine A-B	2521.2	1357.0	0.0	95.7	0.3	0.1	0.0	0.1	0.3	0.2	76.6
	Carbamazepine B-A	0.0	849.0	2521.2	2099.3	0.0	0.1	1.5	1.3	1.5	1.3	88.9
	Loperamide A-B	6795.3	1499.8	0.0	137.2	0.7	0.1	0.0	0.1	0.7	0.2	34.2
	Loperamide B-A	0.0	341.4	6795.3	2244.4	0.0	0.0	4.1	1.3	4.1	1.4	33.9
	Donepezil A-B	5457.2	2532.0	0.0	165.4	0.5	0.3	0.0	0.1	0.5	0.4	64.6
	Donepezil B-A	0.0	783.5	5457.2	3685.8	0.0	0.1	3.3	2.2	3.3	2.3	69.9
	Amprenavir A-B	1348.0	909.2	0.0	71.1	0.1	0.1	0.0	0.0	0.1	0.1	99.1
	Amprenavir B-A	0.0	186.1	1348.0	1110.5	0.0	0.0	0.8	0.7	0.8	0.7	84.7
	Chlorpromazine A-B	1108.6	41.5	0.0	5.5	0.1	0.0	0.0	0.0	0.1	0.0	6.7
	Chlorpromazine B-A	0.0	7.7	1108.6	90.4	0.0	0.0	0.7	0.1	0.7	0.1	8.3
	Thiopental A-B	1074.0	877.8	0.0	90.8	0.1	0.1	0.0	0.1	0.1	0.1	132.5
	Thiopental B-A	0.0	305.8	1074.0	1066.3	0.0	0.0	0.6	0.6	0.6	0.7	104.0
	Topiramate A-B	1565.9	1251.0	0.0	72.0	0.2	0.1	0.0	0.0	0.2	0.2	107.5
	Topiramate B-A	0.0	265.7	1565.9	1516.2	0.0	0.0	0.9	0.9	0.9	0.9	99.7
	Primidone A-B	2581.6	2038.9	0.0	135.9	0.3	0.2	0.0	0.1	0.3	0.3	110.6
	Primidone B-A	0.0	566.5	2581.6	3217.7	0.0	0.1	1.5	1.9	1.5	2.0	128.3

Table A5.7 - Time Point 3 Replicate 1

Replicate	Compound (spiking)	Conc apical start (nM)	conc apical end (nM)	Conc basolateral start (nM)	Conc basolateral end (nM)	amount apical start (nmol)	amount apical end (nmol)	amount basolateral start (nmol)	amount basolateral end (nmol)	Total in well start (nmol)	Total in well end (nmol)	Recovery (%)
1	Haloperidol A-B	2183.0	639.1	0.0	146.1	0.2	0.1	0.0	0.1	0.2	0.2	69.4
	Haloperidol B-A	0.0	914.8	2183.0	1937.3	0.0	0.1	1.3	1.2	1.3	1.3	95.7
	Carbamazepine A-B	2521.2	750.4	0.0	193.7	0.3	0.1	0.0	0.1	0.3	0.2	75.9
	Carbamazepine B-A	0.0	1257.2	2521.2	1906.3	0.0	0.1	1.5	1.1	1.5	1.3	83.9
	Loperamide A-B	6795.3	1483.9	0.0	256.9	0.7	0.1	0.0	0.2	0.7	0.3	44.5
	Loperamide B-A	0.0	1690.2	6795.3	4540.9	0.0	0.2	4.1	2.7	4.1	2.9	71.0
	Donepezil A-B	5457.2	2684.8	0.0	437.1	0.5	0.3	0.0	0.3	0.5	0.5	97.3
	Donepezil B-A	0.0	3156.1	5457.2	5043.4	0.0	0.3	3.3	3.0	3.3	3.3	102.1
	Amprenavir A-B	1348.0	779.7	0.0	70.2	0.1	0.1	0.0	0.0	0.1	0.1	89.1
	Amprenavir B-A	0.0	440.9	1348.0	976.9	0.0	0.0	0.8	0.6	0.8	0.6	77.9
	Chlorpromazine A-B	1108.6	60.8	0.0	13.6	0.1	0.0	0.0	0.0	0.1	0.0	12.9
	Chlorpromazine B-A	0.0	243.6	1108.6	271.1	0.0	0.0	0.7	0.2	0.7	0.2	28.1
	Thiopental A-B	1074.0	637.5	0.0	129.9	0.1	0.1	0.0	0.1	0.1	0.1	131.9
	Thiopental B-A	0.0	631.0	1074.0	991.6	0.0	0.1	0.6	0.6	0.6	0.7	102.1
	Topiramate A-B	1565.9	994.1	0.0	100.8	0.2	0.1	0.0	0.1	0.2	0.2	102.1
	Topiramate B-A	0.0	660.2	1565.9	1524.5	0.0	0.1	0.9	0.9	0.9	1.0	104.4
	Primidone A-B	2581.6	1358.3	0.0	118.5	0.3	0.1	0.0	0.1	0.3	0.2	80.2
	Primidone B-A	0.0	1180.4	2581.6	2568.3	0.0	0.1	1.5	1.5	1.5	1.7	107.1

Table A5.8 - Time Point 3 Replicate 2

Replicate	Compound (spiking)	Conc apical start (nM)	conc apical end (nM)	Conc basolateral start (nM)	Conc basolateral end (nM)	amount apical start (nmol)	amount apical end (nmol)	amount basolateral start (nmol)	amount basolateral end (nmol)	Total in well start (nmol)	Total in well end (nmol)	Recovery (%)
2	Haloperidol A-B	2183.0	606.7	0.0	144.6	0.2	0.1	0.0	0.1	0.2	0.1	67.5
	Haloperidol B-A	0.0	792.0	2183.0	1693.1	0.0	0.1	1.3	1.0	1.3	1.1	83.6
	Carbamazepine A-B	2521.2	1025.6	0.0	221.3	0.3	0.1	0.0	0.1	0.3	0.2	93.3
	Carbamazepine B-A	0.0	1129.5	2521.2	2080.6	0.0	0.1	1.5	1.2	1.5	1.4	90.0
	Loperamide A-B	6795.3	1846.3	0.0	213.6	0.7	0.2	0.0	0.1	0.7	0.3	46.0
	Loperamide B-A	0.0	1273.5	6795.3	5495.3	0.0	0.1	4.1	3.3	4.1	3.4	84.0
	Donepezil A-B	5457.2	2389.5	0.0	363.3	0.5	0.2	0.0	0.2	0.5	0.5	83.7
	Donepezil B-A	0.0	2427.9	5457.2	4417.9	0.0	0.2	3.3	2.7	3.3	2.9	88.4
	Amprenavir A-B	1348.0	812.0	0.0	68.9	0.1	0.1	0.0	0.0	0.1	0.1	90.9
	Amprenavir B-A	0.0	453.2	1348.0	1209.1	0.0	0.0	0.8	0.7	0.8	0.8	95.3
	Chlorpromazine A-B	1108.6	57.5	0.0	9.0	0.1	0.0	0.0	0.0	0.1	0.0	10.1
	Chlorpromazine B-A	0.0	112.4	1108.6	223.5	0.0	0.0	0.7	0.1	0.7	0.1	21.8
	Thiopental A-B	1074.0	553.1	0.0	130.9	0.1	0.1	0.0	0.1	0.1	0.1	124.6
	Thiopental B-A	0.0	520.3	1074.0	983.1	0.0	0.1	0.6	0.6	0.6	0.6	99.6
	Topiramate A-B	1565.9	1002.4	0.0	109.1	0.2	0.1	0.0	0.1	0.2	0.2	105.8
	Topiramate B-A	0.0	504.4	1565.9	1458.2	0.0	0.1	0.9	0.9	0.9	0.9	98.5
	Primidone A-B	2581.6	1496.2	0.0	166.1	0.3	0.1	0.0	0.1	0.3	0.2	96.6
	Primidone B-A	0.0	1207.0	2581.6	3191.0	0.0	0.1	1.5	1.9	1.5	2.0	131.4

Table A5.9 - Time Point 3 Replicate 3

Replicate	Compound (spiking)	Conc apical start (nM)	conc apical end (nM)	Conc basolateral start (nM)	Conc basolateral end (nM)	amount apical start (nmol)	amount apical end (nmol)	amount basolateral start (nmol)	amount basolateral end (nmol)	Total in well start (nmol)	Total in well end (nmol)	Recovery (%)
3	Haloperidol A-B	2183.0	602.4	0.0	121.3	0.2	0.1	0.0	0.1	0.2	0.1	60.9
	Haloperidol B-A	0.0	646.7	2183.0	1401.1	0.0	0.1	1.3	0.8	1.3	0.9	69.1
	Carbamazepine A-B	2521.2	920.3	0.0	247.8	0.3	0.1	0.0	0.1	0.3	0.2	95.5
	Carbamazepine B-A	0.0	1407.6	2521.2	2136.5	0.0	0.1	1.5	1.3	1.5	1.4	94.0
	Loperamide A-B	6795.3	1085.6	0.0	160.4	0.7	0.1	0.0	0.1	0.7	0.2	30.1
	Loperamide B-A	0.0	842.9	6795.3	2825.1	0.0	0.1	4.1	1.7	4.1	1.8	43.6
	Donepezil A-B	5457.2	1902.8	0.0	250.0	0.5	0.2	0.0	0.1	0.5	0.3	62.4
	Donepezil B-A	0.0	2171.5	5457.2	4016.6	0.0	0.2	3.3	2.4	3.3	2.6	80.2
	Amprenavir A-B	1348.0	882.7	0.0	67.8	0.1	0.1	0.0	0.0	0.1	0.1	95.6
	Amprenavir B-A	0.0	452.0	1348.0	1350.0	0.0	0.0	0.8	0.8	0.8	0.9	105.7
	Chlorpromazine A-B	1108.6	41.4	0.0	9.1	0.1	0.0	0.0	0.0	0.1	0.0	8.7
	Chlorpromazine B-A	0.0	44.9	1108.6	276.6	0.0	0.0	0.7	0.2	0.7	0.2	25.6
	Thiopental A-B	1074.0	675.9	0.0	133.4	0.1	0.1	0.0	0.1	0.1	0.1	137.5
	Thiopental B-A	0.0	415.0	1074.0	852.6	0.0	0.0	0.6	0.5	0.6	0.6	85.8
	Topiramate A-B	1565.9	1151.6	0.0	85.1	0.2	0.1	0.0	0.1	0.2	0.2	106.1
	Topiramate B-A	0.0	485.3	1565.9	1541.1	0.0	0.0	0.9	0.9	0.9	1.0	103.6
	Primidone A-B	2581.6	1852.1	0.0	163.5	0.3	0.2	0.0	0.1	0.3	0.3	109.7
	Primidone B-A	0.0	900.1	2581.6	2323.6	0.0	0.1	1.5	1.4	1.5	1.5	95.8

Table A5.10 - Time Point 1 Replicate 1

Replicate	Substrate	initial concentration in donor (µM)	Change in time (s)	Growth area (cm^2)	Final concentration in donor (µM)	Change in concentration (µM)	Papp (cm/s)	Efflux ratio (B-A/A-B)	Vd (cm^3)	Vr (cm^3)	Ct	Pexact (cm/s)	Efflux Ratio (B-A/A-B)
1	Haloperidol A-B	2.2	1800.0	0.3	1.1	1.1	4.09E-05		0.1	0.6	228.9	7.03E-05	0.2
	Haloperidol B-A	2.2	1800.0	0.3	2.5	-0.3	1.82E-05	0.4	0.6	0.1	2155.9	1.67E-05	
	Carbamazepine A-B	2.5	1800.0	0.3	1.5	1.0	1.98E-05		0.1	0.6	256.1	3.09E-05	1.4
	Carbamazepine B-A	2.5	1800.0	0.3	2.0	0.5	3.02E-05	1.5	0.6	0.1	1765.7	4.26E-05	
	Loperamide A-B	6.8	1800.0	0.3	2.6	4.2	2.23E-05		0.1	0.6	493.2	5.25E-05	0.3
	Loperamide B-A	6.8	1800.0	0.3	5.6	1.2	1.37E-05	0.6	0.6	0.1	4878.3	1.74E-05	
	Donepezil A-B	5.5	1800.0	0.3	3.7	1.8	2.92E-05		0.1	0.6	658.6	3.95E-05	0.5
	Donepezil B-A	5.5	1800.0	0.3	5.3	0.1	2.00E-05	0.7	0.6	0.1	4671.3	2.16E-05	
	Amprenavir A-B	1.3	1800.0	0.3	1.0	0.4	2.14E-05		0.1	0.6	164.4	2.75E-05	1.6
	Amprenavir B-A	1.3	1800.0	0.3	0.6	0.7	1.74E-05	0.8	0.6	0.1	543.9	4.26E-05	
	Chlorpromazine A-B	1.1	1800.0	0.3	0.2	0.9	1.23E-05		0.1	0.6	37.6	6.39E-05	0.9
	Chlorpromazine B-A	1.1	1800.0	0.3	0.3	0.8	1.49E-05	1.2	0.6	0.1	311.9	5.45E-05	
	Thiopental A-B	1.1	1800.0	0.3	0.9	0.2	5.93E-05		0.1	0.6	184.9	6.01E-05	0.9
	Thiopental B-A	1.1	1800.0	0.3	0.9	0.2	3.99E-05	0.7	0.6	0.1	791.0	5.6E-05	
	Topiramate A-B	1.6	1800.0	0.3	1.3	0.3	2.21E-05		0.1	0.6	216.3	2.48E-05	1.0
	Topiramate B-A	1.6	1800.0	0.3	1.5	0.1	2.23E-05	1.0	0.6	0.1	1322.2	2.47E-05	
	Primidone A-B	2.6	1800.0	0.3	2.0	0.6	1.57E-05		0.1	0.6	324.3	1.9E-05	1.3
	Primidone B-A	2.6	1800.0	0.3	2.7	-0.1	2.49E-05	1.6	0.6	0.1	2366.4	2.54E-05	

Table A5.11 - Time Point 1 Replicate 2

Replicate	Substrate	initial concentration in donor (µM)	Change in time (s)	Growth area (cm^2)	Final concentration in donor (µM)	Change in concentration (µM)	Papp (cm/s)	Efflux ratio (B-A/A-B)	Vd (cm^3)	Vr (cm^3)	Ct	Pexact (cm/s)	Efflux Ratio (B-A/A-B)
2	Haloperidol A-B	2.2	1800.0	0.3	1.1	1.1	4.50E-05		0.1	0.6	237.2	7.61E-05	0.3
	Haloperidol B-A	2.2	1800.0	0.3	1.8	0.4	1.85E-05	0.4	0.6	0.1	1535.6	2.45E-05	
	Carbamazepine A-B	2.5	1800.0	0.3	1.4	1.1	3.75E-05		0.1	0.6	283.1	5.79E-05	0.7
	Carbamazepine B-A	2.5	1800.0	0.3	2.1	0.4	3.00E-05	0.8	0.6	0.1	1867.2	3.97E-05	
	Loperamide A-B	6.8	1800.0	0.3	3.3	3.5	2.40E-05		0.1	0.6	609.2	4.44E-05	0.3
	Loperamide B-A	6.8	1800.0	0.3	5.3	1.5	8.82E-06	0.4	0.6	0.1	4606.9	1.16E-05	
	Donepezil A-B	5.5	1800.0	0.3	3.5	1.9	3.16E-05		0.1	0.6	650.2	4.4E-05	0.8
	Donepezil B-A	5.5	1800.0	0.3	3.9	1.5	2.38E-05	0.8	0.6	0.1	3463.8	3.64E-05	
	Amprenavir A-B	1.3	1800.0	0.3	0.8	0.5	2.17E-05		0.1	0.6	145.8	3.19E-05	0.6
	Amprenavir B-A	1.3	1800.0	0.3	1.2	0.2	1.60E-05	0.7	0.6	0.1	1017.6	1.94E-05	
	Chlorpromazine A-B	1.1	1800.0	0.3	0.1	1.0	9.37E-06		0.1	0.6	23.0	8.57E-05	0.1
	Chlorpromazine B-A	1.1	1800.0	0.3	0.3	0.8	2.93E-06	0.3	0.6	0.1	295.7	9.75E-06	
	Thiopental A-B	1.1	1800.0	0.3	0.9	0.2	5.93E-05		0.1	0.6	180.0	6.22E-05	0.7
	Thiopental B-A	1.1	1800.0	0.3	1.0	0.1	3.47E-05	0.6	0.6	0.1	850.9	4.35E-05	
	Topiramate A-B	1.6	1800.0	0.3	1.2	0.3	2.07E-05		0.1	0.6	203.8	2.47E-05	0.7
	Topiramate B-A	1.6	1800.0	0.3	1.8	-0.2	1.86E-05	0.9	0.6	0.1	1530.3	1.73E-05	
	Primidone A-B	2.6	1800.0	0.3	2.2	0.3	1.94E-05		0.1	0.6	362.4	2.12E-05	1.1
	Primidone B-A	2.6	1800.0	0.3	2.2	0.4	1.87E-05	1.0	0.6	0.1	1948.7	2.3E-05	

Table A5.12 - Time Point 1 Replicate 3

Replicate	Substrate	initial concentration in donor (µM)	Change in time (s)	Growth area (cm^2)	Final concentration in donor (µM)	Change in concentration (µM)	Papp (cm/s)	Efflux ratio (B-A/A-B)	Vd (cm^3)	Vr (cm^3)	Ct	Pexact (cm/s)	Efflux Ratio (B-A/A-B)
3	Haloperidol A-B	2.2	1800.0	0.3	1.0	1.2	4.06E-05		0.1	0.6	219.5	7.36E-05	0.2
	Haloperidol B-A	2.2	1800.0	0.3	1.7	0.5	1.21E-05	0.3	0.6	0.1	1461.6	1.64E-05	
	Carbamazepine A-B	2.5	1800.0	0.3	1.3	1.2	8.23E-06		0.1	0.6	200.5	1.56E-05	2.3
	Carbamazepine B-A	2.5	1800.0	0.3	2.3	0.2	3.00E-05	3.6	0.6	0.1	2063.1	3.54E-05	
	Loperamide A-B	6.8	1800.0	0.3	1.9	4.9	1.58E-05		0.1	0.6	364.8	4.98E-05	0.3
	Loperamide B-A	6.8	1800.0	0.3	2.4	4.4	5.72E-06	0.4	0.6	0.1	2117.0	1.67E-05	
	Donepezil A-B	5.5	1800.0	0.3	2.5	2.9	2.35E-05		0.1	0.6	467.9	4.57E-05	0.4
	Donepezil B-A	5.5	1800.0	0.3	3.4	2.1	1.14E-05	0.5	0.6	0.1	2925.6	1.94E-05	
	Amprenavir A-B	1.3	1800.0	0.3	1.1	0.2	6.61E-04		0.1	0.6	916.5	0.000476	0.0
	Amprenavir B-A	1.3	1800.0	0.3	1.2	0.2	1.11E-05	0.0	0.6	0.1	1017.6	1.31E-05	
	Chlorpromazine A-B	1.1	1800.0	0.3	0.1	1.0	6.84E-06		0.1	0.6	15.7	9.41E-05	0.1
	Chlorpromazine B-A	1.1	1800.0	0.3	0.2	0.9	2.06E-06	0.3	0.6	0.1	148.5	1.38E-05	
	Thiopental A-B	1.1	1800.0	0.3	1.0	0.1	8.89E-05		0.1	0.6	222.2	8E-05	0.3
	Thiopental B-A	1.1	1800.0	0.3	1.0	0.0	2.01E-05	0.2	0.6	0.1	912.7	2.19E-05	
	Topiramate A-B	1.6	1800.0	0.3	1.4	0.1	1.93E-05		0.1	0.6	228.0	2.03E-05	0.7
	Topiramate B-A	1.6	1800.0	0.3	1.6	-0.1	1.35E-05	0.7	0.6	0.1	1409.9	1.35E-05	
	Primidone A-B	2.6	1800.0	0.3	1.9	0.7	1.32E-05		0.1	0.6	298.5	1.73E-05	0.8
	Primidone B-A	2.6	1800.0	0.3	3.5	-1.0	1.82E-05	1.4	0.6	0.1	3080.1	1.37E-05	

Table A5.13 - Time Point 2 Replicate 1

Replicate	Substrate	initial concentration in donor (µM)	Change in time (s)	Growth area (cm^2)	Final concentration in donor (µM)	Change in concentration (µM)	Papp (cm/s)	Efflux ratio (B-A/A-B)	Vd (cm^3)	Vr (cm^3)	Ct	Pexact (cm/s)	Efflux Ratio (B-A/A-B)
1	Haloperidol A-B	2.2	3600.0	0.3	0.8	1.4	2.5E-05		0.1	0.6	204.1	5.50E-05	0.5
	Haloperidol B-A	2.2	3600.0	0.3	1.8	0.4	2.1E-05	0.8	0.6	0.1	1621.2	2.89E-05	
	Carbamazepine A-B	2.5	3600.0	0.3	1.4	1.1	2.9E-05		0.1	0.6	324.0	4.25E-05	0.9
	Carbamazepine B-A	2.5	3600.0	0.3	2.2	0.4	2.7E-05	0.9	0.6	0.1	1974.0	3.82E-05	
	Loperamide A-B	6.8	3600.0	0.3	2.5	4.3	1.5E-05		0.1	0.6	532.5	3.39E-05	0.5
	Loperamide B-A	6.8	3600.0	0.3	5.0	1.8	1.2E-05	0.8	0.6	0.1	4391.9	1.83E-05	
	Donepezil A-B	5.5	3600.0	0.3	3.3	2.1	2.7E-05		0.1	0.6	722.9	3.66E-05	0.9
	Donepezil B-A	5.5	3600.0	0.3	5.1	0.3	2.6E-05	1.0	0.6	0.1	4627.5	3.26E-05	
	Amprenavir A-B	1.3	3600.0	0.3	0.9	0.4	1.5E-05		0.1	0.6	165.8	2.03E-05	0.8
	Amprenavir B-A	1.3	3600.0	0.3	1.0	0.4	1.1E-05	0.7	0.6	0.1	869.9	1.64E-05	
	Chlorpromazine A-B	1.1	3600.0	0.3	0.1	1.0	5.7E-06		0.1	0.6	27.0	4.49E-05	0.5
	Chlorpromazine B-A	1.1	3600.0	0.3	0.4	0.7	7.2E-06	1.3	0.6	0.1	377.8	2.10E-05	
	Thiopental A-B	1.1	3600.0	0.3	0.7	0.3	4.4E-05		0.1	0.6	185.5	5.14E-05	0.7
	Thiopental B-A	1.1	3600.0	0.3	1.0	0.0	2.9E-05	0.7	0.6	0.1	947.2	3.64E-05	
	Topiramate A-B	1.6	3600.0	0.3	1.3	0.3	2.1E-05		0.1	0.6	235.8	2.28E-05	0.9
	Topiramate B-A	1.6	3600.0	0.3	1.6	0.0	1.9E-05	0.9	0.6	0.1	1434.5	2.00E-05	
	Primidone A-B	2.6	3600.0	0.3	1.7	0.9	2.6E-05		0.1	0.6	354.2	3.32E-05	0.8
	Primidone B-A	2.6	3600.0	0.3	2.4	0.2	2.0E-05	0.8	0.6	0.1	2110.1	2.49E-05	

Table A5.14 - Time Point 2 Replicate 2

Replicate	Substrate	initial concentration in donor (µM)	Change in time (s)	Growth area (cm^2)	Final concentration in donor (µM)	Change in concentration (µM)	Papp (cm/s)	Efflux ratio (B-A/A-B)	Vd (cm^3)	Vr (cm^3)	Ct	Pexact (cm/s)	Efflux Ratio (B-A/A-B)
2	Haloperidol A-B	2.2	3600.0	0.3	0.8	1.4	2.5E-05		0.1	0.6	207.6	5.27E-05	0.7
	Haloperidol B-A	2.2	3600.0	0.3	1.6	0.5	2.2E-05	0.9	0.6	0.1	1496.4	3.55E-05	
	Carbamazepine A-B	2.5	3600.0	0.3	1.5	1.1	3.3E-05		0.1	0.6	353.1	4.62E-05	0.9
	Carbamazepine B-A	2.5	3600.0	0.3	2.1	0.5	2.7E-05	0.8	0.6	0.1	1890.9	4.05E-05	
	Loperamide A-B	6.8	3600.0	0.3	2.7	4.1	1.6E-05		0.1	0.6	568.3	3.46E-05	0.5
	Loperamide B-A	6.8	3600.0	0.3	4.6	2.2	1.0E-05	0.6	0.6	0.1	4035.8	1.64E-05	
	Donepezil A-B	5.5	3600.0	0.3	3.0	2.5	2.6E-05		0.1	0.6	665.4	3.97E-05	0.7
	Donepezil B-A	5.5	3600.0	0.3	4.8	0.7	2.0E-05	0.8	0.6	0.1	4257.5	2.6E-05	
	Amprenavir A-B	1.3	3600.0	0.3	0.9	0.4	3.7E-05		0.1	0.6	215.2	4.45E-05	0.3
	Amprenavir B-A	1.3	3600.0	0.3	1.2	0.2	1.2E-05	0.3	0.6	0.1	1030.4	1.52E-05	
	Chlorpromazine A-B	1.1	3600.0	0.3	0.1	1.0	1.1E-05		0.1	0.6	32.2	9.3E-05	0.1
	Chlorpromazine B-A	1.1	3600.0	0.3	0.4	0.8	3.0E-06	0.3	0.6	0.1	307.7	9.82E-06	
	Thiopental A-B	1.1	3600.0	0.3	0.8	0.3	4.8E-05		0.1	0.6	198.3	5.21E-05	0.6
	Thiopental B-A	1.1	3600.0	0.3	1.0	0.0	2.7E-05	0.6	0.6	0.1	942.3	3.35E-05	
	Topiramate A-B	1.6	3600.0	0.3	1.2	0.3	2.8E-05		0.1	0.6	247.6	3.07E-05	0.8
	Topiramate B-A	1.6	3600.0	0.3	1.6	0.0	2.2E-05	0.8	0.6	0.1	1407.7	2.47E-05	
	Primidone A-B	2.6	3600.0	0.3	1.7	0.8	1.9E-05		0.1	0.6	332.9	2.48E-05	0.8
	Primidone B-A	2.6	3600.0	0.3	2.4	0.2	1.7E-05	0.9	0.6	0.1	2091.6	2.03E-05	

Table A5.15 - Time Point 2 Replicate 3

Replicate	Substrate	initial concentration in donor (µM)	Change in time (s)	Growth area (cm^2)	Final concentration in donor (µM)	Change in concentration (µM)	Papp (cm/s)	Efflux ratio (B-A/A-B)	Vd (cm^3)	Vr (cm^3)	Ct	Pexact (cm/s)	Efflux Ratio (B-A/A-B)
3	Haloperidol A-B	2.2	3600.0	0.3	0.8	1.4	2.1E-05		0.1	0.6	189.7	4.59E-05	0.4
	Haloperidol B-A	2.2	3600.0	0.3	1.4	0.8	1.2E-05	0.6	0.6	0.1	1269.6	2.04E-05	
	Carbamazepine A-B	2.5	3600.0	0.3	1.4	1.2	1.9E-05		0.1	0.6	275.9	3.07E-05	1.4
	Carbamazepine B-A	2.5	3600.0	0.3	2.1	0.4	2.8E-05	1.5	0.6	0.1	1920.6	4.21E-05	
	Loperamide A-B	6.8	3600.0	0.3	1.5	5.3	1.0E-05		0.1	0.6	331.8	3.85E-05	0.4
	Loperamide B-A	6.8	3600.0	0.3	2.2	4.6	4.2E-06	0.4	0.6	0.1	1972.6	1.37E-05	
	Donepezil A-B	5.5	3600.0	0.3	2.5	2.9	1.5E-05		0.1	0.6	503.5	2.87E-05	0.7
	Donepezil B-A	5.5	3600.0	0.3	3.7	1.8	1.2E-05	0.8	0.6	0.1	3271.2	1.98E-05	
	Amprenavir A-B	1.3	3600.0	0.3	0.9	0.4	2.7E-05		0.1	0.6	190.8	3.36E-05	0.5
	Amprenavir B-A	1.3	3600.0	0.3	1.1	0.2	1.2E-05	0.4	0.6	0.1	978.5	1.52E-05	
	Chlorpromazine A-B	1.1	3600.0	0.3	0.0	1.1	2.5E-06		0.1	0.6	10.6	5.23E-05	0.1
	Chlorpromazine B-A	1.1	3600.0	0.3	0.1	1.0	5.8E-07	0.2	0.6	0.1	78.6	7.39E-06	
	Thiopental A-B	1.1	3600.0	0.3	0.9	0.2	4.3E-05		0.1	0.6	203.3	4.27E-05	0.6
	Thiopental B-A	1.1	3600.0	0.3	1.1	0.0	2.4E-05	0.6	0.6	0.1	957.6	2.78E-05	
	Topiramate A-B	1.6	3600.0	0.3	1.3	0.3	2.3E-05		0.1	0.6	240.4	2.57E-05	0.6
	Topiramate B-A	1.6	3600.0	0.3	1.5	0.0	1.4E-05	0.6	0.6	0.1	1337.6	1.6E-05	
	Primidone A-B	2.6	3600.0	0.3	2.0	0.5	2.7E-05		0.1	0.6	407.7	2.92E-05	0.5
	Primidone B-A	2.6	3600.0	0.3	3.2	-0.6	1.8E-05	0.7	0.6	0.1	2839.0	1.61E-05	

Table A5.16 - Time Point 3 Replicate 1

Replicate	Substrate	initial concentration in donor (µM)	Change in time (s)	Growth area (cm^2)	Final concentration in donor (µM)	Change in concentration (µM)	Papp (cm/s)	Efflux ratio (B-A/A-B)	Vd (cm^3)	Vr (cm^3)	Ct	Pexact (cm/s)	Efflux Ratio (B-A/A-B)
1	Haloperidol A-B	2.2	7200.0	0.3	0.6	1.5	1.69E-05		0.1	0.6	216.5	4.05E-05	0.6
	Haloperidol B-A	2.2	7200.0	0.3	1.9	0.2	1.76E-05	1.0	0.6	0.1	1791.2	2.58E-05	
	Carbamazepine A-B	2.5	7200.0	0.3	0.8	1.8	1.94E-05		0.1	0.6	273.2	4.45E-05	1.0
	Carbamazepine B-A	2.5	7200.0	0.3	1.9	0.6	2.10E-05	1.1	0.6	0.1	1813.6	4.26E-05	
	Loperamide A-B	6.8	7200.0	0.3	1.5	5.3	9.55E-06		0.1	0.6	432.2	3.26E-05	0.6
	Loperamide B-A	6.8	7200.0	0.3	4.5	2.3	1.05E-05	1.1	0.6	0.1	4133.7	1.90E-05	
	Donepezil A-B	5.5	7200.0	0.3	2.7	2.8	2.02E-05		0.1	0.6	758.2	3.10E-05	1.3
	Donepezil B-A	5.5	7200.0	0.3	5.0	0.4	2.43E-05	1.2	0.6	0.1	4773.8	3.90E-05	
	Amprenavir A-B	1.3	7200.0	0.3	0.8	0.6	1.31E-05		0.1	0.6	171.6	1.90E-05	1.3
	Amprenavir B-A	1.3	7200.0	0.3	1.0	0.4	1.38E-05	1.0	0.6	0.1	900.3	2.43E-05	
	Chlorpromazine A-B	1.1	7200.0	0.3	0.1	1.0	3.10E-06		0.1	0.6	20.4	3.98E-05	2.2
	Chlorpromazine B-A	1.1	7200.0	0.3	0.3	0.8	9.25E-06	3.0	0.6	0.1	267.2	8.75E-05	
	Thiopental A-B	1.1	7200.0	0.3	0.6	0.4	3.05E-05		0.1	0.6	202.4	3.70E-05	1.1
	Thiopental B-A	1.1	7200.0	0.3	1.0	0.1	2.47E-05	0.8	0.6	0.1	940.1	4.01E-05	
	Topiramate A-B	1.6	7200.0	0.3	1.0	0.6	1.63E-05		0.1	0.6	228.5	2.10E-05	1.1
	Topiramate B-A	1.6	7200.0	0.3	1.5	0.0	1.77E-05	1.1	0.6	0.1	1401.0	2.30E-05	
	Primidone A-B	2.6	7200.0	0.3	1.4	1.2	1.16E-05		0.1	0.6	295.6	1.85E-05	1.3
	Primidone B-A	2.6	7200.0	0.3	2.6	0.0	1.92E-05	1.7	0.6	0.1	2370.0	2.49E-05	

Table A5.17 - Time Point 3 Replicate 2

Replicate	Substrate	initial concentration in donor (µM)	Change in time (s)	Growth area (cm^2)	Final concentration in donor (µM)	Change in concentration (µM)	Papp (cm/s)	Efflux ratio (B-A/A-B)	Vd (cm^3)	Vr (cm^3)	Ct	Pexact (cm/s)	Efflux Ratio (B-A/A-B)
2	Haloperidol A-B	2.2	7200.0	0.3	0.6	1.6	1.67E-05		0.1	0.6	210.6	4.19E-05	0.6
	Haloperidol B-A	2.2	7200.0	0.3	1.7	0.5	1.53E-05	0.9	0.6	0.1	1564.4	2.55E-05	
	Carbamazepine A-B	2.5	7200.0	0.3	1.0	1.5	2.22E-05		0.1	0.6	336.2	3.87E-05	0.8
	Carbamazepine B-A	2.5	7200.0	0.3	2.1	0.4	1.89E-05	0.9	0.6	0.1	1944.7	3.14E-05	
	Loperamide A-B	6.8	7200.0	0.3	1.8	4.9	7.94E-06		0.1	0.6	446.9	2.35E-05	0.5
	Loperamide B-A	6.8	7200.0	0.3	5.5	1.3	7.89E-06	1.0	0.6	0.1	4892.2	1.09E-05	
	Donepezil A-B	5.5	7200.0	0.3	2.4	3.1	1.68E-05		0.1	0.6	652.8	2.93E-05	1.1
	Donepezil B-A	5.5	7200.0	0.3	4.4	1.0	1.87E-05	1.1	0.6	0.1	4133.6	3.19E-05	
	Amprenavir A-B	1.3	7200.0	0.3	0.8	0.5	1.29E-05		0.1	0.6	175.1	1.81E-05	1.1
	Amprenavir B-A	1.3	7200.0	0.3	1.2	0.1	1.41E-05	1.1	0.6	0.1	1101.1	1.91E-05	
	Chlorpromazine A-B	1.1	7200.0	0.3	0.1	1.1	2.06E-06		0.1	0.6	15.9	3.01E-05	0.9
	Chlorpromazine B-A	1.1	7200.0	0.3	0.2	0.9	4.27E-06	2.1	0.6	0.1	207.6	2.81E-05	
	Thiopental A-B	1.1	7200.0	0.3	0.6	0.5	3.08E-05		0.1	0.6	191.2	4.16E-05	0.7
	Thiopental B-A	1.1	7200.0	0.3	1.0	0.1	2.04E-05	0.7	0.6	0.1	917.0	3.02E-05	
	Topiramate A-B	1.6	7200.0	0.3	1.0	0.6	1.76E-05		0.1	0.6	236.7	2.23E-05	0.8
	Topiramate B-A	1.6	7200.0	0.3	1.5	0.1	1.36E-05	0.8	0.6	0.1	1321.9	1.73E-05	
	Primidone A-B	2.6	7200.0	0.3	1.5	1.1	1.62E-05		0.1	0.6	356.1	2.27E-05	0.9
	Primidone B-A	2.6	7200.0	0.3	3.2	-0.6	1.97E-05	1.2	0.6	0.1	2907.6	1.93E-05	

Table A5.18 - Time Point 3 Replicate 3

Replicate	Substrate	initial concentration in donor (µM)	Change in time (s)	Growth area (cm^2)	Final concentration in donor (µM)	Change in concentration (µM)	Papp (cm/s)	Efflux ratio (B-A/A-B)	Vd (cm^3)	Vr (cm^3)	Ct	Pexact (cm/s)	Efflux Ratio (B-A/A-B)
3	Haloperidol A-B	2.2	7200.0	0.3	0.6	1.6	1.40E-05		0.1	0.6	190.0	3.67E-05	0.7
	Haloperidol B-A	2.2	7200.0	0.3	1.4	0.8	1.25E-05	0.9	0.6	0.1	1293.3	2.50E-05	
	Carbamazepine A-B	2.5	7200.0	0.3	0.9	1.6	2.48E-05		0.1	0.6	343.9	4.60E-05	0.9
	Carbamazepine B-A	2.5	7200.0	0.3	2.1	0.4	2.35E-05	0.9	0.6	0.1	2032.4	4.26E-05	
	Loperamide A-B	6.8	7200.0	0.3	1.1	5.7	5.96E-06		0.1	0.6	292.6	2.87E-05	0.5
	Loperamide B-A	6.8	7200.0	0.3	2.8	4.0	5.22E-06	0.9	0.6	0.1	2541.9	1.45E-05	
	Donepezil A-B	5.5	7200.0	0.3	1.9	3.6	1.16E-05		0.1	0.6	486.1	2.60E-05	1.2
	Donepezil B-A	5.5	7200.0	0.3	4.0	1.4	1.67E-05	1.4	0.6	0.1	3753.0	3.12E-05	
	Amprenavir A-B	1.3	7200.0	0.3	0.9	0.5	1.27E-05		0.1	0.6	184.2	1.66E-05	1.0
	Amprenavir B-A	1.3	7200.0	0.3	1.3	0.0	1.41E-05	1.1	0.6	0.1	1221.7	1.67E-05	
	Chlorpromazine A-B	1.1	7200.0	0.3	0.0	1.1	2.07E-06		0.1	0.6	13.7	3.93E-05	0.2
	Chlorpromazine B-A	1.1	7200.0	0.3	0.3	0.8	1.70E-06	0.8	0.6	0.1	243.5	7.35E-06	
	Thiopental A-B	1.1	7200.0	0.3	0.7	0.4	3.14E-05		0.1	0.6	210.9	3.61E-05	0.7
	Thiopental B-A	1.1	7200.0	0.3	0.9	0.2	1.63E-05	0.5	0.6	0.1	790.1	2.69E-05	
	Topiramate A-B	1.6	7200.0	0.3	1.2	0.4	1.37E-05		0.1	0.6	237.5	1.60E-05	1.0
	Topiramate B-A	1.6	7200.0	0.3	1.5	0.0	1.30E-05	1.0	0.6	0.1	1390.2	1.55E-05	
	Primidone A-B	2.6	7200.0	0.3	1.9	0.7	1.60E-05		0.1	0.6	404.7	1.87E-05	1.1
	Primidone B-A	2.6	7200.0	0.3	2.3	0.3	1.47E-05	0.9	0.6	0.1	2120.2	1.99E-05	

Appendix 6

Negative control immunofluorescence images for Figure 3.6 (aSMA - Fig A6.1) and Figure 3.9 (ZO-1 - Fig A6.2). Negative control images were not stained with primary antibody against the target protein; primary antibody was replaced with 2% NGS in PBS. All other methodology was followed as per Section 2.3.4.

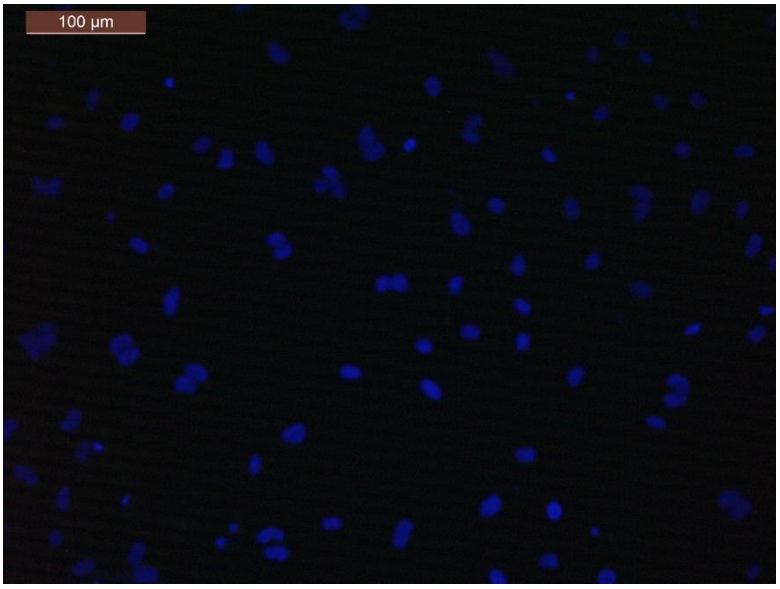

Figure A6.1 – Negative control image for fig 3.6 with no primary antibody was added, secondary staining and DAPI counter staining were carried out as per section 2.3.4.

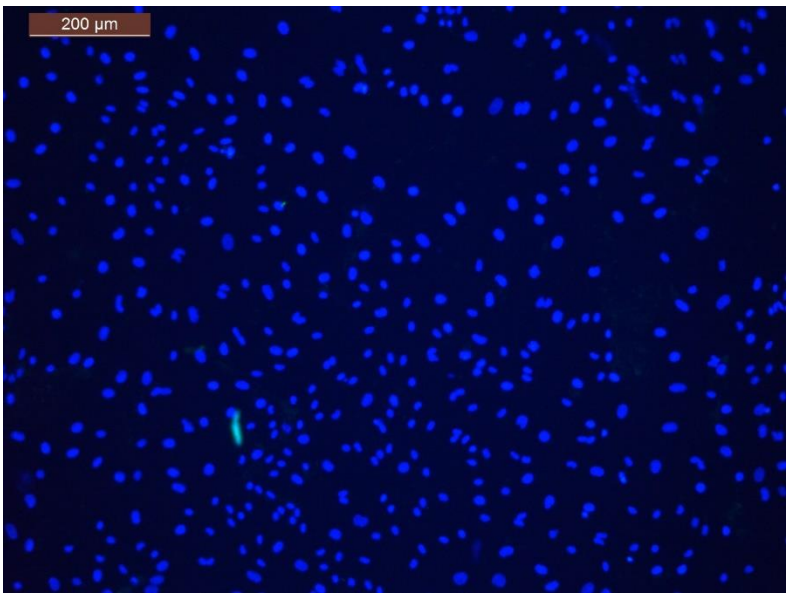

Figure A6.2 - Negative control image for fig 3.9 with no primary antibody was added, secondary staining and DAPI counter staining were carried out as per section 2.3.4

“All models are wrong,

but some are useful.”

- George EP Box